Institut für Geowissenschaften
Sektion 3.2 Deformation und Rheologie des GFZ Potsdam

Fracture Toughness Determination and Micromechanics of Rock Under Mode I and Mode II Loading

Dissertation
zur Erlangung des akademischen Grades
"doctor rerum naturalium"
(Dr. rer. nat.)
in der Wissenschaftsdisziplin " Geologie "

eingereicht an der
Mathematisch-Naturwissenschaftlichen Fakultät
der Universität Potsdam

von
Tobias Backers

Potsdam, den 12. August 2004

Doctoral Thesis
by
Tobias Backers

Supervised by
Prof. Dr. rer. nat. Georg Dresen and Prof. Ove Stephansson, PhD.

Submitted to
University of Potsdam, Germany

2004 – 08 – 12

A pdf-version of the thesis is available through the author.

Set in 9/10/11/12/14 pt Garamond.

This thesis is dedicated to Yvonne Backers. Much too young my mother died.

ACKNOWLEDGEMENTS/CREDITS

I debt my gratitude to a lot of people who helped me to pass the hassles of this thesis. This includes people at the GeoForschungsZentrum (GFZ) Potsdam, Germany, at the Royal Institute of Technology (KTH) in Stockholm, Sweden, and at the Ruhr-Universität Bochum, Germany, but also my friends and family.

I acknowledge the financial support of this work through GFZ and DFG grant DR 213/9-1 and DR 213/9-3.

I want to thank my supervisors, Prof. Dr. rer. nat. Georg Dresen and Prof. Dr. Ove Stephansson for their valuable advice and guidance through my studies. Numerous and intense discussions improved my understanding of fracture mechanics and rock mechanics both from a microstructural and engineering point of view. Besides this academic support there was also room for friendly chats.

The collaboration I had with my co-authors on the publications I want to acknowledge. These are Prof. Dr.-Ing. Michael Alber, MSc (Ruhr-Universität Bochum), Dr. Nader Fardin (KTH Stockholm), Dr. Erik Rybacki (GFZ Potsdam) and Dr. Sergei Stanchits (GFZ Potsdam). It was a very fruitful work that led to good results.

I had valuable discussions with Michael Alber on very principle things that led to satisfying experiments. Further, he let me use his facilities at Bochum University, i.e. a large diameter Hoek-Cell, the loading frame and the sample preparation laboratories. Nader Fardin did surface roughness measurements of samples. Sergei Stanchits did recording of Acoustic Emissions and analysis of the data.

Many others helped at the different research institutes whom I cannot all mention here. Also the reviewers of the manuscripts and guests at GFZ provided good discussions. Nevertheless I want to allude Stefan Gehrman (GFZ Potsdam), who helped me with sample preparation, Dipl.-Ing. Michael Naumann (GFZ Potsdam), whose ideas led to the final design of the devices for testing, and Erik Rybacki, who was always available for a discussion or chat. Thanks also to all my former and recent colleagues at GFZ, Section 3.2.

I would like to express my sincere appreciation to those who read through the thesis or parts of it and gave their comments, namely my supervisors, Ann, Anna, Ann-Elen, Erik, Geoff, Stefan and my father.

I want to thank all those who went for a beer and laughter during the course of the last three years.

For mental support I want to thank my friends, and my sister, Gabi.

For lots of things, which are too many to list here, thanks to Daniela.

Tobias

Potsdam, August 2004

CONTENT

SUMMARY

This thesis work describes a new experimental method for the determination of Mode II (shear) fracture toughness, K_{IIC}, of rock and compares the outcome to results from Mode I (tensile) fracture toughness, K_{IC}, testing using the International Society of Rock Mechanics (ISRM) Chevron-Bend (CB-) method. The fracture toughness describes the resistance of rock to fracturing. This parameter is therefore important when estimating the failure of rock and rock structures using rock fracture mechanics principles.

Critical Mode I fracture growth at ambient conditions was studied by carrying out a series of experiments on a clay bearing sandstone at different loading rates, i.e. clip-gage opening rates of $5 \cdot 10^{-6}$ m/s to $5 \cdot 10^{-10}$ m/s. The range of loading rates provides macroscopic fracture velocities that have been shown to cause time-dependent fracture growth in other test set-ups. The mechanical data shows that time- and loading rate dependent crack growth occurs in the test material. Crack density measurements on scanning electron microscopy micrographs show constant size of the symmetric fracture process zone (~ 700-800 μm) independent of loading rate. Fracture surface roughness is constant for all loading rates. Acoustic emission location data demonstrates that the fracture process zone has a constant size of 5 mm in width and ~ 20 mm in length. The number of located acoustic emission events decreases with slower loading rates. The fracture propagating in the CB-samples is therefore not a pure Mode I fracture on the microscale. On the macroscale the fracture propagates co-planar under the Mode I loading.

Mode I fracture toughness was determined on six rock types, i.e. Flechtingen sandstone, Rüdersdorf limestone, Carrara marble, Äspö diorite, Mizunami granite, and Aue granite. K_{IC} is 1.2 MPa $m^{1/2}$, 1.1 MPa $m^{1/2}$, 2.4 MPa $m^{1/2}$, 3.8 MPa $m^{1/2}$, 2.4 MPa $m^{1/2}$, and 1.6 MPa $m^{1/2}$, respectively.

The newly developed set-up for determination of the Mode II fracture toughness is called the Punch-Through Shear (PTS-) test. It uses drill core that is available from most engineering site investigations. Notches were drilled to the end surfaces of 50 mm long samples. These act as friction free initial fractures. An axial load punches down the central cylinder introducing a high localised shear load in the remaining rock bridge. To the mantle of the cores a confining pressure may be applied to simulate a normal stress on the shear zone. The application of confining pressure favours the growth of Mode II fractures as large pressures suppress the growth of tensile (Mode I) cracks.

The stress intensity factor at the critical loading condition in the PTS- test is calculated using a Displacement Extrapolation Technique (DET) based on Finite Element Modelling (FEM). Comparison of the results to K_{IIC} values from other estimation methods confirmed the results.

Mode II loading experiments were carried out on the same six rock types as used in Mode I testing.

Unstable macroscopic shear fracture growth is achieved at peak load in the PTS-test. Cyclic loading in the post peak region provides controlled fracture propagation and shows constant compliance change for the different rock types. Variation of displacement rates from $3.3 \cdot 10^{-8}$ to $1.7 \cdot 10^{-3}$ m/s do not change the calculated critical stress intensity factor for most rock types. Variation of geometrical parameters, i.e. notch depth, notch diameter, notch width, and sample diameter, leads to an optimisation of the PTS- geometry.

Increase of confining pressure, i.e. normal load, on the shear zone increases K_{IIC} bi-linear. High slope is observed at low confining pressures (< 30 MPa); at pressures above 30 MPa low slope increase is evident. The maximum confining pressure, P, applied is 70 MPa. K_{IIC} increases for the Äspö diorite from 5.1 (at P = 0 MPa) to 12.4 MPa $m^{1/2}$ (at P = 70 MPa), for Aue granite from 4.1 to 13.2 MPa $m^{1/2}$, for Mizunami granite from 4.9 to 14.2 MPa $m^{1/2}$, for Carrara marble from 3.1 to 7.9 MPa $m^{1/2}$, for Flechtingen sandstone from 1.9 to 5.4 MPa $m^{1/2}$, and for Rüdersdorf limestone from 2.3 to 6.7 MPa $m^{1/2}$.

With increase of shear stress from axial loading, primary macroscopic wing fractures develop at about 30 % of the maximum stress. They propagate out of the stressed zone and stop. Further elevation of shear stress results in development of a process zone leading to a secondary 'shear' fracture. Consequently the energy requirement for the formation of the two types of fractures is different. Increase of confining pressure to above 30 MPa is shown to suppress the wing fractures.

Carrara marble develops an asymmetric process zone with two different regimes of preferred microcrack orientation and a straight main separation. The acoustic emission analysis indicates mixed mode cracking on the microscale. Increase of confining pressure changes the orientation of the main fracture and the cracks within the process zone. These tend to reach constant orientation at P = 30-50 MPa.

The Punch-Through Shear (PTS-) test provides controlled testing conditions and reproducible results. Five different evaluation approaches give consistent results for the Mode II fracture toughness. The asymmetry of the evolving fracture process zone in Carrara marble was shown. This result is consistent with the prediction from stress field analysis and it has also been observed in field studies of shear zones.

The existence of Mode II fracture in rock is a matter of debate in the literature. Comparison of the results from Mode I and Mode II testing, mainly regarding the resulting fracture pattern, and correlation analysis of K_{IC} and K_{IIC} to physico-mechanical parameters emphasised the differences between the response of rock to Mode I and Mode II loading. On the microscale, neither the fractures resulting from Mode I the Mode II loading are pure mode fractures. On macroscopic scale, Mode I and Mode II do exist.

ZUSAMMENFASSUNG

Diese Arbeit beschreibt eine neue experimentelle Methode zur Bestimmung der Modus II (Schub) Bruchzähigkeit, K_{IIC}, von Gestein und vergleicht die Ergebnisse mit Resultaten aus Versuchen zur Bestimmung der Modus I (Zug) Bruchzähigkeit, K_{IC}. Für die Modus I Belastung wurde die ‚Suggested Method' der ‚International Society of Rock Mechanics' (ISRM), die Chevron-Bend (CB-) Methode, verwendet. Die Bruchzähigkeit beschreibt den Widerstand eines Gesteins gegen die Ausbreitung eines Risses. Dieser Parameter ist bei der Abschätzung des Versagens von Gestein und Felsbauwerken unter Anwendung der Felsrißmechanik von Bedeutung.

An einer Serie von Versuchen mit verschiedenen Belastungsraten wurde das kritische Modus I Rißwachstum eines tonhaltigen Sandsteines untersucht. Die Clip-gage Öffnungsraten wurden hierbei von $5 \cdot 10^{-6}$ m/s bis $5 \cdot 10^{-10}$ m/s variiert. Diese Bandbreite der Raten resultiert in makroskopischen Rißgeschwindigkeiten, die subkritisches Wachstum zulassen. Dieses wurde in anderen Versuchsaufbauten belegt. Die mechanischen Daten zeigen, daß zeit- und belastungsratenabhängiges Rißwachstum in dem Material stattfindet. Rißdichtemessungen an Rasterelektronenmikroskopaufnahmen weisen unabhängig von der Belastungsrate eine konstante Breite der symmetrischen Rißprozeßzone von etwa 700-800 μm auf. Die Rißoberflächenrauhigkeit der Proben ist unabhängig von der Belastungsrate. Daten aus der Aufnahme der akustischen Emissionen belegen, daß die Rißprozeßzone eine konstante Größe von etwa 5 mm Breite und etwa 20 mm Länge hat. Die Anzahl der aufgezeichneten akustischen Emissionen nimmt zu langsameren Belastungsraten hin ab. Der sich im CB- Versuch ausbreitende makroskopische Riß ist somit kein reiner Modus I Riss auf der mikrostrukturellen Ebene. Makroskopisch hingegen propagiert der Riß unter Modus I Belastung co-planar.

Die Modus I Bruchzähigkeit wurde für sechs Gesteine bestimmt, den Flechtinger Sandstein, Rüdersdorfer Kalkstein, Carrara Marmor, Äspö Diorit, Mizunami Granit und Aue Granit. K_{IC} ist respektive 1,2 MPa $m^{1/2}$, 1,1 MPa $m^{1/2}$, 2,4 MPa $m^{1/2}$, 3,8 MPa $m^{1/2}$, 2,4 MPa $m^{1/2}$, und 1,6 MPa $m^{1/2}$.

Der neu entwickelte Versuchsaufbau zur Ermittlung der Modus II Bruchzähigkeit wurde Punch-Through Shear (PTS-) Test genannt. Die Proben werden aus Bohrkernen hergestellt. In die Endflächen von 50 mm langen Kernstücken werden mit Kernbohrkronen Nuten eingebracht. Diese dienen als reibungsfreie Anfangsrisse. Eine axiale Last auf dem entstandenen Innenzylinder der Proben induziert lokal eine hohe Schubspannung in der verbleibenden Gesteinsbrücke zwischen den Nuten. Auf die Mantelfläche der Proben kann ein Umlagerungsdruck aufgebracht werden. Dieser wirkt als Normalspannung auf die Scherzone. Da durch hohe Normalspannungen das Modus I Rißwachstum unterdrückt wird, wird durch den Umlagerungsdruck das Modus II Rißwachstum gefördert.

Der Spannungsintensitätsfaktor bei kritischer Belastung im PTS- Test wird mittels einer Verschiebungsextrapolationsmethode (Displacement Extrapolation Technique, DET) bestimmt. Der Vergleich der DET Ergebnisse mit K_{IIC} Werten, die mit Hilfe anderer Methoden abgeschätzt wurden, gibt konsistente Resultate.

Die Modus II Belastungsexperimente wurden an denselben sechs Gesteinen wie die Modus I Versuche ausgeführt.

Der Scherriß im PTS- Test wächst bei Maximallast instabil. Zyklische Belastung der Probe in den Postpeak Bereich läßt kontrolliertes Rißwachstum zu. Die Complianceänderung der zyklischen Belastung ist für verschiede Gestein gleich. Die Variation der Verschiebungsrate von $3{,}3 \cdot 10^{-8}$ bis $1{,}7 \cdot 10^{-3}$ m/s hat bei den meisten der untersuchten Gesteine keinen Einfluß auf K_{IIC}. Die PTS- Probengeometrie wurde bezüglich der Nutentiefe, des Nutendurchmessers, der Nutenbreite und des Probendurchmessers optimiert.

K_{IIC} steigt bi-linear mit Zunahme des Umlagerungsdruckes an. Ein starker Anstieg ist bis zu Umlagerungsdrücken, P, von etwa 30 MPa zu beobachten, oberhalb dieses Wertes ist die Steigung geringer. Bisher wurden Umlagerungsdrücke bis maximal 70 MPa aufgebracht. K_{IIC} nimmt für den Äspö Diorit von 5,1 (bei P = 0 MPa) auf 12,4 MPa $m^{1/2}$ (bei P = 70 MPa), für Aue Granit von 4,1 auf

13,2 MPa $m^{1/2}$, für Mizunami Granit von 4,9 auf 14,2 MPa $m^{1/2}$, für Carrara Marmor von 3,1 auf 7,9 MPa $m^{1/2}$, für Flechtinger Sandstein von 1,9 auf 5,4 MPa $m^{1/2}$, und für den Rüdersdorfer Kalkstein von 2,3 auf 6,7 MPa $m^{1/2}$ zu.

Mit steigender Scherspannung entwickeln sich bei etwa 30 % der Maximallast primär Zugrisse, sogenannte ‚wing fractures'. Sie wachsen aus der Zone erhöhter Scherspannung heraus und stoppen. Ein weiterer Anstieg der Scherspannung führt zur Initiierung einer Rißprozeßzone, die sekundär zu einem Scherriß führt. Somit ist der Energiebedarf für das Wachstum der beiden Risse unterschiedlich. Oberhalb eines Umlagerungsdruckes von etwa 30 MPa werden ‚wing fractures' unterdrückt.

Carrara Marmor entwickelt eine asymmetrische Prozeßzone, die zwei Regionen unterschiedlicher bevorzugter Mikrorißorientierung und einen Hauptriß zeigt. Analyse der akustischen Emissionen belegt verschiedene Rißmoden auf der mikrostrukturellen Ebene. Die Orientierung der Mikrorisse und des Hauptrisses ändert sich mit Zunahme des Umlagerungsdruckes. Oberhalb eines Umlagerungsdruckes von etwa 30 MPa wird eine konstante Orientierung erreicht.

Der Punch-Through Shear (PTS-) Test bietet kontrollierte Versuchsbedingungen mit reproduzierbaren Ergebnissen. Fünf verschiedene Evaluierungsmethoden haben konsistente Ergebnisse für K_{IIC} bei P = 0 MPa geliefert. Die Asymmetrie der entstehenden Prozeßzone konnte in Carrara Marmor gezeigt werden. Diese Beobachtung deckt sich mit Vorhersagen aus Spannungsfeldanalysen und konnte auch schon in Feldstudien an Störungszonen belegt werden.

Ob die Entstehung eines Modus II Risses in Gestein möglich ist, wurde vielfach in der Literatur diskutiert. Der Vergleich der Ergebnisse der Modus I und Modus II Experimente, insbesondere bezüglich der entstehenden Rißmuster und der Korrelationsanalysen von K_{IC} und K_{IIC} zu physiko-mechanischen Parametern, zeigt die deutlichen Unterschiede der Reaktion des Gesteins auf Modus I und Modus II Belastung auf. Mikroskopisch gesehen wachsen die Risse weder unter Modus I noch unter Modus II Belastung in einem reinen Modus. Allerdings existieren Modus I und Modus II Risse auf der makroskopischen Betrachtungsebene.

1 INTRODUCTION

Fracture is a failure mechanism of brittle materials that has great importance to the performance of structures. Rapid and violent failures of large-scale geotechnical, mining or civil engineering structures cause significant safety hazards, material damage, and interruption to or even cessation of mining or building activities. Geomechanics and related faulting is also of major importance in structural geology and seismology (Brace & Bombolakis, 1963).

Ability to recognise pre-failure rock mass behaviour may result in predicting or averting the potential for geotechnical and geological failure (Szwedzicki, 2003). Rock fracture mechanics is one approach to resolve this task.

Rock fracture mechanics can be employed not only to improve safety, but also enhance performance and economy of rock engineering structures. Examples are the geological disposal of radioactive waste, terrestrial sequestration of carbon dioxide to ease prejudicial effects on the environment, efficient underground storage of oil, gas or air, enhanced recovery of hydrocarbons and underground constructions at increasing overburden pressure for infrastructure or transport.

Research in rock fracture mechanics in the past has provided major knowledge on tensile, so-called Mode I, fracturing (e.g. Griffith, 1920; Ouchterlony, 1982; Atkinson, 1984; Thouless et al., 1987; Ouchterlony, 1988; Ouchterlony, 1989; Buthenuth & de Freitas, 1995; Zhang et al., 1999; Pyrak-Nolte & Morris, 2000; Zhang, 2002; and many others). Tensile fractures within a rock mass can be generated both in tensile and compressive stress fields and are therefore very common. One might think here of the vertical fractures caused in pillars in excavations due to the weight of the overburden, or fractures from hydraulic stimulation of boreholes. Even shear (Mode II) loading of existing fractures was shown to initiate tensile fractures (e.g. Brace & Bombolakis, 1963; Horii & Nemat-Nasser, 1985; Wong et al., 2001). It was proposed from these that it is unlikely that a shear (Mode II) loaded fracture could extend in its own plane.

Erdogan & Sih (1963) reported that shear loading of a pre-fabricated notch in Plexiglas plates caused presumably tensile fracture propagation. The fracture did not propagate in the assumed Mode II, i.e. shear, direction but turned out of that plane and lined up parallel to the direction of the major principal stress. About twenty years later Ingraffea & Arrea (1982) showed same fracturing behaviour in a shear loaded concrete beam. Bažant & Pfeiffer (1986) cite that following Ingraffea & Arrea "the bon mot 'shear fracture is a sheer nonsense' has been heard in some […] lectures" (p. 111). The existence of Mode II fractures in rock material is a matter of debate in literature still (e.g. Ingraffea & Arrea, 1982; Bažant & Pfeiffer, 1986; Petit & Barquins, 1988; Lockner, 1995; Moore & Lockner, 1995; Katz & Reches, 2004).

Technically the resistance of rock to the initiation and propagation of fractures is described in terms of fracture toughness. Any pre-existing fracture within rock subjected to any kind of loading increases several times the local stresses at the tip of the fracture. The local stress increase at a straight flat fracture tip is mainly governed by the sharpness of the tip of the fracture and its length. The fracture toughness is the limit of local stress increase due to an existing fracture before its critical extension takes place.

For determination of Mode I fracture toughness there exist ISRM (International Society of Rock Mechanics) Suggested Methods to determine the fracture toughness (Ouchterlony, 1988; Fowell, 1995) and several other methods have been proposed (e.g. Evans, 1972; Barker, 1977; Atkinson et al., 1982; Chong & Kuruppu, 1984; Sun & Ouchterlony, 1986; Guo et al., 1993; see also Chang et al., 2002, and Whittaker et al., 1992, and references quoted therein).

For the determination of Mode II fracture toughness some experimental methods were introduced in the literature (e.g. Jumikis, 1979; Ingraffea, 1981; Watkins, 1983; Barr & Derradj, 1990; Rao, 1999). At present no Suggested Method for determination of Mode II rock fracture toughness exists.

Aims and content

This study examines in terms of (rock) fracture mechanics the response of rock material to Mode I (tensile) and Mode II (shear) loading – aiming at *(a)* introducing a new method to apply (pure) Mode II loading, *(b)* determining the Mode II fracture toughness and *(c)* giving new insights to the discussion upon the existence of Mode II itself. Hereby, it is differentiated between the technical applicable stress intensity factor, and description of the microstructural processes.

On one hand tests on Mode I loading have been carried out yielding an understanding of the tensile fracturing process. The influence of loading rate on various parameters during slow fracture propagation of sandstone samples subjected to Mode I loading is examined. The ISRM Suggested Method for Mode I fracture toughness determination (Ouchterlony, 1988) was used to apply pure Mode I loading.

On the other hand a method to apply pure Mode II loading for determination of the Mode II fracture toughness was developed as major part of this thesis. The method is able to apply a confining pressure, i.e. normal stress to the shear loaded zone, independently from the shear load. Confining pressure is most desirable for Mode II fracture growth as large pressures suppress the tensile mode (Mode I) and therefore Mode II is most likely in such environments (e.g. Broberg, 1999; Lawn, 1993; Melin, 1986).

Presentation of the results in papers and at conferences

Majority of findings as presented in this thesis are published or submitted for publication in international journals or conference proceedings.

Tensile fracturing was investigated on behalf of microstructure and Mode I fracture toughness on a sandstone. Emphasis was put on the influence of loading rate on fracture toughness and micromechanics. Furthermore, the roughness of Mode I fracture faces was studied jointly with Dr. Nader Fardin, KTH Stockholm, Sweden. The results are published in:

Backers T., Fardin N., Dresen G. & Stephansson O. 2003a. Effect of Loading Rate on Fracture Toughness, Roughness and Micromechanics of Sandstone. Int. J. Rock Mech. Min. Sci.; 40: 425-433.

This study was extended by the analysis and interpretation of Acoustic Emission (AE) events recorded during testing and a discussion of the (mechanical/chemical) processes evident on the microscale. The AE acquisition and processing was carried out by Dr. Sergei Stanchits, GeoForschungsZentrum Potsdam, Germany. Correlation of micromechanics and AE was described and discussed. The manuscript summarising the findings is submitted to the *International Journal of Rock Mechanics and Mineral Sciences* for a special issue of the EURO-Conference 2003 on Rock Physics and Geomechanics:

Backers T., Stanchits S. & Dresen G. submitted. Tensile Fracture Propagation and Acoustic Emission Activity in Sandstone: The Effect of Loading Rate. Int. J. Rock Mech. Min. Sci..

A general overview of the findings of the two above publications was presented at the EURO-Conference 2003 on Rock Physics and Geomechanics:

Backers T., Stanchits S., Stephansson O. & Dresen G. 2003b. The Influence of Loading Rate on Mode I Acoustic Emission and Micromechanics of Sandstone. In: Makurat A. & Curri P. (eds.). EURO-Conference on Rock Physics and Geomechanics – Micromechanics, Flow and Chemical Reactions. Extended Abstract Volume, Delft, Netherlands.

No method for Mode II loading with application of independent confining pressure is available. Therefore, a new method was

developed. The basis for the testing method for Mode II loading was laid out in a diploma thesis:

Backers T. 2001. Punch-through shear test of drill core – a new method for K_{IIC} testing. Diploma thesis, Division of Engineering Geology, Technical University Berlin, Germany.

It describes the basic layout of the test, the testing procedure and first results from testing. The test was called the Punch-Through Shear test (PTS- test). The principle set-up was presented at the *ISRM Regional Symposium EUROCK 2001* meeting in Finland:

Stephansson O., Backers T. & Rybacki E. 2001. Shear fracture mechanics of rocks and a new testing method for K_{IIC}. In: Särkka, P. & Eloranta, P. (eds.). Rock Mechanics - a challenge for society. Proceedings of the ISRM Regional Symposium EUROCK 2001, Espoo: 163-168. Balkema, Netherlands.

As part of the present study the proposed testing method was revised; this includes re-formulation of the mathematical framework, the interpretations of the resulting macroscopic fractures, the fracture evolution, the influence of geometry and confining pressure. Results are presented in

Backers T., Stephansson O. & Rybacki E. 2002b. Rock Fracture Toughness Testing in Mode II – Punch-Through Shear Test. Int. J. Rock Mech. Min. Sci.; 39: 755-769.

In the discussion of the paper several questions arouse about the influence of the sample size, grain size, and loading rate on fracture toughness, and a detailed analysis of the microstructures.

Analysis of the microstructures within the PTS- test was summarised in a peer-reviewed paper presented at the *International Conference on Structural Integrity and Fracture* held in Perth, Australia, in September 2002:

Backers T., Rybacki E., Alber M. & Stephansson O. 2002a. Fractography of rock from the new Punch-Through Shear Test. In: Dyskin A.V., Hu X. & Sahouryeh E. (eds.). Structural Integrity and Fracture – The International Conference on Structural Integrity and Fracture, Perth, Australia: 303-308. Balkema, Netherlands.

The presentation includes a description of the sequence of macroscopic and microscopic fractures developing in Carrara marble, and the change of macro- and microscopic fracture pattern with variation of confining pressure. The paper and presentation was awarded with 'The Best Student Paper'.

Most recent results from PTS- testing were summarised in a contribution presented at the *SINOROCK 2004 Conference*. The influence of sample size, (grain size,) cyclic loading and loading rate are discussed. The abstract and an electronic-version of this paper are published in a special issue of the *International Journal of Rock Mechanics and Mineral Sciences*:

Backers T., Dresen G., Rybacki E. & Stephansson O. 2004. New Data on Mode II Fracture Toughness of Rock from Punch-Through Shear (PTS) Test – SINOROCK2004 Paper 1A01. Int. J. Rock Mech. Min. Sci.; 41:351-352.

Structure of the thesis

Mode I and Mode II loading and theory of fracturing are described in Chapter 2. Chapter 3 describes the rock types used and testing equipment. The method for Mode I loading, experimental results and discussion are presented in Chapter 4. The new Mode II loading set-up and fracture toughness determination technique, experimental results and discussion are presented in Chapter 5. The Mode I and Mode II fracture toughness values are correlated to selected physico-mechanical properties and the results from Mode I and Mode II loading are compared to each other (Chapter 6). Chapter 7 gives examples for application and outlines a computer modelling application based on fracture mechanics and fracture mechanics data obtained in this thesis. Chapter 8 provides a general discussion of the results.

2 INTRODUCTION TO THEORY OF ROCK FRACTURE MECHANICS AND FRACTURE TOUGHNESS DETERMINATION

An introduction to the theory of rock fracture mechanics and some key references are given. The reader is introduced to the terminology regarding fractures in rock, the mechanical background of fracturing in terms of stress intensity factor and to the process of fracturing including fracture process zone models. Existing methods for determination of the critical stress intensity factor, the fracture toughness, both in Mode I and Mode II are outlined.

2.1 Discontinuities in rocks

In literature terms regarding the description of discontinuities and in particular fractures are frequently used in not clearly specified meanings. This might be due to different nomenclatures in different disciplines. The terms used in this thesis are explained in this section.

A *crack* is any opening in rock that has one or two dimensions much smaller than the third. The width to length ratio, termed crack aspect ratio, is typically 10^{-3} to 10^{-5} (Simmons & Richter, 1976). Cracks can be divided into three scale classes – micro, meso and macro. *Microcracks* are planar discontinuities with their longest dimension in the order of one to few grain diameters. This might be about $1 \cdot 10^{0} - 1 \cdot 10^{4}$ microns (Engelder, 1987). Based on their occurrence within the rock they can be divided into: *grain boundary* cracks – located at the interface between grains –, *intragranular* cracks – cracks restricted within one grain –, and *intergranular* cracks – cracks cutting more than one grain (Engelder, 1987).

A *mesocrack* is a discontinuity spanning a larger number of grains than a microcrack, formed by a complicated rupture event and eventually connecting several microcracks. The extension is several hundreds of microns to few millimetres. Micro- and mesocracks are laxly called cracks whenever a distinct differentiation is not necessary.

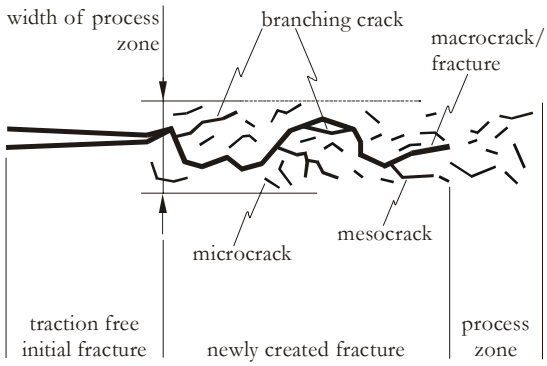

Fig. 2-1. The nomenclature of a fracture system. Fracture with surrounding fracture process zone (FPZ). The process zone consists of micro- and mesocracks. (modified from Liu et al., 2000).

The *macrocrack* spans several millimetres to decimetres. It is also referred to as *fracture*. It consists of the through-going main separation and the surrounding *fracture process zone, FPZ* (Fig. 2-1) (e.g. Hoagland et al., 1973; Atkinson, 1987). This process zone includes microcracks and mesocracks. Prior to the main fracture growth extensive micro-/mesocracking occurs (Fig. 2-2). Meso- or macrocracks propagating off the macrocrack are called *branching cracks*. The *width* of the

fracture process zone depends on grain size (e.g. Hoagland et al., 1973; Labuz et al., 1985; Zang et al., 2000). The size of the FPZ was observed to be about five to ten times the average grain size (e.g. Hoagland et al., 1973; Zang et al., 2000), but greater values up to 40 grain diameters have been reported, too (c.f. Whittaker et al., 1992). Broberg (1999) defines the process zone as the area in state of decohesion, in front of the fracture tip and the wake of it, where microcracks coalesce to form the through-going main separation. Non-elastic deformation within the FPZ is caused by stress concentrations at the fracture tip (c.f. Chapter 2.4 for details on the physical description of the FPZ and related models).

In tectonics and structural geology the genesis of fractures and fracture networks is indicated by the terms *joint* and *fault*. A *joint* is a discontinuity that shows a displacement normal to its surface or trace and no displacement parallel to its surfaces (Pollard & Aydin, 1988). A *fault* has been generated by a shear displacement, therefore showing displacement parallel to the surfaces (Pollard & Aydin, op. cit.). In general these types of discontinuities are much larger than fractures. Figure 2-3 shows the length classification from microcrack to fault.

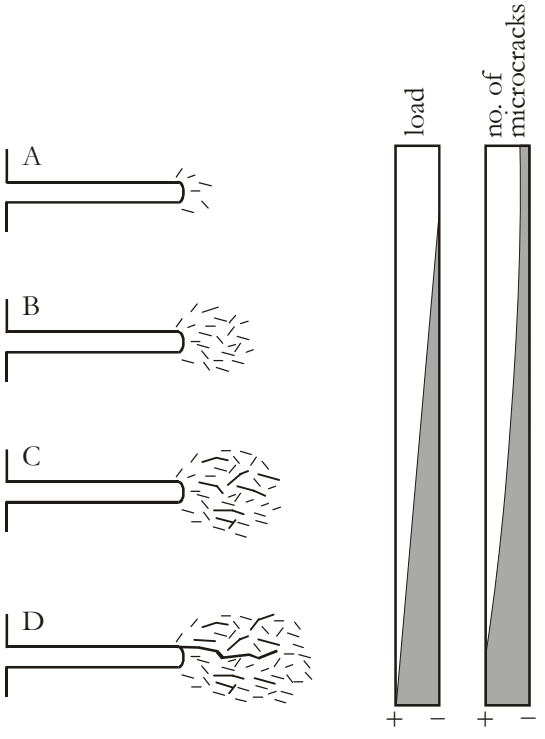

Fig. 2-2. The development of a fracture and fracture process zone (FPZ) under a tensile load perpendicular to a starter notch. The schematic sequence A-D shows micro-, meso-, and macrocrack development with increasing load. Load and number of microcrack evolution is schematically given in bars on the right. (modified from Hoagland et al., 1973).

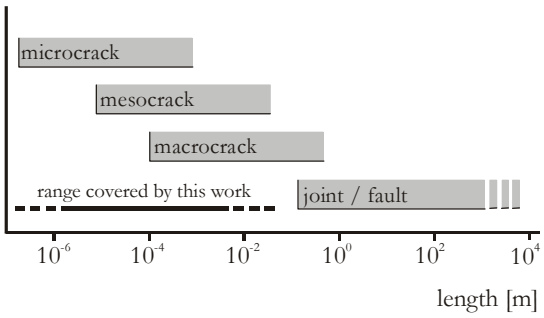

Fig. 2-3. Length range of different types of discontinuities in rock.

2.2 *Mode of fracturing, stress distribution, stress intensity factor and fracture toughness*

In fracture mechanics cracks or fractures are usually subdivided into three basic types, namely Mode I, Mode II and Mode III, from a mostly mathematical viewpoint (Irwin, 1958). The division is based on the crack surface displacement (Lawn, 1993), or crack tip loading (Engelder, 1987; Whittaker et al., 1992). In literature this is indicated as either *mode of crack propagation*, *mode of fracturing* or *mode of loading*. Relating the modes of fracturing to the modes of loading – with the assumption that the fracture propagates within its own plane – is appropriate for most metals (Rao et al., 2003). But for rock a specific *mode of loading* is not necessarily leading to the same *mode of fracturing*. Unfortunately, the reference of mode regarding the applied loading and fracture propagation is often mixed up in literature. For sake of clarity, there will be a clear distinction between *'mode of loading'* – for the applied boundary stresses[1] – and *'mode of fracturing or failure'* – for the mechanical breakdown process defined by relative displacement.

[1] In the following, we shall regard positive stresses as compressive, while negative stresses indicate tension, and principal stresses $\sigma_1 \geq \sigma_2 \geq \sigma_3$.

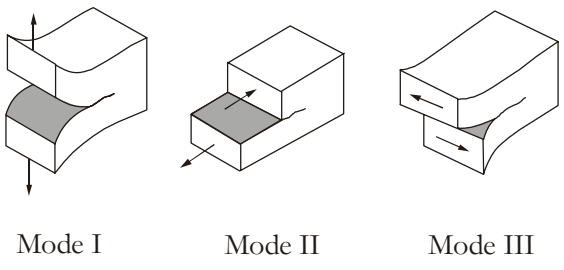

Fig. 2-4. Basic modes of fracturing. Any combination of these is referred to as mixed mode. The principle of superposition is applicable. (modified from Hudson & Harrison, 1997).

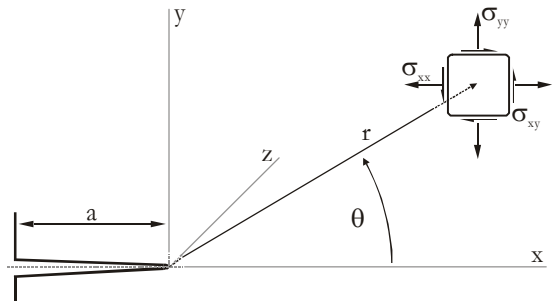

Fig. 2-5. Notations within Cartesian co-ordinate system for stress tensor.

In terms of crack surface displacement (mode of fracturing), the modes can be classified as depicted in Figure 2-4. In *Mode I*, also called the *opening (tensile) mode*, the crack tip is subjected to displacements perpendicular to the crack plane. The crack propagation is in crack plane direction. The crack carries no shear traction and no record of shear displacement is visible. In *Mode II* the crack faces move relatively to each other in the crack plane. Crack propagation is perpendicular to the crack front. Shear traction parallels the plane of the crack. The third mode of fracturing is *Mode III*. Shear displacement is acting parallel to the front in the crack plane. Any combination of the three basic modes is referred to as *mixed mode*. The principle of superposition is sufficient to describe the most general case of crack tip deformation (Atkinson, 1987).

Inglis (1913) could show mathematically that the local stress at a sharp notch or crack could rise to a level several times that of the applied stress. It thus became apparent that even sub-microscopic flaws (or even inhomogeneities) can be considered as potential planes of weakness in materials. This stress concentration concept yields

$$\frac{\sigma_{CT}}{\sigma_A} \sim \frac{1}{\varrho} \qquad (2\text{-}1)$$

where σ_{CT} is the stress at a crack tip, σ_A is the applied stress and ϱ is the curvature of the crack tip. The ratio in equation (2-1) is an elastic stress concentration factor and it depends on the shape (curvature) of a crack or corner.

The stresses and displacements at the tip of an existing crack with a sharp tip (curvature $\varrho \cong 0$) can be calculated using the Westergaard (1939) and Sneddon (1945) stress functions.

The derivation and formulations of the stress and displacement functions can be found in op. cit. or in textbooks like e.g. Lawn (1993) and Whittaker et al. (1992). The stress formulations can be reduced to the simple form

$$\sigma_{ij} = \frac{K_k}{\sqrt{2\pi \cdot r}} \cdot f_{ij}(\theta);\ i, j = x, y, z;\ k = I, II, III \qquad (2\text{-}2)$$

where σ_{ij} is the stress tensor in Cartesian co-ordinates, f_{ij} is a geometric stress factor depending solely on angle θ, and K_k is a factor depending on the outer boundary conditions, i.e. applied loading and geometry (for notations see Fig. 2-5). The subscript k refers to the corresponding mode.

In the theory of fracture mechanics K_k is the *stress intensity factor* that gives the grade of stress concentration at the tip of a crack of length a at a given loading and has the dimension of stress · (length)$^{1/2}$, in units MPa · m$^{1/2}$,

$$K_k = \sigma_A \sqrt{\pi \cdot a} = \sigma_{ij} \sqrt{2\pi \cdot r};\ \theta = 0 \qquad (2\text{-}3)$$

One must be aware that the concept was developed for the case of a fracture propagating in its own plane due to corresponding modes of loading. Any deflection from this plane will result in mixed mode conditions, c.f. equation (2-2).

Crack initiation will occur, when the stress intensity factor reaches a critical value, called *fracture toughness*, K_{kC}.

Each of the modes possesses specific stress symmetry properties near the crack edge (Broberg, 1999) defining the directions for maximised stress intensity. In a Cartesian co-ordinate system as shown in Figure 2-5, the modes may be specified as follows (Fig. 2-6):

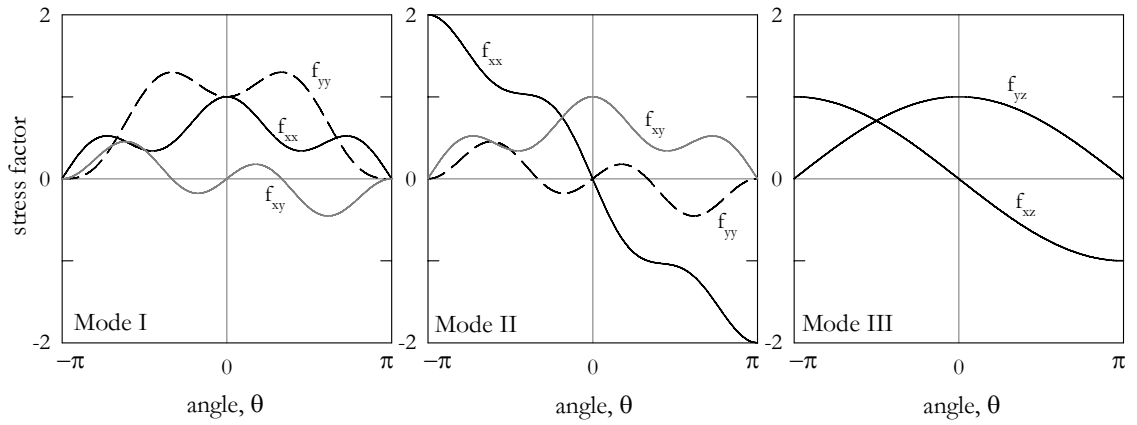

Fig. 2-6. Stress distribution in terms of stress factor f_{ij} around crack tip for different pure modes of loading. Each of the modes possesses specific stress symmetry properties near the crack edge (Broberg, 1999). Notations according to Figure 2-5. Note: positive stress factor as indicative of tension.

Mode I: The lateral (f_{yy}) and the directional stress component (f_{xx}) are symmetric with respect to the crack trace. The shear stress component (f_{xy}) shows point-symmetry.

Mode II: The lateral (f_{yy}) as well as the directional stress component (f_{xx}) are point-symmetric. The shear stress component (f_{xy}) is the only component to be symmetric with respect to the crack trace.

Mode III: f_{yz} appears to be symmetric with respect to the crack trace while f_{xz} shows point-symmetry.

2.3 The Griffith concept and Energy Release Rate

Most materials fail when stressed beyond some critical level. But what is the nature of failure? In 1920 A.A. Griffith considered an isolated crack in an elastic solid subjected to an applied stress and formulated a criterion for its extension from the fundamental energy theorems of classical mechanics and thermodynamics. He modelled a static crack as a reversible thermodynamic system.

The energy-balance concept by Griffith (op. cit.) is given by the equilibrium requirement

$$dU/dc = 0 \qquad (2\text{-}4)$$

where dU is the change in system energy and dc is the crack extension. If equilibrium is not maintained a crack would extend or retract reversibly, according to whether the left hand side of equation (2-4) is negative or positive. Failure is defined by

$$\sigma_F = \sqrt{2E'\gamma/\pi c} \qquad (2\text{-}5)$$

where σ_F is the failure load, E' is Young's modulus (plane stress E'=E or plane strain E'=E/(1-ν²) condition; ν: Poisson's ratio), γ is the crack surface energy and c is the crack length. At outer applied stress $\sigma_A < \sigma_F$ the crack remains stationary (*stable*); at $\sigma_A \geq \sigma_F$ it propagates spontaneously (*unstable*). Equation (2-5) is the Griffith strength relation.

The logical extension from this fundamental concept expounded by Griffith yields the *energy release rate*, G (Irwin, 1958). The parameter has been denoted G in honour of Griffith. Rearranging the energy equilibrium formulation of Griffith leads to

$$\pi\sigma^2 c/E' = 2\gamma = G \qquad (2\text{-}6)$$

Crack extension occurs as G reaches the critical energy release rate, G_C, at the failure stress, σ_F.

Irwin (1958) could show the equivalence of energy release rate and stress intensity factor. As the principle of superposition applies the relationship yields

$$G = K_I^2/E' + K_{II}^2/E' + K_{III}^2(1+\nu)/E' \qquad (2\text{-}7)$$

where ν is Poisson's ratio and E' identifies with Young's modulus (plane stress or plane strain condition).

2.4 *The process of fracturing and fracture process zone (FPZ) models*

2.4.1 *The process of fracturing*

The process of fracturing in rock and rock like materials has been frequently studied. This was done under different loading conditions and for different materials, and by means of different observation scales and techniques, e.g. interpretation of mechanical data, microscopy at different scales and detection and interpretation of Acoustic Emission (AE) events. The reader is referred to textbooks and reviews like Pollard & Aydin (1988), Atkinson (1991), and Dresen & Guéguen (2004).

When subjecting a plate with an isolated fracture to an increasing tensional stress perpendicular to the fracture, it will generally fail by rapid Mode I fracture propagation. The fracture accelerates approaching speeds which's maximum is governed by the speed of elastic waves.

Experimental work on inclined single or multiple pre-fabricated fractures (notches) subjected to compressive loads was carried out by e.g. Brace & Bombolakis (1963), Hoek & Bieniawski (1984) and Sammis & Ashby (1986) in glass, e.g. Erdogan & Sih (1963), Horii & Nemat-Nasser (1985), Ashby & Hallam (1986), and Petit & Barquins (1988) in PMMA, e.g. Shen et al. (1995), Bobet & Einstein (1998), Park et el. (2001), Tang et al. (2001), Wong et al. (2001), and Sagong & Bobet (2002), in model materials, and e.g. Petit & Barquins (1988) in rock samples.

It was recognised that under compressive loading, both tensile and shear stress concentrations develop at pre-existing inclined inhomogeneities at the meso-/macroscopic observation scale. As the compression applied to the sample increases further, tensile cracks will be initiated at the tips of the pre-existing fractures. These are called wing cracks and they grow progressively into the direction of the remote major principal stress and stop (e.g. Brace & Bombolakis, 1963; Kemeny & Cook, 1987, Petit & Barquins, 1988). At the early stages of propagation the growth of the stable wing crack is dominated by the stress field of the originated fracture. As it extends it starts to interact with neighbouring microcracks and this interaction might lead to coalescence and later ultimate failure.

Depending on the geometry and pattern of the interacting fractures, and also the stress condition, different coalescence behaviour was observed. In general, wing cracks initiate at the fracture tips for uniaxial and low confinement biaxial conditions (Fig. 2-7). Bobet & Einstein (1998) report that the location of crack initiation moves to the middle of the flaw for increase of confining pressure and macro-/mesoscopic wing cracks disappear completely for higher confining stresses. Later, secondary fractures are likely to connect the pre-existing fractures. The secondary fracture follows the direction of shear and was found to be unstable (Sagong & Bobet, 2002). The most preferable geometry for shear fractures to develop in a set-up with two initial fractures (Fig. 2-7) is to organise them co-planar, as well with as without confining pressure (Bobet & Einstein, 1998).

For growth of 3D cracks, i.e. cracks with not planar but curved surface, intrinsic limits are reported. For further details on this rarely studied subject refer to e.g. Germanovich & Dyskin (2000) and Dyskin et al. (2003)

While e.g. Brace & Bombolakis (1963) or Horii & Nemat-Nasser (1985) indicated from experiments in glass, that shear fractures will not propagate in their own plane on the micro-/mesoscale, in some experiments shear fractures were found to grow in principle in-plane in rock (e.g. Petit & Barquins, 1988; Reches & Lockner, 1994; Moore & Lockner, 1995), at least on the macroscale.

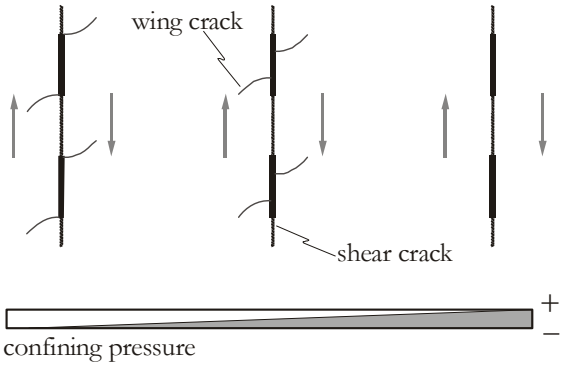

Fig. 2-7. Set-up for fracture coalescence in shear and the influence of confining pressure on the fracture pattern as described by Bobet & Einstein (1998). Refer to text for explanation.

On the microscale Bažant & Pfeiffer (1986) describe the shear fracture resulting from Mode II loading as a zone of inclined tensile microcracks that later connect by shearing. The shear fracture or shear band consists of inclined struts of the material between inclined cracks and shear failure requires these struts to be crushed in compression.

According to Lockner (1995) shearing will take place along surfaces oblique to the maximum principal stress, σ_1, and play an important role in the development of local stress concentrations. The local stresses induced near a fracture tip loaded in shear contain a component of tension as well as shear. This will in general lead to tensile failure before shear failure is achieved. Two processes take place during the loading of fractures in compressive shear. First, the propagation of extensional cracks decreases stress intensity, so that additional deviatoric stress must be applied to cause further fracture propagation. At some point the extensional crack propagates out of the area of high stress concentration and ceases. Second, diagonal flaws propagate out-of-plane parallel to the major principal stress direction. These flaws are favourably oriented to act as initiation points for shear failure. When the flaw density becomes high enough for crack interaction to occur, en-echelon arrays of cracks will develop (Costin, 1987; Lockner, 1995). Finally, the stress concentration is high enough to initiate shear fractures propagating in plane and being governed by their own stress field. The expanse of damaged rock is asymmetrically distributed around the Mode II fracture (Moore & Lockner, 1995). Similar observations on PMMA and sandstone were reported by Petit & Barquins (1988). They state that 'various […] examples show that Mode II propagation from a defect cannot induce the formation of a single crack coplanar with the defect as is suggested by the fracture mechanics model. A macroscopically […] shear zone involving Mode I minor fractures [microcracks] can, however, propagate to prolong the defect' (p. 1254).

Recording of acoustic emission events during loading cylindrical samples in compression in combination with microstructural observations yielded a description of the formation of shear fractures. Below yield strength many dilatant microcracks are formed in random distribution. Near peak strength nucleation and local increase of crack density lead to the development of the process zone in which the shear fracture develops by crushing, buckling and rotation (e.g. Lockner et al., 1992; Reches & Lockner, 1994; Zang et al., 2000).

Glaser & Nelson (1992) did detection of AE events during Mode I and Mode II loading of dolostone samples. They state that in Mode I as well as Mode II loading the most common source kinematic is tensile crack propagation. Mode II crack propagation is due to growth of local tensile crack increments which, in aggregate, produce the macro-failure shear plane. They do not detect any signals until peak load in Mode I loading, which is in direct contrast to observations reported by Hoagland et al. (1973) (c.f. Section 2-1). Evidence for crack growth can be found in microstructural data and acoustic emission events, starting well before peak load at the onset of non-linear deformation in the load-deflection curve (Ouchterlony, 1982). This has also been confirmed by Stanchits et al. (2003) for Mode I loading of granite samples.

It can be concluded that tensile fracturing is dominant in rock and rock-like materials, as usually $K_{IIC} > K_{IC}$. Even in situations where Mode II seems to be favourable, Mode I takes over (Melin, 1989). This is manifested in e.g. the formation of wing fractures on shear loaded fractures. The wing fractures propagate stable and often stop when aligned parallel to the direction of maximum principal stress. Mode II fractures are initiated co-planar with the shear loaded fracture. They form on the microscale as an array of en échelon cracks that are later connected. Microcracks are asymmetrically distributed with respect to the shear plane. Propagation is mostly unstable. Confining pressure enhances the growth of Mode II fractures and suppresses development of Mode I wing cracks.

2.4.2 Static – dynamic versus stable (– subcritical) – critical – unstable fracture growth

There exist two terminological frames for the fracture propagation process. One is defined as a function of fracture propagation velocity; the second is defined as a function of amount of stress intensity factor. The velocity dependent definition-frame is the differentiation between

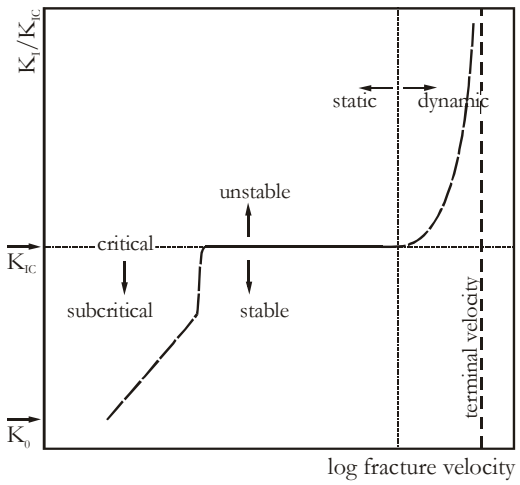

Fig. 2-8. Static – dynamic versus stable (– subcritical) – critical – unstable fracture growth. Schematic plot of K vs. fracture velocity for Mode I. See text for details. (after Zhang et al., 1999, and Atkinson, 1984).

static and *dynamic*, and the stress concentration factor dependent is the differentiation between *stable* and *unstable*. Figure 2-8 shows the different regimes of fracture propagation.

For instability of a crack it is necessary that the stress intensity equals fracture toughness, i.e. $K = K_C$, and that $dK/dc > 0$, where c is the crack length (Lawn, 1993). Otherwise a crack is stable (c.f. Section 2.3). A *stable* crack extends comparably slow and can be stopped at any stage, i.e. requires an increase in stress for each increment of crack growth. An *unstable* crack will be accelerated by excess energy and propagates at speeds approaching a terminal velocity that is governed by the speed of elastic waves. It is referred to as *dynamic*. Instability can be either achieved by reaching a critical crack length or by impact loading. The term *critical* is used for the onset of unstable crack growth, hence the transition from stable to unstable. In terms of stress intensity factor it is called the critical stress intensity factor, K_C (c.f. Section 2.2). Any fracture propagation taking place at fractions of K_C is referred to as *subcritical* crack growth (e.g. Atkinson, 1984). It is governed by several competing mechanisms like diffusion, dissolution, ion exchange, microplasticity and stress corrosion. Latter is important in rock, whilst the other mechanisms have been mainly shown to be active in ceramics and glass. Subcritical fracture propagation takes place at slow speeds, the transition from critical cracking to stress corrosion dominated propagation is reported to be at a crack propagation velocity of about 10^{-3} m/s (Atkinson, op. cit.). At stress intensities lower than K_0, no subcritical crack growth is initiated.

2.4.3 Fracture process zone models

In the previous sections the static stresses and displacements in the vicinity of a loaded crack were introduced in terms of the stress intensity factor, K. It can be seen from equation (2-2) – assuming linear elastic behaviour – that providing any non-zero K results in infinite or singular stresses at the crack tip, i.e. $r \rightarrow 0$. This is a manifestation of Hooke's law applied beyond its limits of validity.[2] Physically, the stress carrying ability of a material is limited by its yield strength. Hence, a small region behaving inelastically is expected immediately ahead of the crack tip. This region is referred to as the plastic zone in metallic materials (Irwin, 1958), but it has been demonstrated to be the microcracking zone or the fracture process zone (FPZ) in rock (e.g. for Mode I loading by Hoagland et al., 1973).

Some fracture process zone models have been proposed. The most important (according to Whittaker et al., 1992) are the maximum normal stress criterion (Schmidt, 1980), the cohesive crack model (Dugdale, 1960; Labuz et al., 1983) and the slip-weakening model (Ida, 1972; Palmer & Rice, 1973).

The maximum normal stress criterion is based on the assumption that the formation of the FPZ takes place when the local minimum principal stress in the vicinity of the crack tip reaches the ultimate uniaxial tensile strength of the rock material. The theory provides formulations for the size and shape of the process zone.

[2] One of the basic assumptions of the classical linear theory of elasticity is not satisfied in problems concerning cracks, namely the assumption about the smallness of changes in the boundary conditions at the surface of the unstrained body. This fact makes the equilibrium of a body with cracks non-linear (Barenblatt, 1962).

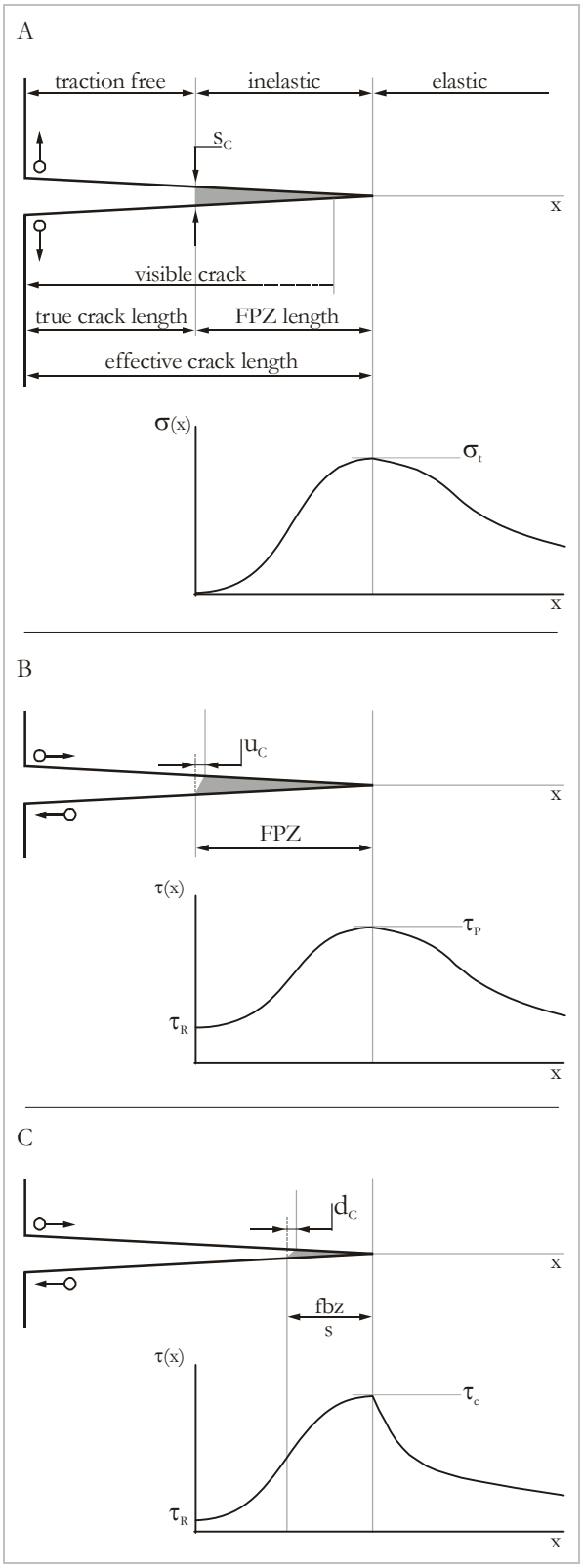

→
Fig. 2-9. Process zone models. Schematic representation of the basic layout, nomenclature and stress distribution of the FPZ models. Shaded area indicates area with stress carrying ability. (A) Cohesion zone model. A tensional force tears the fracture faces apart. When the maximum tensile stress reaches the tensile strength, σ_t, the FPZ develops at a true fracture tip opening, s, of zero. With increasing fracture tip opening the stress is reduced to zero and the corresponding s reaches a critical value s_C. (B) Slip-weakening model. A shear force introduces increased stresses at the fracture tip and FPZ development is initiated on reaching τ_P. During shear displacement the stress is reduced to the level of frictional sliding at a displacement of u_C. (C) Cowie-Scholz Model. At the fracture tip frictional resistance approaches the level of shear strength, τ_C. The stress is reduced in the fracture breakdown zone (fbz) to the residual frictional strength and d_C is the breakdown displacement, which coincides with the inflection point on the stress profile.

The cohesive crack model describing the FPZ for Mode I fracturing in rock is a modification to the Dugdale crack model introduced for metals.[3] The model assumes a crack with an effective crack length (Fig. 2-9.A). This effective length can be diverted into a traction free portion (true crack length) and a length over which cohesive stresses apply. The cohesive stresses tend to close the crack and refer to the FPZ. The material in the process zone is partially damaged but still able to withstand a stress, which is transferred from one surface to the other. The material outside the FPZ is assumed to be linear elastic. The FPZ starts to develop when the minimum principal stress reaches the tensile strength and the corresponding true crack tip opening displacement is zero. With increasing crack tip opening the stress is reduced to zero while the corresponding crack tip displacement reaches a critical maximum value. Hence, the stress singularity problem is overcome. Unlike Dugdale's proposal that the crack closing cohesive stress is assumed to be a constant having the value of the yield strength, the closing cohesive stress is a function of the true crack tip opening displacement.

[3] Barenblatt developed in 1962 a mathematical model of fracture, which is very much comparable to the Dugdale model. It is not further considered here as predominantly used in material sciences.

The so-called slip-weakening model for Mode II fracture problems was stimulated by the previously described cohesive crack model. This mathematical model is based on the assumption that during propagation or slippage of the fracture a shear stress τ exists between the fracture surfaces (Fig. 2-9.B). τ is a function of the amount of slip u as well as the effective normal stress $\sigma'_N = \sigma_N - p_0$, where σ_N is the normal stress across the fracture faces and p_0 is the pore pressure. The peak stress is τ_P and τ_R is the residual value of shear stress. At initiation of slip weakening the slip u is zero, i.e. $u = 0$, and $\tau = \tau_P$. When u reaches a critical value u_C, the stress is reduced to τ_R and the size of the slip-weakening zone corresponds to the FPZ. The stress singularity is eliminated.

A 'post-yield fracture mechanics' model was proposed by Cowie & Scholz (1992) (Fig. 2-9.C). The model is based on laboratory and field observations and is derived from the cohesive crack model by Dugdale. The basic assumptions are very comparable to the slip-weakening model; however, the shape of distribution of stress vs. displacement is different.

2.5 *Fracture toughness testing methods, influencing factors and data*

For determination of the critical stress intensity factors of the different modes, i.e. fracture toughnesses K_{IC}, K_{IIC} (and K_{IIIC}), respectively, laboratory testing methods have been developed. Most matured are the Mode I testing methods (Section 2.5.1), evidently in three ISRM Suggested Methods. Some Mode II methods exist (Section 2.5.2), but most are insufficient to provide reliable results. There are very few methods available that provide Mode III loading conditions (e.g. Cox & Scholz, 1988; Yacoub-Tokatly et al., 1989). Mode I and Mode II fracture toughness testing methods are summarised below and factors influencing fracture toughness and typical data is given.

2.5.1 *Mode I fracture toughness testing methods*

Several testing methods for determination of the Mode I fracture toughness, K_{IC}, have been introduced. Here, for example the SCB (Semicircular Core in three point Bending) test[4] (Chong & Kuruppu, 1984), the chevron-notched SCB test (Kuruppu, 1997), the BD (Brazilian Disc) test (Guo et al., 1993), the RCR (Radial Cracked Ring) test (Shiryaev & Kotkis, 1982), the MR (Modified Ring) test (Thiercelin & Roegiers, 1986), and the DT (Double Torsion) test (Evans, 1972) can be instanced. Reviews of the methods can be found in e.g. Whittaker et al. (1992) and Chang et al. (2002). The DT test is of special importance, as it has been also applied to the study of subcritical crack growth in rock (e.g. Atkinson, 1984).

Three testing methods for rock have been introduced by the International Society for Rock Mechanics (ISRM) as Suggested Methods (Ouchterlony, 1988; Fowell, 1995).

In 1988 the Chevron Bend (CB-) and Short Rod (SR-) method were introduced as ISRM Suggested Methods (Figs. 2-10.A and 2-10.B). The CB-method uses cores with a prefabricated chevron shaped notch that is sub-

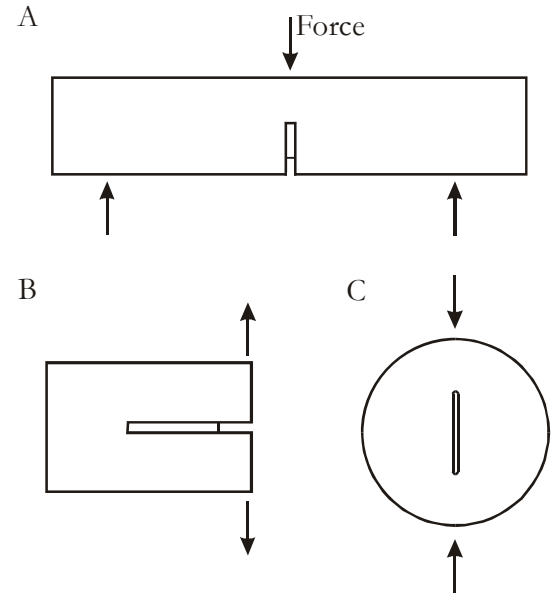

Fig. 2-10. ISRM Suggested Methods for determination of Mode I fracture toughness. A: Chevron Bend (CB-) method; B: Short Rod (SR) method (both Ouchterlony, 1988) and C: CCNBD (Cracked Chevron Notched Brazilian Disc) method (Fowell, 1995).

[4] Sometimes referred to as HDB (single edge Half Disc specimen in three point Bending) test.

jected to three-point bending. The CB- method is used within this thesis – details about testing and evaluation can be found in Chapter 4.

The SR- method uses the remaining halves of the CB- method. A notch is introduced into the core in long axis-direction and is subjected to tension. This combination of CB- and SR-method provides the possibility to study the effect of anisotropy, i.e. determination of K_{IC} parallel and perpendicular to the core axis.

The CCNBD (Cracked Chevron Notched Brazilian Disc) was introduced in 1995 by the ISRM as Suggested Method (Fowell, 1995). It uses Brazilian discs[5] (Brown, 1981) with a notch in the centre of the specimen (Fig. 2-10.C). The evaluation of K_{IC} from this method is still under discussion, e.g. Wang (1998), Wang & Xing (1999) and Wang et al. (2003).

Bearman (1999) introduced a method to estimate K_{IC} using the Point-load test (Franklin, 1985).

2.5.2 Mode II fracture toughness testing methods

Several methods for determining the Mode II fracture toughness have been introduced. Most of the procedures were developed for metals but later applied to rocks. Only those that have been applied to rock or rock like materials (e.g. concrete) are mentioned here.

Ingraffea (1981) introduced the Antisymmetric Four-Point Bending test for application of both mixed Mode I-II and Mode II loading (Fig. 2-11.A). Swartz and Taha (1990) performed numerical analyses and stated that even under pure shear loading in the Antisymmetric Four-Point Bending test tensile stresses inevitably exist around the notch tips. Despite not being able to avoid the tensile stresses, too, the Antisymmetric Four-Point Bending Cube Test has been applied to concrete and rock testing by Barr and Derradj (1990) (Fig. 2-11.B).

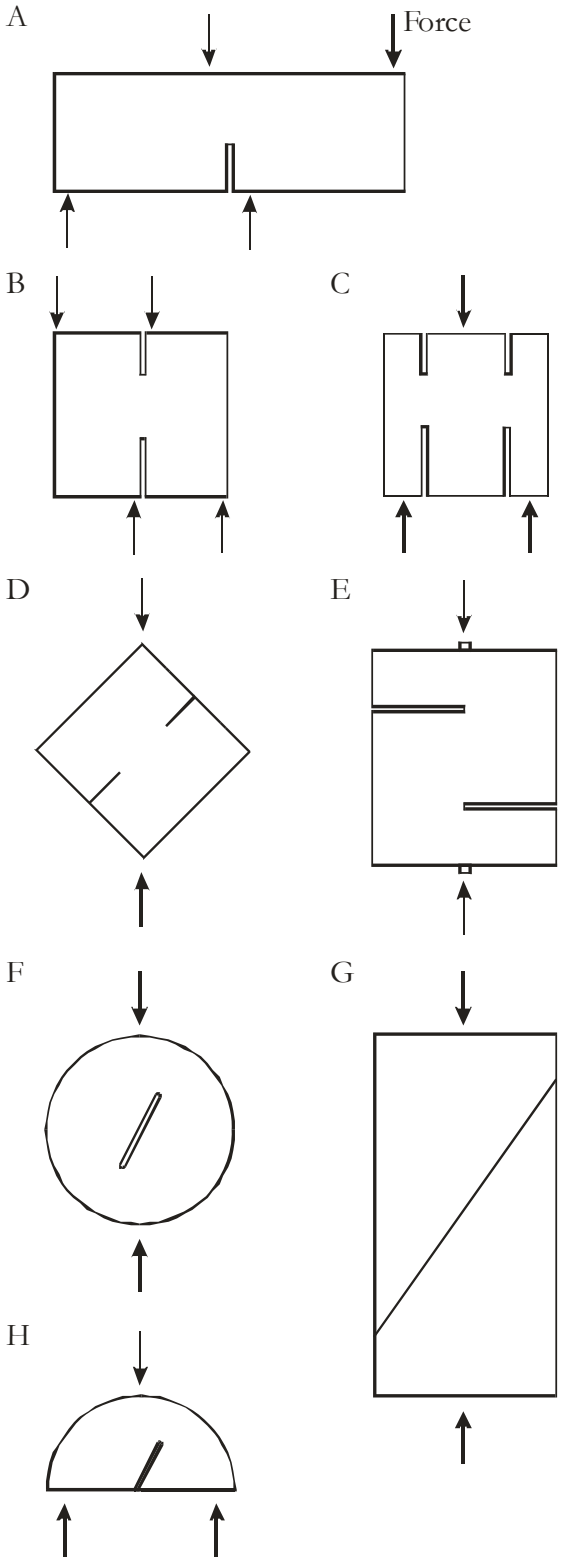

Fig. 2-11. Mode II fracture toughness testing methods. (A) Antisymmetric Four-Point Bending, (B) Antisymmetric Four-Point Bending Cube, (C) Punch Through Shear, (D) Compression-Shear Cube, (E) Short Beam Compression, (F) Centrally Cracked Brazilian Disc, (G) Triaxial Compression, and (H) Three-Point Bending Semi-Disc.

[5] The tale surrounding the Brazilian test tells that the test is called 'Brazilian', because it was developed in Brazil while shifting a church in a small village. Mortar rollers were put underneath the church and the church was moved. During this procedure several rollers split apart. (Gramberg, 1989; Hudson & Harrison, 1997).

Watkins[6] (1983) introduced the rectangular Punch Through Shear Test (Fig. 2-11.C) and argued numerically that failure takes place in Mode II (Davies et al., 1986).

The Compression-Shear Cube test (Fig. 2-11.D) (Jumikis, 1979) was shown to be a potential method for determining K_{IIC} (e.g. Izumi et al., 1986). This method was employed by Rao (1999) to determine K_{IIC} of granite and marble.

The Short Beam Compression test (Fig. 2-11.E) with a special notch orientation was developed by Watkins & Liu (1985). The notches are orientated perpendicular to the loading direction. The K_{IIC} values determined in this test are always less than the K_{IC} values, although K_{IC} is thought to be lower than K_{IIC}. K_{IIC} being smaller or close to K_{IC} is not reasonable for brittle rock, since from experimental experience the shear strength is known to be in general larger than the tensile strength (e.g. Rao et al., 2003). An exception to this might be very porous materials like e.g. some sandstones, mortar and concretes.

Several other testing methods for K_{IIC} have been invented. Some were first developed for the determination of the stress intensity factor for Mode I or mixed mode, but as the stress intensity factors are functions of the angle between applied load and the fracture plane (Atkinson et al., 1982), they were modified to perform K_{IIC}-testing.

The Cracked Chevron Notched Brazilian disc (CCNBD) (Fowell, 1995) was originally introduced by the ISRM as a Suggested Method for determining the Mode I fracture toughness of rocks (c.f. previous section). Mode II loading can be induced with a distinct inclination of the slot (Fig. 2-11.F), but slight inaccuracy in the set-up results in mixed mode conditions. Therefore, this method is not practical for determining the Mode II fracture toughness. In contrast, Chang et al. (2002) claim the CCNBD method is suitable for mixed mode as well as Mode II determination.

The same problem and discussion as for the CCNBD test is evident with the SCB- test (Chong & Kuruppu, 1984). It uses a half 'Brazilian Disk' with an introduced notch at diagonal cut (Fig. 2-11.H).

To estimate the Mode II energy release rate of intact rocks an evaluation method for the Triaxial Compression Test was introduced (Hakami & Stephansson, 1990) following Rice (1980) (Fig. 2-11.G). It was found that the energy release rate and, hence, fracture toughness is influenced by confining pressure (Hakami & Stephansson, op. cit.).

The only tests out of those presented above, that are able to demonstrate the theoretical and in laboratory experiments proven dependency of the fracture toughness on confining pressure, are the Compression Shear Cube and the Triaxial Compression Test. Unfortunately, both methods cannot vary confining pressure and shear stress independently during testing and, hence, are limited in magnitude of confining pressure.

2.5.3 Factors influencing fracture toughness

Fracture toughness was introduced in Section 2.2. The critical stress intensity factor is a mechanical property of the material that may vary with changing environmental and loading conditions (Erdogan & Sih, 1963). Selected factors are briefly discussed below.

Confining pressure

Winter (1983) among others could show experimentally that K_{IC} increases with increasing confining pressure. Tests on three point bending specimen with increasing confining pressures on e.g. Ruhr sandstone showed a linear increase of fracture toughness by a factor of five up to 100 MPa confining pressure. Thallak et al. (1993) confirm a linear increase of K_{IC} with confining pressure for laboratory hydrofracture experiments. Al-Shayea et al. (2000) applied confining pressures up to 28 MPa to Centrally Cracked Brazilian Disc Specimen. K_{IC} for a limestone increased 274 % with an increase of 28 MPa of confining pressure, while K_{IIC} increased 137 % only (c.f. Tab. 2-1) for the same increase in confining pressure. Rao (1999) varied the loading angle in the Compression-Shear Cube testing for determination of K_{IIC} yielding a variation of confining pressure. K_{IIC} was found to linearly increase with increasing confining pressure. For marble K_{IIC} increased approximately 2.5 times for an increase of confining pressure from ambient conditions to 20 MPa. K_{IIC} of granite increased by a factor of 1.7 at P = 10 MPa.

[6] Note that Miss Watkins' name later changed to Mrs. Davies.

Other parameters

Other variations in boundary conditions have shown to influence fracture toughness. These are, for example, temperature (e.g. Al-Shayea et al., 2000; Dwivedi et al., 2000) or moisture content. So, Dwivedi et al. (op. cit.) could show K_{IC} to increase with decreasing temperature (+30° to -50° C) in CCNBD specimen. They relate this effect to the remaining moisture content in the samples. The water freezes and the fracture toughness of the ice adds to the one of the rock. Changing the moisture content changes the degree of K_{IC}-variation with temperature change. With increasing temperature, K_{IC} increases slightly until approx. 100° C, and then starts dropping (Al-Shayea et al., op. cit). K_{IIC} was shown to slightly increase with temperature, at least for temperatures up to 120°C (Al-Shayea, op.cit.).

For the influence of loading rate on fracture toughness refer to Section 2.4.2 (and e.g. Zhang et al., 1999; Atkinson, 1984).

Interestingly, fracture toughness can be related to physico-mechanical properties of rock, like Young's modulus, uniaxial compressive strength, tensile strength, point-load index, Poisson's ratio, compressional wave velocity, grain size, grain contact length, or dry density (c.f. e.g. Whittaker et al., 1992; Bearman, 1999; Zhang, 2002; Alber & Brardt, 2003).

2.5.4 Typical data on K_{IC} and K_{IIC} for rocks

Table 2-1 summarises typical values for K_{IC} and K_{IIC} for several rock types. In general K_{IIC} is larger than K_{IC} in rock, a factor of 2-3 is usually assumed for ambient conditions (e.g. Rao et al., 2003). Lockner (1995) even suggests a factor of 15.

Rock type	Value [MPa m$^{1/2}$]	References
K_{IC}		
Diorite (Äspö)	3.21	Staub et al. (2003)[1]
Diorite	2.22-2.77	Bearman et al. (1989)[1]
Dolostone	0.81-2.57	Gunsallus & Kulhawy (1984)[2]
Granite	~2.0	Ingraffea (1981)[3]
	1.88	Rao et al. (2003)[1]
	0.65-2.47	e.g. Müller & Rummel (1984)[1], Ouchterlony (1988)[1], Ouchterlony & Sun (1983)[1]
Limestone	~0.8	Ingraffea (1981)[3]
	0.82-2.21	e.g. Bearman et al. (1989)[1], Guo (1990)[1], Ouchterlony & Sun (1983)[1]
P=0.1MPa	0.42	Al-Shayea et al. (2000)[5]
P=28MPa	1.57	
Marble	2.21	Rao et al. (2003)[1]
	0.46-2.25	e.g. Bearman (1999)[6], Guo (1990)[1], Müller & Rummel (1984)[1], Ouchterlony (1988)[2]
Sandstone	1.67	Rao et al. (2003)[1]
	0.67-2.56	e.g. Guo (1990)[1], Ouchterlony (1988)[1/2], Meredith (1983)[2]
P=0.1MPa	1.08	Müller (1984)[1]
P=40MPa	2.21	
P=80MPa	2.54	
K_{IIC}		
Granite	~2.2	Ingraffea (1981)[3]
	4.90	Rao et al. (2003)[4]
	1.75-20.60	Singh & Sun (1989)
Limestone	~0.9	Ingraffea (1981)[3]
P=0.1MPa	0.92	Al-Shayea et al. (2000)[5]
P=28MPa	2.18	
Marble	6.1	Rao et al. (2003)[4]
	3.33-6.36	Rao (1999)[4]
Sandstone	4.95	Rao et al. (2003)[4]
	0.32-0.41	Singh & Sun (1989)
K_{IIC}/K_{IC}		
Granite	~1.1	Ingraffea (1981)
	2.6	Rao et al. (2003)
Limestone	~1.1	Ingraffea (1981)
P=0.1MPa	2.1	Al-Shayea et al. (2000)
P=28MPa	1.4	
Marble	2.8	Rao et al. (2003)
Sandstone	3.0	Rao et al. (2003)

Tab. 2-1. Fracture toughness data from various sources. Note the confining pressure, P, dependent data. A compilation of K_{IC} values for different rock types can be found in Whittaker et al. (1992). [1] Chevron Bend (CB-) method, [2] Short Rod (SR) method, [3] Antisymmetric Four-Point Bending method, [4] Compression-Shear Cube, [5] Centrally Cracked Brazilian Disc, [6] Point-load test.

3 EQUIPMENT AND MATERIALS

The loading equipment and Acoustic Emission (AE) recording system employed in this work are described. Selected properties, e.g. elastic properties, strength data and microstructural parameters, of the tested rocks – one diorite, two granites, one limestone, one sandstone and one marble – are presented.

3.1 Loading equipment

A stiff ($1.1 \cdot 10^{10}$ N/m) servo-controlled loading frame (MTS, Material Test Systems Corporation, Minneapolis MI, USA; model-no.: 815-315-03) including a 400 MPa oil pressure vessel is used (Fig. 3-1). The maximum compressive force is 4600 kN. A high accuracy load cell with a range of 0-1000 kN (calibration error < 1 %; sensitivity = ± 1 kN) is used. The confining pressure system is servo-controlled. Maximum oil pressure is 200 MPa (± 0.5 MPa). The system is run by the controlling packages TestStarII and TestWare by MTS. The detailed specifications of the controlling procedures used for testing are listed in Appendix D.

A Hoek-Cell with a maximum pressure of 70 MPa, manufactured by RocTest Ltd., Canada, is used. The inner diameter of the cell is 2 inches. The pressure is applied by an ENERPAC hand pump.

3.2 Acoustic Emission equipment

The acoustic monitoring system consists of eleven piezoelectric transducers glued to the sample surface. A 12-channel fast storage oscilloscope with 10 bit vertical resolution at 10 MHz sampling rate (PSO 9070, Krenz, Germany) was used to store full AE waveforms. During testing, ultrasonic transmission tests were performed periodically to monitor P-wave velocities in different directions and at different loading stages. A 400 V electrical pulse was applied to two transducers and arrival times and AE amplitudes were recorded. Hypocenter location was determined by a least square iterative technique using automatic picking of onset arrivals. Details on the recording system and location analysis were described by Zang et al. (1998). All work related to recording and analysis of acoustic emissions was carried out by Dr. S. Stanchits, GeoForschungsZentrum (GFZ) Potsdam, Germany.

3.3 Tested materials

The rock materials tested in this study are briefly described below. Figure 3-2 shows grain size distributions and Table 3-1 summarises arithmetic and geometric mean grain diameters and corresponding grain size. Figure 3-3 shows micrographs of the undeformed samples. Table 3-2 summarises selected properties of the rocks.

Äspö Diorite

The Äspö diorite is from the Äspö Hard Rock Laboratory, Sweden. It is a reddish grey, medium-grained, porphyric monzodiorite, with feldspar augen of 10-30 mm. The Äspö diorite belongs to the 1700-1800 Ma Småland granite suite (Wikberg et al., 1991). The grain size is 1.3 mm.

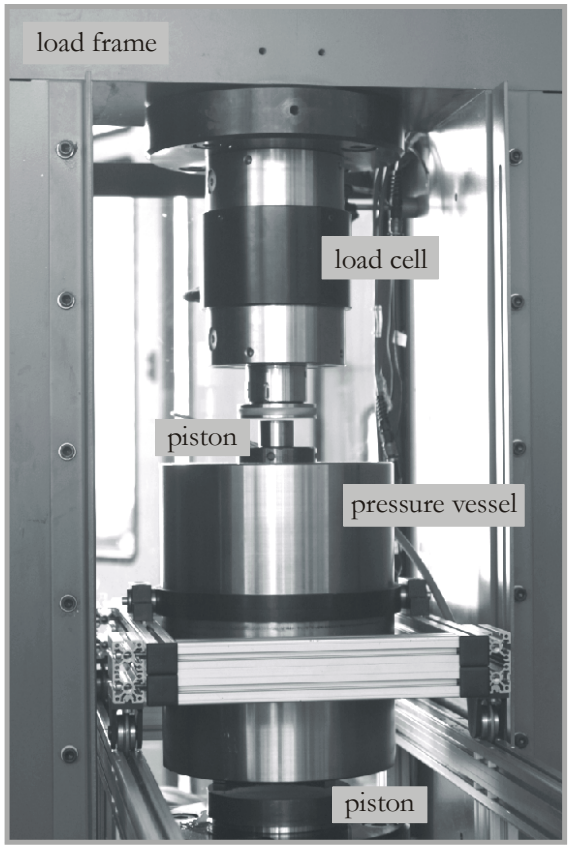

Fig. 3-1. Photograph of the MTS loading frame. Frame, load cell and pressure vessel are indicated.

Rock type	Geometric diameter	Arithmetic diameter	Grain size
	[mm]	[mm]	[mm]
Äspö diorite	0.85	1.37	1.28±1.61
Aue granite	0.66	0.82	0.99±0.67
Mizunami granite	0.43	0.55	0.65±0.43
Carrara marble	0.18	0.19	0.27±0.10
Flechtingen sst	0.15	0.16	0.23±0.08
Rüdersdorf lim	-	-	~0.01

Tab. 3-1. Geometric and arithmetic mean grain diameter as determined from intercept length measurements, and average grain size (Underwood, 1970). Calculation factor for grain size from geometric mean diameter is 1.5, assuming spherical, space-filling grains.

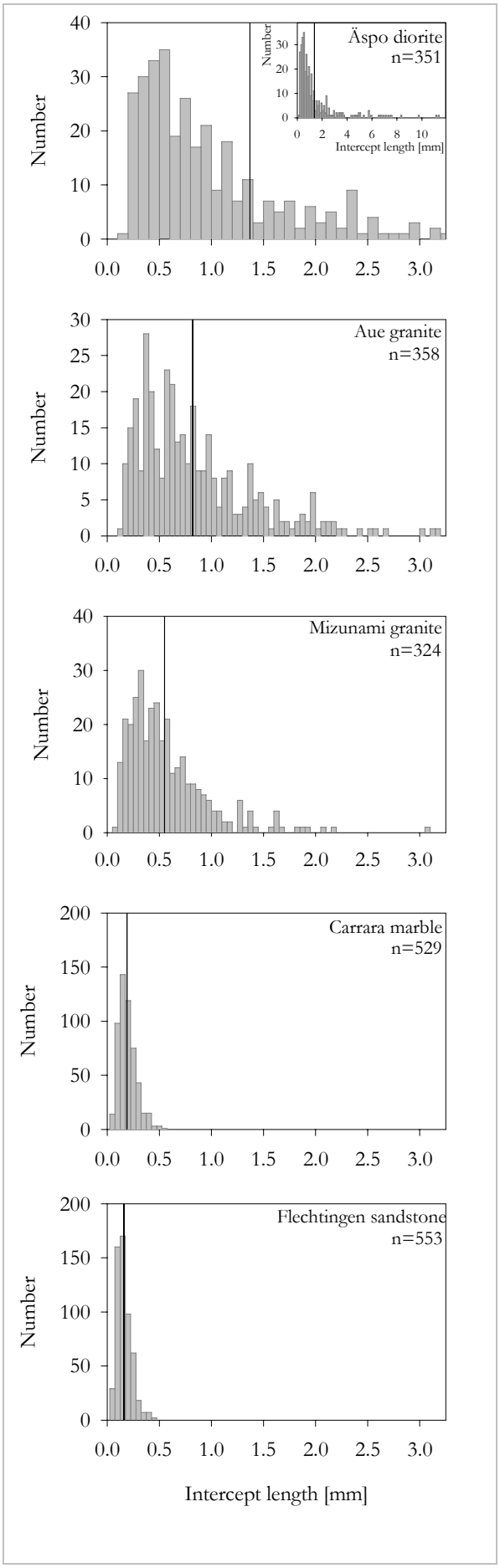

→
Fig. 3-2. Grain size distribution of tested rocks. Intercept length is given; arithmetic mean grain diameter as determined from intercept length measurements (Underwood, 1970) is indicated by vertical line. Rüdersdorf limestone has a grain size about 5-15 μm (not shown). Data for Äspö diorite is cut off at high intercept lengths. Counting traces of length 76 to 447 mm were imprinted to micrographs. Data was taken in two perpendicular directions, showing no anisotropy.

Aue Granite

The Variscian Aue granite from the Erzgebirge, Germany, is a red syeno-monzo-granite. The quartz content is about 30 vol.%, the feldspar content 60 vol.%, and mica 10 vol.%, respectively (Zang, 1997). The grain size is 1.0 mm, but grains up to 5.0 mm can be found. Feldspars are frequently altered to chlorite.

Mizunami Granite

The granite is from a borehole sunk for the Mizunami Underground (MIU) Research Laboratory project in Japan. It is classified as biotite granite (~50 % quartz, ~40 % feldspar and ~10 % others). The medium grained granite is from ~ 200 m to ~ 500 m below surface, grain size is 0.7 mm.

Carrara Marble

The Jurassic marble is from an unknown quarry near Carrara, Italy. It has a mineral content of 99 vol.% calcite with a mean grain size of 0.3 mm. The material appears isotropic and shows no preferred cleavage or lattice orientation.

Flechtingen Sandstone

The red sandstone of Permian age is from a quarry near Magdeburg, Germany, and has frequently been used as building stone. The grain size is about 0.2 mm, varying between 0.1 and 0.5 mm. Grain shape is sub-angular to sub-rounded. The sandstone consists of quartz (~70 vol.%), feldspar (~15 vol.%), and diagenetic cement (~15 vol.%) (Zang, 1997). Besides calcite and dolomite, illite is the main component of the cement (~9 vol.%). The material appears isotropic and shows little to no macroscopic visible layering.

Rüdersdorf Limestone

The mudstone (c.f. nomenclature Dunham, 1962) from the Rüdersdorf open pit mine near Berlin, Germany, has a low fossile content. It is of Triassic age and consists of 90-95 vol.% calcite, and minor percentage (~ 5-10 %) of clay. Clay aggregates have a maximum size of 0.3 mm, grain size is approximately 10 μm.

Rock type	Uniaxial comp. strength σ_C [MPa]	Tensile strength σ_T [MPa]	Young's modulus E [GPa]	Poisson's ratio ν	Dry density ϱ [g/cm³]	Porosity φ [%]
Äspö diorite	219 ± 15 [1]	15 ± 1 [1]	68 ± 8 [1]	0.24 [1]	2.8 [7]	1.1 [7]
Aue granite	134 ± 7 [2]	8 ± 1 [7]	48 ± 8 [2]	0.19 [2]	2.6 [7]	1.8 [7]
Mizunami granite	166 ± 35 [3]	9 ± 2 [3/7]	50 ± 8 [3]	0.37 [3]	2.6 [7]	1.7 [7]
Carrara marble	59[4]/101 ± 6 [7]	~7 [7]	49 [4/5]	0.23 [4/5/7]	2.7 [7]	0.7 [7]
Flechtingen sandstone	96 ± 13 [2/7]	6 ± 1 [7]	21 ± 5 [2/7]	0.12 [7]	2.30 ± 0.03 [7]	13.6 [7]
Rüdersdorf limestone	40 [6]	5 ± 1 [6/7]	22 [6]	0.22 [6]	2.6 [7]	5.5 [7]

Tab. 3-2. Compilation of selected rock properties of the chosen rock types. Values are taken from: [1] Staub et al. (2003), Nordlund et al. (1999), [2] Zang (1997), [3] JNC Development Institute report (2003), [4] Hauptfleisch (1999), [5] Alber & Hauptfleisch (1999), [6] Alber & Heiland (2001) and pers. comm. J. Heiland (1999), and [7] new data – this work.

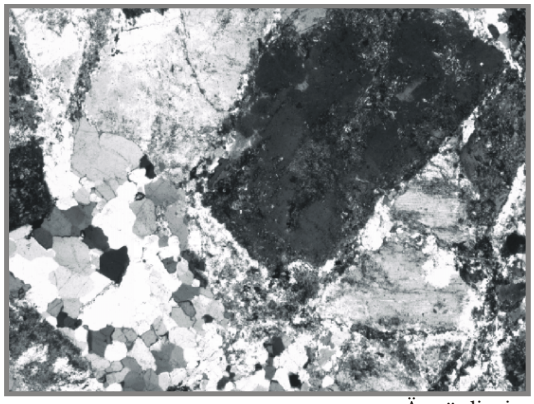

Äspö diorite

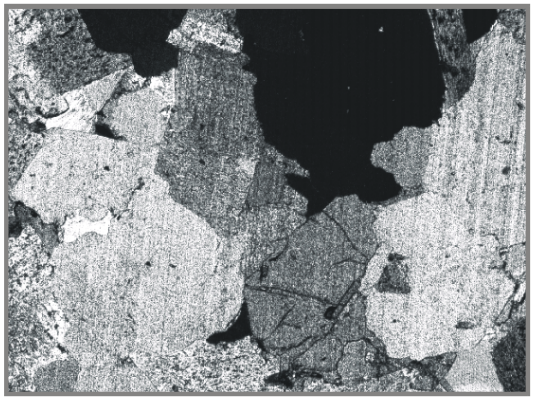

Aue granite

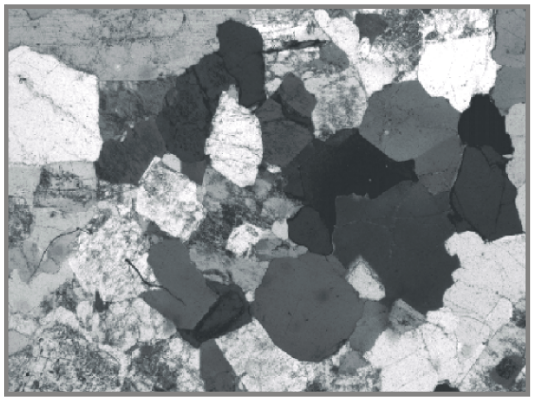

Mizunami granite

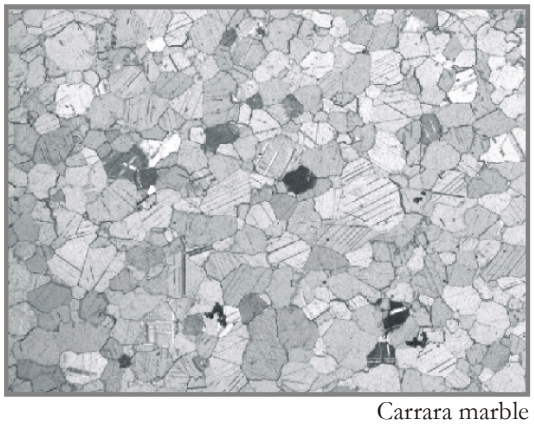

Carrara marble

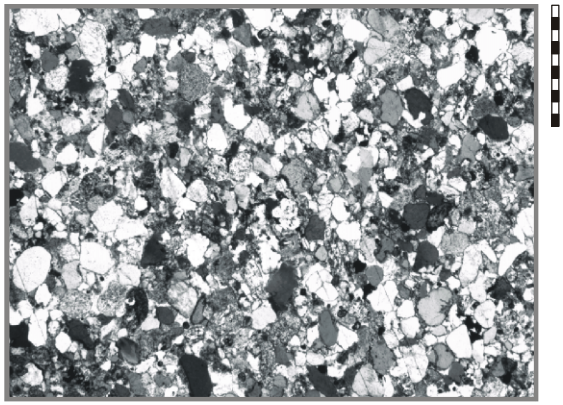

Flechtingen sandstone

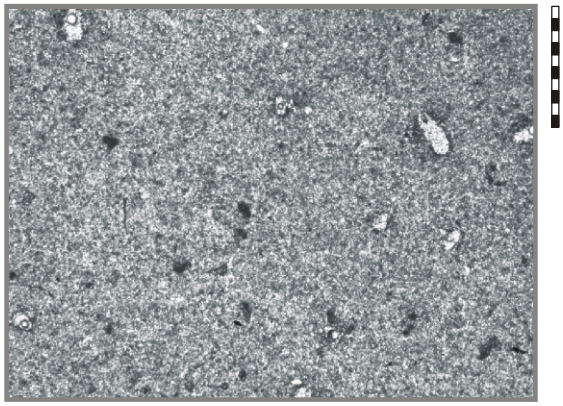

Rüdersdorf limestone

←↑

Fig. 3-3. Micrographs of undeformed samples of each rock type taken with crossed nicols. All micrographs are the same scale.

4 MODE I LOADING – METHODS, RESULTS AND DISCUSSION

The influence of loading rate on various parameters during slow fracture propagation of Flechtingen sandstone samples subjected to Mode I loading is examined in this chapter. The ISRM Suggested Method for Mode I fracture toughness determination (Ouchterlony, 1988) is employed for applying Mode I loading and for determination of K_{IC}.

Fracture velocity is dependent on the stress intensity as is outlined in Section 2.5.2. Fracture roughness increases with increasing loading rate. For example, Marder & Fineberg (1996) showed that slow moving fractures in Plexiglas tend to leave smooth fracture surfaces, whilst fractures travelling at speeds above a critical limit create small branches that can be examined microstructurally. The formation of microcracks in the fracture process zone (FPZ) produces Acoustic Emissions (AE) that allow monitoring fracture propagation in-situ.

The loading rates applied in this study are chosen to provide fracture speeds at which subcritical crack growth is suggested to be a likely mechanism (fracture velocity $< 10^{-3}$ m/s; Atkinson, 1984) and are well below the threshold for which K_{IC} is expected to increase considerably near the terminal velocity (e.g. Zhang et al., 1999). A series of experiments with variation of loading rates from $5 \cdot 10^{-6}$ m/s to $5 \cdot 10^{-10}$ m/s has been carried out, which corresponds to fracture propagation rates of 10^{-2} m/s to 10^{-6} m/s. Mechanical and fracture toughness data are analysed, the surface roughness of the resulting fractures is characterised and resulting microstructures and acoustic emission activity are presented and discussed.

4.1 Methods

4.1.1 The Chevron Bend method

Loading for determination of Mode I fracture toughness, K_{IC}, was done according to the ISRM Suggested Method (Ouchterlony, 1988), using the Chevron Bend (CB-) method. The set-up is outlined in Figure 4-1, and typical dimensions for testing are given in Table 4-1.

Sample preparation and testing set-up

Core samples of 50 mm diameter are used in this study (Fig. 4-1). They are cut to a minimum length of 200 mm. A chevron (V-) shaped notch is cut in the middle of the specimen meeting the requirements defined in Table 4-1. Centred to the notch tip two metal knives are glued on the mantle surface at a distance of approximately 5 mm using a quick hardening glue. A clip-gage for measuring the notch opening (clip-gage opening displacement, COD) is attached to the knives. For accurate measurement of sample bending (load-point displacement, lpd) a saddle equipped with lvdt's (linear variable differential transformers) can be applied, resting on top of the sample. AE transducers are directly glued to the sample surface (Fig. 4-1.B+C). The assembly is placed centred with respect to the notch onto two support rollers with a support span, S, of 166.5 mm. The tip of the notch is pointing downwards. A third roller applies the load opposite the notch tip inducing a three-point bending to the core specimen.

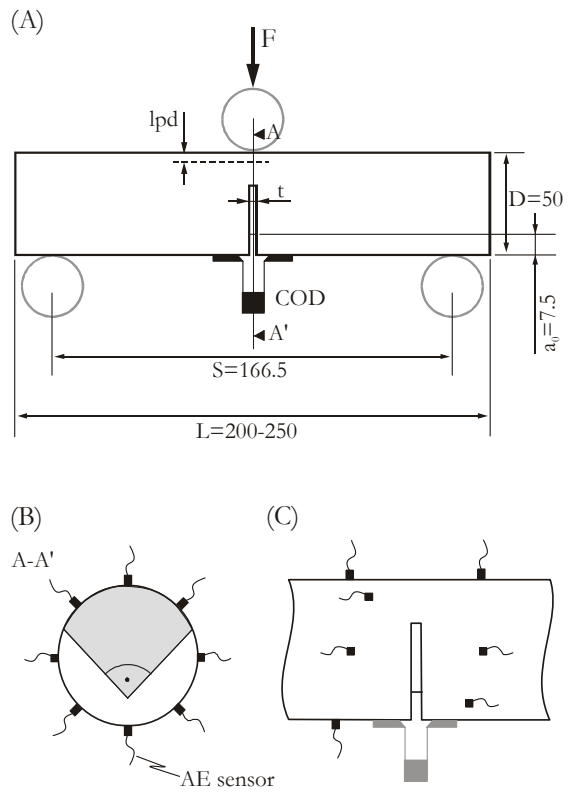

Fig. 4-1. Experimental set-up and loading configuration of the Chevron Bend (CB-) method. (A) The cylindrical sample with a centred notch is subjected to load, F, in three-point bending. Dimensions are indicated [in mm]. Devices for measurement of clip-gage opening displacement (COD) and load-point displacement (lpd) are shown, c.f. Table 4-1 for dimensions. D: specimen diameter, a_0: Chevron tip position, F: applied load, t: notch width, S: support span and L: specimen length. (B) Cross section A-A' of the chevron-shaped notch. Location of the AE sensors is indicated in cross section (B) and along sample (C).

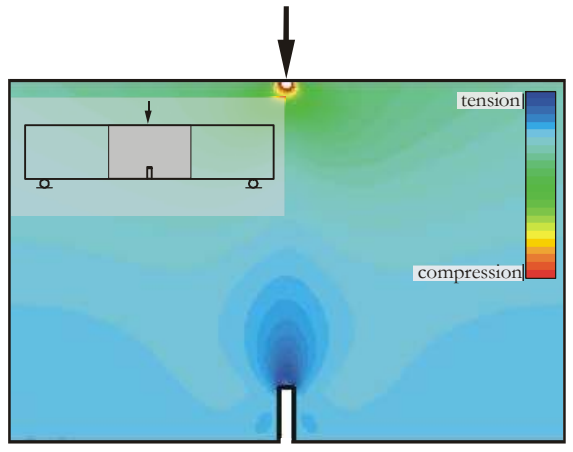

Fig. 4-2. Finite element modelling of CB set-up. Major principal stress is plotted, the scale notifies equal amount of tensile and compressive stress.

Geometry	Value	This study [mm]
Specimen diameter	D	50
Specimen length, L	>3.5 D	200–250
Support span, S	(3.33 ± 0.02) D	166.5
Chevron angle, θ	90.0° ± 1.0°	90°
Chevron tip position, a_o	(0.15 ± 0.01) D	7.50±0.06
Notch width, t	0.03 D	1.5

Tab. 4-1. Dimension of the Chevron Bend (CB-) samples for determination of K_{IC}. The parameters are chosen according to the ISRM Suggested Method (Ouchterlony, 1988).

Figure 4-2 depicts the major principal stress as obtained from FEM in a three point bending set-up. The localised stresses around the notch tip are tensile, i.e. negative; at the load point high compressive stresses are evident. The symmetric stress concentration diminishes quickly away from the notch tip.

Testing procedure

The CB- method suggests two routines for loading, i.e. level 1 and level 2 testing. In level 1 testing the specimen is loaded in load control and unstable fracture propagation leading to catastrophic failure occurs within approximately 10 s. In this study cyclic loading is applied as suggested for level 2 testing; each experiment consists of at least 4 loading/unloading cycles. The experiments are COD controlled. The suggested loading velocity (COD-rate) is $5 \cdot 10^{-7}$ m/s, unless otherwise stated. Unloading and reloading is initiated at least twice before and after peak load for determination of a correction factor, p. Force, F, load-point displacement and clip-gage opening are recorded. Typical recordings are shown in Figure 4-3.

Evaluation

The Mode I fracture toughness is determined by

$$K_{IC} = \left[\left(\frac{1+p}{1-p}\right)^{0.5} \frac{F_C}{F_{max}}\right] \cdot \left[\frac{F_{max} A_{min}}{D^{1.5}}\right] \text{and} \qquad (4\text{-}1)$$

$$A_{min} = \left(1.835 + 7.15\frac{a_0}{D} + 9.85\left(\frac{a_0}{D}\right)^2\right) \cdot \frac{S}{D} \qquad (4\text{-}2)$$

where F_{max} is the peak load, D is the specimen diameter, A_{min} is a geometry correction factor accounting for diameter, support span, S, and

notch depth, a_0 (Ouchterlony, 1988). The first part of equation 1 accounts for non-linearity. F_C is the corrected peak load and p is determined following the proposal of Barker (1979) which bases on energy considerations. It describes the change in slope of two neighbouring unloading/reloading loops spanning the peak load and is

$$p = \frac{x_l}{x_u} \tag{4-3}$$

with notations as shown in Figure 4-4. According to Barker "p can be interpreted as the degree of plasticity exhibited by the specimen between two points on the loading curve where the [fracture] is growing" (Barker, 1979, p. 526) (Fig. 4-4.A). p = 0 means that the specimen suffered no additional 'plastic deformation' during loading and fracture growth (Fig. 4-4.B). An increase of p therefore exhibits an increase of 'plasticity' during fracture propagation. The upper limit p = 1 (Fig. 4-4.C) represents a completely irreversible fracture propagation.

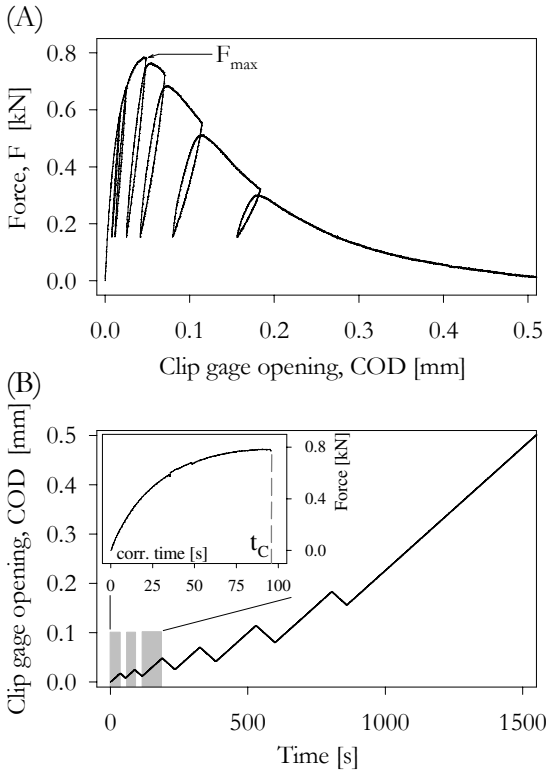

Fig. 4-3. Typical results from testing. (A) Force vs. clip gage opening, COD, plot containing six loading cycles. (B) COD vs. time. The loading and unloading is ruled by constant COD-rate. The inlay shows load vs. corrected time to determine the critical time, t_C, which is necessary to reach the peak load. Only the time intervals indicated grey are considered.

For details about sample preparation, testing and evaluation the reader is referred to the ISRM Suggested Method (Ouchterlony, 1988), Barker (1979) and Ouchterlony (1989). An instructive description for the evaluation procedure is given in Hams (1991).

4.1.2 Roughness determination

To determine the surface roughness of a fracture, its face is digitised using a 3-D laser scanner (Lanaro et al., 1998; Fardin et al., 2001). The obtained raw co-ordinate data points are reconstructed to a digital replica using Surfacer software package (Imageware, 2000). A binary object (digital replica) of 250 000 data points is obtained from the whole fracture surface of each sample. A square sampling window of size 30.0 mm by 30.0 mm (90 000 data points) is selected from each sample to describe its surface roughness.

The surface roughness is characterised using fractal dimension, D, and amplitude parameter, A. Parameter D typically describes how roughness changes with scale and A specifies the variance or surface slope at a reference scale (Kulatilake & Um, 1999). The Roughness Length Method (RLM) (Malinverno, 1990) is used to

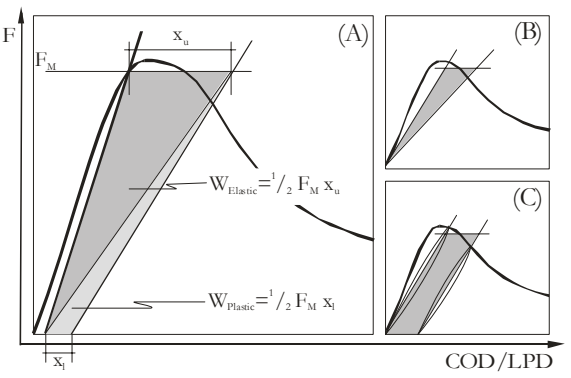

Fig. 4-4. Definition of plasticity factor, p. p is defined as x_l/x_u. The slopes are constructed as regressions to the cyclic loading branches prior to and post peak. The grey area is the elastic and irrecoverable (plastic) work, $W_{Elastic}$ and $W_{Plastic}$, done in advancing the crack an additional distance. The area trapped by the regressions, abszissis and curve is approximated by the indicated trapezoid. (A) Schematic example of testing. p is between zero and one. $W = W_{Elastic} + W_{Plastic}$. (B) At p = 0 the deformation is perfectly elastic. $W = W_{Elastic}$. (C) At p = 1 the deformation derived from plastic deformation is at a maximum.

estimate the fractal parameters. To calculate D and A of digital sampling windows of each fracture surface, a series of increasing window sizes, w, of 1.0, 1.5, 2.0, 3.0 and 6.0 mm are selected and the standard deviation of reduced asperity heights, S(w), are calculated three dimensionally (Fardin et al., 2001). As

$$S(w) = A \cdot w^{H} \qquad (4\text{-}4)$$

in case of a surface, the calculated S(w) are plotted in a log-log diagram as function of w. The Hurst exponent, H, and therefore fractal dimension D = 3-H, is obtained as the slope of the line fitted on S(w) vs. w data. The amplitude parameter, A, is directly extracted from the S(w)-intercepts.

All work related to recording and analysis of surface roughness was carried out by Dr. N. Fardin, KTH Stockholm, Sweden.

4.1.3 Microstructural analysis

The microcrack characteristics within the vicinity of the main fracture were analysed by scanning electron microscopy (Zeiss DSM 962). Microcrack density close to the fracture trace is determined from a mosaic of backscattered scanning electron micrographs at a magnification of 200x using the line intercept method (c.f. Underwood, 1970). Pores, grain-boundaries and intragranular cracks are counted along 34 to 44 traces per sample, oriented perpendicular to the fracture trace. Line length was about 1350 μm starting at the main fracture trace. 'Open grain boundaries' include grain boundaries coated with illite or other cement minerals.

4.2 Results

Results from the detailed study of the influence of loading rate on several parameters of Flechtingen sandstone are described. Additional information and observations from other rock types are given. A compilation of Mode I fracture toughness data for the rock types from Chapter 3 is presented. Dimension, failure load and determined fracture toughness of the individual specimens can be found in Appendix B.1.

4.2.1 K_{IC} determined by the Chevron Bend method for several rock types

Mode I fracture toughness, K_{IC}, was determined for the rock types described in Chapter 3. Table 4-2 summarises the results. Note the variation in the p-values. The limestone shows a low $p \approx 0.1$ whilst the sandstone shows high $p \approx 0.5$. The other rock types display p-factors between ~0.2 and ~0.3.

4.2.2 The influence of loading rate on different parameters in Mode I testing of Flechtingen sandstone

Mechanical data and Fracture Toughness

Figure 4-5.A displays the maximum force, F_{max}, versus COD-rate. Although COD-rates span five orders of magnitude, F_{max} remains almost constant; the average is $F_{max.} = 0.72 \pm 0.04$ kN. The deviation is less than 6 %, which is within the expected experimental scatter. The critical time, t_C (Fig. 4-3), is the loading time interval necessary to reach the peak load (Zhang et al., 1999) at load point displacement, δ_F. Figure 4-5.B shows the influence of COD-rate on t_C and δ_F. The time to reach the peak load increases exponentially with decreasing clip gage opening rate and the load point displacement necessary to reach the peak load stays constant.

From each experiment the uncorrected Mode I fracture toughness, K_{IC}, the correction factor, p, and the corrected fracture toughness, K^C_{IC}, have been evaluated according to Ouchterlony (1988). The loading rate, k', was calculated following Zhang et al. (1999): $k' = K_{IC}/t_C$. The fracture velocity, a', may be expressed as (Ouchterlony, 1989):

Rock type	no. of tests	K_{IC} [MPa $m^{1/2}$]	p [ ]
Äspö diorite	4	3.83 ± 0.03	0.22 ± 0.07
Aue granite	5	1.60 ± 0.13	0.29 ± 0.04
Mizunami granite	6	2.38 ± 0.12	0.29 ± 0.04
Carrara marble	5	2.44 ± 0.07	0.31 ± 0.02
Flechtinger sandstone	5	1.15 ± 0.05	0.47 ± 0.02
Rüdersdorf limestone	4	1.12 ± 0.06	0.10 ± 0.02

Tab. 4-2. Mode I fracture toughness data. K_{IC} and plasticity correction factor, p, for different rock types.

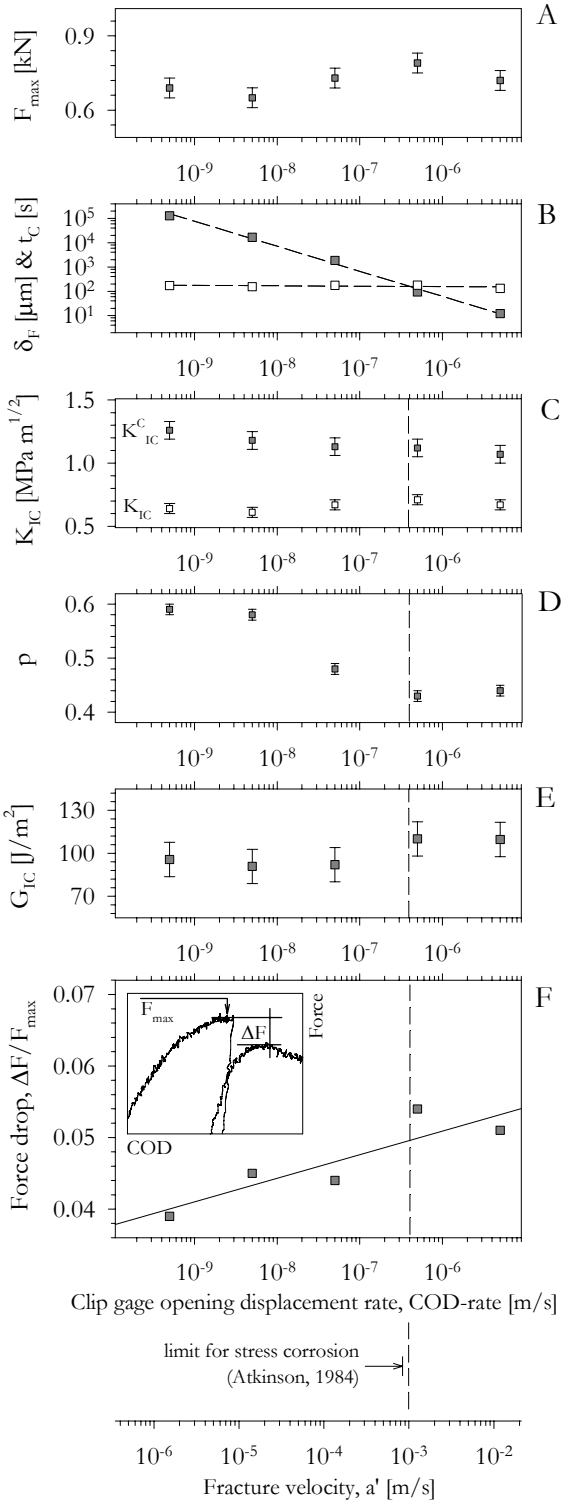

Fig. 4-5. Compilation of mechanical data of Flechtingen sandstone. (A) Peak load, F_{max}, (B) maximum load point displacement, δ_F (hollow squares), and critical time, t_C (grey squares), (C) corrected and uncorrected Mode I fracture toughness, K^C_{IC} and K_{IC}, (D) plasticity factor, p, (E) energy release rate, G_{IC}, and (F) force drop, ΔF, during reloading near peak load vs. COD-rate and fracture velocity, a'. a' is calculated according to Ouchterlony (1989), equation (34). Vertical dashed line indicates limit for stress corrosion (Atkinson, 1984).

$$a' \approx \frac{E \cdot \sqrt{D}}{6.4 \cdot K_{IC}} \cdot \delta'_F \qquad (4\text{-}5)$$

where E is the Young's modulus, D is specimen diameter, and $\delta'_F = \delta_F / t_C$.

The influence of the loading rate on both the uncorrected and the corrected stress intensity as calculated from equation 1 of the sandstone is negligible (Fig. 4-5.C). The average value is $K_{IC} = 0.66 \pm 0.03$ MPa m$^{1/2}$ and $K^C_{IC} = 1.15 \pm 0.05$ MPa m$^{1/2}$, respectively. However, K^C_{IC} increases slightly with lower loading rate. Zhang et al. (1999) report slight increase of the fracture toughness of marble for slower loading rates, and a moderate decrease of K^C_{IC} of gabbro for slower loading rates. Winter (1983) reports moderate increase of fracture toughness with loading rate for Ruhr sandstone.

The correction factor, p, increases towards lower loading rates (Fig. 4-5.D). At 'high' fracture velocities (a' = 10^{-2} – 10^{-3} m/s) the correction factor is about 0.44. For 'lower' velocities p increases up to 0.59. The limit for stress corrosion was estimated by Atkinson (1984) to be about a' = 10^{-3} m/s. For Flechtingen sandstone p indicates a threshold at a fracture velocity of about $3 \cdot 10^{-3}$ m/s, which is in agreement with Atkinson's estimation. The above-mentioned slight increase of the corrected fracture toughness, K^C_{IC}, is governed by the increase in p-value. The scatter of the results from several experiments with Flechtingen sandstone is obtained from reprocessing data available in Donath (2002). The errors for p, K_{IC} and K^C_{IC} are $\pm$ 0.01, $\pm$ 0.04 and $\pm$ 0.07, respectively.

The energy release rate, G_{IC}, was estimated by integrating the force-displacement data. G_{IC} remains almost constant at ~100 J/m² (Fig. 4-5.E). Using $K = (G \cdot E')^{1/2}$ (Irwin, 1958; cf. equation 2-7), K_{IC} was calculated from G_{IC} to about 1.45 MPa m$^{1/2}$. This K_{IC} value is higher but still in good agreement with K_{IC} estimated using the CB- test.

On reloading within the cycles the load does not reach the load level evident at initiation of unloading. Figure 4-5.F shows the influence of loading rate on the normalised force drop between unloading and reloading near peak load. The normalised force drop, ΔF, is larger for faster COD-rates and increases log-linear. During the

Sample	COD-rate [m s^{-1}]	a' [m s^{-1}]	k' [MPa m$^{1/2}$ s^{-1}]	$F_{max.}$ [kN]	δ_F [μm]	t_C [s]	K_{IC} [MPa m$^{1/2}$]	K^c_{IC} [MPa m$^{1/2}$]	p	G [Jm^{-2}]	cal. K_{IC} [MPa m$^{1/2}$]	$\Delta F/F_{max}$
FB4	$5 \cdot 10^{-6}$	$1.2 \cdot 10^{-3}$	$8.9 \cdot 10^{-2}$	0.72	176	12	0.67	1.07	0.44	109.7	1.52 ± 0.13	0.051
FB1	$5 \cdot 10^{-7}$	$1.9 \cdot 10^{-3}$	$1.1 \cdot 10^{-2}$	0.79	174	95	0.71	1.12	0.43	110.1	1.52 ± 0.12	0.054
FB2	$5 \cdot 10^{-8}$	$1.0 \cdot 10^{-4}$	$6.1 \cdot 10^{-4}$	0.73	130	1838	0.67	1.13	0.48	92.1	1.42 ± 0.12	0.044
FB5	$5 \cdot 10^{-9}$	$1.1 \cdot 10^{-5}$	$7.1 \cdot 10^{-5}$	0.65	154	16585	0.61	1.18	0.58	90.8	1.38 ± 0.11	0.045
FB6	$5 \cdot 10^{-10}$	$1.5 \cdot 10^{-6}$	$9.8 \cdot 10^{-6}$	0.69	173	128101	0.64	1.26	0.59	95.7	1.42 ± 0.12	0.039

Tab. 4-3. Mechanical and fracture toughness data. COD-rate: Clip-gage opening displacement rate; k': loading rate (Zhang et al., 1999); a': crack velocity (Ouchterlony, 1989); F_{max}: peak load, δ_F: vertical displacement of the loading roller necessary to reach the peak load; t_C: time necessary to reach the peak load; K_{IC}: uncorrected fracture toughness in Mode I; K^C_{IC}: corrected fracture toughness; p: correction factor; G: Energy release rate; cal. K_{IC}: fracture toughness calculated from G; $\Delta F/F_{max}$: force drop in un-/reloding cycles near peak load normalised by peak load.

initial phase of the force drop close to peak load, COD stays almost constant. Above presented data is summarised in Table 4-3.

Fracture Roughness

The 'isometric view' of the digital replicas, which were taken at a resolution of 0.1 mm (distance between points in two parallel scanned lines), is shown in Figure 4-6. From the calculated standard deviation of reduced asperity heights, S(w) (Tab. 4-4), a linear relationship between S(w) and window size, w, can be established, yielding fractal dimension, D, and amplitude parameter, A (Tab. 4-5).

The calculated D and A of all sampling windows and samples are plotted as function of the applied loading rate (Fig. 4-7). Although both D and A show some scatter with respect to applied loading rate, there is no clear trend to support a variation of surface roughness as a function of loading rate. The fractal parameters for characterising the surface roughness of all samples are obtained as $D = 2.247 \pm 0.016$ and $A = 0.0241 \pm 0.0012$.

Microstructure

The fracture resulting from three-point bending in the CB- test appears on sample-/macroscale as a single fracture that starts at the chevron shaped notch and propagates upwards in loading direction. It follows a rough path, deviating in a 'zig-zag' manner (Figs. 4-8.A and 4-9). Microscopically, the fracture also shows a 'zig-zag' path. From optical microscopy and SEM images of marble it can be seen that the fracture tends to follow planes of weakness, like e.g. grain boundaries or cleavage planes (Fig. 4-8.B). Frequently branching of the main fracture is observed (Fig. 4-8.C). No fracture process zone (FPZ) could be isolated from the background microcracking for marble at magnifications of up to 1 000 in SEM.

The density of the intragranular cracks shows an exponential decay of sub-parallel cracks from the main fracture front in Flechtingen sandstone (Fig 4-9). In all samples investigated [FB1; FB4; FB6] crack density dropped from about 25 mm^{-1} to background (4 mm^{-1}) within 350-400 μm distance from the fracture (Fig. 4-10). From these observations the width of the fracture process zone (FPZ) was estimated to about 700-800 μm. It is symmetric with respect to the loading direction. Among samples subjected to different loading rates, no change in crack density is evident. The density of open grain boundaries and pores remained constant.

Acoustic Emission

AE hypocenter locations indicate progressive fracture propagation and an elongated process zone surrounding the fracture trace (Fig. 4-11). Prior to peak load very few AE signals were detected close to the notch tip for the Flechtingen sandstone. In map view of the fracture, AE signals were evenly distributed (Fig. 4-11.A, xy-plane) forming a narrow band in cross section. AE activity started at about 85 % of the maximum load but was low during the first cycle (Fig. 4-11.B+C). For subsequent cycles activity increased and remained approximately constant. A cloud of AE hypocenters initiated at the notch tip and progressively extended into the sample with increasing COD. During unloading no AE was detected. In consecutive loading cycles continuous AE activity started after maximum COD of the previous cycle was

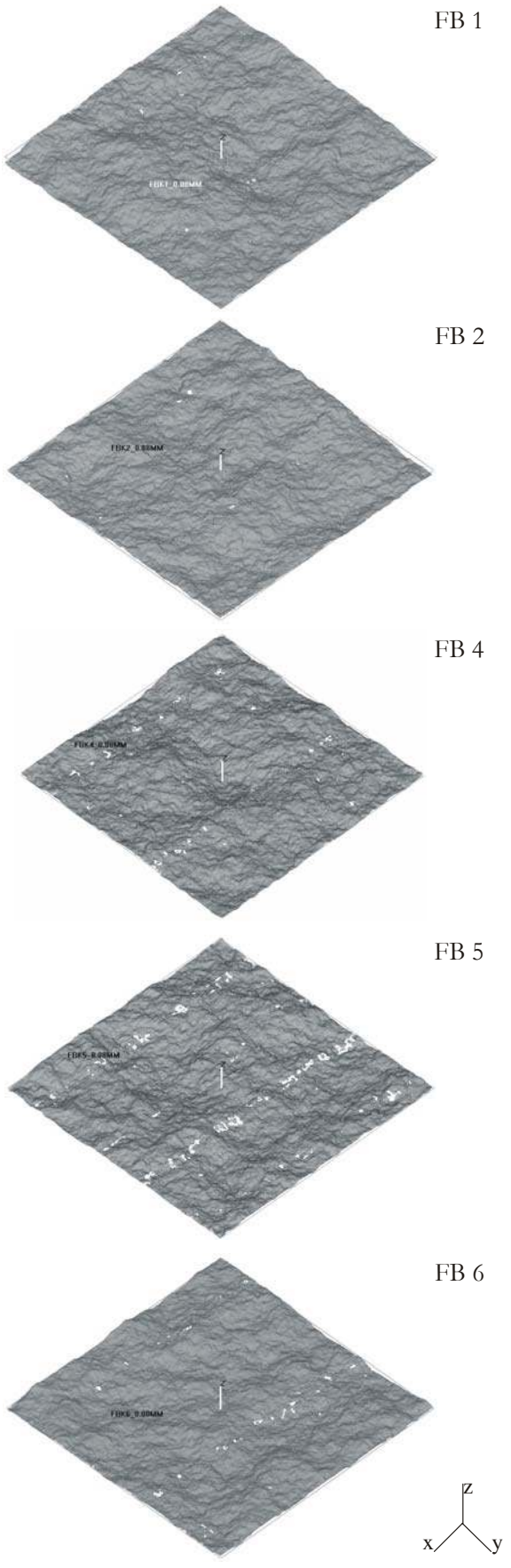

Fig. 4-6. Isometric view of the digital sampling window of the samples.

w	S(w) FB1	FB2	FB4	FB5	FB6
[mm]	[10^{-2} mm]	[10^{-2} mm]	[10^{-2} mm]	[10^{-2} mm]	[10^{-2} mm]
1.0	2.2481	2.3234	2.3912	2.5443	2.2346
1.5	3.1491	3.2079	3.3050	3.5331	3.1553
2.0	3.9154	4.0132	4.1404	4.3341	3.9843
3.0	5.3754	5.5031	5.5993	5.8537	5.4518
6.0	8.8154	8.9834	9.0653	9.4018	8.9428

Tab. 4-4. Data from profilometry for all samples. S(w) is the standard deviation of the reduced asperity heights and w is the sampling window size.

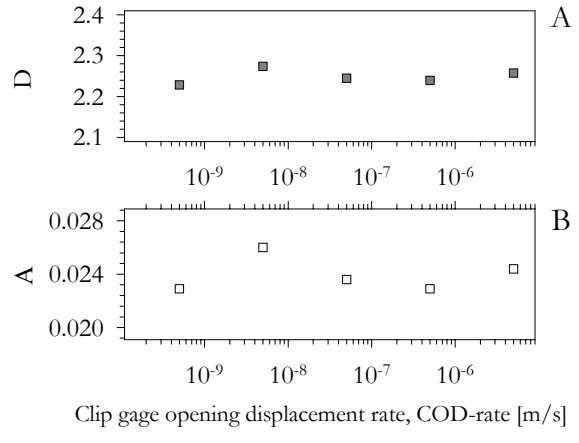

Fig. 4-7. The fractal dimension, D, and amplitude parameter, A, as function of loading rate for Flechtingen sandstone samples.

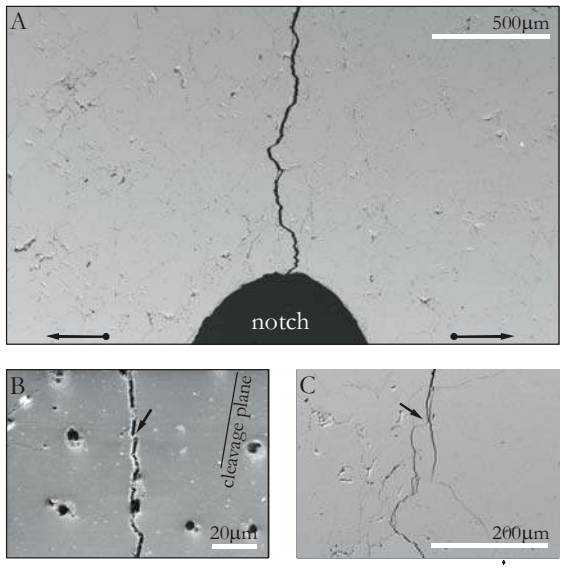

Fig. 4-8. SEM backscatter images of CB-sample of Carrara marble showing fractures from Mode I loading. (A) Main fracture trace starting at notch tip and propagating into sample. The fracture describes a rough path. (B) Fracture within one marble grain follows cleavage planes oblique to loading direction. It frequently jumps to next cleavage plane to maintain the loading direction. (C) Branching fracture. Fracture is split at a grain and propagates along two paths around grains. Later a single track is maintained.

Sample	A	D	Total number of AE	Ratio of AE sample/FB4
FB4	0.0244	2.2573	317	1.00
FB1	0.0229	2.2392	181	--
FB2	0.0236	2.2447	160	0.50
FB5	0.0260	2.2737	143	--
FB6	0.0229	2.2282	77	0.24

Tab. 4-5. Fracture roughness and Acoustic Emission (AE) data. D: fractal dimension; A: amplitude; normalised number of located AE is used to scale axes in Fig. 4-13.

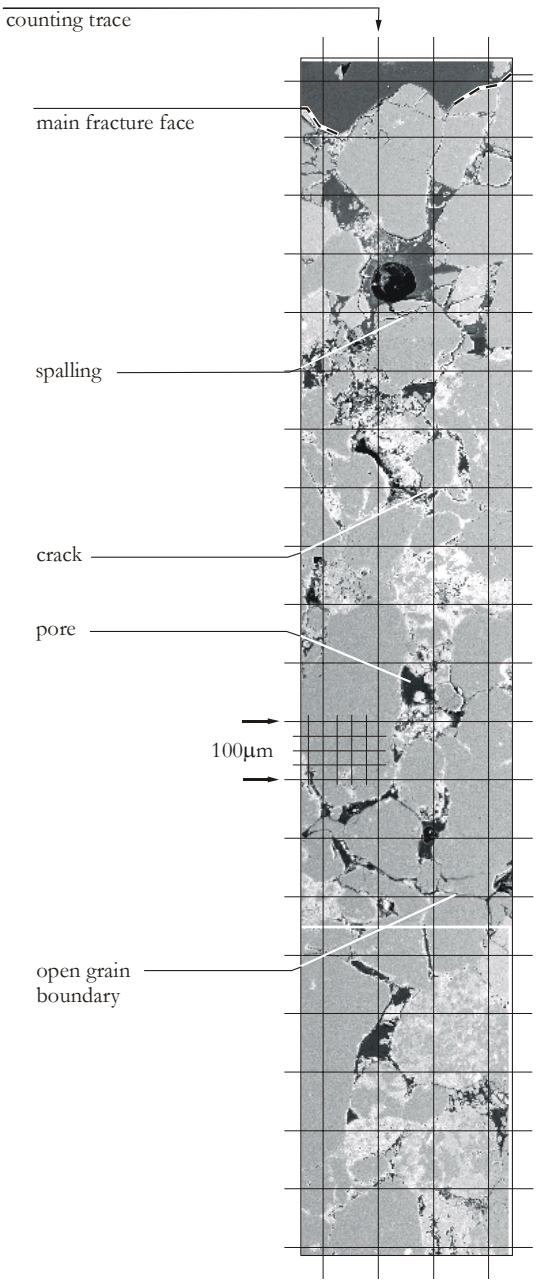

Fig. 4-9. SEM backscattered microstructures. Photomosaic of SEM images across main fracture face (top) into intact sample (bottom) [FB 2]. Intragranular cracks, pores and open grain boundaries are indicated.

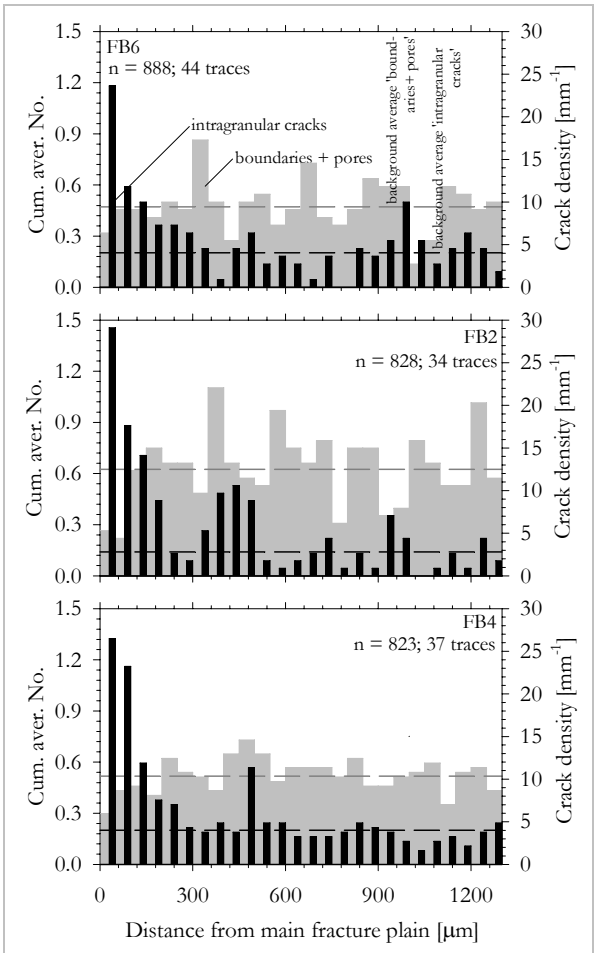

Fig. 4-10. Bar charts showing the crack density of deformed samples; FB 6 (slow) to FB 4 (fast loading rate). Intragranular cracks are in black. Open grain boundaries and pores are in grey. Dashed lines show the average background distribution of cracks, pores and grain boundaries. The density of intragranular cracks shows an exponential decay from the fracture trace into the undeformed sample. No difference in crack density of samples deformed at the range of applied loading rates.

attained (Kaiser effect; see horizontal dashed line in Fig. 4-11.C). The total number of AE events decreased markedly for slower COD rates (Fig. 4-12 and Tab. 4-5).

The width of the FPZ as indicated by AE activity is approximately 5-6 mm (Fig. 4-13) and the length is about 20 mm, irrespective of loading rate (Fig. 4-11) showing an elliptical shape. This is about 6-9 times wider than the FPZ width estimated from crack density. The shape of AE- and crack density distributions perpendicular to the fracture trace closely correspond (Fig. 4-13 and 4-10).

Same observations are made in principle for Mizunami granite. Hypocentre location and axial force vs. time recording of Mizunami granite

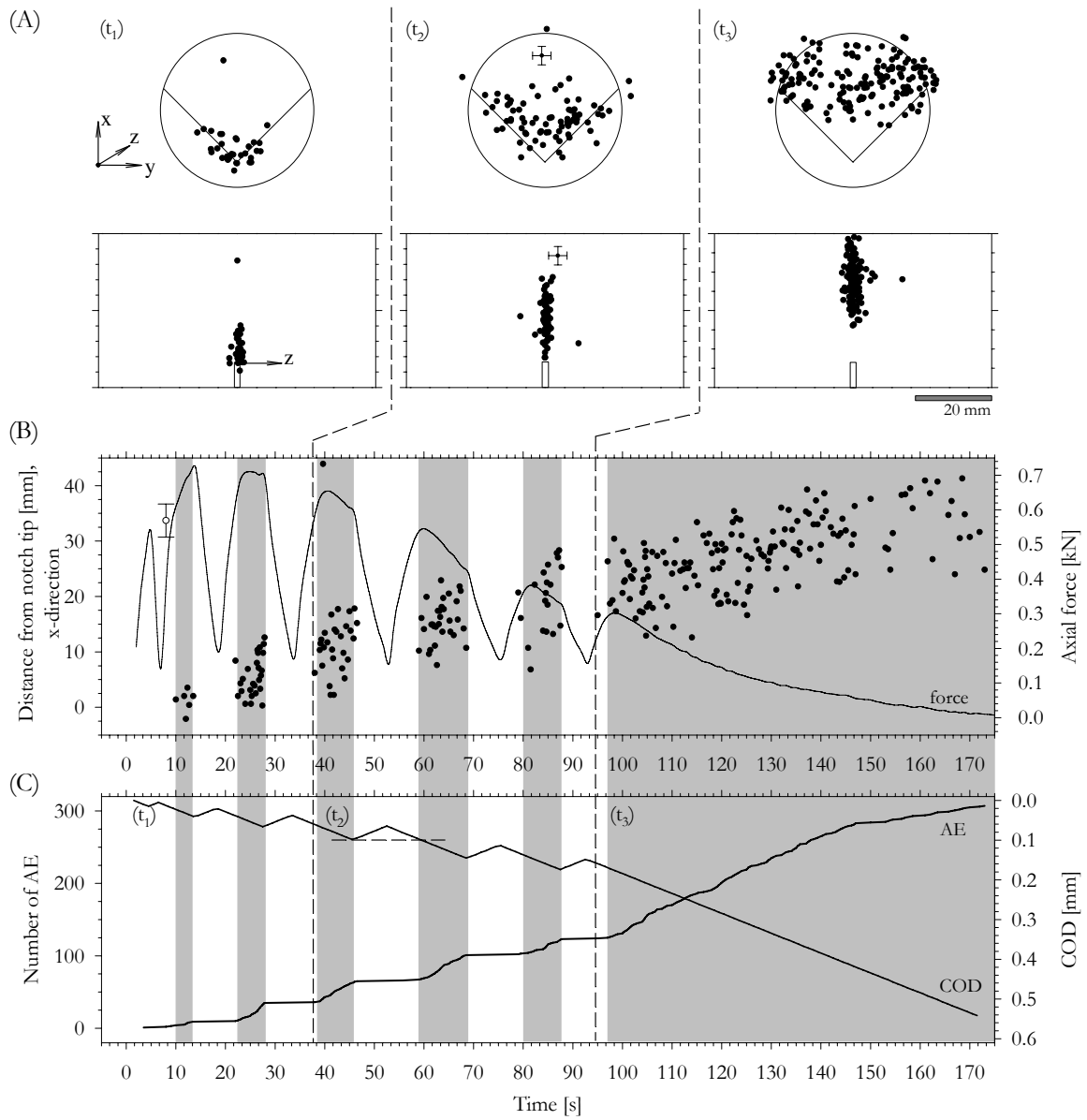

Fig. 4-11. Time dependent visualisation of axial force and AE location of CB- experiment on Flechtingen sandstone [FB4]. (A) Cross sections normal (top) and parallel to specimen long axis. Three time steps of the propagation of tensile fracture as indicated by located AE. (B) AE location with reference to the initial notch tip versus time of the experiment. Shading indicates crack propagation and arrest stages as indicated by AE activity. Load cycles are indicated by continuous line. (C) Cumulative number of AE events and COD. No AE are detected during unloading. Dashed horizontal line on COD data indicates onset of AE activity on reloading at a level at which unloading was initiated in previous cycle (Kaiser effect).

are shown in Figure 4-14. AE hypocentre locations indicate progressive fracture propagation. An elongated process zone surrounding the fracture can be interpreted from the location data (Fig. 4-14.A). The fracture propagates in a narrow band (~7-9 mm) through the sample (Fig. 4-14.B). A considerable number of events were detected prior to peak load indicating early development of the process zone at the notch tip. Continuous AE activity starts at about 80 % of the maximum load. The length of the zone of AE events ahead of the fracture tip increases with increasing clip gage opening displacement (COD) to reach a constant length of ~ 30 to 35 mm.

The AE process zone of Mizunami granite is larger than the one of Flechtingen sandstone. The total number of AE is very much less for the sandstone compared to the granite (~200 vs. ~4800) at the same loading rate. Whilst continuous AE activity started for Flechtingen sandstone at about 85%, Mizunami granite showed onset of activity at already 80%.

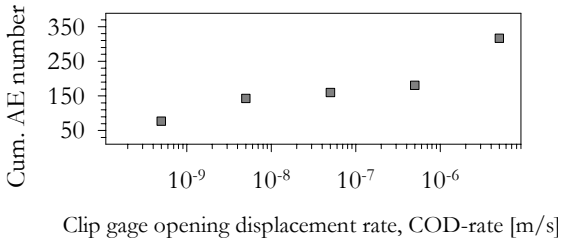

Fig. 4-12. Influence of loading rate on the cumulative number of AE events. The amount of located AEs increases about four times from the slowest to fastest experiment.

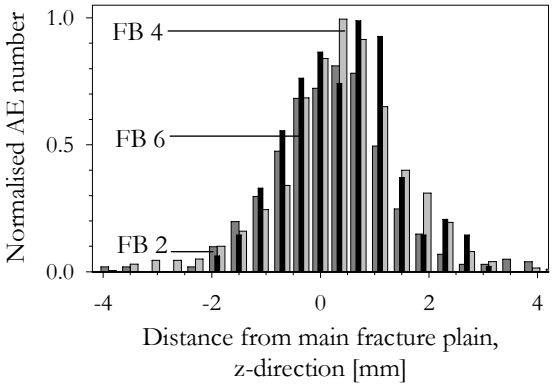

Fig. 4-13. Normalised AE density across fracture trace (see text). The width of the process zone as determined from AE remains constant irrespective of loading rate for slow [FB 6], intermediate [FB 2] and fast [FB 4] loading rates.

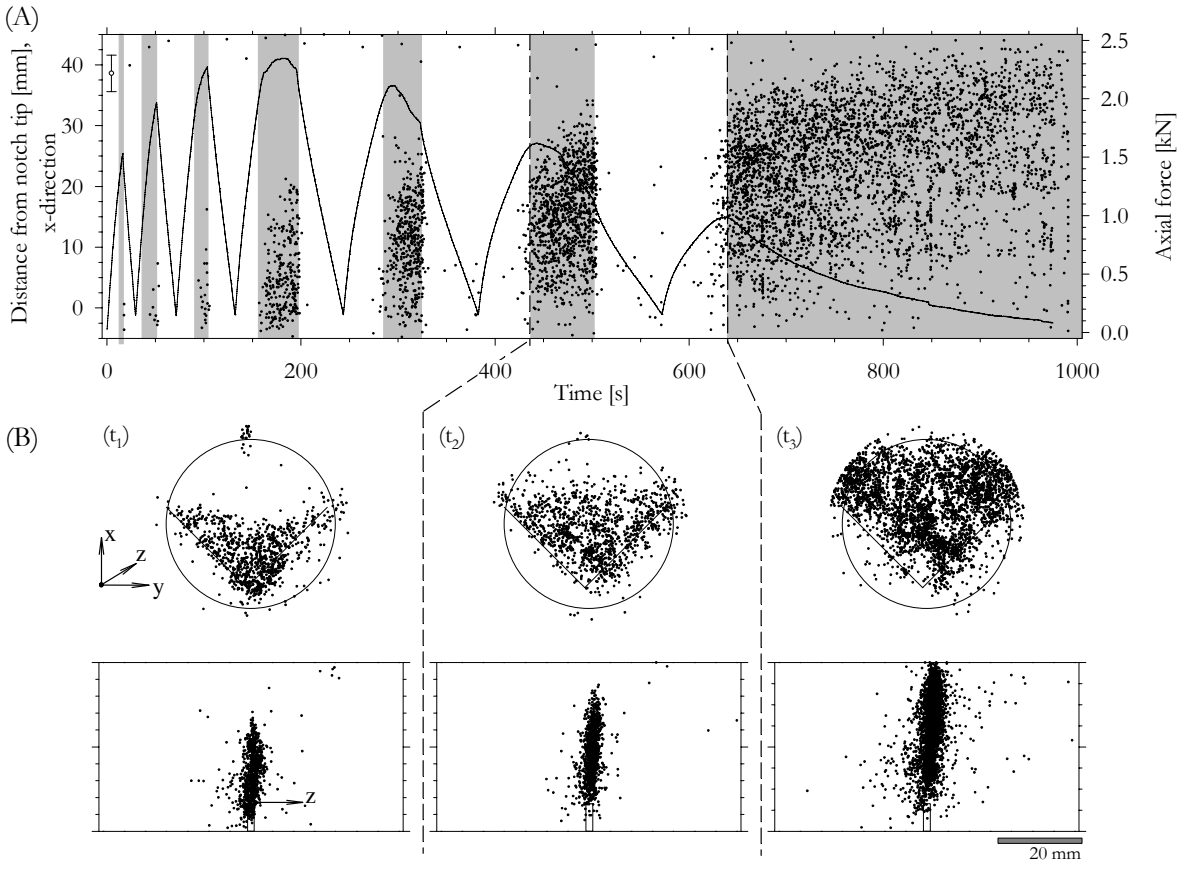

Fig. 4-14. Time dependent visualisation of axial force and AE location of CB- experiment on Mizunami granite [LT1]. (A) Time sequence of AE distribution. The AE fracture signature propagates with time through the sample, starting at the notch tip. In map view of the fracture it can be seen that the signals are evenly distributed. The time intervals of sequences 1 to 3 are indicated in (B). (B) AE events projected into fracture propagation direction, and axial force vs. time. Very few events are detected during unloading and reloading of the sample. AE activity starts again on reaching the COD level evident at unloading (Kaiser effect). Grey columns indicate the COD at which the fracture is extended. Events at top of sample are due to top loading roller.

4.3 Discussion

4.3.1 Determined fracture toughnesses

The corrected K_{IC} values obtained in this study are in good agreement with data presented in literature (c.f. Section 2.6.4). The obtained p-factors show a broad range of values. For Rüdersdorf limestone p indicates high portion of elastic deformation during fracture propagation. In contrast, for Flechtingen sandstone a comparably high percentage of 'plastic' deformation is reflected by the high p. This is further discussed below. The other rock types tested show moderate p values. All determined p values are in the reported range for rock (c.f. Whittaker et al., 1992).

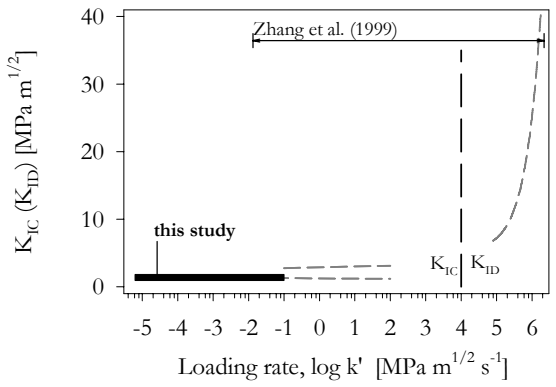

Fig. 4-15. Compilation of data on the influence of loading rate on Mode I fracture toughness. Data by Zhang et al. (1999) (dashed lines) is shown together with results of this study for low loading rates. K_{IC}: static Mode I fracture toughness; K_{ID}: dynamic Mode I fracture toughness.

4.3.2 The influence of loading rate on Mode I testing of Flechtingen sandstone

Mechanical data and Fracture Toughness

The experimental results clearly show that loading rates 10^{-6}-10^{-10} m/s do not significantly change the maximum load, F_{max}, required to propagate the fracture.

At some specific point during testing, the critical stress intensity factor is reached at the fracture tip and the fracture propagates. Using a constant COD- rate and the geometry of the CB-test keeps stored elastic energy at a minimum in the combined sample and loading system, since the applied load is reduced instantly as the fracture propagates. This immediately stabilises crack propagation and the fracture stops upon unloading, once $K < K_C$ (c.f. Section 2.4.2).

For the range of loading rates investigated in this study, stress intensity factors (and Energy Release Rate) remained constant within the scatter (Fig. 4-5.C). This indicates that fracture propagation occurred at constant energy consumption.

Figure 4-15 shows the fracture toughness as a function of the loading rate in the context of Zhang et al.'s (1999) data. The loading rates applied in this study are five orders of magnitude slower than the onset of dynamic fracture as proposed by Zhang et al. (op. cit.) and extends their data by three orders of magnitude towards slower crack velocities. The ISRM suggested method for the Mode I fracture toughness determination states that "changing [COD-rate] by a factor of ten will cause a change of only 2-10 % in measured fracture toughness" (Ouchterlony, 1988) which is in agreement with this study.

Stress corrosion effects in rock are reported to be small when cracks propagate at speeds faster than 10^{-3} m/s (Ouchterlony, 1988), even at air humidity (Atkinson, 1984; Nara et al., 2002). The limit is indicated in Figure 4-5. Three loading rates examined in this study are below this limit. If stress corrosion cracking had been the effective mechanism at lower rates, the maximum force would have decreased with decreasing loading rate, as the fracture would propagate subcritical and thereby reducing the rock ligament between load point and fracture tip. This was not observed (Fig. 4-5.A). Instead, even the displacement required to reach peak load remains constant (Fig. 4-5.B).

The peak load on reloading in force-displacement cycles at/post peak load defines the (re-) onset of crack propagation. It is lower than the load at initiation of unloading of the previous cycle. If subcritical crack growth was effective during unloading/loading one would expect to see a stronger decrease of peak load, ΔF, in low velocity cycles. Instead, the decrease of peak load between cycles is more pronounced for fast loading rates (Fig. 4-5.F).

Based on R-curve analysis from three-point bending, Ferreira et al. (2002) report evidence for

some crack extension in the rock upon unloading. After initiation of unloading, the COD stays almost constant and as the calculated crack resistance remains unchanged during this relaxation process the observed force drop might be caused by crack extension. This is in agreement with the observations presented in this work and suggests that the fracture continues to propagate a longer distance at unloading within the cycles for fast loading rates. AE sensitivity and time resolution appears not to be able to picture the remnant crack propagation. Therefore, these considerations give no evidence for subcritical crack growth.

However, it cannot be ruled out that the small force drop, ΔF, between loading cycles is possibly due to the response time of the COD-controlled loading system and crack arrest or shielding in the fracture process zone (Lawn, 1993, p. 210). For faster COD rates, ΔF increased. Again, this may be related to the finite response time of the servo-controlled loading frame and increase in the amount of stored elastic energy in the combined sample and loading system leading to small scale instability.

The correction factor p decreased significantly with increasing loading rate (Fig. 4-5.D). This indicates that the amount of non-elastic deformation is rate-dependent.

Interpreting the irreversible displacement of COD as volume increase acquires the p-factor as a tool for relative measurement of the process zone formation. $p = 0$ means that on unloading the fracture faces match perfectly and the formation of the process zone did not cause any volume increase (c.f. Fig. 4-4). Assuming that on unloading frictional effects are completely decomposed within the hysteresis, any $p > 0$ indicates formation of process zone (Fig. 4-16). The higher p the larger the volume created by the process zone development. In this testing series the p-factor, indicating 'plasticity', decreases by almost 40 % with increasing loading rate. The mechanism producing this increase in irrecoverable deformation is not known. It is not attributed to additional detectable crack formation in the FPZ, as the crack density was shown to stay constant (Fig. 4-10). However, the change in p may be related to a contribution of subcritical crack growth or viscous sliding along clay-coated grain boundaries at the low loading rates.

Fracture Roughness and Microstructure

Issa et al. (2003) suggest a linear relationship between fractal dimension and fracture toughness. This implies that with constant toughness the roughness should stay the same. This is confirmed in this study.

The size of the fracture process zone and total fracture surface area are proportional to fracture toughness and energy release rate, respectively (e.g. Atkinsson, 1991). Fracture toughness and energy release rate are constant for a broad range of loading rates and also fracture process zone width and crack density remain unaffected as was observed in the study. This is also to some extend reflected by the constant roughness.

Acoustic Emission

Bursts of acoustic emission associated with fracture propagation indicate that fracture propagation on the grain scale is dynamic. A fraction of the total energy dissipated during fracture growth is radiated as high-frequency elastic waves, although the tip of the macroscopic fracture may propagate quasi-statically (Zang et al., 1998). AE hypocenter locations show that the fracture initiates at the notch tip and then propagates upwards through the sample (Fig. 4-11). Macroscopic fracture propagation velocity estimated post peak from AE hypocentre locations ranges from $2 \cdot 10^{-4}$-$3 \cdot 10^{-8}$ m/s. Growth rates estimated from macroscopic observations during the experiment give similar values (Tab. 4-6). However, these velocity estimates are generally lower by 1-2 orders of magnitude than those derived from equation (4-5).

Only few AE events were recorded before the first load peak. For sandstone and granite, Zietlow & Labuz (1998) and Labuz & Biolzi (1998) also found onset of AE activity between 50-95 % of maximum load. In subsequent loading cycles the process zone, as indicated by AE hypocenters, attained a constant elliptical shape of about 5 times 20 mm in cross section for the Flechtingen sandstone. Zietlow & Labuz (1998) report a process zone size of 5 times 25 mm from three-point bending tests performed on Berea sandstone, which has a grain size similar to Flechtingen sandstone.

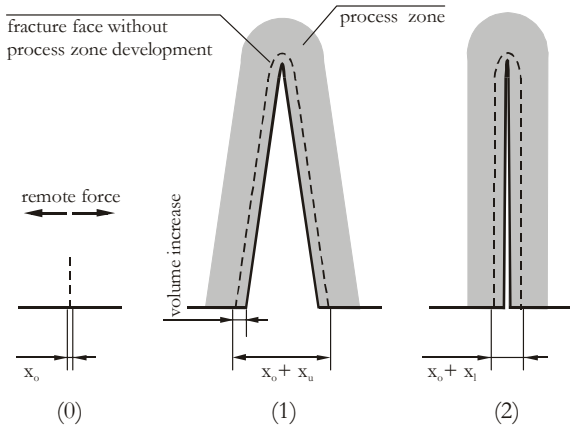

Fig. 4-16. p-factor and process zone evolution. p is defined in Fig. 4-4. Evolution of the process zone within one loading cycle (not to scale). (0) Initial state. The dashed line indicates the future fracture path. Clip gage opening displacement, COD = x_o. (1) The fracture has propagated some distance and a process zone is established. The dashed line indicates the hypothetical position of the fracture face, if no volume increase due to the formation of the process zone were evident. COD = $x_o + x_u$. (2) Fracture is closed after unloading. The original displacement could not be reached due to the volume increase. COD = $x_o + x_l$.

Total number of AE increased with increasing COD- rates (Figs. 4-12). Maximum amplitude increases with increasing COD- rates while the shape of the amplitude-frequency distribution remains similar for all loading rates (Backers et al., subm; Backers et al., 2003b). Amplitude of AE signals can be correlated with the relative length of initiated cracks. This indicates that the relative length distributions remain similar, although the increase in maximum amplitude promotes a shift towards longer cracks. The recorded smaller AE number at low loading rates is probably due to the fixed amplitude trigger level and the resulting low amplitude cut-off. But, the possibility that the total AE number is smaller at low loading rates because other mechanisms are more important, for example stress corrosion, cannot be excluded. The reported shift towards larger amplitude AE with increasing loading rate is consistent with the increase in force drop, ΔF, between load cycles.

Sample	COD-rate [m s^{-1}]	a_L [m s^{-1}]	a_{AE} [m s^{-1}]
FB4	$5 \cdot 10^{-6}$	$2 \cdot 10^{-4}$	$2 \cdot 10^{-4}$
FB1	$5 \cdot 10^{-7}$	$4 \cdot 10^{-5}$	$2 \cdot 10^{-5}$
FB2	$5 \cdot 10^{-8}$	$5 \cdot 10^{-6}$	$3 \cdot 10^{-6}$
FB5	$5 \cdot 10^{-9}$	$5 \cdot 10^{-7}$	$3 \cdot 10^{-7}$
FB6	$5 \cdot 10^{-10}$	$5 \cdot 10^{-8}$	$3 \cdot 10^{-8}$

Tab. 4-6. Estimated fracture growth rates. a_L: average fracture speed, estimated from the time necessary to propagate the fracture through the sample, and a_{AE}: fracture speed as derived from propagation speed of the AE front in x-direction (c.f. Fig. 4-11).

It was reported by Backers et al. (subm) and Stanchits et al. (2003) that AE analysis of Flechtingen sandstone and Mizunami granite indicates that tensile fracture propagation is associated with different source types, which likely represent different types of microcracks. They observed that shear and tensile cracks are evenly distributed in space and time during fracture propagation. This shows that growth of a macroscopic tensile fracture under pure Mode I loading conditions involves the formation of both shear and tensile microcracks and occurs in mixed-mode on the microscopic scale. In polycrystalline rocks intergranular and intragranular cracks are commonly deflected from a straight path. Cracks and grain boundaries that are sufficiently inclined with respect to the maximum compressive stress are likely activated in shear. However, typically the displacement across shear cracks is too small to be resolved even in SEM. Consequently, contribution of shear cracks to process zone damage may be underestimated in micromechanical models (Reches & Lockner, 1994).

5 MODE II LOADING – METHOD, RESULTS AND DISCUSSION

The intention of this part of the study was to develop an experimental method which provides Mode II fracture propagation. This should supply the development of a testing method for determination of Mode II fracture toughness and analysis of structural aspects to give insight to the mechanisms of Mode II loading induced fracture propagation.

It was stated by several researchers that under conditions of overall compression Mode II fracture propagation is most likely (e.g. Melin, 1986, Lawn, 1993). This was experimentally confirmed by Bobet & Einstein (1998) who demonstrated that macroscopic wing fractures (Mode I) can be omitted by applying confining pressure, i.e. normal stress. Consequently, confining pressure had to be applicable to the test geometry. Design of the geometry of the new testing method was governed by three guidelines: *(1)* Samples should be fabricated from ordinary drill core. Hence, the diameter, D, was dictated to be about 50 mm (corresponding closely to NX drill size). Moreover, with a cylindrical geometry it is convenient to apply a confining pressure either by a pressure vessel or a conventional Hoek-Cell. *(2)* Mode II fracture toughness should be determined on samples previously tested for Mode I fracture toughness. Using the two remaining parts from Chevron Bend K_{IC} determination has the advantage of obtaining fracture toughness for both Mode I and II on one and the same sample. *(3)* Geometry is based on experience from a testing method for Mode II fracture toughness proposed by Davies and Watkins (e.g. Davies, 1988; Davies, 1991; Davies, 1995; Watkins, 1983; Watkins & Liu, 1985). Refer to Section 2.5.2 for details on the geometry.

The most preferable geometry for shear (Mode II) fractures to develop in a set-up with two initial fractures is to organise them co-planar, with (Bobet & Einstein, 1998) or without confining pressure (e.g. Bobet & Einstein, op. cit.; Park et el., 2001; Shen et al., 1995). It was shown that at zero to low confining pressures (i.e. lateral stress) co-planar pre-fabricated fractures first initiate wing fractures at their tips and later coalesce by secondary cracks in shear rather than tension. Increase of confining pressure suppresses wing fracture initiation (c.f. Section 2.4.1).

Above considerations resulted in the basic design of the sample geometry.

5.1 Method – Punch-Through Shear (PTS-) test

The new method for Mode II fracture toughness determination proposed here is called the Punch-Through Shear (PTS-) test. The PTS-test uses cylindrical samples with circular notches drilled centred into the end surfaces where the notches serve as friction free initiation locus for fractures. The suggested sample geometry, its dimension and principle loading are given in Figure 5-1 and Table 5-1.

Devices

Special devices were developed for the PTS- test (Figure 5-2.A and Appendix C). They are designed to work with a conventional Hoek-Cell and in a high pressure vessel. All parts are made from cold working steel 1.2343 (X 38 CrMoV 5.1; HRC 42; RM 1320 N/mm²), or hot working steel 1.2363 (X 100 CrMoV 5.1; HRC 55; RM 1990 N/mm²) when exposed to high loads (i.e. stamp and devices for changing diameter).

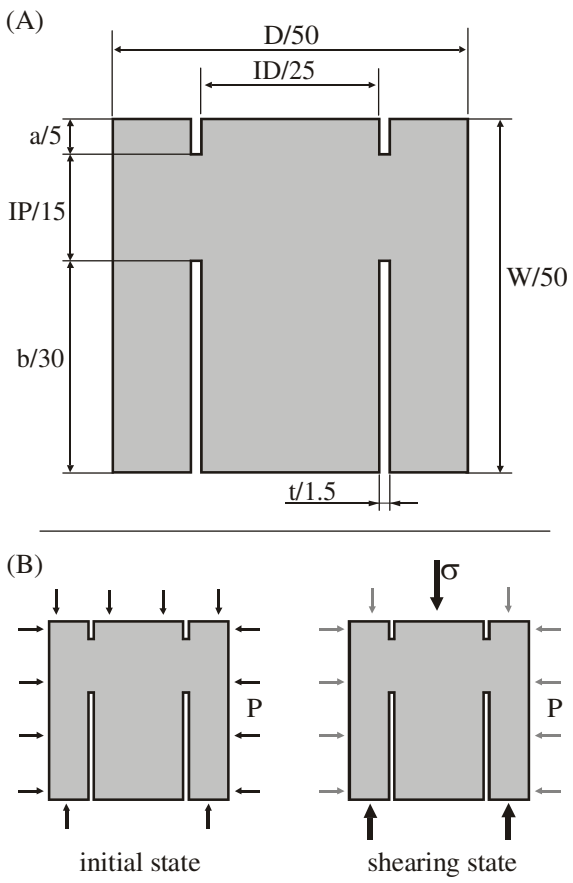

Fig. 5-1. Sample geometry, principle loading, and dimension for the PTS-Test. (A) Suggested sample geometry and dimension in [mm]. W: sample height, D: sample diameter, ID: inner notch diameter, a: upper notch depth, b: lower notch depth, IP: intact rock portion and t: notch width. (B) Loading. σ: axial stress, and P: confining pressure. Left hand side indicates initial stress state due to confining pressure (initial state in the pressure vessel, in the Hoek-Cell the upper outer 'ring' surface is traction-free) and right hand side indicates loading during application of shear stress (shearing state). The applied confining pressure acts perpendicular to the notch plane and the inner part is punched through the sample by an axial load.

Geometry	Identifier	Tested dimension [mm]	Suggested [mm]
Specimen height	W	25 & 50	50
Specimen diameter	D	50 & 113	50
Notch diameter	ID	22 - 64	25
Upper notch depth	a	2.8-31.1	5
Lower notch depth	b	0.0-41.4	30
Notch tip width	t	0.8, 1.5, 3.0	1.5
Intact portion	IP	2.2-35	15

Tab. 5-1. Suggested and tested dimension of the Punch-Through Shear (PTS-) samples for determination of K_{IIC}.

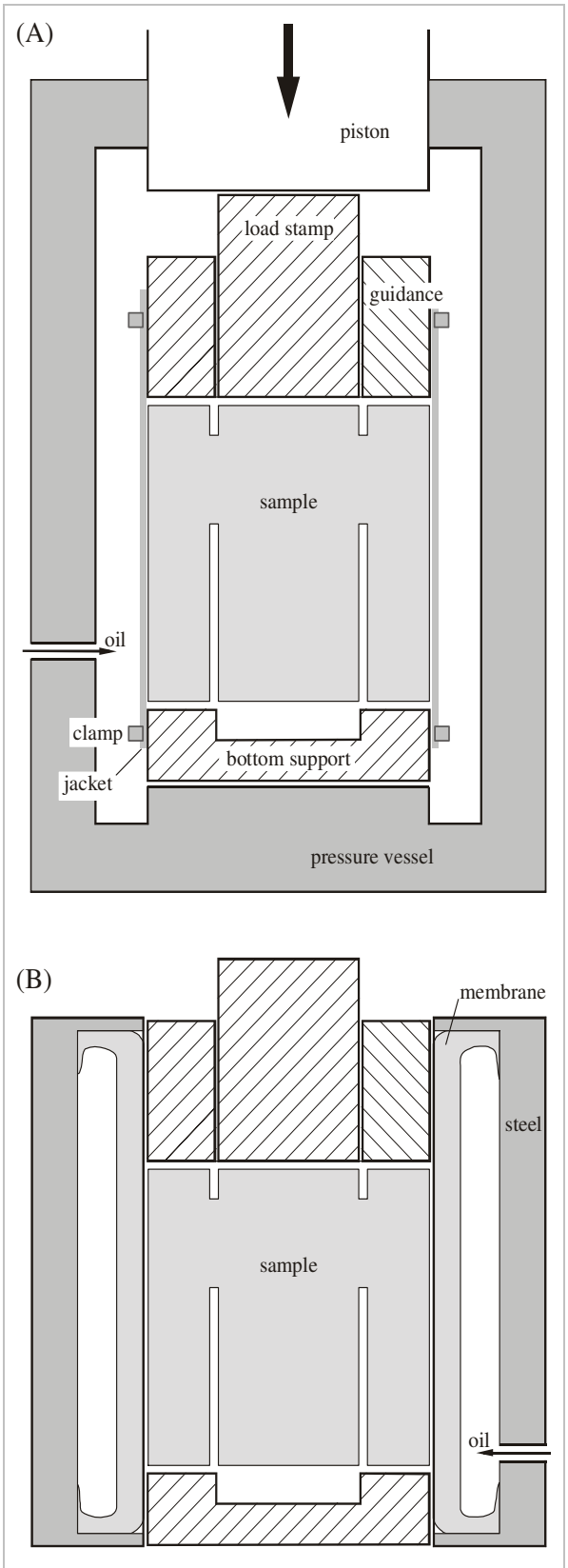

Fig. 5-2. Punch Through Shear test set-up. The sample and assembly are placed (A) in the pressure vessel or (B) in a Hoek-Cell (schematic, crosscut view).

The bottom support is a solid cylinder with a centred 5 mm deep circular gap at its top surface. This device supports the outer bottom 'ring' of the sample during testing, while the central bottom part is unconstrained. Rings to change the diameter of the gap are available for testing with different notch diameters, ID (∅: 22, 25, 30 mm).

The hardened stamp is guided by a hollow-cylinder. A combination of Teflon ring and high pressure sealing supports the stamp and prevents migration of oil into the sample during testing. Bits for changing the stamp tip diameter are available (∅: 22, 25, 30 mm).

For a test series with larger sample diameter, D, special devices were manufactured (Appendix C), designed for use with a Hoek-Cell only. These are designed for D = 113 mm and inner diameters, ID, of 25, 50 and 64 mm. The tests were run at Ruhr-University Bochum, Department of Engineering Geology. The Hoek-Cell is designed for a maximum sample diameter of 116 mm.

Sample preparation and testing set-up

From the remaining core bits from Mode I fracture toughness determination (diameter D = 50 mm) and from drill core samples specimens are prepared. For the range of tested dimensions, refer to Table 5-1. Samples of length W are cut. The end surfaces are ground with a lathe to provide flat end surfaces perpendicular to the core mantle. Surface roughness is approximately 100 μm. The sample is fixed and centred using a large diameter chuck for manufacturing the notches of inner diameter ID. The circular notches of width t = 1.5 mm are drilled using standard drill bits. Other notch widths are inserted by a CNC (Computerised Numerical Control) milling machine (0.8 mm) or by combination of drill bits of different diameter (3.0 mm). The depths of the notches are indicated as a (top) and b (bottom).

The ready prepared sample is placed between bottom support and loading stamp assembly. For confining pressures of P < 20 MPa the assembly with sample is placed into a conventional Hoek-Cell (Hoek & Franklin, 1968) (Fig. 5-2.B). For higher confining pressures the set-up is covered by a rubber sleeve to prevent intrusion of confining pressure medium into the sample. Alternatively, an oil resistant shrinking tube might be used. The ends of the sleeve/tube are clamped. The assembly is placed into the pressure vessel (Fig. 5-2.A).

Testing procedure

Prior to the actual testing procedure, a small pre-load (typically ~2 kN) is added to the stamp to provide good adjustment and secure fixture of the assembly. Subsequently, the confining pressure is applied. The inner cylinder of the sample is then punched down at a constant displacement rate of 0.2 mm/min ($3.3 \cdot 10^{-5}$ m/s), unless otherwise stated. The applied axial stress, σ, generates an increasing shear stress in the intact rock portion between the notches until failure. Axial force, confining pressure and axial displacement are recorded during an experiment. Figure 5-3 shows typical recordings.

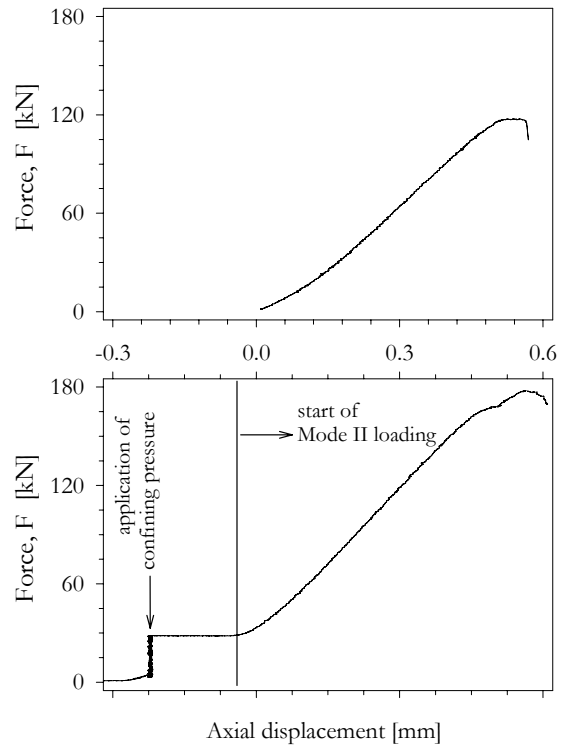

Fig. 5-3. Typical recordings of force vs. displacement for Mode II loading using the PTS-test. The data shown is from Mizunami granite. Top graph shows deformation of a sample at P = 15 MPa in the Hoek-Cell [T1-1c]. Bottom graph shows deformation of a sample at 50 MPa in pressure vessel [T3-1a]. (This data is not corrected for confining pressure. The increase in axial load without increase in displacement is caused by the confining pressure medium acting on the stamp of the pressure vessel. The stamp is larger in diameter than that of the PTS assembly (c.f. Fig. 5-2.A). Hence the measured load has to be reduced by the force increase caused by the oil.) The deflection prior to the peak is caused by flaking off of rock from the inner cylinder.

Evaluation (Displacement Extrapolation Technique)

Several methods for determination of the Mode II fracture toughness, K_{IIC} were developed or employed; these are abstracted in the *BOX: EVALUATION* (pp. 57-60) and briefly discussed therein.

At this stage in the development of the PTS- test it is suggested to estimate K_{IIC} as outlined in the following. The technique is based on a displacement extrapolation technique (DET) for finite element modelling (FEM) as frequently used in literature, e.g. Lim et al. (1993) or Rao (1999).

The formulations are based on Irwin's crack tip displacement equations (c.f. Whittaker et al., 1992). In Cartesian coordinates the displacements are given as

$$u = \frac{K_I}{4G}\sqrt{\frac{r}{2\pi}}\cdot\left[(2k-1)\cos\frac{\theta}{2}-\cos\frac{3\theta}{2}\right]+ \frac{K_{II}}{4G}\sqrt{\frac{r}{2\pi}}\cdot\left[(2k+3)\sin\frac{\theta}{2}+\sin\frac{3\theta}{2}\right] \quad (5\text{-}1a)$$

$$v = \frac{K_I}{4G}\sqrt{\frac{r}{2\pi}}\cdot\left[(2k+1)\sin\frac{\theta}{2}-\sin\frac{3\theta}{2}\right]+ \frac{K_{II}}{4G}\sqrt{\frac{r}{2\pi}}\cdot\left[-(2k-3)\cos\frac{\theta}{2}-\cos\frac{3\theta}{2}\right], \quad (5\text{-}1b)$$

where u is the displacement in shear direction, v is the displacement perpendicular to u, G is the shear modulus, $k = 3\text{-}4\nu$, and θ is the angle from the shear direction (c.f. Fig. 5-4).

In case of $\theta = \pm 180°$, i.e. on the notch faces, equations (5-1a) and (5-1b) become

$$u = \frac{K_{II}}{4G}\sqrt{\frac{r}{2\pi}}\cdot\left[(2k+3)\sin\frac{\theta}{2}+\sin\frac{3\theta}{2}\right] \text{ and } \quad (5\text{-}2a)$$

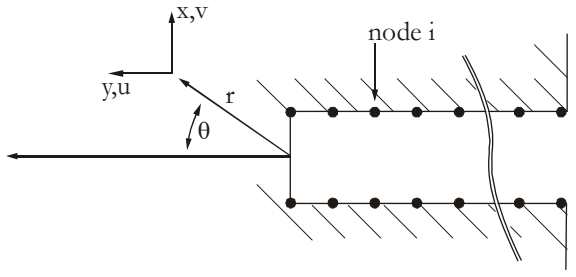

Fig. 5-4. Notations at the notch for derivations of the displacement extrapolation technique (DET).

$$v = \frac{K_I}{4G}\sqrt{\frac{r}{2\pi}}\cdot\left[(2k+1)\sin\frac{\theta}{2}-\sin\frac{3\theta}{2}\right]. \quad (5\text{-}2b)$$

Thus K_I and K_{II} can be determined separately by the x- and y- direction displacements. In case of K_{II}, u is measured at the nodal points of the notch faces, i.e. $\theta = \pm 180°$, thus

$$u_i^+ = \frac{K_{II}^i}{2G}\sqrt{\frac{r_i}{2\pi}}\cdot[k+1], \text{ at } \theta = +180° \quad (5\text{-}3a)$$

$$u_i^- = -\frac{K_{II}^i}{2G}\sqrt{\frac{r_i}{2\pi}}\cdot[k+1], \text{ at } \theta = -180°. \quad (5\text{-}3b)$$

The relative y-direction displacement of the corresponding nodes is

$$\Delta u_i = u_i^+ - u_i^- = \frac{K_{II}^i}{G}\sqrt{\frac{r_i}{2\pi}}\cdot[k+1] \quad (5\text{-}4)$$

and consequently K^i_{II} is defined by

$$K_{II}^i = \frac{G}{k+1}\sqrt{\frac{2\pi}{r_i}}\cdot\Delta u_i . \quad (5\text{-}5)$$

The K^i_{II} at given boundary stresses for different r_i are determined and plotted as function of the distance from the notch tip. To the linear part of that function a linear regression extrapolates K^i_{II} to the notch tip, i.e. $r = 0$ and K^{i*}_{II}.

For the suggested geometry (c.f. Table 5-1) and rock types used the corresponding relations are determined on the bottom notch. In the following the derivation is demonstrated for the case of Mizunami granite. Influence of axial loading, σ_A, and confining pressure, P, is evaluated.

For determination of the displacements, the FEM package Phase² was used (Rocscience, 1999). The set-up is schematically shown in Figure B-2, p.58. In contrast to Figure B-2 the full model used here has 550 external nodes that yield 3558 internal nodes on 3294 elements. The uniform quadrilateral mesh has eight midside nodes. The matrix is solved by Gaussian elimination.

Figure 5-5.A depicts the data as obtained for different σ_A at constant confining pressure. K^{i*}_{II} increases linearly with increase in σ_A (Fig. 5-5.B). Confining pressure changes the slope of K^i_{II} vs. r_i (Fig. 5-6.A). The slope increases with

increasing P. Extrapolation to the notch tip, i.e. r = 0, gives decreasing K^{i*}_{II} with increase of P (Fig. 5-6.B).

The formulation for determination of the fracture toughness is given in the form

$$K_{IIC} = \omega \cdot \sigma_{Amax} + \beta \cdot P\,, \qquad (5\text{-}6)$$

where σ_{Amax} is the axial load at failure, P is the applied confining pressure and ω and β are parameters obtained from the regressions.

The parameters ω and β for the different rock types are given in Table 5-2. The FEM calculations carried out in the context of this thesis are not accurate due to several reasons, e.g. the code is not capable to create homogeneous meshes, and therefore it is legitimate to give a single formulation for all rock types based on the averages to Table 5-2. Hence,

$$K_{IIC} = 0.0378 \cdot \sigma_{Amax} - 1.795 \cdot 10^{-3} \cdot P\,; \qquad (5\text{-}7)$$

σ_{Amax} and P are in [MPa] to yield K_{IIC} in [MPa $m^{1/2}$]. Despite the generalised formulation (5-7) the individual values in Appendix B are calculated using the parameters from Table 5-2. The formulations are valid strictly speaking for the suggested geometry only, but are used at this stage also for a broader range of IP (i.e. 12 < IP < 18 mm), taking into account some inaccuracy.

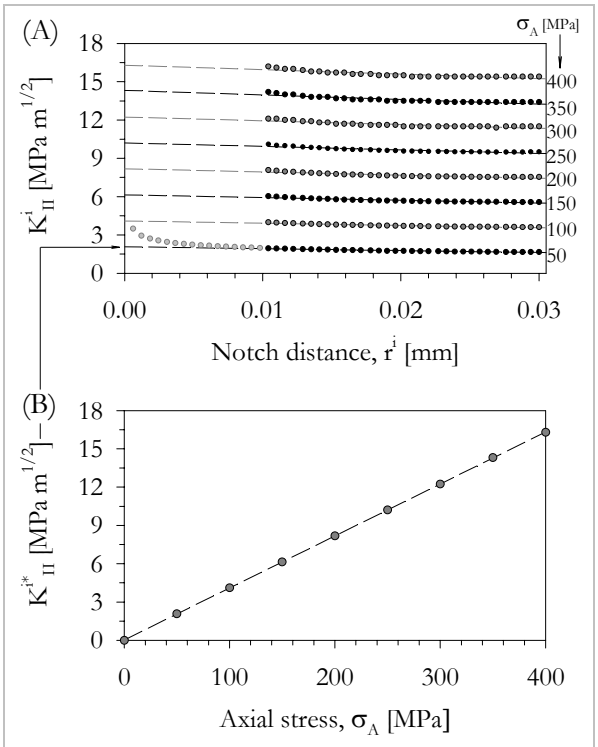

Fig. 5-5. Displacement Extrapolation Technique. (A) K^i_{II} as determined from the displacements calculated by FEM as function of the distance from the notch tip, r_i. Extrapolation to r = 0 for determination of axis intercept K^{i*}_{II} is indicated by dashed lines for increasing axial loads, σ_A, at constant confining pressure, P, of 5 MPa. (B) K^{i*}_{II} as determined from (A) as function of σ_A. The obtained stress intensity factor increases linearly with increase in axial load. Elastic properties of Mizunami granite.

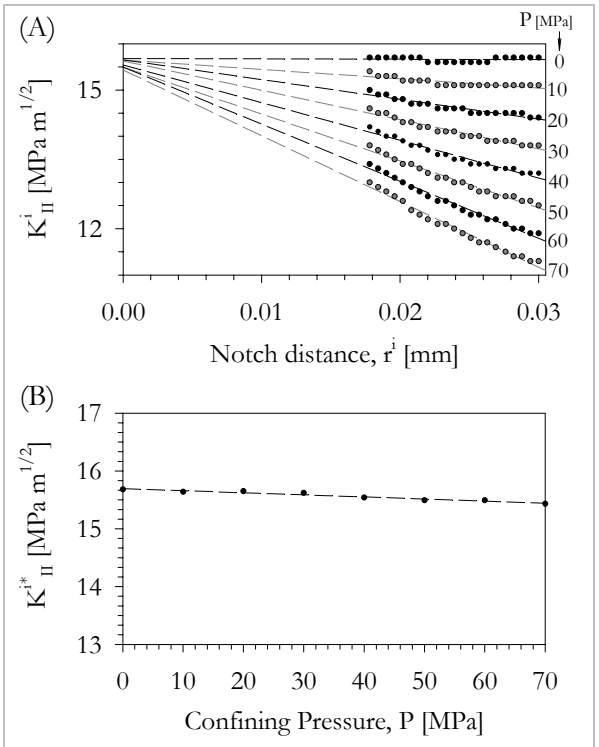

Fig. 5-6. Displacement Extrapolation Technique. (A) K^i_{II} as determined from the displacements calculated by FEM as function of the distance from the notch tip, r_i. Extrapolation to r = 0 for determination of axis intercept K^{i*}_{II} is indicated by dashed lines for increasing confining pressure, P, at constant axial load, σ_A, of 400 MPa. (B) Influence of confining pressure on K^{i*}_{II} at σ_A = 400 MPa. Elastic properties of Mizunami granite; corresponding plots for other rock types are given in Appendix E.

Rock type	ω	β [10^{-3}]
Äspö diorite	0.03755	-1.952
Aue granite	0.03748	-1.321
Mizunami granite	0.03924	-3.640
Carrara marble	0.03762	-1.857
Flechtinger sandstone	0.03753	-0.405
Rüdersdorf limestone	0.03745	-1.595
Average	0.0378 ± 0.0005	-1.795 ± 0.688

Tab. 5-2. Parameters ω and β from DET analysis for the different rock types.

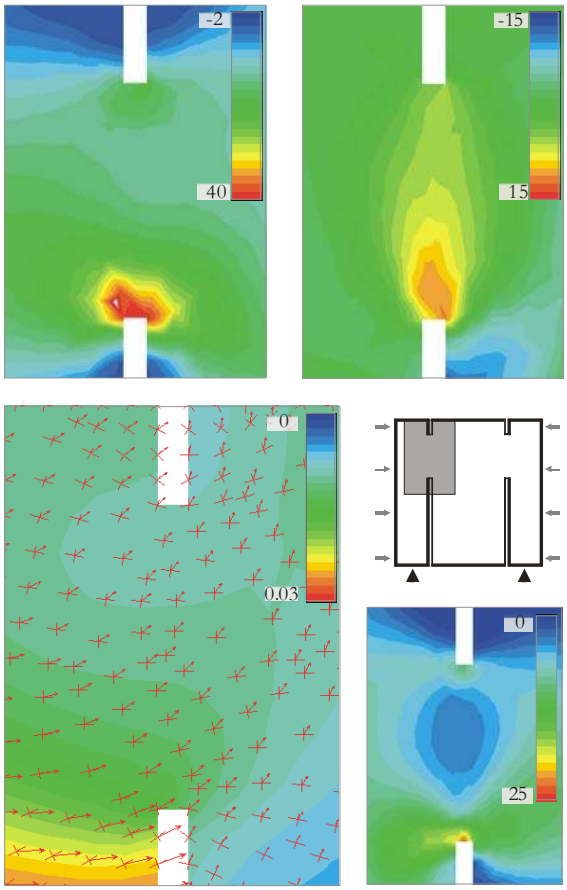

Fig. 5-7. Stresses and displacements within PTS sample in the area between upper and lower notch at σ = 0 MPa and P = 10 MPa. [E=25000, ν=0.25, plane strain, eight noded quadrilaterals]. Top left: σ_1 (colour code refers to stress in MPa); top right: σ_3 (colour code refers to stress in MPa); bottom left: stress trajectories, displacement vectors, and displacements (colour code refers to displacement in mm); bottom right: maximum shear stress, τ_{max} (colour code refers to stress in MPa). White area of inlay indicates area depicted.

FEM analysis of suggested geometry

The stress and displacement situation at initial loading and at the shearing state of the suggested geometry is analysed, yielding results shown in Figures 5-7 and 5-8.

When loaded with a confining pressure on the mantle surface only (Fig. 5-7), stress concentrations are evident at the notches. At the bottom notch tip the highest compressive stresses, both minor and major principle stress, are concentrated. At the top notch the stresses are slightly increased.

Consider a sample loaded with a confining pressure and axial load of ratio σ/P = 10. Stress concentrations are evident at the notch tips (Fig. 5-8). At the outer bottom notch the highest compressive stresses are concentrated. At the inner tip of the bottom notches both the least and major principal stresses are negative (tensile). At the inner top notch both σ_1 and σ_3 are positive (compressive).

From this stress distribution results that the highest shear stresses are concentrated at the outer bottom notch tip.

5.2 *Results from experimental testing and analysis*

This chapter portrays experimental results on the influence of geometrical parameters, loading rate, confining pressure and cyclic loading in PTS- testing. The evolution of microstructure is studied and results are presented. A total of 219 experiments are evaluated. The sample dimension and results of the individual experiments are given in Appendix B.2.

5.2.1 *Results from geometry variation*

Influence of notch depths

To study the influence of the intact rock portion, IP, on failure stresses in the PTS- test, the upper notch depth, a, is fixed to 5 mm and the lower notch depth, b, is varied. Figure 5-9 shows the determined loading (σ_{max}-P) and average shear stress between the notches, τ_{av}, vs. IP at constant confining pressure (P = 5 MPa) for Aue granite, Rüdersdorf limestone and Carrara marble. Maximum loading (σ_{max}-P) increases with increasing IP (Fig. 5-9.A), a power law regression may be discussed. τ_{av} is steady for the tested range

of IP/W for marble (IP/W ≈ 0.08 – 0.45; IP ≈ 4 - 23 mm) and limestone (IP/W ≈ 0.05 – 0.5; IP ≈ 2 - 25 mm) (Fig. 5-9.B+C), and remains constant for IP/W ≈ 0.2 – 0.4 (IP ≈ 9 - 20 mm) for Aue granite. For the granite, at smaller IP the shear stress necessary for failure increases (IP/W > 0.2; IP > 9 mm) (Fig. 5-9.D). Hence, the suggested value for standard testing of IP = 15 mm (a = 5 mm; b = 30 mm) is in the constant shear stress region for the three rock types.

The proposed depth of the notches is non-symmetrical as the upper notch depth is fixed to 5 mm. This is to avoid compressive failure of the upper part of the inner cylinder during axial loading. Tests on samples of W = 25 mm with a = b = 5 mm, that is, with a similar length of IP as for the suggested geometry, are performed. τ_{av} is the same within sample-to-sample scatter for both geometries (Fig. 5-10.A). To investigate the influence of notch length, tests were performed with a = 20/30 mm and b = 5 mm, i.e. with the (suggested) specimen turned upside down, and compared to testing of samples with suggested set-up.

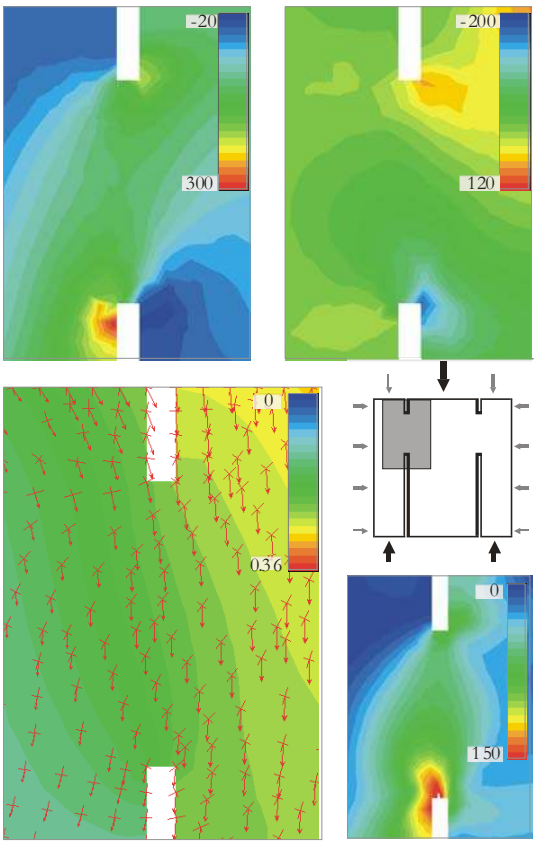

Fig. 5-8. Stresses and displacements within PTS sample in the area between upper and lower notch at σ = 100 MPa and P = 10 MPa. [E=25000, ν=0.25, plane strain, eight noded quadrilaterals]. Top left: σ_1 (colour code refers to stress in MPa); top right: σ_3 (colour code refers to stress in MPa); bottom left: stress trajectories, displacement vectors, and displacements (colour code refers to displacement in mm); bottom right: maximum shear stress, τ_{max} (colour code refers to stress in MPa). White area of inlay indicates area depicted.

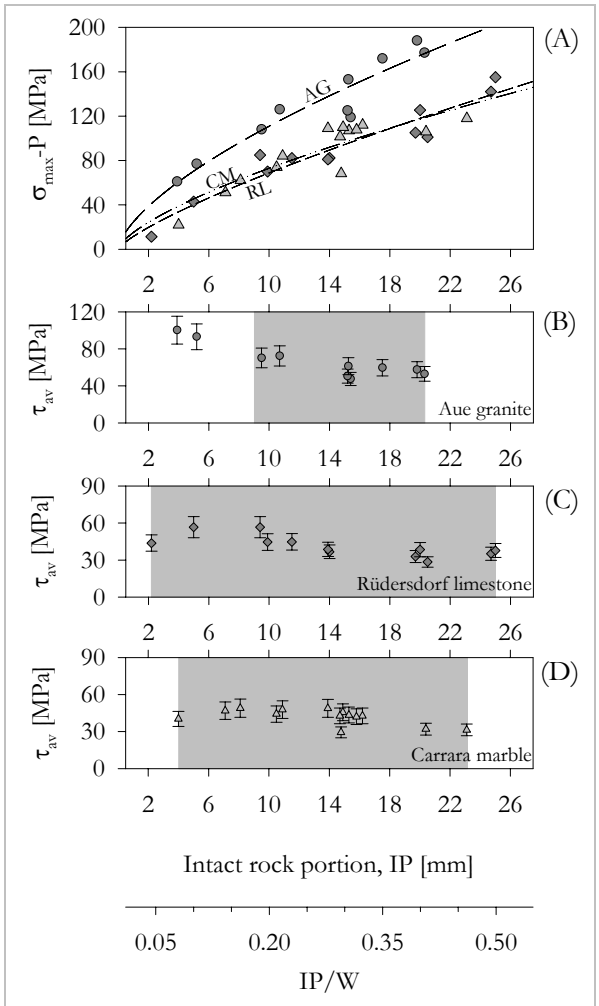

Fig. 5-9. Influence of the intact portion, IP, on the acting stresses. (A) With increasing IP the (σ_{max}-P) necessary for failure increases. The data may be fit by a power law. However, in the range of IP = 6-22 mm the data may be approximated by a linear regression. (B-D) τ_{av} vs. IP. The average shear stress on the cylindrical plane between the notches [$\tau_{av} = [\sigma_{max} \cdot 0.25 \cdot (ID)^2]/[(ID+t) \cdot IP]$] remains almost constant for Rüdersdorf limestone and Carrara marble, but increases for small IP for Aue granite. It is constant between IPs of approximately 9 and 20 mm for the three rock types. RL: Rüdersdorf limestone, CM: Carrara marble and AG: Aue granite. [W=50mm, D=50mm, a≈5mm, P=5MPa].

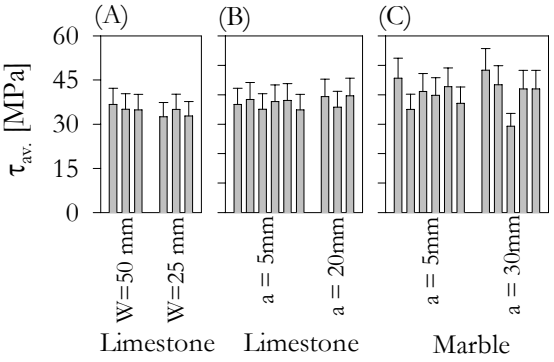

Fig. 5-10. (A) Influence of symmetrical and unsymmetrical sample geometry. τ_{av} is similar for symmetrical [W = 25 mm] and unsymmetrical [W = 50 mm] limestone samples. [IP ≈ 15mm, D = 50mm, P = 5 MPa].
(B+C) Influence of the upper notch length, a, on τ_{av} of Carrara marble and Rüdersdorf limestone. Results for upper notch depth a = 5 mm and a = 20/30 mm with similar IP are given. There is no evidence for a significant influence of the notch depth on τ_{av}. [W=50mm, D=50mm, P=5MPa].

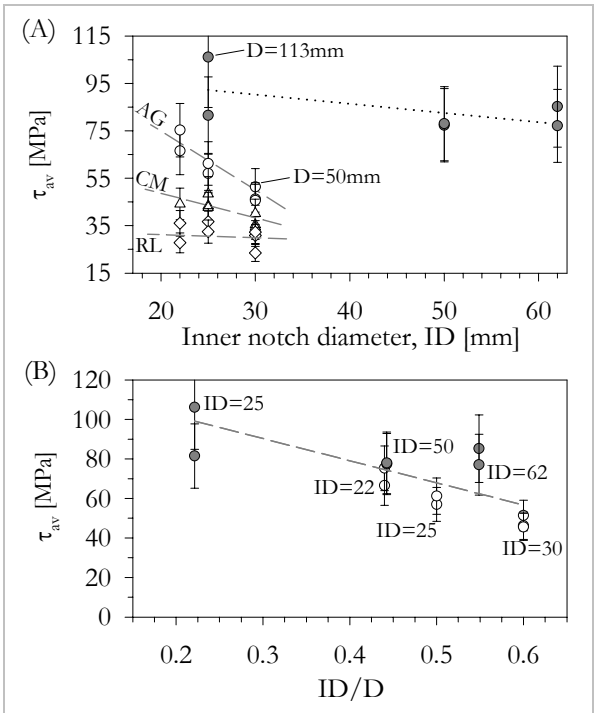

Fig. 5-11. Influence of ID and D on τ_{av} for Aue granite (AG, circles), Rüdersdorf limestone (RL, diamonds) and Carrara marble (CM, triangles). (A) Influence of inner notch diameter, ID. (B) τ_{av} increases with decreasing ratio of ID/D, which is a measure for the wall thickness between sample boundary and notch. Open symbols: D = 50 mm, grey circles: D = 113mm. [W≈50mm, D=50/113mm, a=5mm, IP≈15mm, P=5MPa].

Figures 5-10.B+C give no evidences for a noteworthy influence of the notch depth on τ_{av}. During this series of testing frequently compressive failure of the top of the inner cylinder was observed for specimen with a = 20/30 mm.

Influence of notch curvature and sample diameter

The average shear stress between the notches, τ_{av}, for Carrara marble and in particular Aue granite changes with variation of inner diameter, ID, while Rüdersdorf limestone shows no variation of τ_{av} with ID. Figure 5-11.A illustrates the results of experiments with D = 50 mm and IDs of 22, 25 and 30 mm at P = 5 MPa. For Carrara marble and Aue granite, τ_{av} decreases with increasing inner diameter. As the effect is greatest for the granite, additional experiments with samples of diameter D = 113 mm were carried out for IDs of 25, 50 and 62 mm, respectively. Still, τ_{av} decreases with increasing ID, but at a smaller rate. The average shear stress values for D = 113 mm are higher than for the small diameter, i.e. D = 50 mm.

Increasing the ratio of ID/D, which is a measure of the thickness of the outer cylinder of the specimen, from 0.2 to 0.6 results in a decrease of τ_{av} from 102 to 57 MPa (Fig. 5-11.B).

Influence of notch width

Experiments with notch widths, t, of 0.8, 1.5 and 3.0 mm are carried out on Carrara marble. The 0.8 mm notch is manufactured using a CNC (Computerised Numerical Control) milling machine, the 1.5 mm notch is prepared using a standard drill bit, the 3.0 mm notch is introduced by two drill bits with overlapping diameters. Results from this series of experiments are given in Figures 5-12 and 5-13.

The force vs. displacement plots for the different t show almost same stiffness (Fig. 5-12). Minor differences apply, presumably due to differences in IP (c.f. Appendix B and Fig. B-4). The samples with t = 0.8 mm show a wider peak plateau compared to the other geometries; it was observed that at the bottom surface of the samples crushing was taking place at the outer edge of the notch. The differences in peak load yield τ_{av} that show no clear trend for the tested t,

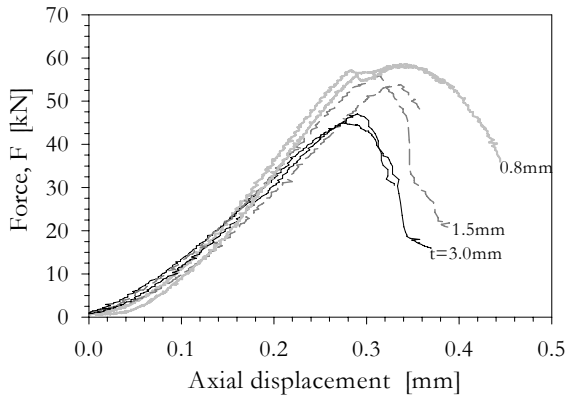

Fig. 5-12. Force vs. displacement data for different notch width in Carrara marble. (MT-6 and MT-7 [grey solid lines]; ZM-10 and ZM-11 [grey dashed lines], ZM-12 and ZM-13 [black solid lines]). [W=25/50mm, D=50mm, a≈5mm, ID≈25mm, IP≈15 mm, t≈0.8-3.0mm].

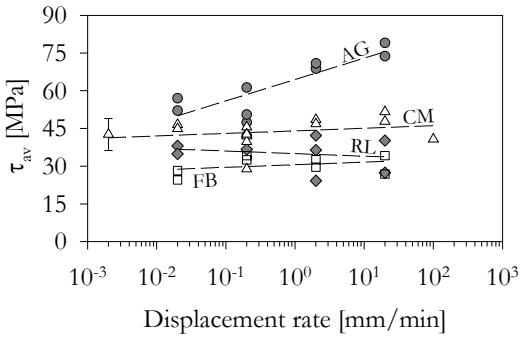

Fig. 5-14. Influence of displacement rate on τ_{av}. AG: Aue granite, grey cycles; RL: Rüdersdorf limestone, grey diamonds; CM: Carrara marble, open triangles; FB: Flechtingen sandstone, open squares. An exemplary error bar for the individual shear stress measurement is given for marble. Other errors are in the same range.

but remains almost constant (Fig. 5-13). The displacements achieved at failure are slightly increasing with decrease of notch width and so are the loads.

5.2.2 Influence of displacement rate

The displacement rate is varied between $3.3 \cdot 10^{-7}$ and $3.3 \cdot 10^{-4}$ m/s for Aue granite, Rüdersdorf limestone and Flechtingen sandstone and for Carrara marble between $3.3 \cdot 10^{-8}$ and $1.7 \cdot 10^{-3}$ m/s at a constant confining pressure (P = 5 MPa) (Fig. 5-14). τ_{av} remains almost constant irrespective of loading rate for marble, limestone and sandstone. For the granite, τ_{av} increases non-linearly with increasing loading rate. At peak load instantaneous, i.e. unstable, fracture propagation took place for all applied loading rates; however, Carrara marble shows some stable softening.

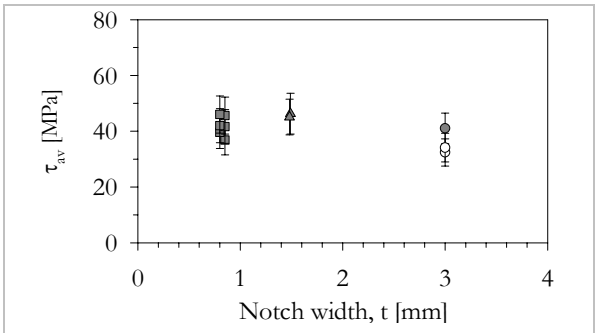

Fig. 5-13. Influence of the notch width, t, on τ_{av} for Carrara marble. The shear stress at failure – calculated for the outer notch diameter – remains similar for the tested t. [White circles: W=50mm, D=50mm, a≈5mm, ID≈25mm, IP≈15 mm, t≈3mm; Grey circles: W=50mm, D=50mm, a≈5mm, ID≈22mm, IP≈15 mm, t≈3mm; grey triangles: W=50mm, D=50mm, a≈5mm, ID≈25mm, IP≈15 mm, t≈1.5mm; grey squares: W=25mm, D=50mm, a≈5mm, ID≈25mm, IP≈15 mm, t≈0.8mm].

5.2.3 Influence of confining pressure

The PTS- test is currently performed at confining pressures, P, up to 70 MPa.

Analysing the stress data with respect to confining pressure, it becomes clear that two regimes can be recognised (Fig. 5-15). At low confining pressures the maximum axial stress, σ_{max}, and average shear stress between the notches, τ_{av}, steeply increase with P, while at high P the σ_{max} and τ_{av} necessary for fracture propagation increase moderately with increase in confining pressure. Transition from steep to shallow slope is at about 25-35 MPa.

K_{IIC} shows a behaviour analogue to τ_{av} with increasing P (Fig. 5-16). Regression parameters and average magnitudes of K_{IIC} are presented in Table 5-3.

Rock type	K^0_{IIC} [MPam$^{1/2}$]	a	K^I_{IIC} [MPam$^{1/2}$]	b	K^∞_{IIC} [MPam$^{1/2}$]
Äspö diorite	5.09	0.23	10.59	0.04	12.4
Aue granite	4.11	0.28	10.03	0.07	13.2
Mizunami granite	4.90	0.29	13.25	0.02	14.2
Carrara marble	3.06	0.15	6.32	0.04	7.9
Flechtinger sst	1.86	0.12	5.09	<0.01	5.4
Rüdersdorf lim	2.30	0.14	5.55	0.02	6.7

Tab. 5-3. Mode II fracture toughness data. K^0_{IIC}: fracture toughness at zero confining pressure; a: slope of linear regression to K_{IIC} at low P; K^I_{IIC}: fracture toughness as extrapolated to ordinate from linear regression to K_{IIC} at high confining pressure, i.e. axis intercept of linear regression; b: slope of linear regression to K_{IIC} at high P; K^∞_{IIC}: average fracture toughness for a confining pressure range of $30 < P < 70$ MPa.

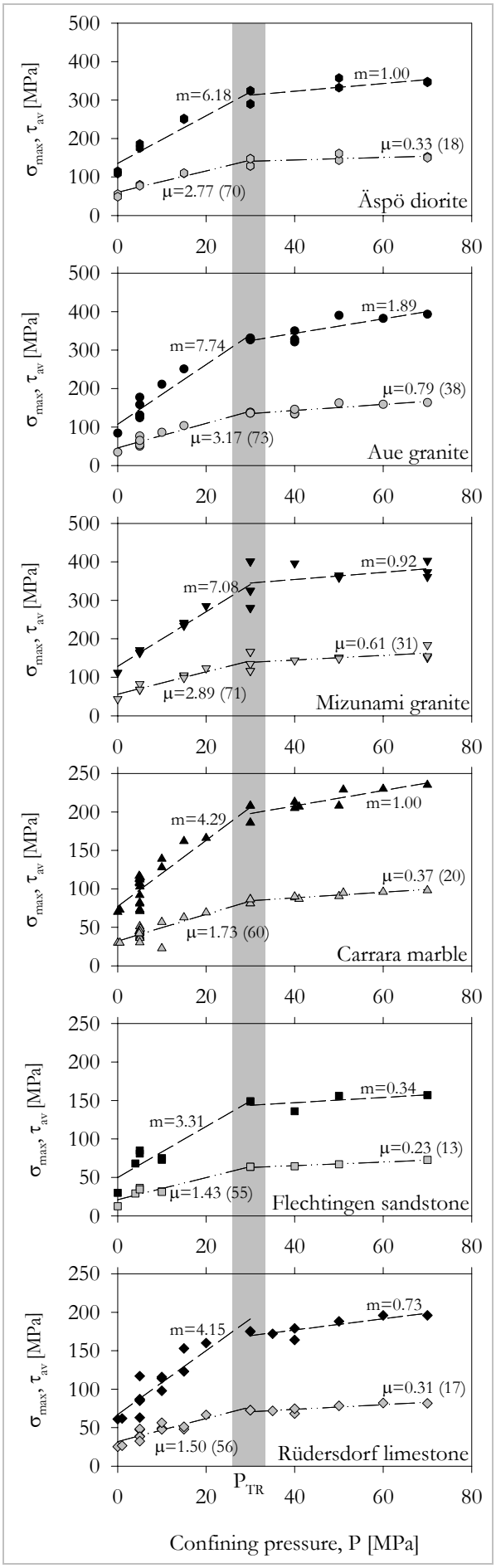

←

Fig. 5-15. Influence of confining pressure, P, on σ_{max} and τ_{av} for the six different rock types. The rock types are organised from top to bottom by decreasing grain size. Two regimes of different slopes are separated. m and μ indicate slopes of regression; in brackets Φ = arctan μ is given. Black symbols: σ_{max}, grey symbols: τ_{av}. Grey vertical mark indicates transitional regime. [W=50mm, D=50mm, a=5mm, IP=15 mm].

5.2.4 Cyclic loading

Repeated (cyclic) loading was performed on Aue granite, Mizunami granite and Carrara marble samples with the intention of studying controlled fracture propagation in the post peak region. If no cyclic loading is performed, as is in the suggested testing procedure, the sample is loaded until peak load and then fails by almost instant loss of its load carrying ability (unstable). Instead the load is repeatedly released in the pre-peak region, at peak, and in the post-peak region. However, mostly the fracture propagated unstable.

The data presented in this section is the outcome of a series of altogether 19 experiments of which most samples suffered catastrophic failure (14 samples; mostly not included in Appendix B.2) instead of controlled fracture propagation (five samples). Peak loads obtained from cyclic and monotonic procedures are comparable.

Figure 5-17 shows the stress vs. displacement data from a test on Carrara marble at P = 40 MPa, i.e. in the region of constant fracture toughness. The top right plot shows the complete axial stress vs. displacement plot. Individual unloading/reloading loops are depicted in the eleven smaller plots. For each un-/reloading loop the slope was determined by linear regression.

→

Fig. 5-16. Influence of confining pressure, P, on K_{IIC}. for the six different rock types. [W=50mm, D=50mm, a=5mm, IP=15 mm]. Inlay graphs show scatter at P = 5MPa; open diamonds in limestone plots show samples of height W = 25 mm.

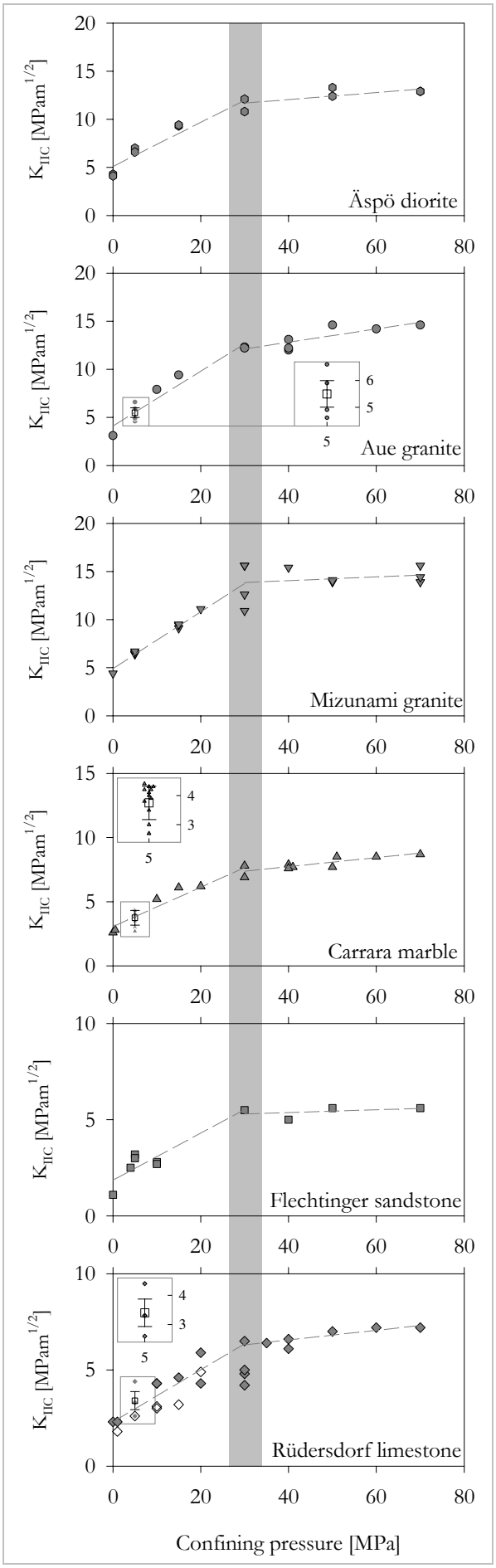

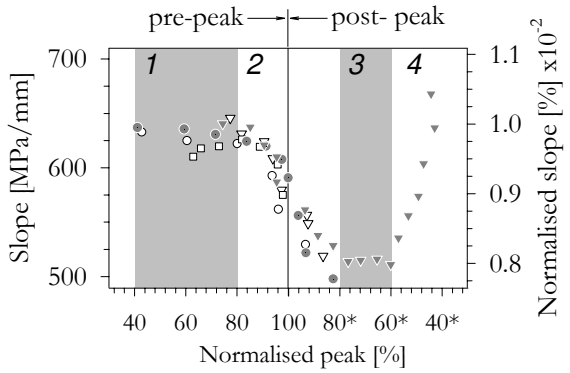

Fig. 5-18. Cyclic loading. Slope of unloading/reloading loops of Carrara marble (M12-1 [open triangles]; M12-2 [filled triangles]), Aue granite (G12-1 [open cycles]; G12-2 [filled cycles]) and Mizunami granite samples (T3-1d [open squares]) at P = 40 MPa.

Figure 5-18 shows the slopes of the regressions to the individual loops of experiments on Mizunami granite, Aue granite and Carrara marble. The slopes remain constant below 80% of peak load (regime *1* in Fig. 5-18). At about 85% the slopes start to decrease (regime *2*). In the post peak regime the slopes remain constant between ~80*% and 60*% of the maximum load (regime *3*). With further cycling the slopes start to increase again (regime *4*). The slope vs. normalised peak data is about the same for the three rock types; the three rock types have a similar Young's modulus of roughly 50 GPa.

5.2.5 Fracture evolution

Fracture evolution with progressive displacement at predominately low confining pressure of P = 5 MPa was examined. Samples were loaded to increasing fractions of maximum load and then terminated. The deformed samples were soaked and coated with coloured epoxy-resin and cut parallel to the displacement direction, i.e. parallel to the fracture plane. Thin-sections of the failure planes have been made to illustrate and analyse the fracture characteristics.

For Aue granite, Carrara marble and Rüdersdorf limestone the evolution appears in principle the same, although showing minor differences; the principle fracture content is also the same for Mizunami granite, Äspö diorite and Flechtingen sandstone. No differences in macroscopic fracture pattern appear for tests run in the Hoek-Cell or pressure vessel. The observations are summarised in Figure 5-19.

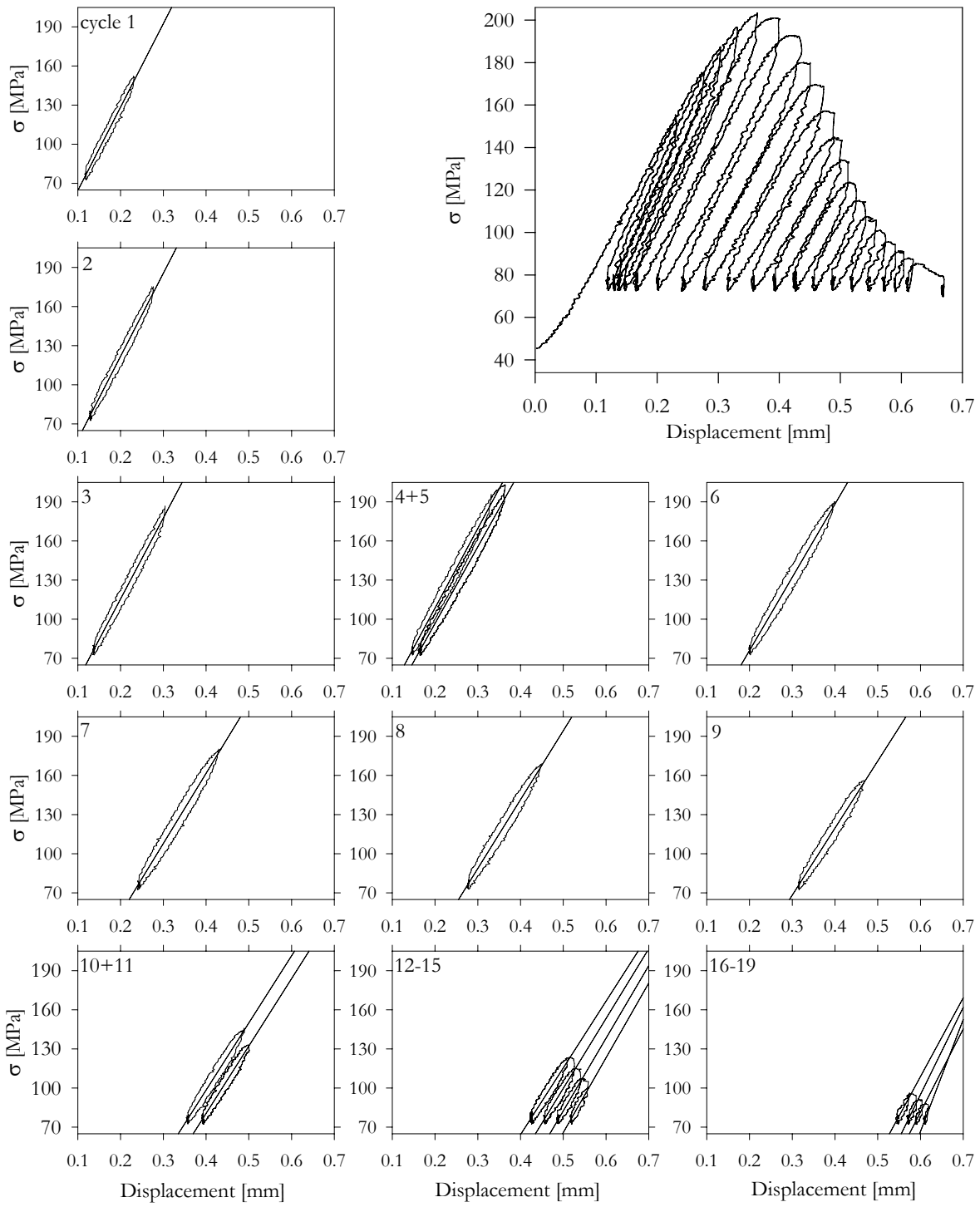

Fig. 5-17. Cyclic loading of Carrara marble sample (M12-2) at P = 40 MPa. Refer to text for details.

In Rüdersdorf limestone the first fracture that appears is a wing shaped crack initiated at the inner tip of the bottom notch at about 30 % of the maximum load. The crack is inclined 60-80° to the notch plane at the notch tip. During propagation it turns towards the centre of the sample until it is oriented almost vertically and then stops. Frequently, it stops even before being aligned parallel to the displacement direction. The length of the wing crack decreases with increasing confining pressure; at confining pressures > 30 MPa it frequently is suppressed. At about 60 % of the peak load small wing cracks initiate at the top notch and sometimes propagate outwards. These are referred to as 'doughnut fractures'. They are frequently suppressed at confining

pressures > 30 MPa. At about 95 % of the peak load macroscopic en échelon fractures are initiated between the notches. They are inclined 30-50 ° to the notch plane. At peak load, or immediately after, the en échelon fractures are connected by an almost straight fracture between the outer lower notch tip and the inner upper notch tip. Shear failure happens by connection of the notches, mostly from bottom to top notch. The main fracture is slightly inclined to the straight plane between the notches. In crosscut view the fracture frequently does not show a circular but polygonal shape in limestone.

In contrast to limestone, in marble a very distinct fracture evolves at the bottom notch and propagates to the upper notch. En échelon fractures are only visible on the scale of grain size (Fig. 5-20). Figure 5-21.A shows a micrograph of

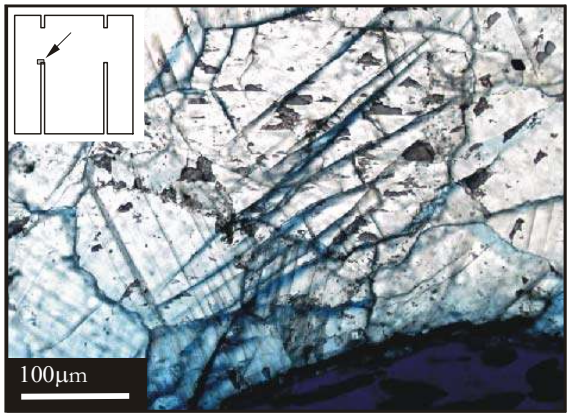

Fig. 5-20. Micrograph of the bottom notch at ~ 99 % of the maximum axial stress in Carrara marble. Only en échelon cracks are visible.

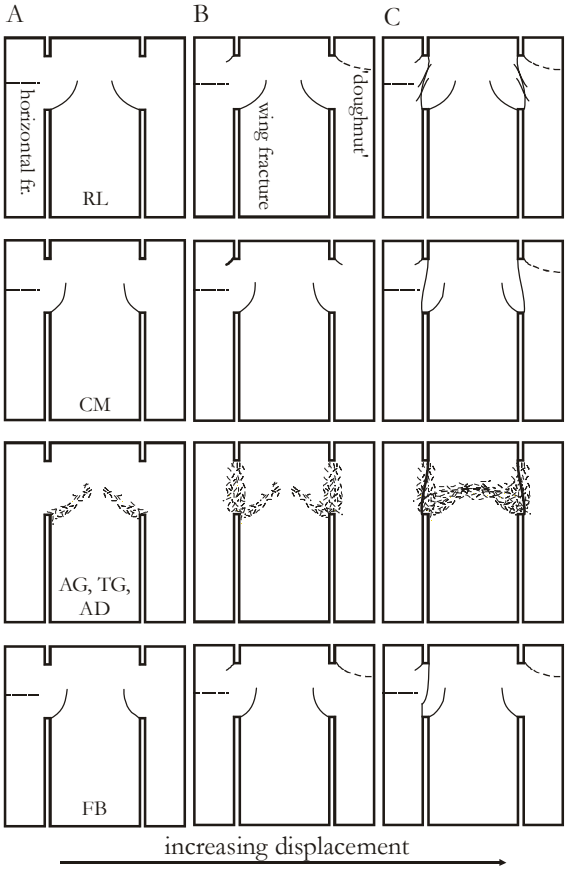

Fig. 5-19. Sketch of macroscopic fracture initiation and propagation for Rüdersdorf limestone (RL), Carrara marble (CM), Aue granite (AG), Mizunami granite (TG), Äspö diorite (AD) and Flechtingen sandstone (FB). (A) at 30 % of maximum load, (B) at 60 % of maximum load and (C) at peak load. [P = 5 MPa].

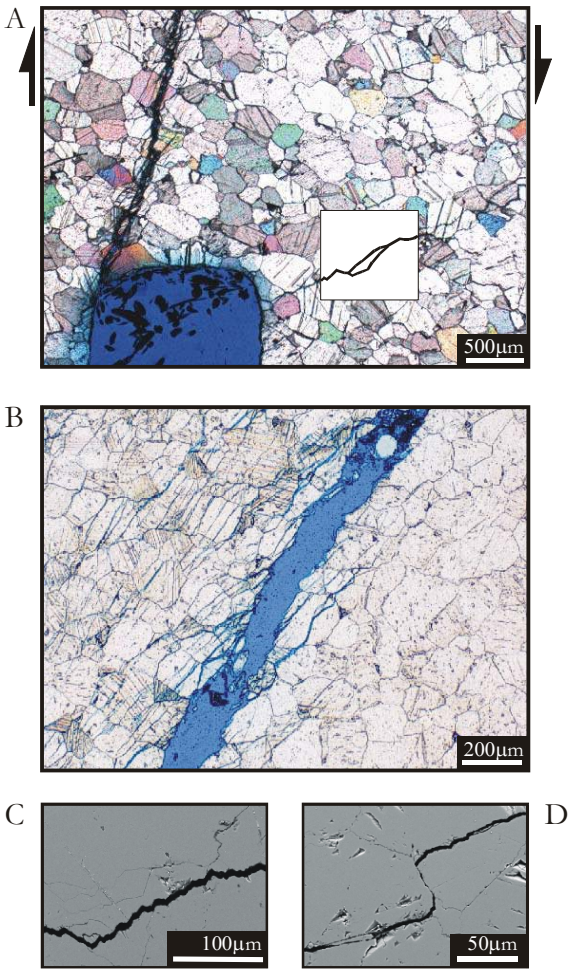

Fig. 5-21. Micrograph of bottom notch fractures within PTS- test. (A) Overview of bottom notch in Carrara marble sample. (B) Fracture (shear) connecting the notches. (C) Close-up of wing fracture. Fracture shows a rough path following cleavage planes. (D) Close-up of fracture following grain boundary. (C+D from SEM).

Carrara marble loaded to peak stress taken in the plane between the notches. The surface of the wing fracture is comparably smooth and a distinct opening is visible (Fig. 5-21.C). In contrast, the shear fracture consists of a main fracture including an array of en échelon microcracks (Fig. 5-21.B) and shows no opening. In marble, 'doughnut' fractures are seldom found.

The granite and diorite samples develop a wide process zone that is initiated at about 30 % of the maximum load. In this intensely microcracked zone the main fracture develops and connects the notches at the peak load. Thereafter, a circumferential zone of microcracks sometimes develops at the lower notch. The magmatic rock types develop a network of predominantly grain boundary cracks, but also intragranular cracks. Typically features show the direction of en échelon fracturing. The width of the shear zone qualitatively increases with grain size.

The sandstone shows on the macroscale a straight vertical fracture at the bottom notch, which then deviates from its trace. It follows a curved path to the upper notch. Microscopically, the sandstone develops in a narrow zone a network of micro-/mesocracks in random orientation with a trough-going main fracture showing indication of grain rotation. Individual en échelon cracks are not observable.

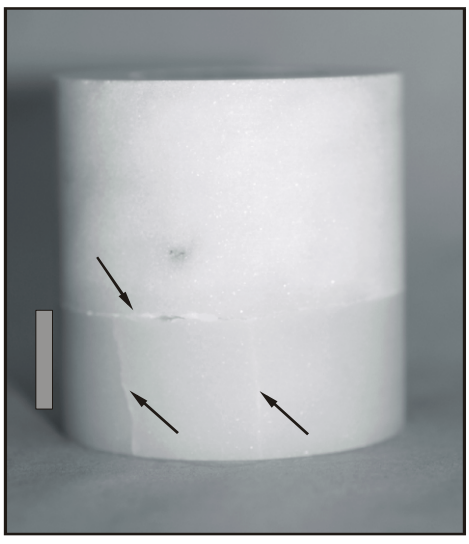

Fig. 5-22. Photography of Carrara marble sample showing doughnut fracture and radial splitting fractures. The doughnut fracture is formed prior to the vertical fractures. Grey bar indicates approximate position of IP [M10-7; a=31.1, b=5.2].

The reported formation of the bottom wing fracture (~30 % peak load) and upper horizontal 'doughnut' fracture (~60 % peak load) (Fig. 5-19) are not detectable in the stress vs. displacement data (Fig. 5-3) for the rock types tested.

A horizontal fracture sometimes develops in the samples at low P that connects the shear zone and the mantle surface.

In the post-peak region the inner rock cylinder is further moved downwards. Displacement of the inner cylinder initiates radial fractures (Fig. 5-22) at zero or low confining pressure (typically below 30 MPa). For fine grained rock types the confining pressure necessary to prevent the radial fractures is lower. Granite shows this kind of fractures up to confining pressures of 30 MPa, marble up to almost 10 MPa. Limestone rarely shows radial fracturing, and if so at zero confining pressure only.

5.2.6 Influence of confining pressure on the fracture pattern of Carrara marble

This section describes the evolution of microstructures in Carrara marble at different levels of confining pressure and different observation scales in the PTS- test in order to investigate the developing fractures. The fracture pattern and microstructures of samples subjected to confining pressures of 5 MPa, 30 MPa and 50 MPa [M5-2; M10-5; M10-2] are studied, representing samples that were loaded in the high-slope, transitional and low-slope K_{IIC}-regime, respectively. In each test the sample was loaded up to the peak plateau and then terminated. Thin-sections in the notch plane parallel to the sample axis illustrate the microcrack characteristics and fracture pattern. The observations are divided into two classes, i.e. macro scale and micro scale.

Macro Scale observations

Figure 5-23 shows the fracture traces at different confining pressures. At all P macroscopic fractures develop in the zone of highest shear deformation, i.e. in the region

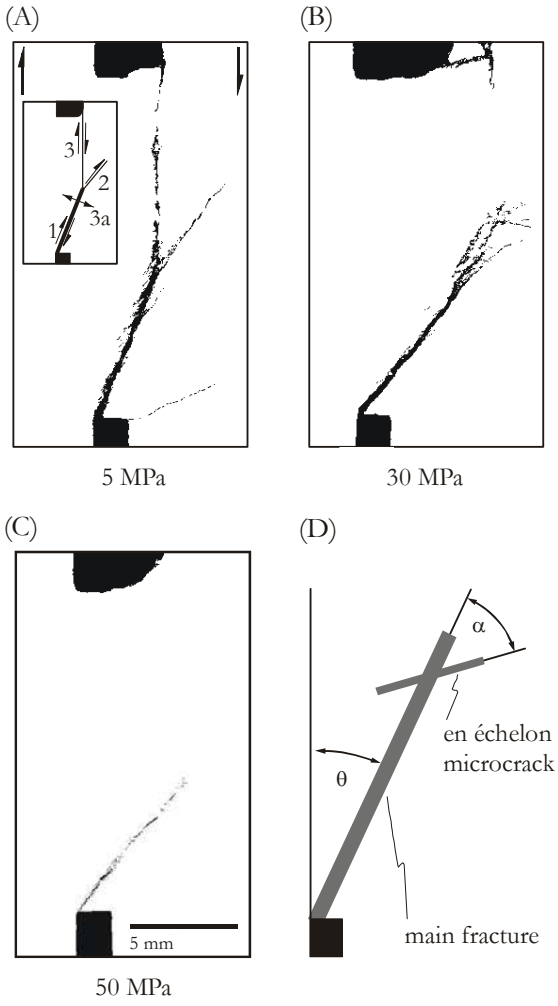

Fig. 5-23. Fracture traces in deformed marble at different level of confining pressure and at onset of axial peak load. (A) P = 5 MPa, a fracture connects the notches and a wing crack develops at the lower notch; sequence of fracturing is indicated by numbers. (B) P = 30 MPa, non-coalescing fractures develop at bottom and top notch. (C) P = 50 MPa, fracture develops at lower notch only. (D) Drawing of notations concerning the fractures. (Note: the edges of the upper notch split off due to high uni-axial compression).

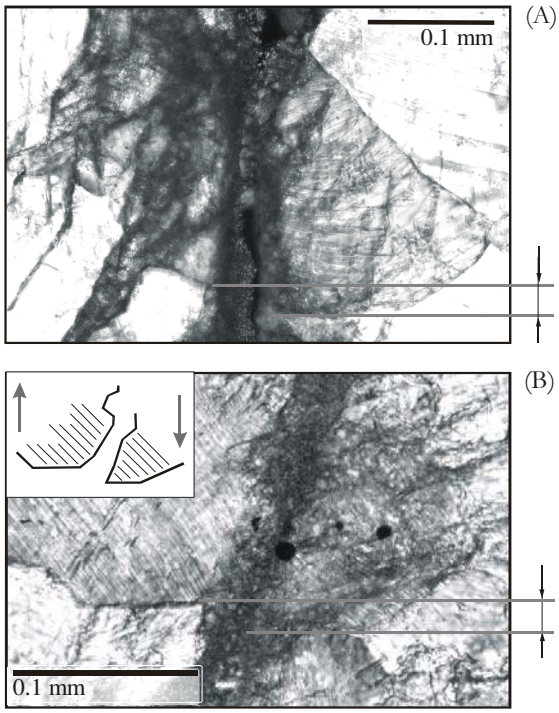

Fig. 5-24. Micrographs of the upper fracture at different confining pressures showing fractured calcite grains. The shear displacement is indicated. (A) P = 5 MPa and (B) P = 30 MPa.

between the notches. The sample subjected to P = 5 MPa (Fig. 5-23.A) shows a fracture starting at the outer tip of the bottom notch that is inclined towards the centre of the specimen. From the upper inner notch tip a fracture propagates vertically down and coalesces with the inclined bottom fracture. The vertical fracture shows some shear displacement (Fig. 5-24). The bottom fracture shows some opening from this junction to the notch, but it is not opened in the prolongated part from the junction towards the centre of the sample. The sequence of fracturing is indicated in the inlet of Figure 5-23.A. At P = 30 MPa the sample also shows a fracture evolving at the bottom notch (Fig. 5-23.B). It is slightly opened and spreads out at the end of the trace. At the top notch a small vertical fracture is visible that stops after a few millimetres. The sample subjected to 50 MPa confining pressure (Fig. 5-23.C) contains an inclined fracture at the bottom notch only. No fracture is visible at the top notch as well as no opening of the bottom fracture.

The angle formed by the bottom fracture and the vertical direction, θ, changes with increasing P. θ increases from about 20 ° at 5 MPa to about 40 ° at 30 MPa and 42 ° at 50 MPa (Fig. 5-25.A).

Only the 5 MPa sample displays a wing fracture at the bottom notch (Fig. 5-23). None of the samples shows a 'doughnut' fracture.

Micro Scale observations

In general, the matrix in the region of high shear displacement is more dispersed and grains show more deformation lamellae than compared to the remaining parts of the specimen.

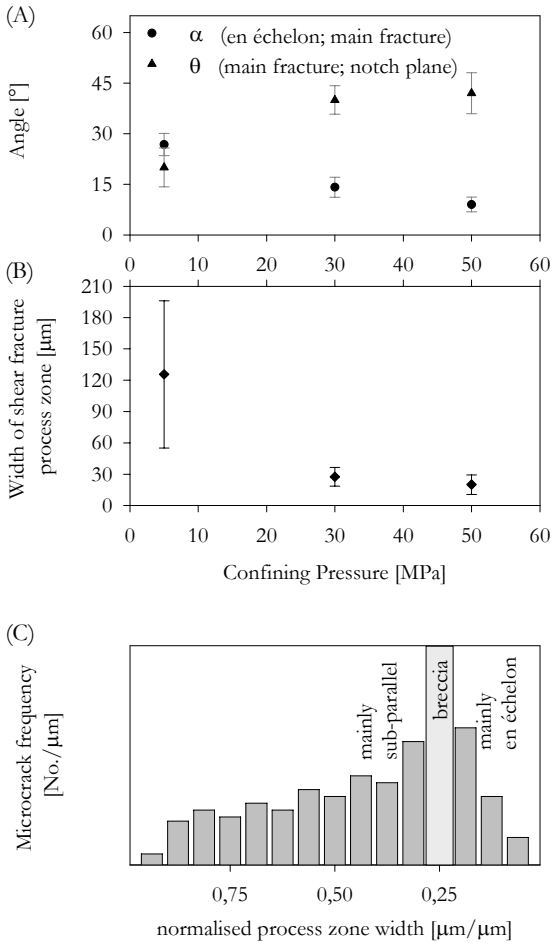

Fig. 5-25. Parameters of the fractures. (A) Influence of confining pressure on the angle of main fracture and en échelon fracture with each other and vertical direction. (B) Influence of confining pressure on the width of the process zone. (C) Distribution of the microcrack density perpendicular to a main fracture.

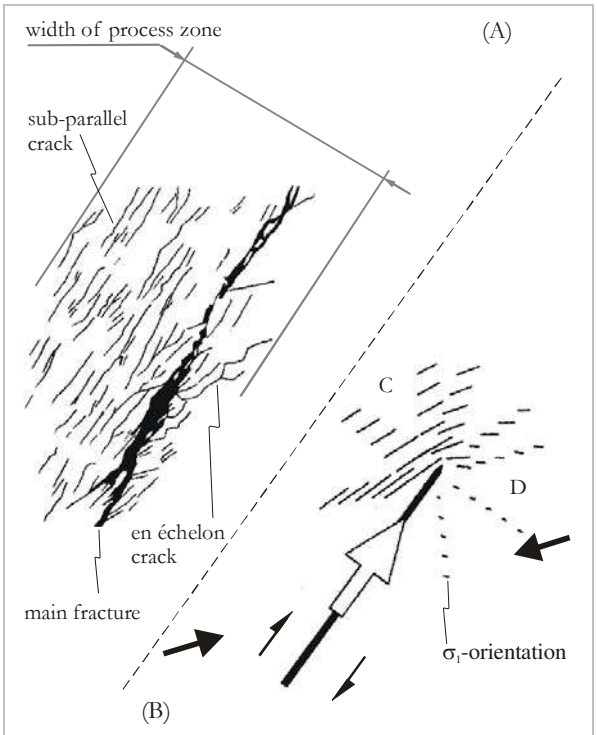

Fig. 5-26. (A) Schematic re-drawing of the main fracture and process zone at the bottom notch with inclined (en échelon) and sub-parallel cracks. The main fracture predominately propagates intragranularly. (B) Plot of the calculated maximum compressive stress directions surrounding the tips of a Mode II crack, showing rotation to lower angles with the fracture in the compressive quadrant, C, and higher angles in the dilatational quadrant, D. Open arrow indicates fracture propagation direction, solid arrows remote major principal stress direction. The small lines indicate orientation and magnitude (proportional to length) of major principal stress (after Vermiliye & Scholz, 1999).

Samples terminated at about onset of the peak load only show en échelon fractures at the bottom notch (Fig. 5-20). They are located where later shear fracture growth takes place.

The shear fractures consist irrespective of the magnitude of confining pressure of a narrow zone of branching, predominantly intra- and transgranular microcracks (Fig. 5-21), in the following referred to as main fracture, and of an array of inclined (en échelon) and sub-parallel microcracks (Fig. 5-26.A).

With increasing P the angle, α, between the en échelon cracks and the main fracture (Fig. 5-23.D), decreases from about 27° (P = 5 MPa) to 9° (P = 50 MPa) (Fig. 5-25.A).

The influence of P on the width of the measurable process zone of the main fracture is shown in Figure 5-25.B. It decreases considerably from ~ 130 µm at P = 5 MPa to ~ 30 µm at 30 MPa and remains almost constant up to 50 MPa. The variability of the process zone width, shown as error bars, is very high for the sample deformed at low confining pressure, but small for 30 MPa and 50 MPa confining pressure.

Figure 5-25.C shows the average density distribution of microcracks perpendicular to the main fracture (see Fig. 5-26.A). The microcrack distribution is similar for all three specimens irrespective of confining pressures.

The microcrack density increases from both sides towards the main fracture, which is indicated as breccia in Figure 5-25.C. The main fracture separates two microcrack regimes with

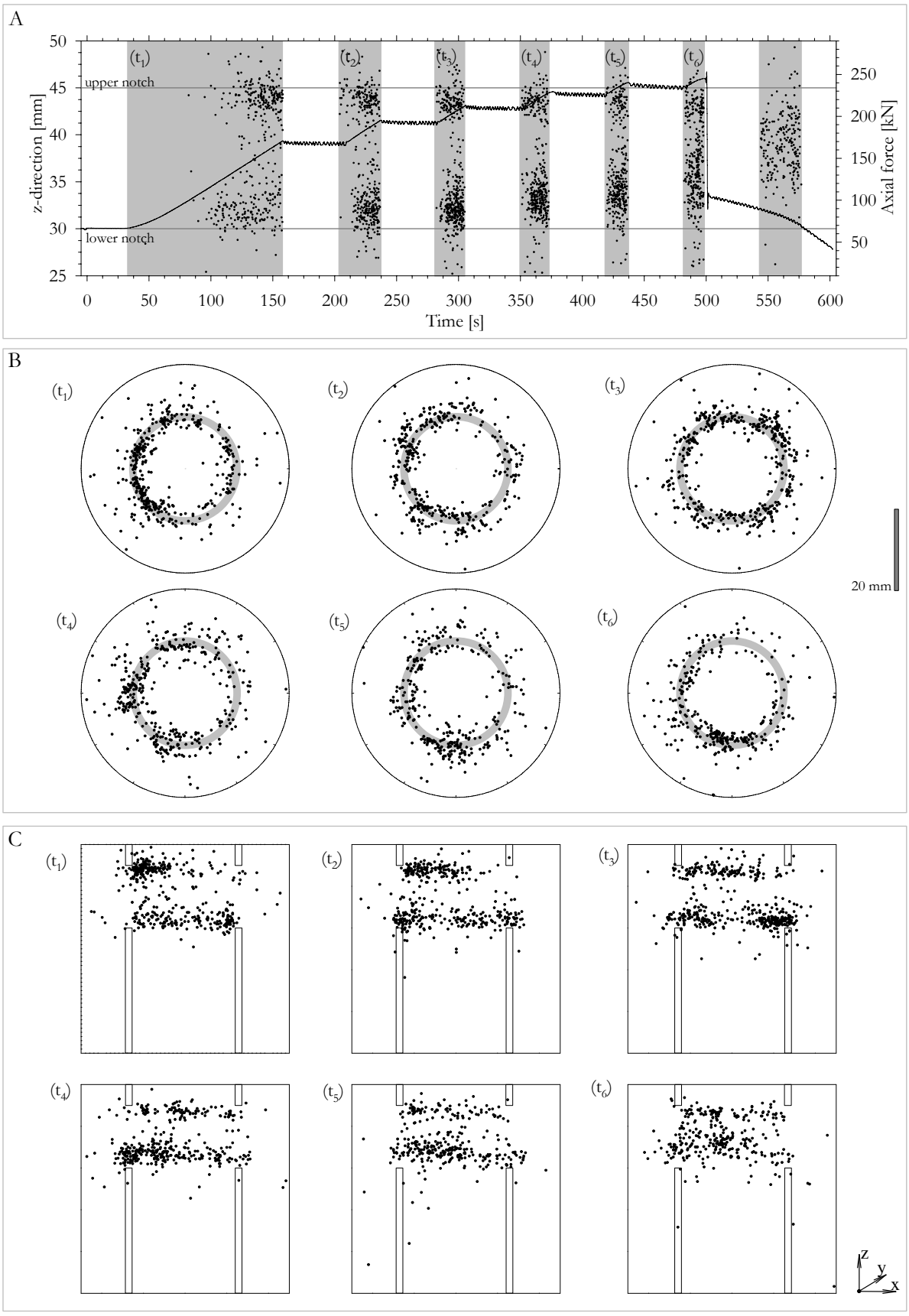

Fig. 5-27. Acoustic Emission (AE) events in space and time for Mizunami granite sample [T1-1d] at P = 30 MPa. (A) AE events projected into z-direction vs. time and force vs. time is given. AE signals start at top and bottom notch and successively propagate from bottom notch into sample. White areas indicate dead-time of AE acquisition system. (B) AE distribution in map view of sample for time slices from (A). Events are localised in the narrow zone between the notches. (C) Side view of sample, all events projected onto xz-plane.

about 75 % of the total amount of cracks, oriented predominantly sub-parallel, on one side (above) and about 25 %, mainly en échelon cracks, on the other (lower) side. Hence, the process zone is unsymmetrical with respect to the main fracture, both in shape and crack angle.

5.2.7 Results from Acoustic Emission recording

The fracture evolution for a sample loaded at P = 40 MPa as observed by AE analysis is shown in time sequences in Figure 5-27. Continuous AE activity starts at about 45 % of the failure load. The located events form clusters at top and bottom notch. With increase in axial load the bottom cluster starts to propagate upwards with approximately constant speed. The length of the AE process zone increases (~5-6 mm). The top cluster remains stationary (length: ~2-3 mm). After failure load the events are evenly distributed between the notches at lower rate. Formation of the reported wing and 'doughnut' fracture cannot be identified, this in consistency with the observation that the wing and 'doughnut' fracture are not initiated at P ≥ 30 MPa. Unfortunately the fracture propagation at peak load itself was not recorded as the data acquisition buffer was being stored at that moment. Altogether ~7200 signals were recorded. For further details about AE monitoring see Stanchits et al. (2003).

5.3 Discussion

The results presented in this chapter included variation of geometrical and procedural parameters of the PTS- method, mechanical and acoustic emission data, analysis of stress distribution and microstructural analysis. These matters are discussed below.

5.3.1 Geometry variation

Notch depths and Sample height

Variation of rock ligament between the notches, IP, illustrates a plateau of τ_{av} (Fig. 5-9) for a certain range of IP. Same relation is reported by Yoon & Jeon (2003) for Daejeon granite. They report constant K_{IIC} for IP of about 17 to 40 mm. Numerical analyses performed by Watkins (1983) on samples with similar, but cubic geometry give evidence of constant stress intensity factor in Mode II for IP/W ratios of 0.3-0.5 (IP= 15 - 25 mm in case of PTS- geometry) for experimental Mode II fracture toughness determination of mortar without confining pressure.

With small ligament length the notches are expected to influence each other by presumably coalescence and interaction of the initial process zones before actual fracture propagation takes place at peak load; a decrease of shear stress necessary for fracture propagation is to be expected at small IP. The initial FPZ were shown by means of AE to be few millimetres in length (~ 2-3 mm for Mizunami granite). However, constant τ_{av} is approved for almost the full range of IP. Nevertheless, the applied axial stress for failure shows some indication for a power law rise (Fig. 5-9.A) which is not clearly reflected by τ_{av} due to the scatter in the data. If the process zones of top and bottom notch interact at low IP, as is suggested by AE, cannot be conclusively confirmed by the stress data. Coalescence of the FPZs should result in a magnified loss of strength. This is only vaguely supported by the shape of the stress vs. IP plot at low IP in Figure 5-9.A.

The elevated average shear stress necessary for fracture growth in Aue granite (Fig. 5-9.B), might be explained by the comparably large grains (average is 1 mm, but up to 5 mm are included). At low IP only a handful of grains are located between the notches and hence coalescence might be aggravated by inter- as well as intragranular crack propagation accompanied by interlocking and crack arrest.

Unsymmetrical shape of the sample, i.e. notch depth $a \neq b$, and sample height, W, are shown to have minor influence on the obtained τ_{av} (Fig. 5-10). Hence, bending of the unsupported outer ring does not (or only little) contribute to the Mode II fracture process.

Notch diameter

Variation of the diameter of the notches, ID, and of the sample diameter, D, are shown to influence τ_{av} (Fig. 5-11). The effect increases with increase in grain size. The experimental results show that τ_{av} increases with increasing thickness of the outer ring between sample boundary and notches. This is most pronounced for the coarse-grained granite, evident for the medium-grained

marble, but not for the very fine-grained limestone. Hence, the grain size may be the influencing parameter. In principle, also bending of the bottom ring might be considered to influence the fracturing process. But as it was discussed in the previous paragraph, the notch depth, which should directly influence the amount of bending, does not change τ_{av}. Further, if bending were the reason for the variation of τ_{av} with ID change, it is not clear why the grain size should have a pronounced influence, as it obviously does.

During formation of the shear fracture, grains have to slide and, consequently, induce dilatancy. The induction of dilatancy is larger for coarse grained rocks, as the amount of sliding is greater. Another mechanism most likely contributing to dilatancy is tensile (Mode I) microcracking in the fracture process zone.

Direct comparison of the average shear stress at failure of samples with constant ID but increased sample diameter, D, shows τ_{av} to be higher for the larger D (Fig. 5-11.B). The increase of wall between sample boundary and notch/fracture plane is considered to be the reason. If the process zone interacts with the mantle surface of the sample, decreased shear stress for failure is to be expected. Decreasing ID/D results in restricted interaction of the FPZ and mantle surface. This is supported by the fact that the change of τ_{av} with variation of ID is smaller for smaller grained rocks, which produce smaller FPZ. The explanation has to be verified in future experiments. Unfortunately, no metrology (e.g. strain gauges) for determination of radial extension was available which would have helped to quantify the dilatancy and hence study the influence of dilatancy in the fracturing behaviour.

The samples tested at the largest ID show elevated τ_{av} compared to the smaller ID. The reason for this weak observation might be found in the curvature of the notches. On the other hand it was observed in limestone, that the fracture sometimes reorganises itself forming polygonal shape in crosscut view, hence propagating planar rather than cylindrical. At this stage it cannot be conclusively conversed what is the influence of the curvature on τ_{av}, and hence K_{IIC}.

Notch width

The force vs. displacement data from variation of notch width, t, showed minor differences for the tested t. Changes in compliance are consistent with the differences in IP (c.f. Fig. B-4, p.60) and W, and should be also ruled by the notch width. Wider t should result in higher compliance. The variation of peak load and related shear stress can be dedicated to some extend to the variation of IP, too (c.f. Fig. 5-9).

Slight variation of τ_{av} may apply due to the different methods to introduce the notches, i.e., the CNC moulding technique and different drill bits. The somewhat lower τ_{av} for the wider notch may also be related to the fact that in a wider notch more grains are intersected at the bottommost of the notch, and hence more grain boundaries might be preferably oriented for local failure.

The shear strain as estimated from elastic strain solution calculates as

$$\gamma = \frac{du}{dt}, \qquad (5\text{-}8)$$

where u is the displacement in shear direction and t the notch width. In case of the PTS- test at given displacement a wide notch will generate less shear strain than a narrow notch (c.f. Fig. B-1.D, p.57) assuming that the full deformation is taking place at the inner notch tip and that the deformed front is straight, hence $d\gamma$ is constant.

Figure 5-28.A shows the shear strain as calculated from equation 5-8 for different t. The approximated shear strain is lower for wider notches, suggesting that the local shear stress is higher for narrower notches.

However, as the displacement of the outer notch tip is not known, the correct du cannot be deduced, hence, the above argument is weak. FEM modelling suggests very similar displacement profiles for different notch width (Fig. 5-28.B). This is consistent with the fact that the average shear stress at failure (c.f. Fig. 5-13) is almost constant. Improved metrology should clarify this in future work.

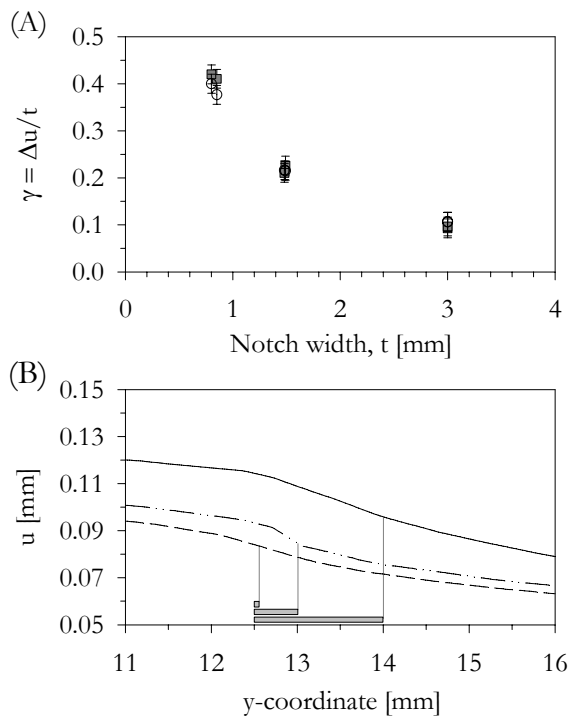

Fig. 5-28. Analysis of the displacement as function of the notch width. (A) Shear strain, γ, as calculated from the displacement at peak load for different notch width, t. Refer to text for discussion. (B) Axial displacement, u, as derived from FEM modelling at constant loading. The shape of the axial displacement along a trace (trace-coordinates [x;y]→ [11,33.3/16,33.3]) vertical to the shear direction at a distance s = 0.3 mm in front of the notch is very similar for different notch width, t. (solid line: t = 1.5 mm; dash-dotted line: t = 0.5 mm; dashed line: t = 0.05 mm). Hence it is to expected that the accurate du for solving equation 5-8 is very similar for the different notch widths. Grey bars indicate the location of the notch. [E=50GPa, ν=0.37, P=0MPa, W=50mm, D=50mm, a=5mm, IP=15 mm].

Above discussion in combination with the observation of constant average shear stress at failure, leads to the conclusion that the notch width is not the ruling parameter for fracture initiation, too.

5.3.2 Sample geometry and testing procedure

Geometry

The circular geometry of the PTS- test is in terms of structural stability superior to a straight geometry as is favoured in several Mode II testing methods (c.f. Section 2.5.2). The tubular (hollow-cylindrical) layout of the PTS- test in the notch regions is able to withstand high confining pressures due to the tangential stresses (comparable to principle of an arch). The tubular geometry of the top and bottom part of the limestone sample showed no sign of specimen failure up to 120 MPa[1]. A geometry with straight notches can be studied at low confining pressures only, as bending stresses introduced by the confining pressure would cause failure. However, for reasons of comparison and validation, it is recommended, that a geometry with straight notches, i.e. without curvature, is tested and the results are compared to those of the PTS- test. Although it was observed in limestone that the fracture reorganises in sections with planar surfaces, it cannot be excluded that a curved geometry results in altered peak stresses and hence measured fracture toughness.

Application of loading and confining pressure

The PTS- test has the unique ability to independently from each other apply an external shear load and a normal stress perpendicular to the plane of shear loading. Some other methods do have in principle the possibility to vary the confining pressure, but not independently from an external shear loading (i.e. Triaxial Compression test (Hakami & Stephansson, 1990) and Compression Shear Cube test (Jumikis, 1979)). The very important influence of overall compression (confinement) on Mode II loading induced fracturing (e.g. Lawn, 1993; Melin, 1986) can be adequately studied by the Punch-Through Shear test only.

The sample is loaded hydrostatically before shear load is applied. After application of confining pressure, the inner cylinder is punched down in displacement control. The ratio of confining pressure and shear stress, $\varkappa = P/\tau$, will therefore decrease on punching down the inner cylinder. It was shown numerically by Melin (1986) that at high ratios of $\varkappa$ Mode II is preferred. Lower ratio will cause preferred initiation of Mode I fracture. When P is high enough K_{II} will reach K_{IIC} before τ has reached the level at which Mode I is preferred. $\varkappa$ is decreased from high values in the PTS- testing procedure, hence Mode II is preferred if P is sufficiently high. In the previously mentioned method (Jumikis, 1979), Mode II loading is

[1] Limestone sample [L15-0] was subjected to increasing P for specification of structural integrity.

applied by adjusting the loading angle (c.f. Fig. 2-11.D) and confining pressure also depends on the loading angle. Hence, $\varkappa$ is governed by the limited angle to achieve Mode II loading and then is kept constant with simultaneous increase of shear stress and confining pressure.

At high confining pressure (> 30 MPa) the macroscopic wing fractures are suppressed, this as indicative that $\varkappa$ is sufficiently high for preferred macroscopic Mode II fracture growth.

Displacement rate

Variation of displacement rate showed that for a broad range τ_{av}, and therefore K_{IIC}, does not significantly change for the majority of rock types tested (Fig. 5-14). Applying the terminology introduced for Mode I fracturing regarding fracture velocity as a function of stress intensity factor level (e.g. Atkinson, 1984), it can be concluded that the PTS- tests determines the critical stress intensity factor, i.e. fracture toughness. However, τ_{av} of the coarse-grained Aue granite increases with increasing loading rate. It remains unclear if this is due to a different mechanism of fracture propagation at low P. Possibly, the kaolinitisation of large feldspars may induce time-dependent deformation mechanisms. Nevertheless, from changing loading rates in Mode I fracture toughness testing slight decrease or increase of K_{IC} with loading rate in the critical regime is reported (Zhang et al., 1999). The increase of τ_{av} and, hence, K_{IIC}, is not as conspicuous as would be necessary to indicate dynamic fracture toughness (c.f. Backers et al., 2003a; Atkinson, 1984).

Cyclic loading/Displacement control

Displacement control was chosen anticipating to control fracture propagation, i.e. to achieve stable fracture propagation at the onset of critical stress intensity. As machine stiffness is too low this was not possible. However, in some experiments it was possible to propagate the fracture at increments by cyclic loading at elevated confining pressure, P = 40 MPa (Figs. 5-17 and 5-18).

The change in rock stiffness during loading/ unloading cycles can be separated into four distinct regimes (c.f. Fig. 5-18). *(1)* Up to 80 % of the maximum load the stiffness is constant and is consistent with the linear elastic part of the stress vs. displacement curve, suggesting that no significant cracking occurs (Fig. 5-29). *(2)* Above the yield point the stiffness decreases as considerable microcracking forms the process zone (Stanchits et al., 2003). The fracture propagates and the stiffness decreases as the intact rock portion becomes shorter. *(4)* The observed increase of stiffness below 60* % of peak stress in the post peak region may be due to interlocking of the formed Mode II fracture faces, grain rotation and compaction. The interlocked grains of the rough fracture faces are pressed against each other by the shear displacement (Fig. 5-29). Elevated confining pressure suppresses dilatancy resulting from sliding. *(3)* In the regime between decreasing (regime *2*) and increasing (regime *4*) stiffness the two mechanisms of fracture propagation and interlocking might superimpose, leading to an apparent constant stiffness.

The stiffness evolution is almost the same for the examined rock types, i.e. Carrara marble, Mizunami granite and Aue granite. The geometry, loading procedure, and confining pressure was alike for all samples. The Young's modulus is also very similar. Hence, comparable stiffness in the initial phase is plausible. Interestingly, the decrease of stiffness is similar for the tested samples. Let us assume that only the region between the notches is altered due to the formation of the process zone and main fracture. As the rock types show very different average grain sizes (0.3, 0.7 and 1.0 mm) the size of the

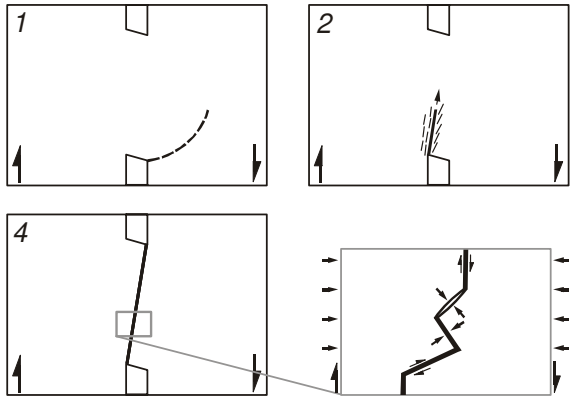

Fig. 5-29. Development of fracturing. The numbering refers to the regimes indicated in Figure 5-18. (Top left) Elastic deformation, wing crack is initiated at low confining pressures only. (Top right) FPZ and fracture formation decrease the stiffness. (Bottom) Grain interlocking after connection of the notches leads to increase of stiffness.

fracture process zone should be different (c.f. Section 2.1). Hence, one could expect differences in the deformation behaviour as reflected by the stiffness after formation of FPZ. This is not observed.

The formation of the process zone and reduction of ligament length could be detected. However, it was not possible to determine when the fracture connected the notches. Knowledge of the moment of coalescence would provide the possibility to develop an evaluation technique by applying the concept of the J-integral (Rice, 1968). Knowing the displacement and force drop necessary to connect the notches by the Mode II fracture, one could calculate the J-integral. Assuming small scale yielding in testing, the J-integral is equal to the Energy Release Rate. From this the fracture toughness can be calculated.

5.3.3 Evaluation method

The basic equation for calculating the stress intensity factor is

$$K_{II} = \tau \cdot \sqrt{\pi \cdot a}\,, \tag{5-9}$$

where a indicates the effective fracture length.

Analysing the geometry of the PTS- test, the notch depth is the favourable macroscopic feature introducing the stress concentration. It was found experimentally that the fracture stress is independent of the notch depth for changing notch depth (Fig. 5-9) and constant IP (Fig. 5-10). Minor variations of peak stress may be dedicated to the sequential longer rock cylinder deforming elastically, inaccuracies in providing an exact IP and the usual geological scatter. The notch depth consequently is not the correct initial crack length for determining K_{IIC}.

In case of an inclined fracture in a solid subjected to compression, the deformation necessary for fracture propagation is accumulated over the fracture length. In case of the PTS- test the shear deformation is generated over the notch width (c.f. Section 5.3.1). It could be shown that the notch width is not the correct initial fracture length for K_{IIC} estimation, also.

Considering the K_{IIC} values reported in Appendix B for the samples with suggested geometry using DET, estimation of the effective crack length as described in equation 5-9 yields

$$a = \left(\frac{K_{IIC}}{\tau_{av}} \right)^2 \pi^{-1} \tag{5-10}$$

of about 3 mm for all rock types. It may be speculated that this dimension is related to microstructural features. These might be the damage introduced by sample preparation and subsequent formation of the process zone. Damage due to the sample preparation could not be specified in microscopy at this stage.

A variety of different evaluation methods were applied to the PTS-test. These are summarised and briefly discussed in the *BOX: EVALUATION*. All methods applied deliver fracture toughness values of comparable magnitudes.

Displacement Evaluation Technique (DET)

At this stage in developing the testing method for determination of the critical stress intensity factor of rock in Mode II it is suggested to estimate K_{IIC} by the Displacement Extrapolation Technique (DET, c.f. Section 5.1).

The methodology is not exact at this stage of development due to several reasons. The discussion of the DET methodology as itself is beyond the scope of this thesis; the reader is referred to literature (e.g. Lim et al., 1993).

The computer code used shows inaccuracies in the evaluation of a homogeneous stress field. Local stress variations appear that do not correctly reflect the stress fields (compare contour plots in Figs. 5-7 and 5-8). This may be – to some extend – related to the generation of the mesh. It is not possible to create a symmetric mesh in a symmetric set-up. Hence, if the DET approach will be used in future, a more appropriate code should be used.

Besides the problems with the code, other assumptions give inaccuracies in the obtained K_{IIC} values as listed below:

(a) The displacement gradient used for calculation of the stress intensity factor is calculated assuming linear elastic behaviour. As an inelastic process zone is formed prior to macroscopic fracture growth, this assumption is not valid.

(b) During application of axial load, wing fractures are introduced in the sample. The stress field presumably is altered and the maximum shear stress can be expected to be somewhat

BOX EVALUATION

For determination of the Mode II fracture toughness several methods were employed and developed. For comparison the Mizunami granite sample T4-1a is evaluated for each individual method where possible. The FEM package Phase² was used (Rocscience, 1999) for all computer modelling.

Displacement Gradient Method

Backers et al. (2002b) published a method to calculate K_{IIC} from the PTS- test that used FEM for back calculation, which is presented in corrected form here. According to the theory of linear elastic fracture mechanics, the stresses around a fracture tip can be calculated by (e.g. Lawn, 1993; cf. Section 2.2, equation 2-2 and Fig. B-1.A for notations)

$$\begin{Bmatrix} \sigma_{rr} \\ \sigma_{\theta\theta} \\ \sigma_{r\theta} \end{Bmatrix} = \frac{K_{II}}{\sqrt{(2\pi \cdot r)}} f(\theta) \quad \text{.....(B-1)}$$

The shear stress has a maximum in the direction of the notch ($\theta = 0$) – at least for perfectly sharp slots –, hence, the stress intensity factor can be calculated by

$$K_{II} = \sigma_{r\theta} \cdot \sqrt{2\pi \cdot r} \quad \text{.....(B-2)}$$

Transformation from the Polar coordinate system into a local Cartesian coordinate system is operated by

Polar co-ordinates: {0;r;θ};
$r \geq 0$; $-\pi < \theta < \pi$
Cartesian co-ordinates: {0;x;y};
$-\infty < x < \infty$; $-\infty < y < \infty$
$\{0;r;\theta\} \rightarrow \{0;x;y\}$:
$x = r \cos\theta$; $y = r \sin\theta$

The principle adopted to calculate the Mode II fracture toughness, K_{IIC}, is to exploit the shear displacement in the shear plane between the notches at peak stress conditions. Intense shear deformation evolves across the notch tip (Fig. B-1.B). FEM calculation shows that the lateral component, v, is very small compared to the vertical displacement, u.

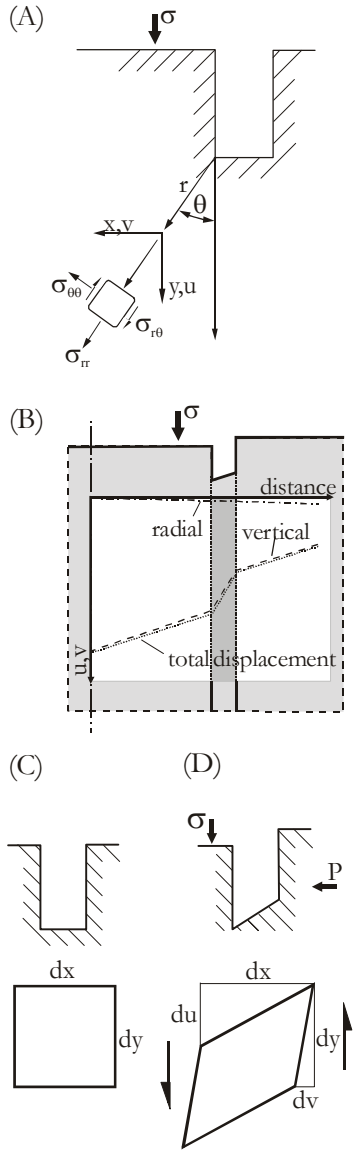

Fig. B-1. The notch region: notations, stresses and displacements. (A) Notations at notch in polar and rectangular coordinate system. (B) Elastic displacements at the notch (schematic). The change in slope at the notch tip due to stress concentration is obvious. (C+D) Close-up of the notch tip region; (C) undeformed and (D) deformed. The axial load, σ, introduces shear displacement at the notch tip.

Neglecting the third dimension the infinitesimal shear strain e_{xy} is (Means, 1976)

$$e_{xy} = \frac{1}{2}\gamma_{xy} \quad \text{.....(B-3)}$$

where γ_{xy} is the shear strain (Fig. B-1.C+D). γ_{xy} can be expressed in terms of gradients of the displacements v and u in x and y direction as

$$\gamma_{xy} = \frac{dv}{dy} + \frac{du}{dx} \text{ and} \quad \text{.....(B-4)}$$

$$e_{xy} = \frac{1}{2}\left(\frac{dv}{dy} + \frac{du}{dx}\right) \quad \text{.....(B-5)}$$

The shear stress is defined as

$$\tau_{xy} = e_{xy} \frac{E}{2(1+\nu)} \quad \text{.....(B-6)}$$

where E is the Young's modulus and ν is the Poisson's ratio. Substituting equations (B-5) and (B-6) into (B-2) yields

$$K_{II} = \frac{1}{2}\left(\frac{dv}{dy} + \frac{du}{dx}\right) \cdot \frac{E}{2(1+\nu)}\sqrt{2\pi \cdot r} \quad \text{.....(B-7)}$$

The displacement gradient at the notch tip cannot be measured directly in the course of an experiment. A back analysis of the applied stresses using FEM has to be performed. The maximum total gradient is utilised at the measured peak stress conditions at a distance y = 0.3 mm from the notch tip. As was found the stress field is in rough approximation almost square root like in that region (c.f. Fig. B-3).

For determination of the maximum displacement gradient, the FEM package Phase² was used (Rocscience, 1999). The model (Fig. B-2) has 680 external nodes that yield 11053 internal nodes on 21424 elements. The uniform triangular mesh has three midside nodes. The matrix is solved by Gaussian elimination.

The maximum total gradient is utilised at the measured peak stress at a distance $\Delta y = 0.3$ mm from the notch tip along a line perpendicular to the shear direction assuming ideally elastic behaviour. The length of the line has to cover the maximum displacement gradient. Displacement data is taken every 0.012 ± 0.002 mm along that line; the gradient is calculated between two data points locating the maximum displacement gradient.

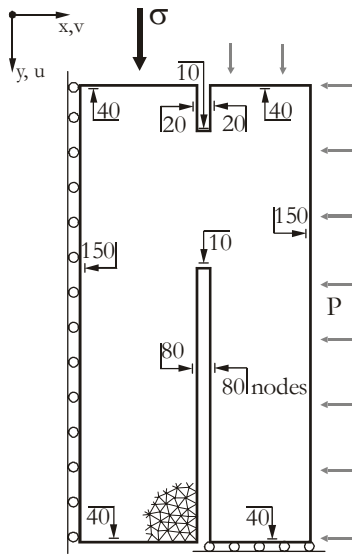

Fig. B-2. Schematic set-up of FEM simulation for Displacement Gradient Approach. The model consists of half a sample. The loading and restraints for the model are given. A cutaway of the mesh is shown at the bottom of the axisymmetric FEM set-up. The arrows indicate the number of external nodes for the corresponding model boundary.

While validating the displacements with the FE-code it was found that the results very much depend on the mesh generated. Hence the approach as described above is not accurate. Furthermore it is far too complicated for a standard procedure.

Whatsoever, several other assumptions might influence the fracture toughness values as listed below:

(a) The displacement gradient used for determination of the stress intensity factor is calculated assuming linear elastic behaviour. As an inelastic process zone is formed prior to macroscopic fracture growth, this assumption is not valid.

(b) During application of axial load, wing fractures are introduced in the sample. The stress field presumably is altered and the maximum shear stress can be expected to be somewhat lowered. This apparently results in overestimation of K_{IIC} at low confining pressures, as the wing fractures are not considered in the back calculations. The influence of the wing fracture on the stress distribution does not apply at confining pressures above 30 MPa, as those fractures are not initiated.

For the Mizunami granite sample T4-1a the displacement gradient analysis yielded a fracture toughness of $K_{IIC} = 3.7$ MPa $m^{1/2}$ at ambient pressure.

Stress Approach

The maximum shear stress concentration is not in the direction of the notch/shear loading, but at one notch tip. Hence the maximum drop in stress is oblique to the shear load direction. Therefore, within the shear stress field as calculated by FEM at peak load conditions the direction was searched for which the shear stress, τ, drop showed a 'square root' shape. When plotting

$$K_{II} = \tau\sqrt{2\pi \cdot r} \quad \text{.....(B-8)}$$

as a function of the distance, r, from the notch tip, the curve is almost constant (Fig. B-3). However, for small r ($r<0.2$ mm) the FEM could not reflect the stress singularity properly, and the K_{II} dropped. Extrapolation of the almost horizontal part provides K_{IIC} at given peak load values.

In the case of Mizunami sample T4-1a $K_{IIC} \approx 3.6$ MPa $m^{1/2}$ as calculated by the stress approach.

This procedure is however very time consuming and not reproducible with the used code as the direction of appropriate 'square root' stress drop is very much depending on the mesh generated.

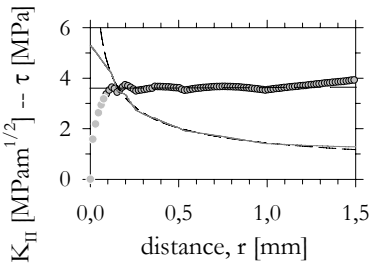

Fig. B-3. K_{II} and τ vs. distance from the notch tip. K_{II} is calculated from the shear stress in the region of the notch tip along a trace that shows an almost 'square root' stress shape at applied peak load conditions. K_{II} remains almost constant until 0.2 mm from the tip and then shows erratic behaviour due to the incapability of the code to handle stress singularities. A regression to the almost constant part yields $K_{IIC} \approx 3.6$ MPa $m^{1/2}$. [T4-1a]. Dashed black line: τ as calculated from $K_{IIC} = 3.6$ MPa $m^{1/2}$; grey solid line: τ as given by the FE modelling.

Energy Approaches

Alternative approaches use energy considerations for estimation of K_{IIC}. Here the Energy Release Rate, G (c.f. Section 2.3), and the J-integral can be instanced. These are converted to K_{II} by

$$K_{II}^2 = G \cdot E' \text{, or} \quad \text{.....(B-9a)}$$

$$K_{II}^2 = J \cdot E' \quad \text{.....(B-9b)}$$

where E' is the effective Young's modulus in plane strain or plane stress case as defined in Section 2.3.

J-Integral

The J-integral, introduced by Rice (1968), estimates the energy release rate. In case of the PTS- test it becomes

$$J \approx \tfrac{1}{2}\Delta u \cdot \Delta\tau \quad \text{.....(B-10)}$$

where Δu is the adjusted shear displacement and Δτ the drop of average shear stress from peak to residual shear stress across the fracture faces. Δu and Δτ can be obtained from the post peak part of the shear stress vs. strain diagram (for details see e.g. Hakami, 1988).

The Energy Release Rate obtained from the J-integral from PTS-testing of limestone sample L 2-2 at P = 5 MPa is about $4 \cdot 10^4$ J/m², which gives $K_{IIC} \approx 3.0$ MPa $m^{1/2}$. The Mode II fracture toughness for limestone determined from back calculation stress gradient evaluation is about 3.3 MPa $m^{1/2}$. DET gives $K_{IIC} \approx 3.3$ MPa. For T4-1a the J-integral estimation is not reliably possible due to radial expansion that led to a lack of residual strength.

Results for G of various rocks (mainly granites) calculated from the J-integral reported by Hakami (op. cit.) and references quoted therein are in the same order of magnitude as for the PTS- test (~ 10^4 J/m²). However, at higher confining pressures in PTS- testing the stress drop after reaching the peak load, where the Mode II fracture is readily established, is very moderate and not accurately determinable; this is presumably due to the tubular geometry of the test sample. Using these low values for Δu and Δτ consequently results in very low G_{IIC}. This is unlikely, as the shear stress necessary to introduce the Mode II fracture increases with increasing confining pressure. The J-integral cannot be reliably solved for the PTS- test, yet.

Energy Release Rate

Determination of the Energy Release Rate, G, estimates the total energy of the system and calculates from this the energy required for fracture formation and propagation. The Energy Release Rate, G, can be estimated by

$$G = d(W - U_C)\frac{1}{dA} \quad \text{.....(B-11a)}$$

where W is the work done by external forces, i.e. axial force, F, U_C is the elastic strain energy released by the introduction of the crack and A is the crack area. With

$$d(W) = F \cdot d(\delta) \text{ and } \text{.....(B-11b)}$$

$$d(U_C) = d(\tfrac{1}{2}F\delta), \text{.....(B-11c)}$$

where δ is the measured axial displacement, equation B-11a becomes

$$G = \frac{1}{d(A)}\left[Fd(\delta) - d\left(\tfrac{1}{2}F\delta\right)\right] \text{..... (B-11d)}$$

Partial derivation yields

$$G = \frac{1}{d(A)}\left\{\begin{matrix} Fd(\delta) - \\ \tfrac{1}{2}\left[Fd(\delta) + \delta d(F)\right] \end{matrix}\right\}$$

$$= \frac{1}{d(A)}\left\{\tfrac{1}{2}Fd(\delta) - \tfrac{1}{2}\delta d(F)\right\} \text{..... (B-11e)}$$

The change in crack area, d(A), can be expressed as

$$d(A) = \pi \cdot ID \cdot d(a) \text{ ..... (B-11f)}$$

where ID is the diameter of the notches and a is the crack length, measured from the bottom notch tip. Hence,

$$G = \frac{1}{2\pi ID d(a)}\left\{\begin{matrix} Fd(\delta) \\ -\delta d(F) \end{matrix}\right\} \text{.. (B-11g)}$$

Introduction of the compliance, λ, which is defined as the displacement per unit load, i.e.

$$\lambda = \frac{\delta}{F} \text{ ..... (B-11h)}$$

into equation B-11g yields

$$G = \frac{1}{2\pi ID d(a)}\left\{Fd(F\lambda) - F\lambda d(F)\right\}$$

$$= \frac{1}{2\pi ID d(a)}\left\{\begin{matrix} F\left[Fd(\lambda) + \lambda d(F)\right] \\ -F\lambda d(F) \end{matrix}\right\}$$

$$= \frac{1}{2\pi ID d(a)}\left\{F^2 d(\lambda)\right\}$$

$$= \frac{1}{2\pi ID}F^2\frac{d(\lambda)}{d(a)} \text{ ..... (B-11i)}$$

Inserting equation B-11i into equation B-9a gives the formulation for the stress intensity factor

$$K = \sqrt{G \cdot E'}$$

$$= \sqrt{\frac{1}{2\pi ID} \cdot E' \cdot F^2 \cdot \frac{d(\lambda)}{d(a)}}$$

$$= F \cdot \sqrt{\frac{E'}{2\pi ID} \cdot \frac{d(\lambda)}{d(a)}} \text{ . ..... (B-11j)}$$

Except d(λ)/d(a) all input for equation B-11j is known.

Figure B-4.A shows force vs. displacement data as generated by a finite element modelling of the PTS geometry with different IP, i.e. with upper notch depth a = 5 mm and varying b. This set-up is not correct for solving d(λ) as IP is varied, which is not corresponding to a propagating fracture, but is instructive to understand the principle. Increasing ligament length, IP, results in an increase of stiffness, s (Fig. B-4.B). Hence, λ decreases with increase in IP, consequently the compliance increases with increasing total bottom notch length, c (Fig. B-4.C); c corresponds for a fracture that propagates through the full height of the sample to a in equation B-11j. d(λ) from this example is

$$d(\lambda) = 9.593 \cdot 10^{-10} - 4.692 \cdot 10^{-8} c + 3.080 \cdot 10^{-6} c^2$$

and its derivation with respect to c is

$$\frac{d(\lambda)}{d(c)} = 6.160 \cdot 10^{-6} c - 4.692 \cdot 10^{-8} \text{ ..... (B-12)}$$

The previously given example does not take into account the change of compliance due to the crack propagation, but due to change in prefabricated notch depth.

However, it is very complicated, perhaps hardly possible to determine the compliance of the PTS test – unlike the case of a Mode I loading where the fracture faces are out of contact in first approximation –, but from the data of the cyclic loading tests of Mizunami granite (c.f. Section 5.2.4)

the compliance was estimated after taking several assumptions.

Assumption 1. The main fracture as is relevant for compliance change is initiated at 100% of the maximum load.

Assumption 2. The fracture connects the notches at a force drop to 70% of the maximum force.

Assumption 3. Force drop and fracture growth are linearly related.

Assumption 4. The stiffness of the loading cycles is similar for different confining pressures.

The postulations partly account for the fact, that the position of the fracture tip is not measurable yet. In the light of above assumptions the data from the cyclic Mizunami testing prints in Figure B-4.B+C as grey squares. The change in compliance is described as a linear regression

$$d(\lambda) = 2.541 \cdot 10^{-9} + 3.223 \cdot 10^{-8} c$$

and its derivation with respect to c is

$$\frac{d(\lambda)}{d(c)} = 3.223 \cdot 10^{-8} \quad \text{..... (B-13)}$$

For the sample T4-1a the fracture toughness as calculated by the above introduced procedure is 5.5 MPa $m^{1/2}$.

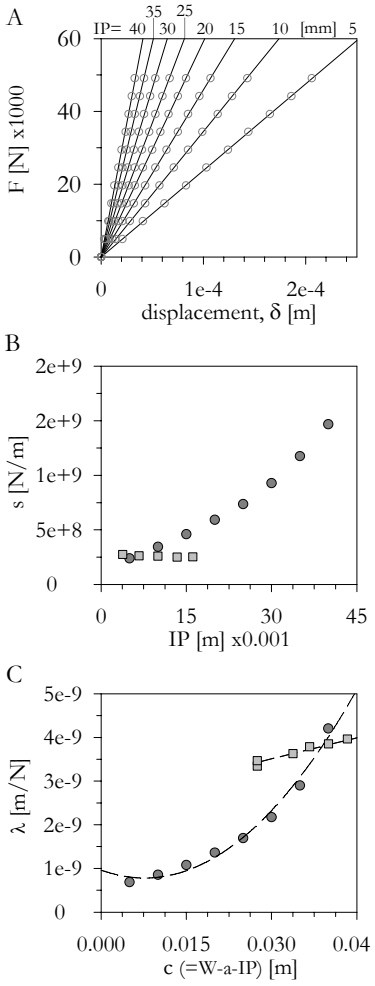

Fig. B-4. Derivation of the compliance calibration for the Energy Release Rate Approach. (A) Force, F, vs. displacement, δ, data as generated by a finite element modelling of the PTS geometry with different IP, i.e. with upper notch depth a = 5 mm and varying b. [E=50GPa, ν=0.37]. (B) Increasing ligament length, IP, results in an increase of stiffness, s. (C) λ, i.e. 1/s, decreases with increase in IP, consequently the compliance increases with increasing total bottom notch length, c. Cycles show results from FEM modelling of different IP, squares give results from analysis of data from cyclic loading of Mizunami granite. Refer to text for discussion.

The procedure does not take into account any lateral deformation (due to e.g. confining pressure) and related change in total energy. Furthermore, if the fracture tip position with respect to the force has been estimated incorrectly, the d(λ) may be lower, and hence is K_{IIC}.

The geometry is very complex, and consequently, the energy calculated by equations B-11a to B-11j is only a first approximation. Further development is needed, if this track shall be developed to an appropriate method to determine K_{IIC}. The most difficult task will be to calibrate the compliance correctly, if possible at all.

lowered. This apparently results in overestimation of K_{IIC} at low confining pressures, as the wing fractures are not considered in the back calculations. The influence of the macroscopic wing fracture on the stress distribution does not apply at confining pressures above 30 MPa, as those fractures are not initiated.

It was shown that the notch width has minor influence on the shear stress at failure, and Figure 5-28 indicated similar displacement gradients for the different notch widths.

Error

The input parameters for the determination of K_{IIC} are the geometrical dimensions, confining pressure and peak load. Confining pressure and peak stress can be directly measured with high accuracy in the course of an experiment; estimated error is less than 1 %. In general, the dimensions can be measured to an accuracy of better than 0.1 mm. The input parameters give errors of about 2%.

The error (relative) from the code is about 2%. This was determined on a series of runs with the same set-up and repeated generation of mesh and later calculations.

The absolute error of the code due to the above mentioned reasons cannot be determined satisfyingly yet.

The error from the extension of equation (5-7) to IP of 12 - 18 mm was estimated from a modelling for elastic parameters of Mizunami granite to be less than 10 %.

Conclusion

The different methods applied to evaluation of K_{IIC}, which are based on very different principles, give very similar results. Nevertheless, the DET is not conclusively developed. It is suggested to develop the calculation method along the lines of the energy approaches as outlined in the *BOX: EVALUATION*. This might more accurately consider the formation of the process zone and related non linear elastic behaviour.

5.3.4 Fractography

The fracture pattern as observed on sample scale at zero to low confining pressures usually consists of a wing fracture at the bottom notch, a doughnut fracture at the top notch, that might also be suggested to be a wing fracture, and the fracture developing at peak load that connects the top and bottom notch. Sometimes a horizontal fracture is initiated at low P at the mantle surface approximately in the middle of the intact portion. The principle development in space and time is confirmed by AE recording. Bulk fracture content from experiment was confirmed by Yoon & Jeon (2003) for Daejeon granite.

The wing fractures at bottom and top notch are introduced at low confining pressures by the shear loading of the notches in the dilatational quadrant of the stress field. In agreement with the principles of the sliding crack model (case with zero friction) they are Mode I wing fractures. The barrelling of the sample (i.e. bending of the notches), introduced by application of confining pressure, introduces compression to the notch tips, where the wing fractures develop. Both the major and minor principal stress are compressive at the respective notch tip if a confining pressure is applied (Fig. 5-7). The axial loading introduces high tensile stresses at the inner bottom notch tip (Fig. 5-8).

The wing fractures developing in the sample propagate out of the zone of high shear stress (or shear deformation) and stop. Hence, very few strain energy is released and no stress drop is seen in the stress-displacement plot (Bažant & Pfeiffer, 1986; Stephansson et al., 2001).

Application of confining pressure superimposes a negative K_I and this results in shorter wing fractures that stop before being aligned with the major principle stress. No wing fractures are initiated at the notches in samples subjected to confining pressures > 30 MPa. According to Melin (1986) pure macroscopic shear fracture growth occurs, if the level of confining pressure is high enough that all tensile stresses at the fracture tips vanish or even become compressive. The stresses at the bottom notch in PTS- testing at higher confining pressures are consequently below a critical level to allow macroscopic wing fracture initiation.

That Mode I fracturing is suppressed above a certain level of confining pressure was experimentally proven by Bobet & Einstein (1998) and is consistent with this study.

The horizontal fracture in the middle of the rock bridge is most likely initiated due to the barrelling of the sample. The confining pressure is applied to the mantle surface and because of the notches bending stresses are induced. As the confining pressure acts on the outer top surface also, in case of running the experiment in the pressure vessel that is, elevated confining pressure increases friction of the sample on the bottom surface and hence limits the bending. Above a confining pressure of approximately 20 MPa the initiation of this kind of fractures is omitted.

The fracture connecting the notches always starts at the bottom notch where the highest local shear stresses act. It generally shows a 'S'-like path. Yoon & Jeon (2003) could confirm this from particle flow model simulations.

5.3.5 Influence of confining pressure on the fracture pattern of Carrara marble

The crack orientations and density distributions were analysed for the Carrara marble only, as the rock type is (almost) monomineralic, relative homogeneous and has a convenient grain size suitable for microscopy.

Macro Scale

The inclination angle of the macroscopic main fracture increases with increasing confining pressure in Carrara marble (Fig. 5-25). Analogue to the shear stress data, the rotation/increase is large for increase of confining pressure from 5 to 30 MPa and then shows a slight increase only. At low confining pressure, P, the difference of P and axial peak load, σ_A, is ~ 112 MPa, while at high P (30 MPa and 50 MPa), σ_A-P is ~ 178 MPa and 179 MPa, respectively.

The lack of a vertical main fracture connecting the notches at high confining pressure is thought to be ruled by the confinement. The stress applied perpendicular to the shear plane increasingly suppresses sliding and the stored energy at peak stress is not sufficient to propagate the fractures all way long. Note that all tests were immediately stopped on reaching the peak load. The bottom fracture opening observed in the sample deformed at P = 5 MPa is provided by the displacement of the vertical fracture (Fig. 5-24) and the displacement induced by the dispersion of the matrix. Hence, the portion of the prolongated fracture towards the centre of the specimen is not opened. The dispersion is most likely providing the opening of the bottom fracture in the sample deformed at P = 30 MPa.

Micro Scale

On microscopic scale new features show up: asymmetry of the process zone, change of inclination angle of microcracks, and variation of width of the process zone with confining pressure.

Following Vermilye & Scholz (1999) the asymmetric distribution of microcracks with respect to the main fracture (Fig. 5-25.C) can be referred to as a Mode II signature. It closely corresponds to the asymmetry in the stress field (c.f. Section 2.2 and Section 7.3). Figure 5-26.B shows the major principal stress distribution at the tip of a shear fracture as proposed by Scholz et al. (1993) compared to the PTS microcrack signature in the process zone.

The development of the process zone is governed by the stress concentration of the main fracture, which is compressive in the region of sub-parallel microcracks, and dilatational in the part of the process zone, where en échelon cracks are formed (Fig. 5-26.B).

Initially, at the bottom notch tip cracks inclined (~ 30°) to the notch plane direction develop at peak load (Fig. 5-21). If the fracturing process forming the main fracture and FPZ was as proposed by e.g. Bažant & Pfeiffer (1986), the readily developed shear fracture should consist of these inclined cracks and a main fracture connecting these cracks by crushing of the struts (c.f. Section 2.4.1). Hence, the fracturing process must be different.

The angle of inclined fractures in the dilatational quadrant decreases for increasing P to become almost constant for P = 30-50 MPa. Increasing confining pressure increases the stiffness of the main fracture, hence increases friction. Increasing coefficient of friction was shown to decrease the inclination angle of wing fractures considerably along with a decrease of curvature or the wing crack (e.g. Shen et al., 1995; Wong & Chau, 1998; Wong et al., 2001). Hence, the inclined fractures are suggested to be wing cracks, i.e. Mode I cracks.

The mode of sub-parallel cracks in the process zone cannot be judged upon conclusively. The stress field as presented in Figure 5-26 can only give vague indication of the mode of fracturing for the individual crack regimes. A first comparison of FE stress field and crack orientation in the vicinity of the main fracture suggests emphasis on mixed mode fracturing.

Away from the crack tip magnitude and orientation of stresses decrease and change, respectively. Unfortunately, it is not known at what stage of main fracture propagation the cracks are initiated. Depending on the distance between the main fracture tip – assuming we are able to define it – and the crack initiation locus, the stresses are very different and hence is the mode of cracking. Thus, the comparison of stress field and fracture pattern cannot give a conclusive answer to the question of mode of cracking on the microscale. Nevertheless, the cracks in the compressional quadrant are always sub-parallel to the main fracture; hence any change in stress distribution does not substantially change their orientation. Hence, if a rotation of the stress field is induced by the confining pressure, the sub-parallel cracks change mode to maintain orientation.

Furthermore, a crack propagating in the granular structure of the rock does not necessarily

follow the direction a crack would propagate in homogeneous and isotropic media. As the cracks in the FPZ predominately follow the direction of grain boundaries and cleavage planes (c.f. Fig. 5-21), locally mixed mode fracturing is presumably introduced anyway.

Polarity analysis of AE recordings in PTS experiments showed contribution of both tensile and shear events to the fracturing process at P = 30 MPa (Stanchits et al., 2003). At small fractions of maximum axial load, tensile events dominate, corresponding to formation of the initial process zones. At loads close to failure a shift to shear dominated fracturing is observed. The observation from the polarity analysis suggests that mixed mode cracking is evident in the PTS-fracturing process.

The main fracture predominantly propagates intragranularly. It seems not to be formed by interaction of the local tensile stress fields of single Mode I microcracks, since no 'zig-zag'-type coalescence occurs, which is typical for connection of shear loaded pre-existing cracks by wing cracks.

The width of the FPZ was shown to decrease with increase of confining pressure (Fig. 5-25.B) in the PTS- samples to become almost constant about P ≥ 30 MPa. Same result was reported for thickness of shear bands on triaxial compression tests on Fontainebleau sandstone (El Bied et al., 2002). The thickness of the shear bands decreased non-linearly from about 1.2 mm at ambient conditions to 0.6 mm at a confining pressure of 42 MPa, approaching almost constant thickness above 28 MPa. To some extend the decreasing width of the FPZ can be explained by the rotation of the inclined cracks. Additionally, the sub-parallel cracks are suppressed by presumably the increased confining pressure.

The fracture content of the examined samples is not the same, i.e. the fractures have propagated to different length. Especially in the case where the fracture has connected top and bottom notch, i.e. P = 5 MPa, additional post-connective cracking due to sliding of the fracture faces might have induced additional damage to the FPZ. From the microstructural observation only small shear displacements could be detected (Fig. 5-24). Furthermore, the fracture faces show minor indication of grain crushing or grain rotation. Hence, no influence of the different fracture propagation length on the FPZ characteristics as measured here is considered.

5.3.6 Confining pressure

The test results indicate a bi-linear relationship between the average shear stress at failure and, hence, Mode II fracture toughness, and the confining pressure (Fig. 5-15 and 5-16). Studies on the influence of confining pressure on the shear strength of rock show a similar behaviour (e.g. Lundborg, 1968), but low slope behaviour for the shear strength is reached at confining pressures about 15-20 times higher compared to the PTS- data.

At low confining pressure, P, the increase of stress as function of P may be approximated by a linear regression with large slope, while at high P the slope of linear regression is shallow. Alternatively, one might consider an exponential rise to a maximum value. However, that would imply constant fracture toughness at very high P and no frictional influence.

The change in slope in the axial stress, shear stress and fracture toughness vs. confining pressure plot indicates a change in mechanism. Domination of time dependent mechanisms can in general be excluded, as the variation of loading rate showed neglecting effects. As the transitional pressure is very similar for very different rock types, also change of dominant mechanism by means of mineralogy, e.g. change from cracking to sliding in calcite, is most unlikely.

Kemeny (1993) reports from triaxial laboratory testing of a tuff the same principle shape of axial stress vs. confining pressure data (Fig. 5-30). Transition from steep to shallow slope was at P = 15 MPa for that rock type. Transition from macroscopic axial splitting to faulting was at about P = 10 MPa. He performed a numerical modelling that was based on the sliding crack model (Kemeny & Cook, 1987). The set-up included N = 2500 cracks and each microcrack was specified by its orientation (random), initial length, cohesion and coefficient of friction. The modelling results yielded the same strength envelope as the laboratory data. From analysis of active cracks in the model, it was shown that with increase in confinement the number of active tensile cracks first increases to produce a peak of activity and then drops considerably. At low

confining pressure no shear cracks grow during the entire loading process. At about P = 5-15 MPa the number of active shear cracks considerably increases and then remains constant for higher P. The activation of the shearing mode coincides with the change in slope of the strength envelope. It is concluded that the change in slopes agrees with the transition from tensile to shear dominated fracturing. The explanation by Kemeny (op. cit.) is suggested to be applicable to the results from PTS- testing.

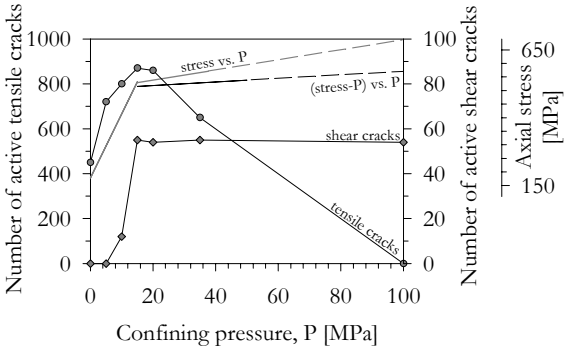

Fig. 5-30. Compilation of data from Kemeny (1993). Grey solid line indicates strength envelope (axial stress, σ, vs. confining pressure, P); black solid line indicates (σ-P) vs. P. Dashed lines indicate extrapolation. Circles: active tensile cracks; diamonds: active shear cracks. Refer to text for discussion.

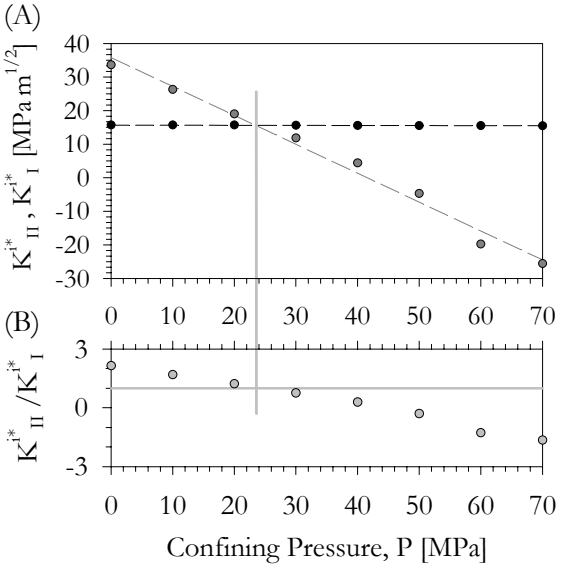

Fig. 5-31. Influence of confining pressure, P, on the magnitude of Mode I and Mode II stress intensity factor at given axial loading, σ_A, of 400 MPa. (A) While K^{i*}_{II} (black circles) remains almost constant with increase in P, K^{i*}_{I} (grey circles) considerably decreases. At about P ≈ 25 MPa the ratio of K^{i*}_{II} and K^{i*}_{I} drops below unity (B).

With increasing confining pressure, existing cracks are closed and a further opening of these cracks is suppressed. This is supported by the vanishing wing and doughnut fracture. Furthermore, the radial fractures developing at lower confining pressures seem to be introduced by radial expansion (c.f. Section 5.2.5) as the inner cylinder is punched down. If radial expansion leading to extensional fractures is apparent, an opening mode is involved in the generation of the main fracture between the two notches. Hence, mixed mode is most probably evident. The higher the confining pressure, the more the radial expansion and resulting radial fracturing frequently is suppressed.

Analogue to the procedure to determine K_{II} as presented in Section 5.1, K_I was estimated at the bottom notch from the displacements in lateral (v-) direction using the Displacement Extrapolation Technique. Figure 5-31 displays the influence of confining pressure, P, on the magnitude of Mode I and Mode II stress intensity factor at given axial loading. While K^{i*}_{II} remains almost constant with increase in P, K^{i*}_{I} considerably decreases. At about P ≈ 25 MPa the ratio of K^{i*}_{II} and K^{i*}_{I} drops below unity (Fig. 5-31.B), may be correlated to the change of slope in the experimental K_{IIC} vs. P data.

The slopes of regression as obtained from the shear stress, τ_{av}, versus confining pressure data might be considered as indicative of the internal friction angle. The corresponding values are given in Figure 5-15. Table 5-4 summarises friction data from literature. The slopes from Figure 5-15 on data at low P (0 < P < 30 MPa) is in general much larger than the data presented in Table 5-4, while the slopes for large P (P < 30 MPa) are lower than the data compiled. This is very prominent for e.g. Mizunami granite, as a coefficient of friction of 1.66 is reported for that rock type (JNC, 2003), while data from Figure 5-15 yields 2.89 and 0.61. For direct comparison in case of Carrara marble confer to Figure 5-32. The classical coefficient of friction concept in terms of the Mohr envelop is not applicable to the PTS- data. This was already suggested by the data as cited above from Lundborg (1968). Most likely the boundary conditions of the PTS- test have some influence the frictional behaviour.

Microstructurally the measured fracture characteristics tend to show the similar behaviour as the stress data, i.e. the width of the process zone does not change significantly from P = 30 – 50 MPa and the en échelon angle as well as the main fracture inclination do not considerably vary above P = 30 MPa. This was discussed in Section 5.3.5. Furthermore, at P = 30 – 70 MPa K_{IIC} does not change significantly.

Rock	μ [ ]	Φ [°]	Reference
Diorite			
Äspö drt	*0.97*	44	Nordlund et al., 1999
Äspö drt	*1.15*	49	Rinne et al. 2003
Granite			
	1.0-1.8	45-60	Farmer, 1968
Bohuslän grn	2.0	*63*	Lundborg, 1968
Inada grn	*1.11*	48	Goodman, 1980
Mizunami grn	*1.66*	59	JNC, 2003
Rixö grn	1.8	*61*	Lundborg, 1968
Stone Mountain grn	*1.23*	51	Goodman, 1980
Marble			
	0.7-1.2	35-50	Farmer, 1968
Georgia mbl	*0.47*	25	Goodman, 1980
Tenessee mbl	0.39	*21*	Albert & Rudnicki, 2001
Yuen Long mbl	0.7	*35*	Wong et al., 1996
Sandstone			
	0.7-1.2	35-50	Farmer, 1968
Bartlesville sst	*0.75*	37	Goodman, 1980
Berea sst	*0.53*	28	Goodman, 1980
Gothland sst	0.7	*35*	Lundborg, 1968
Pottsville sst	*1.00*	45	Goodman, 1980
Limestone			
	0.7-1.2	35-50	Farmer, 1968
Borghamn lst	1.0	*45*	Lundborg, 1968
Indiana lst	*0.90*	42	Goodman, 1980
Johnstone†	*0.58*	30	Lim et al., 1994
Wolf Camp lst	*0.70*	35	Goodman, 1980

Tab. 5-4. Compilation of friction data from literature. Values given in *italics* are calculated from the reported data. † synthesised mudstone.

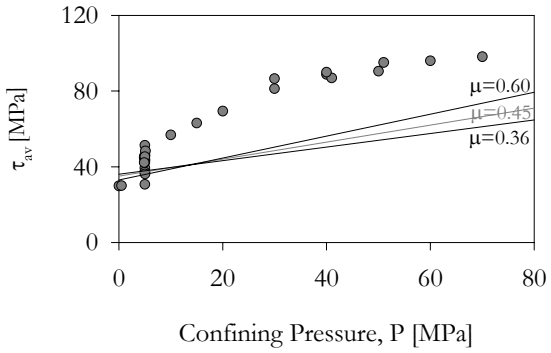

Fig. 5-32. Average shear stress at failure, τ_{av}, vs. confining pressure, P, for Carrara marble and linear Mohr envelope for different friction coefficients. The cohesion was estimated from the UCS (uniaxial compressive strength) using the corresponding coefficient of friction; c (μ=0.36) = 36 MPa, c (0.45) = 35 MPa and c (0.60) = 33 MPa.

Constant microstructural appearance/ content might be considered to be indicative of constant created fracture/crack surface. Therefore, constant energy requirement for macroscopic fracture growth can be considered. This is in consistency with the observation of only slight increase of K_{IIC} above P > 30 MPa which may be dedicated to friction.

It is suggested that the shift in mechanism as indicated in the mechanical data is caused by a change in dominant mode of fracturing. The increasing confining pressure increasingly suppresses the tensile mode. At high P, Mode II may be dominant.

It seems most relevant to define the fracture toughness in Mode II for high confining pressure and not at low confinement only. At confining pressures higher than 30 MPa, average K_{IIC} values were obtained for the tested rock types as presented in Table 5-3.

6 COMPARISON OF RESULTS OF MODE I AND MODE II LOADING AND CORRELATION ANALYSES

Fracture toughness has been shown to correlate with various physico-mechanical parameters like Young's modulus, uniaxial compressive and tensile strength, porosity, dry density, grain size and some others (e.g. Whittaker et al., 1992). Correlations for the K_{IC} and K_{IIC} values obtained in this work are presented in the next sections. Finally, the experimental results and correlation analyses for the two modes are compared and discussed.

6.1 Mode I fracture toughness correlation analyses

Figure 6-1 shows the relationship between Mode I fracture toughness at ambient conditions, K_{IC}, and physico-mechanical parameters, i.e. Young's modulus, uniaxial compressive and tensile strength, porosity, dry density, and maximum as well as average grain diameter.

It is obtained that higher *Young's modulus* results in higher K_{IC}. A linear fit trough the origin is plotted (Fig. 6-1.A). Whittaker et al. (1992) give a regression as obtained from a variety of rock types that yields a lower slope and shows positive axis intercept.

Uniaxial compressive strength also positively correlates with K_{IC} (Fig. 6-1.B). The regression from the data compilation by Bearman (1999) and Whittaker et al. (1992) again shows a shallower slope than the data obtained in this study.

Tensile strength as obtained from Brazilian tests shows a positive correlation with Mode I fracture toughness, too (Fig. 6-1.C). The regression data presented in this thesis deviates from data given by Bearman (1999), Whittaker et al. (1992) and Zhang (2002).

Bearman's (op. cit.) data includes twelve different rock types of various lithology. Whittaker et al. (op. cit.) did their analysis for various rock types, not specified and collected from a variety of sources. Zhang's regression for tensile strength is based on more than 50 different rocks, i.e. basalts, coals, dolostones, gabbros, granites, limestones, marbles, sandstones, oil shales, siltstones, syenites and tuff. K_{IC} determination was carried out by mainly the Short Rod and Chevron Bend methods. Regressions given by Whittaker et al. (op. cit.) give non-zero K_{IC} for zero tensile and uniaxial compressive strength. If a material is not able to carry any load, it is not clear why it should show resistance to crack propagation. Hence, the regression ought to pass origin.

In general, higher *porosity* results in lower Mode I fracture toughness for the dataset of this study. Alber & Brardt (2003) state that porosity does not correlate with K_{IC}, but indicate an exponential correlation between *dry density* and fracture toughness (Figs. 6-1.D+E). However, their density data can be represented by a linear regression similar to that by Brown & Reddish (1997), if one discounts the single data point of Ytong in their dataset. Ytong has a very high porosity (77.7 %, Alber & Brardt, 2003) and thus it should be discussed, if it is a good representative of rock. However, the data obtained in this study could as part of a larger dataset be represented by Brown & Reddish's as well as Alber & Brardt's regressions.

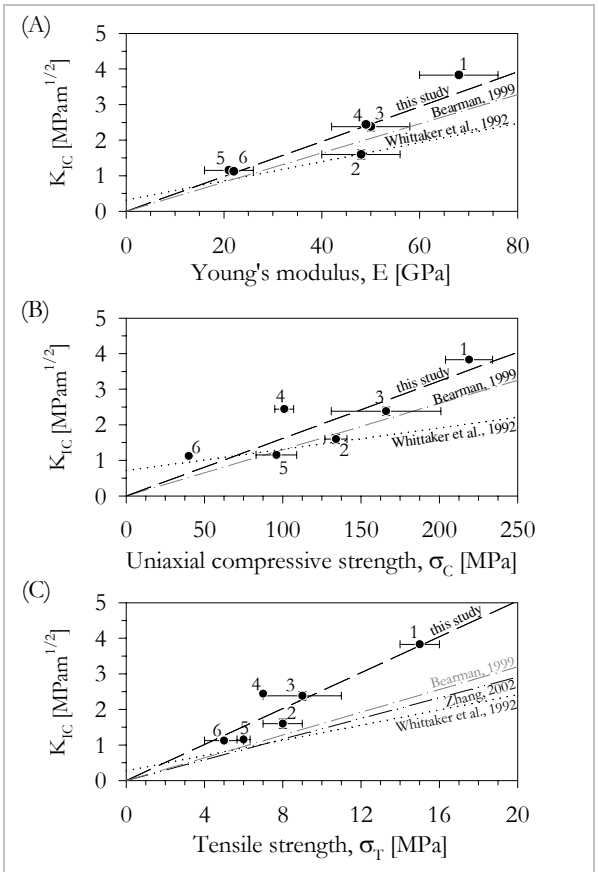

Fig. 6-1. Correlation analysis of different physico-mechanical parameters and K_{IC}. [1] Äspö diorite, [2] Aue granite, [3] Mizunami granite, [4] Carrara marble, [5] Flechtingen sandstone, [6] Rüdersdorf limestone. Dotted and dashed-dotted lines indicated regression to data from Huang & Wang (1985), Meredith (1989), Whittaker et al. (1992), Brown & Reddish (1997), Bearman (1999), Zhang (2002) and Alber & Brardt (2003), respectively. Dashed and solid lines are regressions to the presented data (linear fit through origin for E, σ_C and σ_T). [$K_{IC} = 0.05\ E$; $K_{IC} = 0.02\ \sigma_C$; $K_{IC} = 0.25\ \sigma_T$, $K_{IC} = 2.19\ gd_{av} + 0.91$; $K_{IC} = 0.82\ gd_{max} + 0.91$].

Continued next column.

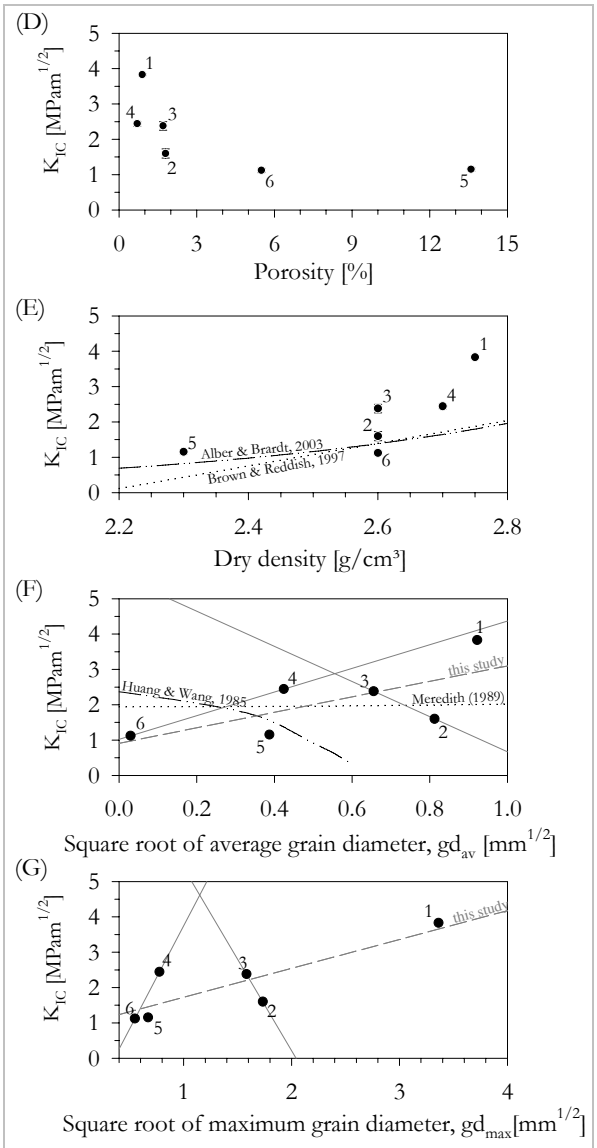

Fig. 6-1. *Continued.*

Larger average and maximum *grain diameter* of the rocks tested result in general in higher fracture toughness values if one ignores that the rocks are of different mineralogy (Figs. 6-1.F+G). This is illustrated by the dashed grey line. However, arranging the data by mineralogy/rock type the picture is more erratic. Regression to Carrara marble and Rüdersdorf limestone data yields positive slope of regression while the two granites show a negative correlation.

Huang & Wang (1985) could show for basalt and syenite samples a negative linear correlation of fracture toughness with increasing grain size. Meredith (1989), however, showed the opposite for granitic rocks. Their regressions are recalculated to square root of average grain diameter and plotted in Figure 6-1.F+G.

6.2 Mode II fracture toughness correlation analyses

The influence of physico-mechanical parameters on K_{IIC} as obtained for the rock types in this study is shown in Figure 6-2. Differentiation is made between K^0_{IIC}, i.e. at zero confining pressure, and K^∞_{IIC}, i.e. at high confining pressure (P ≈ 30-70 MPa).

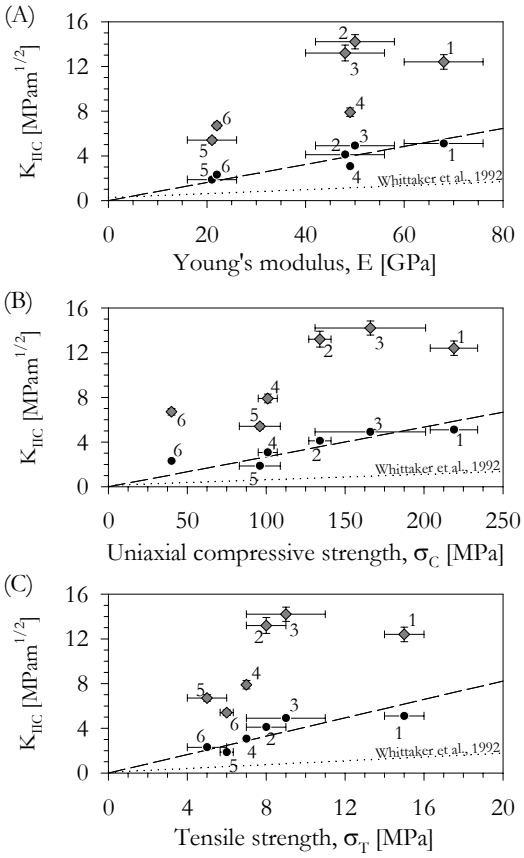

Fig. 6-2. Correlation analysis of different physico-mechanical parameters and K_{IIC}. Black circles indicate K^0_{IIC}; grey diamonds refer to K^∞_{IIC}. [1] Äspö diorite, [2] Aue granite, [3] Mizunami granite, [4] Carrara marble, [5] Flechtingen sandstone, [6] Rüdersdorf limestone. Dotted lines indicated linear regressions as observed by Whittaker et al. (1992). Dashed lines are regressions to the presented data (linear fit through origin for E, σ_C and σ_T). [$K^0_{IIC} = 0.08$ E; $K^0_{IIC} = 0.03\ \sigma_C$; $K^0_{IIC} = 0.41\ \sigma_T$; $K^0_{IIC} = 3.49\ gd_{av} + 1.68$; $K^0_{IIC} = 1.08\ gd_{max} + 2.00$].

Continued next column.

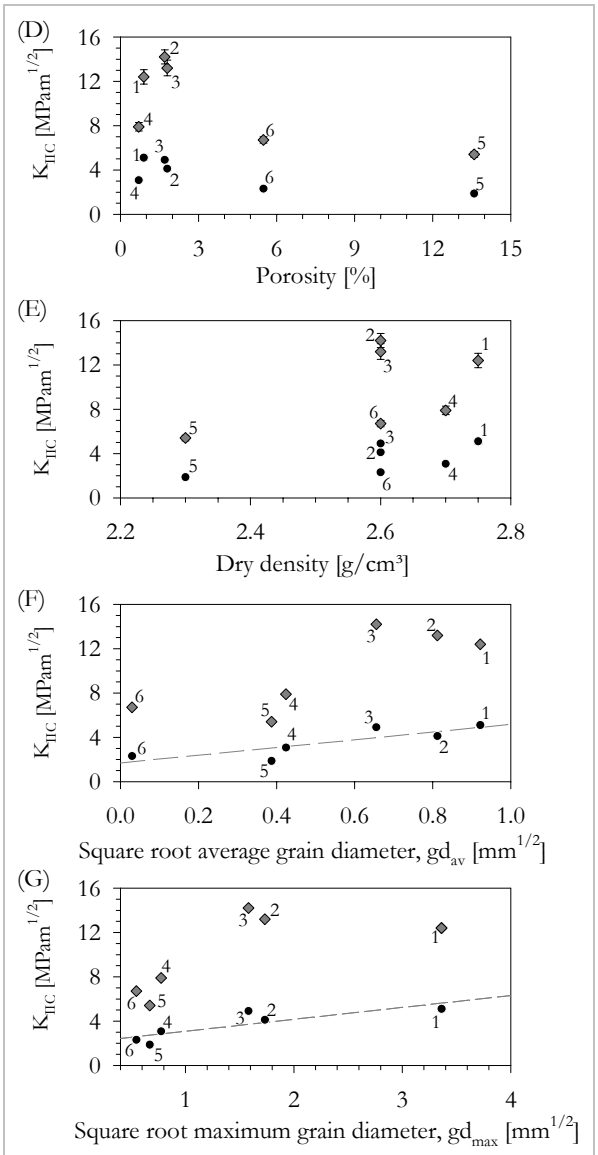

Fig. 6-2. *Continued.*

K^0_{IIC} shows (like K_{IC}) fair to good linear correlation for all parameters and weak correlation to porosity and dry density. K^∞_{IIC} fails to show good correlation with Young's modulus, uniaxial compressive strength and tensile strength.

Linear regressions as given by Whittaker et al. (op.cit.) for *Young's modulus*, *uniaxial compressive strength* and *tensile strength* are indicated (Figs. 6-2.A-C). They all show a less steep slope than the regressions to the K^0_{IIC} data obtained in this study.

The regression by Whittaker et al. (op. cit.) for K_{IIC} vs. tensile strength always gives smaller values than regression to K_{IC} vs. tensile strength data, hence, $K_{IC} > K_{IIC}$. This is inconsistent with most experimental results of rocks showing that K_{IIC} is usually larger than K_{IC} (see Section 2.5.4 also).

For influence of *porosity* and *dry density* on Mode II fracture toughness no references in literature are available. For the data obtained in this study weak correlation for K^0_{IIC} and porosity and dry density exist (Figs. 6-2.D+E). But for K^∞_{IIC} no persuasive correlation is evident. Correlation of square root of average and maximum *grain diameter* to both Mode II fracture toughness at zero and elevated confining pressure is indicated in Figures 6-2.F+G. Again, the physical implication of the regressions is doubtful

due to combined treatment of rocks of different mineralogical composition.

6.3 Comparison of the response of rock to the applied modes of loading

In Chapters 4 and 5 and in the previous sections results and correlations for fracturing subject to both Mode I and Mode II loading have been presented. In this section selected observations are compared to each other (Fig. 6-3).

(A) It was shown from experiment that the fracture toughness for both modes of loading remains constant for a broad range (five to six orders of magnitude) of loading rates (Fig. 6-3.A).

(B) The influence of confining pressure on Mode I fracture toughness was studied by several researchers, e.g. Winter (1983), Al-Shayea et al. (2000) (see Section 2.5.3). A linear increase of K_{IC} with increase of confining pressure is reported (Fig. 6-3.B). Contrarily, K_{IIC} increases bi-linearly with increasing confining pressure and shows a shallow slope at elevated P. Rao (1999) and Al-Shayea et al. (2000) presented in studies on granite, marble, limestone and sandstone a linear increase of K_{IIC} with confining pressures of 0.1-20 MPa and 0.1-28 MPa, respectively. This is in reasonable agreement with data presented in this study at low confining pressures.

Mode I fracture toughness was found to linearly increase with confining pressure. As K_{IIC} shows a bi-linear behaviour when subjected to confining pressure, this has major impact on the ratio of Mode I and Mode II fracture toughness with increase of confining pressure. The ratio of the fracture toughnesses (K_{IIC}/K_{IC}), denoted χ, produces a maximum at low P and drops for further increase of confining pressure (Fig. 6-4).

(C) The correlation analyses showed linear relationship between K_{IC} and Young's modulus, uniaxial compressive strength and tensile strength. The slopes of the regressions are given in the corresponding figure caption. Same analysis for K^0_{IIC} yields almost the same slope of regression. K^∞_{IIC} does not convincingly correlate to these parameters.

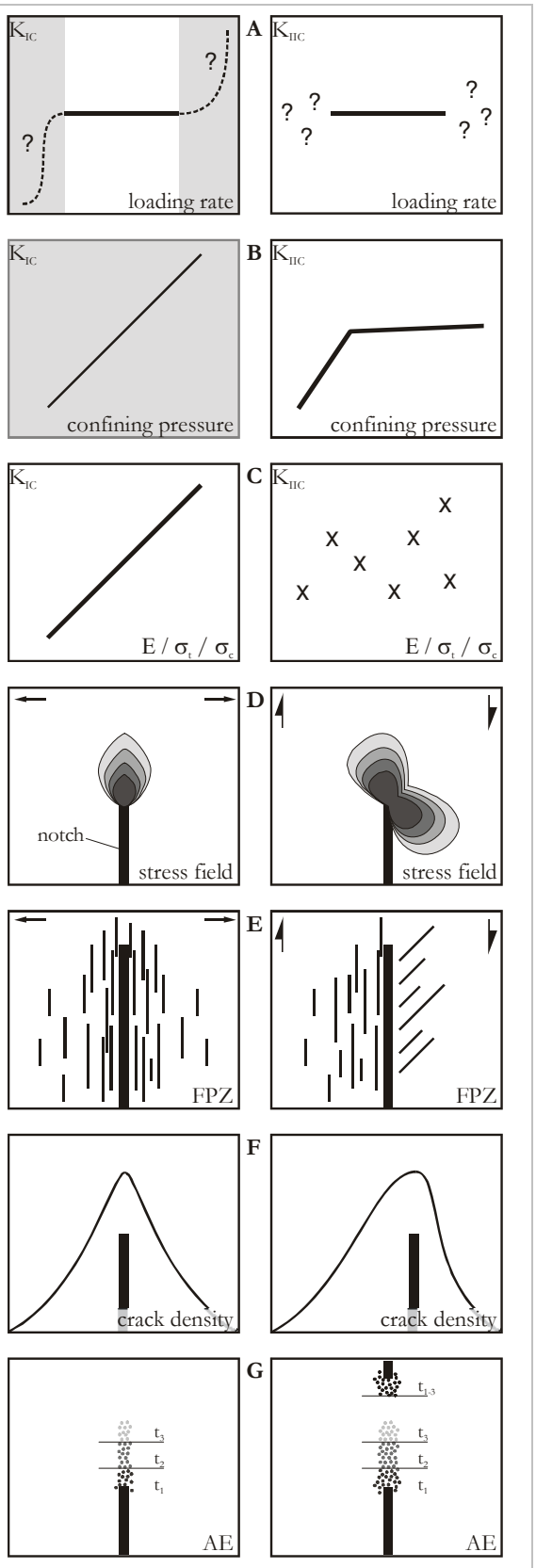

Fig. 6-3. Comparison of Mode I and Mode II fracturing. Depicted are influence of (A) loading rate, (B) confining pressure, (C) Young's modulus/tensile strength/uniaxial compressive strength, (D) σ_1 stress field, (E) fracture process zone (FPZ), (F) crack density and (G) AE locations. Areas highlighted grey are data from literature; Loading rate: Atkinson (1984), confining pressure: Winter (1983).

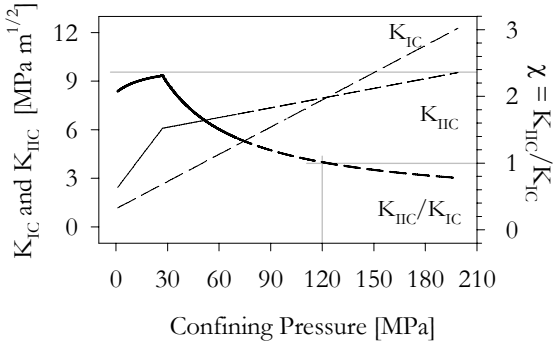

Fig. 6-4: K_{IC}, K_{IIC} and the ratio $\chi = K_{IIC}/K_{IC}$ vs. confining pressure, P, exemplarily for limestone. Assume $K_{IC} = K^0_{IC} + 0.05 \cdot P$ for the increase of Mode I fracture toughness with increase of confining pressure, as shown by Winter (1983) for Ruhr sandstone up to P = 100 MPa, extension of the linear trend for K_{IC} up to higher confining pressures, and low slope increase of K_{IIC} above the tested range of confining pressures. Dashed lines indicate assumed data. χ produces a maximum at a confining pressure of about 10-20 MPa, unity is reached at P ≈ 120 MPa.

(D-F) The stress field of Mode I loading is symmetrical, while that of Mode II loading is unsymmetrical (Fig. 6-3.D). This is reflected by the fracture process zones geometry and by the shape of the crack density plots (Fig. 6-3.E+F), this at least for Carrara marble. Asymmetric shape of FPZ of faults is reported by Vermilye & Scholz (1999) and Moore & Lockner (1995). It was qualitatively shown that the fracture propagating under Mode II loading creates more fractures and hence more fracture surface. For marble in Mode I no FPZ could be resolved at magnifications of up to 1 000 in SEM, while in Mode II marble showed a wide process zone in optical microscopy.

(G) Location analysis of AE events shows formation of a process zone prior to fracture propagation for both modes of loading. The Mode II FPZ as measured by AE is not as localised, i.e. longer and wider, around the notch tip as for Mode I (Fig. 6-3.G). Recording of AE under Mode I loading of Mizunami granite yielded ~ 4800 signals, while under Mode II loading conditions at elevated confining pressure (P = 30 MPa) ~ 7200 signals were recorded; ratio of signals is 1.5.

Rock type	K^0_{IIC}/K_{IC}	K^∞_{IIC}/K_{IC}	K^∞_{IIC}/K^0_{IIC}
Äspö diorite	1.4	3.2	2.4
Aue granite	2.6	8.3	3.2
Mizunami granite	2.1	6.0	2.9
Carrara marble	1.3	3.2	2.6
Flechtingen sandstone	1.6	6.6	2.9
Rüdersdorf limestone	2.1	7.8	2.9

Tab. 6-1. Ratios of Mode I and Mode II fracture toughnesses for the six rock types tested in this study. $K^0_{IIC}/K_{IC} \approx 2$, and $K^\infty_{IIC}/K^0_{IIC} \approx 3$.

Ratios of K^0_{IIC} and K^∞_{IIC} to K_{IC} are given in Table 6-1. Comparing K_{IC} and K^0_{IIC} shows fracture toughness to be on average nearly twice as large as K_{IC}. This is in fair agreement with the ratios of 2 to 3 commonly referred in literature (c.f. Section 2.5.4). Ratio of $K^\infty_{IIC}/ K^0_{IIC}$ is about three.

6.4 Discussion

The comparison of results and correlation analysis from Mode I and Mode II testing yielded few similarities, but even more differences.

Tensile and uniaxial failure are both suggested to be generated by the coalescence of tensile microcracks (e.g. Kemeny, 1993), hence they should depend on K_{IC}. This is reflected by the obtained data (Figs. 6-1.B+C). Most interestingly, also K^0_{IIC} shows positive correlation to uniaxial compressive strength and tensile strength, σ_T. Slopes of regressions for K_{IC} and K^0_{IIC} vs. σ_T and σ_C are of comparable magnitude.

From Kemeny's (op. cit.) statement intuitively one would consent a correlation between Mode I fracture toughness and, in particular, tensile strength. But why is K^0_{IIC} correlated with σ_T? This gives evidence to the suspect that Mode I microcracking contributes considerably to fracture propagation under Mode II loading at zero to low confining pressure.

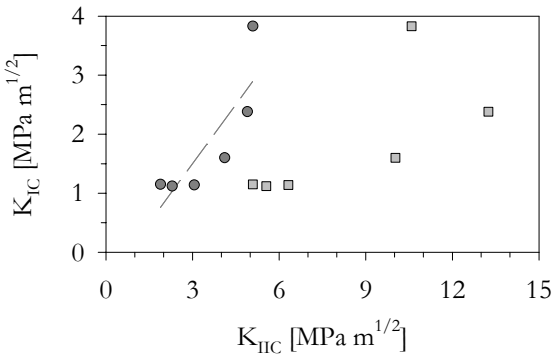

Fig. 6-5. Mode II vs. Mode I fracture toughness. Circles are for K^0_{IIC} at ambient pressure and squares are for K^∞_{IIC} at terminal confining pressure. Dashed line indicates correlation of K_{IC} and K^0_{IIC} at ambient conditions.

A commonly accepted hypothesis is that crack extension starts in the plane perpendicular to the direction of maximum tension (e.g. Erdogan & Sih, 1963, Horii & Nemat-Nasser, 1985). Consequently, fracture toughness, irrespective of mode, were controlled by tensile strength. This implies an inherent relationship between fracture toughness and tensile strength, i.e. $\sigma_T \sim K_{IC}$, $\sigma_T \sim K_{IIC}$ and, hence, $K_{IIC} \sim K_{IC}$. The first two proportionalities are proven to be valid for the data obtained in this study, as a linear relationship between K_{IC} and K^0_{IIC} versus σ_T applies. Furthermore, it can be shown that $K^0_{IIC} \sim K_{IC}$ (Fig. 6-5). It is concluded from these considerations that Mode I is the dominant, or at least effective, mode of microfracturing at low confining pressure in the PTS- test.

Contrarily, the Mode II fracture toughness at elevated confining pressure, K^∞_{IIC}, shows only a weak correlation with tensile strength. It is concluded that the relative contributions of mechanisms change and Mode I is not the dominant mode of fracturing at elevated confining pressure. As was shown that $\sigma_T \sim K_{IC}$, consequently K^∞_{IIC} should be proportional to shear strength. Unfortunately no data on shear strength from direct shear box testing was available or obtainable.

K_{IC} as well as K_{IIC} were shown to in general decrease with increase in porosity. With increase in porosity pore collapse and failure of slender columns between pores become more likely. In the case of very high porosity, e.g. some sandstones, only the small rock bridges (pillars) between the pores have to be fractured instead of forming a through-going fracture.

This is supported by the reported correlation between density and Mode I fracture toughness (e.g. Alber & Brardt, 2003; Brown & Reddish, 1997) and the interrelations shown in this chapter. Increase in porosity will commonly result in lower density. So, regressions of fracture toughness vs. density and porosity should show opposite sign of slope, which is also confirmed from the test data. For sure, the mineral composition, and therefore the densities of the individual minerals of the rocks are very different; hence large scatter is to be expected and is confirmed.

The physical implication of the correlation between fracture toughness and grain size needs further discussion. As observed in some studies, a decrease in grain size generally results in an increase in fracture toughness (e.g. Huang & Wang, 1985; Rice et al., 1981), whereas also the opposite was reported (Meredith, 1989). Further we know that the initial crack size is frequently related to grain size (e.g. Nur & Simmons, 1970; Lawn, 1993) and that fracture toughness, irrespective of mode, is proportional to square root of half crack length (Irwin, 1958). Consequently, an increase in grain size should result in higher local stress intensities for rock samples subjected to same loading with otherwise constant properties. As neither loading at failure nor properties are likely the same on determining K_{IC} for different rocks – even of comparable mineralogy – the explanatory power solely of above statements is limited. Mode I fracture growth is dependent on the yield strength as argued in the cohesion zone model. Assuming the yield strength to be proportional to the macroscopic tensile strength, the ratio η of Mode I fracture toughness, K_{IC}, and tensile strength, σ_T, might be more appropriate to examine the influence of grain size on fracturing. Figure 6-6 displays the influence of the square root of grain diameter on η, which remains constant.

Fredrich et al. (1990) have shown the yield stress, σ_Y, to be a function of the inverse of the square root of grain size, g. Hence, if

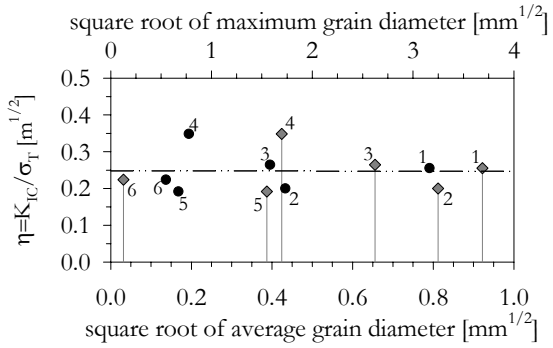

Fig. 6-6. Ratio of Mode I fracture toughness and tensile strength, η, as a function of square root of grain diameter, dg. η remains constant irrespective of dg. Grey diamonds indicate average grain diameter, black cycles designate maximum grain diameter. [1] Äspö diorite, [2] Aue granite, [3] Mizunami granite, [4] Carrara marble, [5] Flechtingen sandstone, [6] Rüdersdorf limestone.

$$\sigma_Y \sim \sigma_T, \text{ and} \tag{6-1}$$

$$\sigma_Y \sim \frac{1}{\sqrt{g}} \text{ then} \tag{6-2}$$

$$\sqrt{g} \sim \frac{K_I}{\sigma_Y} \sim \frac{K_I}{\sigma_T}. \tag{6-3}$$

Contrarily, it was shown (Fig. 6-6) that

$$\sqrt{g} \sim \frac{K_I}{\sigma_T} = \text{const}, \tag{6-4}$$

consequently, this suggests that the grain size as presented in Figures 6-1 and 6-2 is not physically correlated to fracture toughness. Hence, a correlation of grain size and fracture toughness for combined treatment of several rock types together is not sensible.

Conformity of results is evident for the dependency on loading rate. Both Mode I and Mode II fracture toughness show almost constant values for a broad range of loading rates indicating determination of the critical stress intensity factor.

The magnitudes of K_{IC}, K^0_{IIC} and K^∞_{IIC} indicate that the energy requirement for propagation of the fractures is different for the different modes and confining pressures. Assuming a ratio $\zeta = K^0_{IIC}/K_{IC}$ of two to three, as usually referred to in literature and was confirmed in this study, calculated G_{IIC} would be four to nine times G_{IC}. For a $\zeta = 6$, which is suggested by the obtained data to be relevant at high P for Mizunami granite, i.e. K^∞_{IIC}/K_{IC}, G_{IIC}/G_{IC} is 36. If the crack surface energy for any cracks is the same and independent of confining pressure, a fracture including FPZ would create four ($\zeta = 2$), nine ($\zeta = 3$), or 36 ($\zeta = 6$) times more fracture surface under Mode II than under Mode I conditions. It was qualitatively shown that the fracture propagating under Mode II loading creates more fractures and hence more fracture surfaces. In AE recording for Mizunami granite the number of recorded AE was about 1.5 times higher in Mode II (P = 30 MPa) than Mode I (P = 0.1 MPa) loading. Assuming that it is admissible to equalise radiated energy and number of AE signals in first approximation, this indicates a factor of roughly 1.5 between G_{IIC} and G_{IC}. This is considerably lower than the expected ratio of about 36. Assuming above considerations to be valid, this rough estimation indicates that many AE events are not detected/recorded, presumably due to the fixed amplitude trigger level and the resulting low amplitude cut-off.

The stress field, FPZ and crack density distribution show different symmetries for Mode I and Mode II induced fracturing. The Mode I normal stress field is symmetric with respect to the crack plane (c.f. Section 2.2). Same symmetry was shown for the fracture process zone and crack density distribution within the FPZ for Flechtingen sandstone from Mode I loading. The Mode II normal stress field was shown to be point symmetric. This compares well to the two regimes in the fracture process zone cracking and the asymmetric shape of the FPZ as described for Carrara marble from PTS- testing.

The variation of the Mode I and Mode II fracture toughnesses with confining pressure and the change of ratio χ was shown in Figure 6-4. Change of the relative magnitudes of the fracture toughnesses changes the likely mode of fracturing as confining pressure increases. Due to the different shapes of the fracture toughness vs. confining pressure plots, χ continuously decreases after reaching a maximum at ~ 20 MPa. At low χ it is more likely that fracturing predominantly takes place in Mode II rather than Mode I (Melin, 1986). χ drops below unity at P ≈ 120 MPa in the assumed scenario of Figure 6-4, therefore $K_{IIC} < K_{IC}$.

7 APPLICATION OF ROCK FRACTURE MECHANICS TO ROCK ENGINEERING PROBLEMS

Application of fracture mechanics in rock engineering is not as common as the physical importance of the fracturing in e.g. failure and long-term stability might let expect. But with recent increase in computer capacities and new developments of computer codes fracture mechanics is more often applied.

This chapter gives an overview to the possible application of fracture mechanics to geomechanical problems. Additional information can be found in e.g. Whittaker et al. (1992) and references quoted therein. In Section 7.2 an explicit example for fracture mechanics modelling is given.

7.1 Overview

The best-known application in geomechanical engineering that can be treated with fracture mechanics is hydraulic fracturing. It is used e.g. as a method to determine in-situ stresses (e.g. Haimson & Fairhurst, 1967; Rummel & Winter, 1982; Rummel et al., 1986; Amadei & Stephansson, 1997) and in hydrocarbon industry as secondary EOR[1] method (e.g. Dietzel & Koehler, 1998). The relevant fracture mechanics parameter for these applications is the Mode I fracture toughness.

In civil and mining engineering various types of rock cutting machines are used for rock excavation purposes, e.g. tunnel boring machines (TBM), raise borers and longwall shearers. Up to now the rock cutting tools are mounted in some experience-optimised pattern on the cutting heads of the machines. Application of fracture mechanics principles to rock cutting problems has been carried out by various researchers using both Mode I and Mode II fracture toughness, see Whittaker et al. (1992) for further references.

Drilling and blasting have been the principle excavation methods for hard rock for centuries and is always in favour in very hard rocks, where cutting actions are inefficient. Fracture mechanics based on Mode I has been applied in numerous cases, but the fundamental fracture process still needs clarification (Whittaker et al., 1992).

Further examples of application of rock fracture mechanics are the analysis and prediction of borehole breakouts (e.g. Germanovich & Dyskin, 2000; Shen et al., 2002), slope stability (e.g. Scavia, 1995; Kemeny, 2003) and rock comminution machines (Bearman, 1999).

Computer modelling of rock failure has become increasingly important. Several codes are available, but most are based on empirical relationships for rock mass breakdown. Only some of them use the basic principles of fracture mechanics, e.g. DIGS (e.g. Napier, 1990; Napier & Hildyard, 1992; Napier & Malan, 1997) and FRACOD (Shen, 2002).

During the course of this thesis fracture mechanics testing was carried out for a number of computer modelling studies using FRACOD. These are the Äspö pillar stability project (Backers, 2003a; Rinne et al., 2003), the mortar Couple project (Backers, 2003b; Lee et al., 2003) and the Mizunami Underground Research

[1] Abbreviation for Enhanced Oil (or gas) Recovery

Laboratory (URL) project. The latter is presented in the next sections to give an example of fracture mechanics modelling.

7.2 *Fracture mechanics modelling of shafts and galleries of the URL in Mizunami, Japan*

Comprehensive understanding of the Excavation Disturbed Zone (EDZ) is required to build confidence in the safety of shafts and tunnels. The Japan Nuclear Cycle Development Institute (JNC) has initiated a research program named "Mizunami Underground Research Laboratory", or MIU, in granite at a depth of 1000m. The shaft excavation started in summer 2003. Prior to construction, numerical evaluation of the EDZ started in 2001. Modeling was carried out by FRACOM Ltd., Finland, using the FRACOD code. The determination of the relevant fracture mechanical properties for this project was carried out as part of this thesis (c.f. Chapters 4 and 5).

FRACOD is a two-dimensional computer code designed to simulate fracture initiation, propagation and coalescence in rocks. The code employs the Displacement Discontinuity Method (DDM) principles. It predicts the explicit fracturing process including fracture sliding/opening, fracture initiation and fracture propagation in rock masses. More details can be found in Shen & Stephansson (1993) and Shen (2002).

In the following section some results of the FRACOD modelling are briefly outlined to show the capability of today's rock fracture modeling codes. The full details of the modeling and parameter determination were presented at the *1st Kyoto International Symposium on Underground* Environment in Japan, March 2003 (Stephansson et al., 2003).

7.2.1 *Laboratory tests of fracture toughness*

FRACOD needs a number of input parameters, i.e. the elastic properties of the intact rock, the deformation parameters of the fractures and the Mode I and Mode II fracture toughness.

A testing series on three varieties of Mizunami granite from different depth levels (200 m, 500 m, 950 m) from the MIU site was carried out to determine the desired parameters.

The Mode I toughness was determined according to the ISRM Suggested Method (Ouchterlony, 1988). The Mode II toughness tests were performed using the Punch Through Shear Test Method as developed in this thesis.

Three tests for Mode I fracture toughness determination of each depth level were carried out. Mode II fracture toughness was determined on a series of samples with confining pressures of 5, 15, 25, 30, 50 and 70 MPa.

The determined Mode I and Mode II fracture toughnesses are summarised in Table 7-1 (c.f. Backers, 2002).

Depth [mm]	K_{IC} [MPam$^{1/2}$]	K^0_{IIC} [MPam$^{1/2}$]	K^∞_{IIC} [MPam$^{1/2}$]
200 m	2.39	3.10	8.97
500 m	2.37	3.69	8.62
945 m	1.73	3.07	10.04

Tab. 7-1: Summary of tests results on Mizunami granite. Mode I fracture toughness and Mode II fracture toughness at zero and terminal confining pressure. Discrepancy of results between Table 5-3 and data given here is caused by different ways of regression, i.e. bilinear fit vs. asymptotical rise to maximum value.

7.2.2 *Modelling of a shaft and gallery*

Based on laboratory results reported by Hata et al. (2001) and the fracture toughness tests by Backers (2002), modelling of the planned shaft and galleries was carried out and is summarised here. Stephansson et al. (2003) also modelled galleries in four different directions at two depth levels. Here only one example for shaft and gallery modelling is given.

Rock mass behaviour was simulated considering an explicit joint network. Three joint sets are observed at the MIU project site. The orientations of the joint sets are:

Set 1: N41E (500 m); Set 2: N88W (500 and 945 m); Set 3: N59E (945 m)

Shaft

The proposed vertical shaft of circular shape has an excavation diameter of 7.3 m. Results from modelling of two excavation depths, 500 m and 945 m, respectively, are presented. Shaft sinking at the depth of 945 m will take place across a major fault.

For the 500 m level the stresses as derived from overcoring stress measurement are 20.5 MPa (NS), 18.8 MPa (EW), 12.8 MPa (vertical) and τ are 1.4 MPa (N45E) and 2.3 MPa (N45W); for the 945 m level located in the fault zone stresses are 19.5 MPa (NS), 3.2 MPa (EW), 24.1 MPa (vertical) and τ is 5.6 MPa. The typical cases of predicted fracture initiation, propagation and coalescence in the immediate vicinity of the shaft are shown in Figure 7-1. At 500 m depth, fractures in the immediate vicinity of the shaft propagate and coalesce to form failure zones in NE/SW directions. The shape of the failure zone is strongly affected by the distribution of fractures. At 945 m depth in the fault zone, joints propagate in tension in the NNW/SSE direction, and propagate in shear in the ENE/WSW direction. The tensile and shear fractures together form an elliptical failure (caving) zone.

Gallery

Modelling of the galleries was conducted to find the optimal direction for them in the virgin stress field, i.e. the direction that minimises rock fall and development of EDZ. Stresses are 25 MPa perpendicular to shaft direction and 13 MPa in vertical direction. Results from modelling of a gallery in N45E direction at the 500 m level are presented here (Fig. 7-2). Existing fractures are prolonged and form 'key blocks'. This shows that rock fall is not necessarily depending on the existing joint geometry, only. Stress-redistribution prolongs and connects the existing joints and faults forming new fracture geometries.

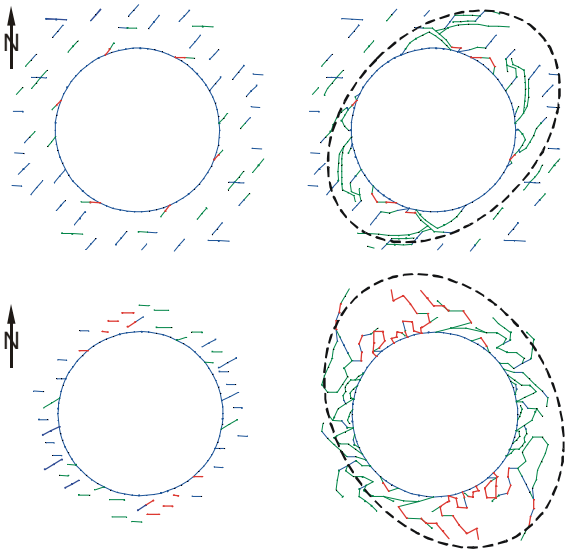

Fig. 7-1. Fractures in the shaft walls before (left) and after (right) failure for the 500 m level (top) and 945 m level (bottom). Dashed ellipse indicates EDZ. Fracture colour code: undeformed – blue, tensile – red, shear – green. After Stephansson et al., 2003.

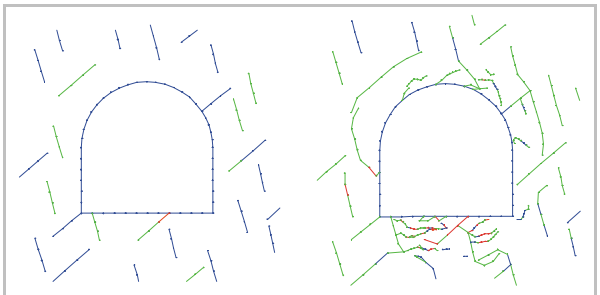

Fig. 7-2. Fractures in the gallery walls at 500 m before and after failure (direction N45E). Fracture colour code: undeformed – blue, tensile – red, shear – green. After Stephansson et al., 2003.

Conclusions

FRACOD's mathematical framework is based on properties of the rocks that are physically relevant. The elastic properties of the intact rock material and the deformation properties of the pre-existing discontinuities are employed to derive the displacements within the rock mass. Fracture initiation and propagation are determined by means of the Mode I and Mode II fracture toughness. As can be seen from Figures 7-1 and 7-2, quite a number of fractures propagate in shear, hence have exceeded K_{IIC}.

With classical (empirical) failure criteria it would not be possible to describe the fracture propagation and resulting fracture network at this resolution. This provides us with the ability to recognise potential failure modes that would not be predicted with existing methods, like e.g. key block analysis (Goodman & Shi, 1985). The extended fracture network in the EDZ forms new key blocks that can be examined and evaluated on behalf of their risk potential.

The study of fracture network development around rock engineering structures helps to better understand the influence of geometry and orientation of structures on stability, with implication to hydro-mechanical properties also. Hence, the orientation and shape of structures can be optimised and rock support can be designed better and more efficient.

8 GENERAL DISCUSSION

Individual results as presented in Chapters 4 and 5 were discussed in the subsequent sections. Based on those discussions, this chapter deliberates the results in a more broad and general frame.

8.1 Mode I loading

Mode I loading was applied by the Chevron Bend (CB-) method. It provides a localised tensile stress concentration at the notch tip as is shown by the FE modelling. The CB- test is widely accepted to offer a reliable and valid methodology to provide Mode I fracture growth and thus determination of pure K_{IC}. Conversely, it was shown that there is indication for the suspect that the assumed Mode I in CB- testing is not a pure Mode I fracture process.

The fracture propagates along a rough path both on the sample and microscopic scale when subjected to Mode I loading. This leads to 'direction-deviation' induced small scale mixed mode cracking. Acoustic Emission (AE) polarity analysis of the fracture process shows a significant contribution of shear events for Flechtingen sandstone and Mizunami granite (Backers et al., subm.; Stanchits et al., 2003). Hence, the determined Mode I fracture toughness, K_{IC}, is not pure Mode I fracturing from the viewpoint of microstructure. K_{IC} as evaluated from the ISRM Suggested Method (Ouchterlony, 1988) includes a combination of different modes of fracturing on the microscale. But on sample scale the small scale increments of fracturing combine to a macroscopic Mode I fracture. It is initiated and propagated by Mode I loading and, in first approximation, propagates co-planar.

Evidence for contribution of different mechanisms, i.e. subcritical and dynamic processes, to the fracture process on the microscale were discovered from analysis of mechanical and acoustic emission data at different loading rates. However, bulk energy consumption of the fracturing process remained constant, indicating critical loading rate regime on the sample scale. While microscale instability increases for faster loading rates, subcritical crack growth effects decrease. Hence, the competing mechanisms of instability and subcriticality seem to budge the portions of individual energy consumption contributing to the process. It may be speculated that small scale instability (i.e. dynamic cracking) and subcriticality (i.e. subcritical crack extension) are end members of a row of mechanisms. With increase in loading rate the amount of small scale instability increases further to result in instability of the sample whilst the subcritical component vanishes. Vice versa it may be argued that with decrease of loading rates the small scale instability effects vanish leading to subcritical growth only.

In conclusion it can be said that relative to the sample size, the fracture developing due to the loading is a Mode I fracture propagating at critical stress intensity factor. On the microscale mixed mode fracturing is evident and different mechanisms contribute to crack propagation.

8.2 What is the fracture toughness of rock?

The conclusion from the Mode I testing initiates a discussion about what the fracture toughness of rock is.

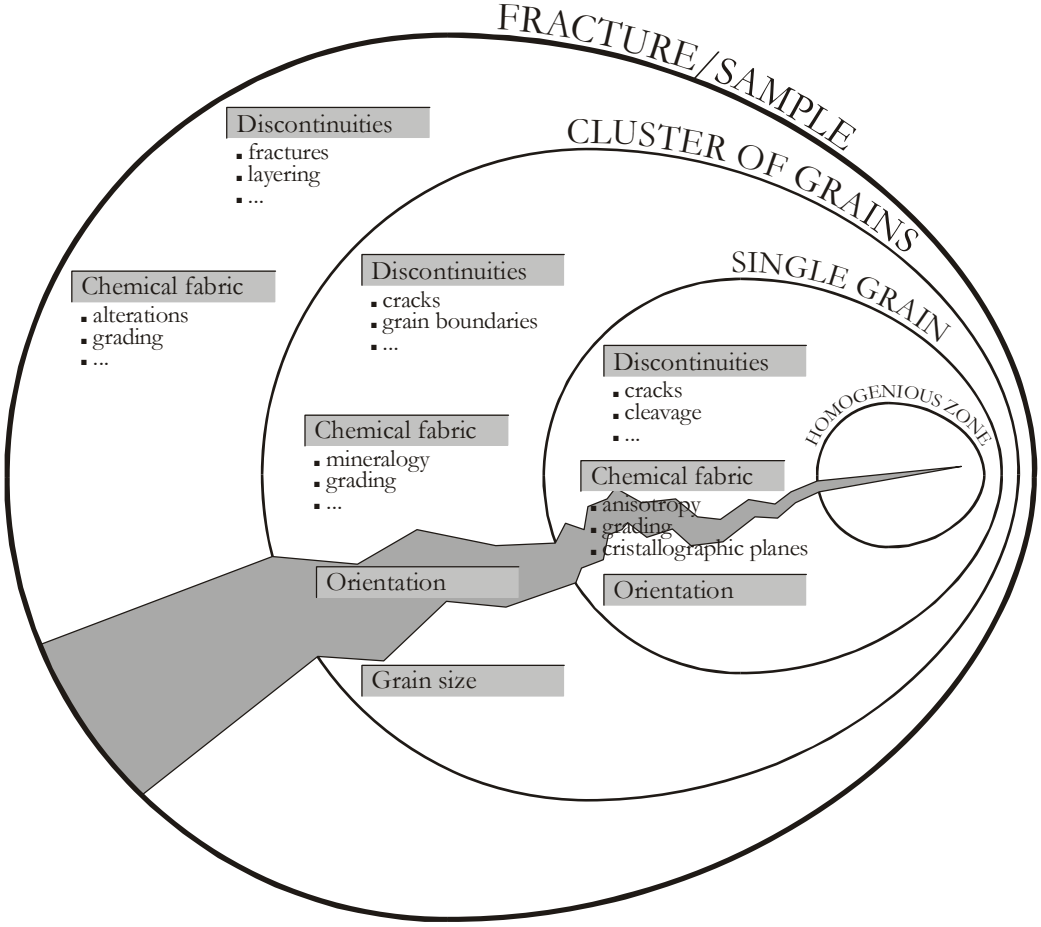

Fig. 8-1. The pertinent scale. Increasing the reference scale introduces new features and properties in rock material. Refer to text for discussion. Above a minimum scale the rock appears to be adequately represented.

The concept of 'mode of fracturing' has been developed for perfect linear elastic, homogeneous and isotropic media. These media are obligated to fulfil these requirements on the small as well as large scale. Adopting the concept to rock material bears several problems that are born in its granular structure. It introduces different materials with different properties, anisotropy on the large and small scale, discontinuities of all kinds and scales, etc.. One might guess that all these features make the simple concept of the mode of fracturing very complex for rock material (Fig. 8-1).

No one dares to claim that the fracture toughness, irrespective of mode, is the same for a quartz grain[1] or a quartzite. Even an isolated quartz grain has more than one fracture toughness. Subject to tension, it will be easier to break the grain when the stress is acting perpendicular to the mineralogical c-axis than parallel to it. A feldspar mineral in tension perpendicular to the cleavage will result in smaller yield stress than parallel to it. Hence, on the single grain scale, there is at least one (mostly more) fracture toughness(es) for the 'chemical component' and one for each plane of weakness.

At the scale of a cluster of grains, new fracture toughnesses arise. Firstly, it is the fracture toughnesses of the individual grains, which might be also of different kinds, e.g. quartz, feldspar, mica, etc.. In addition, the 'connection' between the grains, the cement, has its own fracture toughness. And this might vary depending on the grains that neighbour each other. For an ordinary granite, consisting of quartz, feldspar and mica – ignoring variations of chemical composition – this summarises to at least seven fracture toughnesses per mode of fracturing.

[1] Strictly speaking, the quantity of fracture toughness is valid for small scale yielding conditions only, which are not evident at the reference-scale of grain size.

The individual grains, with their bundle of fracture toughnesses, are usually randomly oriented within the reference-frame of the rock. Assuming an otherwise crack free rock, the increased stress field at the tip of an isolated introduced fracture in a loaded sample will cause instantaneous crack propagation where the stress intensity exceeds locally the fracture toughness. This might be in any direction at an angle that maximises the stresses to exceed the critical level of stress concentration. The crack direction might be governed by discontinuities rather than the direction of maximised Mode I or Mode II (or even Mode III) fracture toughness. Hence, it is unlikely that a fracture will propagate in its own plane – depending on the scale of observation. On the scale of grain size it will inevitably deviate from its straight path and hence introduce mixed mode fracturing on the local scale. Hence, a fracture, even when at the scale of observation propagating in its own plane, is always propagating in mixed mode on the small scale.

Consequently it depends very much on reference scale. The *fracture toughness of a rock* is accordingly understood as the bulk of its component 'toughnesses' participating to the fracturing process at a scale that *adequately represents the rock material*, the *pertinent* scale. The pertinent scale is a minimum scale requirement; further increasing the scale of observation will not change the fracture toughness unless new features appear in the region the fracture toughness is determined in. The *pertinent fracture toughness* does explicitly not imply a scale dependency of fracture toughness, which would put the fracture toughness as a material property in question. It accounts for the inhomogeneity of rock material only. The *pertinent fracture toughness* also accounts for different mechanisms and processes contributing to the integral fracture process forming the main fracture.

The *pertinent fracture toughness* adequately represents the response of the *rock* material at otherwise given boundary conditions.

8.3 Mode II loading

The Chevron Bend method for Mode I fracture toughness determination is a well examined procedure, which was employed to study certain aspects of the Mode I fracture propagation. Anyhow, as was pointed out in the Introduction to this thesis, for determination of Mode II fracture toughness some methods exist, but none of them was introduced as a Suggested Method. This might be due to several reasons. One reason might be the insufficient understanding of the complex Mode II fracture propagation as is reflected in the discussion about the existence of Mode II fracture propagation in rock material. A second reason might be that theoretical aspects for preferred Mode II fracture propagation, i.e. confining pressure, could not be satisfied by the proposed testing methods.

Hence, one goal of this thesis was to develop an experimental technique that provides a most preferable set-up for Mode II fracture toughness determination. This is a major part of the thesis. Along with the development of a method for application of Mode II loading, the resulting fracture content was examined on a first step basis. The microstructural examinations were carried out yielding at new insights to the discussion upon the Mode II fracturing process in rock.

Mode II fracture toughness determination

The developed Punch-Through Shear (PTS-) test is a method that provides a most preferable Mode II loading geometry.

It has an easy set-up that uses drill-core, as available from most geotechnical site-investigation campaigns. The sample preparation does not require special tools; hence any laboratory doing rock mechanics testing can prepare the samples. For running the experiments, any conventional loading frame and pressure vessel (or Hoek-Cell) will do the job. Only the required top and bottom assembly are special devices.

It has been stated by Lawn (1993) that 'shear fractures do occur in rocks where large geological pressures suppress the tensile mode' and this is supported by the calculations by Melin (1986). Therefore it is demanded for pure Mode II fracturing that the confining pressure is sufficiently high to limit the Mode I stress intensity to non-critical levels. The loading geometry of the PTS- test meets the reported requirement of a confining pressure (normal load) perpendicular to the shear direction. It was shown that the macroscopic fracture pattern developing

in this set-up is in agreement with the basic predictions from the sliding crack model at ambient conditions and low confining pressures. At elevated confining pressure the tensile features, i.e. macroscopic wing fractures, were increasingly suppressed suggesting increasing pureness of macroscopic Mode II.

Increasing Mode II loading of the sample has shown that first a wing fracture is initiated, this at least at zero to low confining pressures. Even though the wing fractures, which are tensile by nature, are initiated, with increase in shear load a 'secondary' fracture is instigated. Hence, the energy requirement for formation of the two types of fractures is very different.

Variation of geometrical parameters led to an optimisation of the PTS- geometry. Variation of loading rate proved that the stress intensity at failure was determined in the critical regime, hence, that the fracture toughness is determined. The most important result from variation of boundary conditions is the influence of confining pressure. Increasing confining pressure separates the mechanical response of the rocks to the Mode II loading into two regimes. This is reflected by the shape of maximum axial load and K_{IIC} vs. confining pressure. This change in regimes is mirrored also by the change of microstructural features in Carrara marble.

Microstructural breakdown process

Carrara marble developed a distinct asymmetric process zone with two regimes and a straight main separation. Indication of mixed mode cracking on the microscale is evident from AE analysis and geometrical aspects. The layout of this FPZ and main fracture is very much different from the Mode I induced fractures. The Mode II induced fracture propagates in first approximation in its own plane and the FPZ shape is governed by the own stress field. Increase of confining pressure was shown to change the orientation of these features which tend to reach constant values for P = 30-50 MPa.

Correlation analysis

The two regimes as indicated from mechanical and microstructural analysis are also reflected in the correlation analysis. Mode I fracture toughness, K_{IC}, and the Mode II fracture toughness at ambient conditions, K^0_{IIC}, can both be correlated to the same parameters. Most prominently, this result indicates that in both cases the same mechanisms are likely activated, although the energy requirement is different in the two cases. This is probably due to the increased crack surface area introduced in the Mode II fracturing process. The observation of radial fractures and dilatancy from diameter variation in the PTS- testing at low confining pressures also indicates strong influence of opening mechanisms. This macroscopic visible indicative of extension is not frequently evident at high confining pressures. Coincidentally, Mode II fracture toughness at elevated confining pressure, K^∞_{IIC}, shows no convincing correlation to parameters reflecting involvement of tensile cracking.

Application

For fracture mechanics based design of large scale structures in rock like tunnels, it is important to know about the resistance of the material to propagation of, if one wants so, shear introduced fractures. With increase in confining pressure it was shown that the wing fractures are omitted, hence only the 'secondary' fractures are initiated. The increase in confining pressure simulates greater overburden.

The confining pressures applied in experiments so far, i.e. 70 MPa, simulate a horizontal pressure at a depth of about 4000 m, assuming a generic unit weight of $\varrho \approx 0.027$ MN/m³ and a ratio of average horizontal to vertical stress of $k \approx 0.6$ (e.g. Hudson & Harrison, 1997).

For application of fracture mechanics in rock engineering a property that reliably describes the fracturing resistance of the rock material to Mode II loading is needed; irrespective of the microstructural breakdown process. In the PTS-test a most preferable set-up for Mode II fracturing is realised.

In conclusion it can be said that relative to the sample size, the fracture developing due to the loading is a Mode II fracture propagating at critical stress intensity factor. It is initiated and propagated by Mode II loading and, in first approximation, propagates co-planar. The microstructural features show typical pattern for a Mode II stress field. On the microscale mixed

mode fracturing is evident and different mechanisms contribute to crack propagation. K_{IIC} as provided from PTS- testing must be therefore understood as the pertinent Mode II fracture toughness.

It is suggested that the Mode II fracture toughness determined above terminal confining pressure is the valid K_{IIC}. This is supported by several indications.

(1) Elevation of confining pressure results in a bi-linear rise of Mode II fracture toughness. From the correlation analysis it was shown that the Mode II fracture toughness at low confining pressure could be described as a function of tensile strength, while Mode II fracture toughness at high P is not convincingly correlated to tensile strength.

(2) Coherence between observations in PTS- testing and by Kemeny (1993) suggest that above a certain level of confining pressure, i.e. ~ 30 MPa for the examined rock types, shear cracking is the active mechanism.

(3) Above a confining pressure of approximately 30 MPa in PTS- testing several aspects do not show strong change with increase in confining pressure any more. These are most obviously the micro- and macroscopic crack/fracture pattern and fracture toughness.

On the other hand, the rise of K_{IIC} with increase of confining pressure is important for application in cases of low confining pressure.

The status of the Punch Through Shear test

In the course of the development of the experimental method for determination of the Mode II fracture toughness several aspects of the geometry and testing procedure were illuminated. Nevertheless, a number of aspects were not touched that need clarification before the method can deliver trustworthy results. The Punch Through Shear test must be ranked as 'under development' still.

Most important, the sample size effect must be further examined and a testing procedure that provides controlled fracture propagation should be developed. Some other aspects for further study are summarised in Chapter 9.

Also, the microstructural observations are a first step to understand the fracturing process under Mode II loading. No final conclusions about the mechanisms can be drawn, there are indicatives that the fracturing process initiated by the PTS- test includes not only a singular Mode II crack propagating in its own plane as proposed by the theory of classical fracture mechanics.

Despite the critical analysis above, the results so far have shown the potential of the testing method to provide reliable and reproducible testing conditions. Most motivating the Mode II fracture toughness as derived from five different evaluation approaches, i.e. stress, displacement gradient, Energy Release Rate, J-integral and DET approach, give at ambient conditions very consistent results. The asymmetry of the evolving fracture process zone in Carrara marble could be shown. This was only seldom shown as clear in experiment before. This result is very consistent with the prediction from stress field analysis and was shown in field studies already.

9 CONCLUSIONS & OUTLOOK

The response of rock to loading under Mode I (tensile) and Mode II (shear) boundary conditions was studied. Results from Mode I loading obtained insights to the mechanisms involved on the microscopic level in large/sample scale fracturing. Further research along that line is desirable. From the attained results a concept for the 'relevant', pertinent fracture toughness was developed.

A new method to apply a Mode II loading, the Punch-Through Shear (PTS-) test, was developed. Although many parameters were illuminated, still several aspects have to be studied. The development is a first step towards establishing a standard method for determination of the Mode II fracture toughness. Using the Punch-Through Shear test the influence of confining pressure on fracturing and resulting fracture toughness was studied. A first approach to the microstructural evolution under Mode II loading was presented.

Several points are emphasised below and suggestions for further research are formulated. The idea for a detailed study of the microstructural development of the fracturing process is outlined in the Outlook section.

9.1 Conclusions

From this study the following conclusions are drawn.

9.1.1 Mode I

- The fracture toughness, the Energy Release rate and the fracture roughness of the generated fracture stay constant irrespective of crack opening rate between $5 \cdot 10^{-6}$ m/s to $5 \cdot 10^{-10}$ m/s in the Chevron-Bend test in Flechtingen sandstone. Resulting macroscopic average fracture propagation velocities range from $2 \cdot 10^{-4}$ to $3 \cdot 10^{-8}$ m/s.
- Macroscopic tensile fracture propagation in Flechtingen sandstone occurs at critical stress intensities even at very low loading rates. The fracture velocities are up to five orders of magnitude smaller than the velocity limit below which Atkinson (1984) suggested considerable participation of subcritical crack growth.
- Crack propagation in Flechtinger Bausandstein shows evidence for a contribution of subcritical as well as dynamic crack growth. The correction factor for the plasticity, p, increases with decreasing loading rate, suggesting an increase in plastic, presumably subcritical, deformation. Acoustic emission activity increases with increasing loading rates suggesting that dynamic crack propagation on the grain scale is important.
- Fracture process zone width and crack density in the sandstone remain constant in the range of applied loading rates, in good agreement with constant stress intensities. The shape of the process zone is elliptical with a length of about 25 mm and a width of about 5 mm.

9.1.2 Mode II

- A new testing method that is able to independently from each other apply a Mode II loading and a confining pressure was developed. It is called the Punch-Through Shear (PTS-) test.

- The magnitude of confining pressure (normal stress) is most important when studying the response of rock to Mode II loading. The determined fracture toughness increases bi-linear with increase in confining pressure and shows a change in slope at about 30 MPa for the tested rock types. Tests were performed for confining pressures from ambient conditions to 70 MPa.
- Tensile crack propagation is increasingly suppressed with increase in confining pressure. The confining pressure increases the 'pureness' of Mode II in the fracturing process. In PTS-testing a wing fracture develops at the bottom notch first, then another wing fracture initiates at the upper notch. Both propagate out of the shear zone and stop. They are frequently suppressed at elevated confining pressure.
- At peak load, the shear fracture initiates and propagates.
- Data of K_{IIC} should be given for high as well as low (zero) confining pressure.
- K_{IIC} is found to be almost independent of loading rate for the range of applied experimental conditions.
- The fractures forming in the PTS-Test are macroscopic Mode II fractures.
- On microscopic scale the fractures consist of a main fracture and an asymmetric process zone containing presumably Mode I and mixed mode microcracks as was shown for Carrara marble. The microcrack pattern in the wake of the process zone changes with increasing confining pressure; the process zone width decreases, as well as the microcrack inclination angle. At P = 30-70 MPa the observed microstructural parameters and K_{IIC} do not change significantly.
- Compared to other methods, the Punch-Through Shear (PTS-) test has a major advantage. The confining pressure, i.e. normal stress on the fracture, can be applied independently from the shear stress.

9.2 Suggestions for Further Research

During the discussion of the results, some aspects remained unsolved or could not be satisfyingly explained. Below possible future research topics and recommendations are outlined.

Mode I

- Extension of the range of loading rates in Mode I loading to faster and slower loading rates for several rock types to verify the hypothesis of shift of mechanism and to study if it holds for other rock types.
- Detailed analysis of microstructure and in particular acoustic emission polarity both in space and time for clarification of mixed mode characteristics.

Mode II

- Variation of rock ligament, IP, at elevated confining pressure. Additional study of the influence of IP on K_{IIC} for other rock types is desirable.
- Variation of notch diameter, ID, and sample diameter, D, at elevated confining pressure for different rock types of different grain sizes. The confining pressure should omit the radial expansion due to interlocking. The radial expansion should be measured by an appropriate extensometer instrument.
- Experimental study of the influence of notch tip shape on the fracture stress and hence K_{IIC}.
- Development of a lvdt that measures the displacement of the inner cylinder at its bottom surface. As the fracture frequently starts to propagate at the bottom notch, the propagation process is expected to be easier to control. The wing fracture at the bottom notch might create a problem. The formation should be measurable by the introduced lvdt as the fracture opens during propagation. On formation of the secondary, i.e. shear, fracture the wing fracture should close (c.f. Bobet & Einstein, 1998), hence the measured cylinder velocity is smaller than the true fracture speed, or a back-bouncing of the bottom surface of the inner cylinder is measured.

- Study of the notch coalescence. It is suggested to apply acoustic emission techniques in combination with volumetric strain measurements and above outlined control system to resolve this issue.
- Development of an 'easy-to-perform' evaluation method. This might be a method that determines the Mode II fracture toughness in terms of the J-integral of controlled propagating fractures.
- A higher resolution of the types of fracturing as derived from AE analysis in space and time should be carried out for the PTS- test. It is believed that the separation into basically two(three) types of fracturing, i.e. tensile and shear (and pore collapse), is insufficient to describe the fracturing process. A system that provides a more detailed classification of the polarity analysis is desirable.
- Extension of loading/displacement rate spectrum, especially into the region of subcritical fracture propagation. This is a major issue in long-term stability design of e.g. underground structures.
- It is suggested at this stage, that the influence of loading rate and sample geometry on Mode II fracture toughness has to be studied for a broader range of loading rates and at elevated confining pressure in the constant K_{IIC} regime; this to examine the mechanisms of fracture propagation and the most important influence of confining pressure on the mechanisms.

9.3 Outlook

To better understand the process of fracturing, the concept of a new type of rig is under development. Samples can be deformed while it is possible to see through them. First uniaxial loading tests have shown that it is possible to observe the process of fracturing of thin slices of rock in real time.

The *'Guillotine'* (working title) uses 2 mm thick Carrara marble samples, which appear to be transparent at that thickness. Maximum size of the tabular specimen is 30 · 60 mm. The sample is located between two PMMA plates; hence it is possible to observe the sample during loading and fracturing (Fig. 9-1). Usage of adapters makes it possible to operate different loading geometries, up to now quasi biaxial and triaxial loading of squared samples and a 2-D version of the PTS-test are possible.

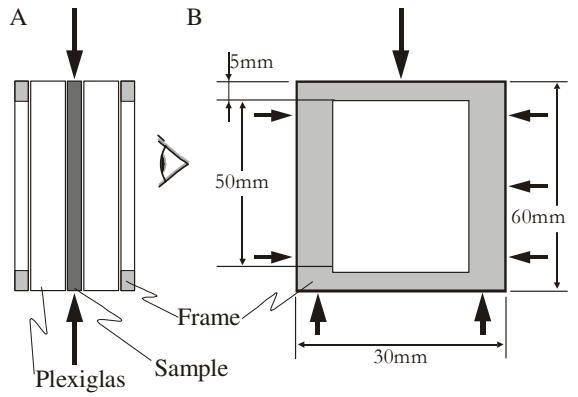

Fig. 9-1. Loading configuration and dimensions of the '*Guillotine*' (schematic, not to scale). (A) The sample is prevented from buckling by the Plexiglas plates and the frame. A strong light illuminates the sample from one side and the response of the marble to loading can be observed. (B) Normal stress is acting on the sides of the sample.

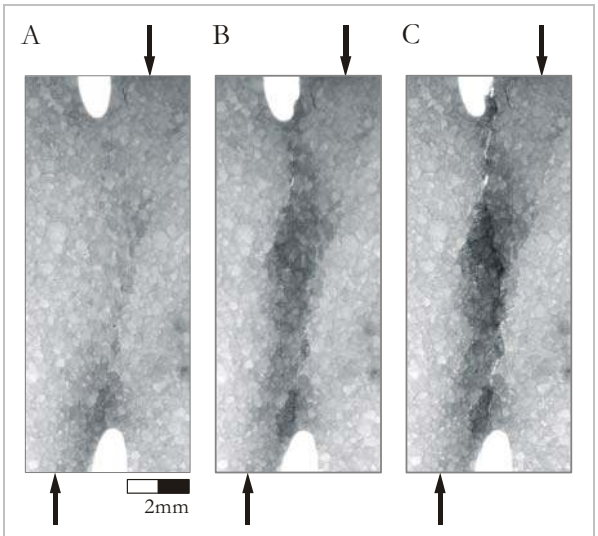

Fig. 9-2. Fracture development between the notches in the PTS- geometry (σ_N = 0.1 MPa) for Carrara marble. The future fracture trace becomes greyish on loading. The darker area in the pictures marks the fracture and process zone. (A) The fracture starts at the bottom notch. (B) Fractures have formed at top and bottom notch and introduce a fractured zone between the notches. (C) Some parts of the main fracture are opened and appear white.

Axial load is applied by the MTS loading frame, the load is applied to the rig's stamp. The horizontal loading system for simulation of a confining pressure is under construction. Maximum pressure will be about 30 MPa. It is planned to design the horizontal loading system so it can be servo-controlled by the MTS system. Load is applied by a hydraulic cylinder that is pressurised by the MTS confining pressure system.

The design provides the possibility to deform the specimens directly on a glass plate that is later used to prepare thin sections. The sample can be removed from the rig with the glass plate.

First tests on a quasi (uni-) biaxial and PTS- geometry (Fig. 9-2) showed typical fracture patterns.

This test set-up is thought to have a great potential to give new insights to the fracture propagation mechanisms, as the process can be observed in real time.

10 REFERENCES

A

Alber, M. & Brardt, A. 2003. Factors influencing fracture toughness K_{IC} from simple screening tests. Int. J. Rock Mech. Min. Sci.; 40: 779-784.

Alber, M. & Hauptfleisch, U. 1999. Generation and visualization of microfractures in Carrara marble for estimating fracture toughness, fracture shear and fracture normal stiffness. Int. J. Rock Mech. Min. Sci.; 36: 1065-1071.

Alber, M. & Heiland, J. 2001. Investigation of a Limestone Pillar Failure. Part 1: Stress History and Application of Fracture Mechanics Approach. Rock Mech. Rock Eng.; 34: 187-199.

Albert, R.A. & Rudnicki, J.W. 2001. Finite element simulations of Tennesee marble under plane strain laboratory testing: Effects of sample-platen friction on shear band onset. Mech. Mater.; 33: 47-60.

Al-Shayea, N.A., Khan, K. & Abduljauwad, S.N. 2000. Effects of confining pressure and temperature on mixed-mode (I-II) fracture toughness of a limestone rock. Int. J. Rock Mech. Min. Sci.; 37: 629-643.

Amadei, B. & Stephansson, O. 1997. Rock stress and its measurement. Chapman & Hall, London, UK.

Ashby, M.F. & Hallam, S.D. 1986. The failure of brittle solids containing small cracks under compressive stress states. Acta Metall.; 34: 497-510.

Atkinson, B.K. 1984. Subcritical crack growth in geological materials. J. Geophys. Res.; 89: 4077-4114.

Atkinson, B.K. 1987. Introduction to fracture mechanics and its geophysical applications. In: Atkinson, B.K. (ed.). 1991. Fracture mechanics of rock. Academic press geology series. Academic Press, London: 1-26.

Atkinson, B.K. 1991. Fracture mechanics of rock. Academic press geology series. Academic Press, London.

Atkinson, C., Smelser, R.E. & Sanchez, J. 1982. Combined mode fracture via the cracked Brazilian disk test. Int. J. Fract.; 18: 279-291.

B

Backers, T. 2001. Punch-through shear test of drill core – a new method for K_{IIC} testing. Diploma thesis, Division of Engineering Geology, Technical University Berlin, Germany.

Backers, T. 2002. Mode I and Mode II fracture toughness testing and fracture normal stiffness estimation of Tono granite. Report prepared for FRACOM Ltd.

Backers, T. 2003a. Determination of Mode I and Mode II Fracture Toughness and Fracture Normal Stiffness of Äspödiorite. Report prepared for Svensk Kärnbränslehantering (SKB) AB, Sweden.

Backers, T. 2003b. Mode I and Mode II Fracture Toughness Testing and Fracture Normal Stiffness Estimation of Mortar. Report prepared for Hazama Coorp., Tokyo, Japan.

Backers, T., Dresen, G., Rybacki, E. & Stephansson, O. 2004. New Data on Mode II Fracture Toughness of Rock from Punch-Through Shear (PTS) Test – SINOROCK2004 Paper 1A01. Int. J. Rock Mech. Min. Sci.; 41:351-352.

Backers, T., Fardin, N., Dresen, G. & Stephansson O. 2003a. Effect of Loading Rate on Mode I Fracture Toughness, Roughness and Micromechanics of Sandstone. Int. J. Rock Mech. Min. Sci.; 40: 425-433.

Backers, T., Rybacki, E., Alber, M. & Stephansson, O. 2002a. Fractography of rock from the new Punch-Through Shear Test. In: Dyskin, A.V., Hu, X. & Sahouryeh, E. (eds.). Structural Integrity and Fracture – The International Conference on Structural Integrity and Fracture, Perth, Australia: 303-308.

Backers, T., Stanchits, S. & Dresen, G. submitted. Tensile Fracture Propagation and Acoustic Emission Activity in Sandstone: The Effect of Loading Rate. Int. J. Rock Mech. Min. Sci..

Backers, T., Stanchits, S., Stephansson, O. & Dresen, G. 2003b. The Influence of Loading Rate on Mode I Acoustic Emission and Micromechanics of Sandstone. In: Makurat A. & Curri P. (eds.). EURO-Conference on Rock Physics and Geomechanics – Micromechanics, Flow and Chemical Reactions. Extended Abstract Volume, Delft, Netherlands.

Backers, T., Stephansson, O. & Rybacki, E. 2002b. Rock Fracture Toughness Testing in Mode II – Punch-Through Shear Test. Int. J. Rock Mech. Min. Sci, 39: 755-769.

Barenblatt, G.I. 1962. The mathematical theory of equilibrium cracks in brittle fracture. Adv. Appl. Mech.; 7: 55-125.

Barker, L.M. 1977. A simplified method for measuring plane strain fracture toughness. Eng. Fract. Mech.; 9: 361-369.

Barker, L.M. 1979. Theory for determining K_{IC} from small, non-LEFM specimens, supported by experiments on aluminum. Int. J. Fract.; 15: 515-536.

Barr, B. & Derradj, M. 1990. Numerical study of a shear (mode II) type test specimen geometry. Eng. Fract. Mech.; 35: 171-180.

Bažant, Z.P. & Pfeiffer, P.A. 1986. Shear fracture tests of concrete. Matér. Constr.; 16: 111-121.

Bearman, R.A. 1999. The use of the point load test for the rapid estimation of Mode I fracture toughness. Int. J. Rock Mech. Min. Sci.; 36: 257-263.

Bearman, R.A., Pine, R.J. & Willis, B.A. 1989. Use of fracture toughness testing in characterising the comminution potential of rock. Today's Technology for the Mining and Metallurgical Industries, Symp. of MMIJ/IMM, Kyoto, Japan: 161-181.

Bobet, A. & Einstein, H.H. 1998. Fracture Coalescence in Rock-type Materials under Uniaxial and Biaxial Compression. Int. J. Rock Mech. Min. Sci.; 35: 863-888.

Brace, W.F. & Bombolakis, E.G. 1963. A Note on Brittle Crack Growth in Compression. J. Geophys. Res; 68: 3709-3713.

Broberg, B. 1999. Cracks and Fracture. Academic Press, Cambridge.

Brown, E.T. 1981. Rock Characterization, Testing and Monitoring, ISRM Suggested Methods, Pergamon Press, Oxford.

Brown, G.J. & Reddish, D.J. 1997. Experimental relations between rock fracture toughness and density. Int. J. Rock Mech. Min. Sci.; 34:153-155.

Buthenuth, C. & de Freitas, M.H. 1995. The character of rock surfaces formed in Mode I. In: Ameen, M.S. (ed.). Fractography: Fracture topography as a tool in fracture mechanics and stress analysis. Geological Society Special Publication No. 92: 83-96.

C

Chang, S.-H., Lee, C.-I. & Jeon, S. 2002. Measurement of rock fracture toughness under modes I and II and mixed-mode conditions by using disc-type specimens. Eng. Geol.; 66: 79-97.

Chong, K.P. & Kuruppu, M.D. 1984. New specimen for fracture toughness determination of rock and other materials. Int. J. Fract.; 26: 59-62.

Costin, L.S. 1987. Deformation and failure. In: Atkinson, B.K. (ed.). 1991. Fracture Mechanics of Rock. Academic Press, New York: 167-215.

Cowie, P.A. & Scholz, C.H. 1992. Physical explanation for the displacement-length relationship of faults using a post-yield fracture mechanics model. J. Struct. Geol.; 14: 1133-1148.

Cox, S.J.D. & Scholz, C.H. 1988. Rupture Initiation in Shear Fracture of Rocks: An Experimental Study. J. Geophys. Res.; 93: 3307-3320.

D

Davies, J. 1988. Numerical study of punch-through shear specimen in mode II testing for cementitious materials. The Int. J. Cement Composites Lightw. Concrete; 10: 3-14.

Davies, J. 1991. Fracture characteristics of cement-stabilized soils. J. Mat. Sci.; 26: 4095-4103.

Davies, J. 1995. Study of shear fracture in mortar specimens. Cement and Concrete Research; 25: 1031-1042.

Davies, J., Morgan, T.G. & Yim, A.W. 1986. The finite element analysis of specimens giving a mode II type of failure. Fracture Toughness and Fracture Energy of Concrete. In Wittmann, F.H. (ed.), Elsevier Science Publishers, Amsterdam: 209-211.

Dietzel, H.J. & Koehler, M. 1998. Stimulation of a Low Permeability Natural Fractured Reservoir in the North-West German Carboniferous. SPE 39913. SPE Rocky Mountain Regional/Low-Permeability Reservoirs Symposium and Exhibition, Denver, Colorado, USA., 13p.

Donath, B. 2002. Stiffness of rock fractures – an experimental investigation. Unpublished Diploma thesis. Technical University of Berlin, Germany.

Dresen, G. & Guéguen, Y. 2004. In: Guéguen, Y. & Boutéca, M. (eds.). Mechanics of Fluid Saturated Rocks. Academic Press.

Dugdale, D.C. 1960. Yielding of steel sheets containing slits. J. Mech. Phys. Solids; 8: 100-104.

Dunham, R.J. 1962. Classification of carbonate rocks according to depositional texture. In: Ham, W.E. (ed.). Classification of carbonate rocks. Amer. Assoc. Petrol. Geol. Memoir 1: 108-121.

Dwivedi, R.D., Soni, A.K., Goel, R.K. & Dube, A.K. 2000. Fracture toughness of rocks under sub-zero temperature conditions. Int. J. Rock Mech. Min. Sci.; 37: 1267-1275.

Dyskin, A.V., Sahouryeh, E., Jewell, R.J., Joer, H. & Ustinov, K.B. 2003. Influence of shape and loacations of initial 3-D cracks on their growth in uniaxial compression. Eng. Fract. Mech.; 70: 2115-2136.

E

El Bied, A., Sulem, J. & Martineau, F. 2002. Microstructure of shear zones in Fortainebleau sandstone. Int. J. Rock Mech. Min. Sci.; 39: 917-932.

Engelder, T. 1987. Joints and shear fractures in rock. In: Atkinson, B.K. (ed.). 1991. Fracture mechanics of rock. Academic press geology series. Academic Press, London: 27-69.

Erdogan, F. & Sih, G.C. 1963. On the crack extension in plates under plane loading and transverse shear. J. Basic Eng.; 85: 519-527.

Evans, A.G. 1972. A method for evaluating the time dependent failure characteristics of brittle materials and its application to polycrystalline alumina. J. Mater. Sci.; 7: 1137-1146.

F

Fardin, N., Stephansson, O. & Jing, L. 2001. The scale dependence of rock joint surface roughness. Int. J. Rock Mech. Min. Sci.; 38: 659-669.

Farmer, I.W. 1968. Engineering properties of rocks. Spon, London.

Ferreira, L.E.T., Bittencourt, T.N., Sousa, J.L.A.O. & Gettu, R. 2002. R-curve behaviour in notched beam tests of rocks. Eng. Fract. Mech.; 69: 1845-1852.

Fowell, R.J. 1995. Suggested methods for determining Mode I fracture toughness using cracked chevron notched Brazilian disc specimens. Int. J. Rock Mech. Min. Sci. & Geomech. Abstr.; 32: 57-64.

Franklin, J.A. 1985. Suggested method for determining the point load strength. Int. J. Rock Mech. Min. Sci. & Geomech. Abstr.; 22: 51-60.

Fredrich, J.T., Evans, B. & Wong, T.-F. 1990. Effect of Grain Size on Brittle and Semibrittle Strength: Implications for Micromechanical Modelling of Failure in Compression. J. Geophys. Res.; 95: 10,907-10,920.

G

Germanovich, L.N. & Dyskin, A.V. 2000. Fracture mechanics and instability of openings in compression. Int. J. Rock Mech. Min. Sci.; 37: 263-284.

Glaser, S.D. & Nelson, P.P. 1992. Acoustic Emission Produced by Discrete Fracture in Rock. Int. J. Rock Mech. Min. Sci. & Geomech. Abstr.; 29: 253-265.

Goodman, R.E. 1980. Introduction to rock mechanics. Wiley, New York.

Goodman, R.E. & Shi, G.-H. 1985. Block Theory and its Application to Rock Engineering. Prentice-Hall, London: 338p.

Gramberg, J. 1989. A non conventional view on rock mechanics and fracture mechanics. Balkema, Rotterdam.

Griffith, A.A. 1920. The phenomena of rupture and flow in solids. Phil. Trans. Royal Soc. London; A221: 163-197.

Gunsallus, K.L. & Kulhawy, F.H. 1984. A comparative evaluation of rock strength measures. Int. J. Rock Mech. Min. Sci. & Geomech. Abstr.; 21: 233-248.

Guo, H. 1990. Rock cutting using fracture mechanics principles. PhD Thesis, University of Wollongong, NSW, Australia.

Guo, H., Aziz, N.I. & Schmidt, L.C. 1993. Rock fracture toughness determination by the Brazilian test. Eng. Geol.; 33: 177-188.

H

Haimson, B.C. & Fairhurst, C. 1967. Initiation and extension of hydraulic fractures in rock. Soc. Petrol. Eng.: 310-318.

Hakami, H. 1988. Post-failure behaviour of brittle rock. Doctoral Thesis, Division of Rock Mechanics, Luleå University of Technology, Sweden.

Hakami, H. & Stephansson, O. 1990. Shear fracture energy of Stripa granite – results of controlled triaxial testing. Eng. Fract. Mech.; 35: 855-865.

Hams, S. 1991. Dreipunktbiegeversuche zur Bruchzähigkeitsbestimmung von Gesteinen an künstlich verlängerten Rundstabproben. Studienarbeit, Institut für Geophysik der Ruhr-Universität Bochum.

Hata, K., Maruyama, M. & Toriihara, M. 2001. Shear Tests of Jointed Rock in Toki Granite. Japan Nuclear Cycle Development Institute Report.

Hauptfleisch, U. 1999. Erzeugung von Mikroklüften in Carrara Marmor, ihre geometrische Erfassung und dreidimensionale Darstellung. Diplomathesis, Technical University Berlin.

Hoagland, R.G., Hahn, G.T. & Rosenfield, A.R. 1973. Influence of Microstructure on Fracture Propagation in Rock. Rock Mechanics; 5: 77-106.

Hoek, E. & Franklin, J.A. 1968. Simple Triaxial cell for field or laboratory testing of rock. Trans. Inst. Min. Metall.; 77: A22.

Hoek, E. & Bieniawski, Z.T. 1984. Brittle fracture propagation in rock under compression. Int. J. Fract.; 26: 276-294.

Horii, H. & Nemat-Nasser, S. 1985. Compression-Induced Microcrack Growth in Brittle Solids: Axial Splitting and Shear Failure. J. Geophys. Res.; 90: 3105-3125.

Huang, J-A. & Wang, S. 1985. An experimental investigation concerning the comprehensive fracture toughness of some brittle rocks. Int. J. Rock Mech. Min. Sci.; 22: 99-104.

Hudson, J.A. & Harrison, J.P. 1997. Engineering rock mechanics: an introduction to the principles. Elsevier, Oxford.

I

Ida, Y. 1972. Cohesive force across the tip of a longitudinal shear crack and Griffith specific surface energy. J. Geophys. Res; 77: 3796-3805.

Imageware, Inc. 2000. Surfacer User's Guide, Ver. 10. Imageware Inc., Ann Arbor, Michigan, USA.

Inglis, C.E. 1913. Stresses in a plate due to the presence of cracks and sharp corners. Trans. Inst. Naval Archit.; 55: 219-230.

Ingraffea, A.R. 1981. Mixed Mode fracture initiation in Indiana limestone and Westerly granite. In: Proc. 22nd US Symp. Rock Mech., Cambridge, MA.: 186-191.

Ingraffea, A.R. & Arrea, M. 1982. Mixed-mode crack propagation in mortar and concrete. Department of Structural Engineering, Cornell University, Report No. 81-13.

Irwin, G.R. 1958. Fracture. In: Handbuch der Physik. Springer Verlag, Berlin, Vol. 6.

Issa, Mo.A., Issa, Ma.A., Islam, M.S. & Chudnovsky, A. 2003. Fractal dimension – a measure of fracture roughness and toughness of concrete. Eng. Fract. Mech.; 70: 125-137.

Izumi, M., Mihashi, H. & Nomura, N. 1986. Fracture toughness of concrete for mode II Fracture Toughness and Fracture Energy of Concrete. In Wittmann, F.H. (ed.), Elsevier Science Publishers, Amsterdam: 347-354.

J

JNC (Japan Nuclear Cycle) Development Institute. 2003. Mizunami Underground Research Laboratory Project; Results from 1996-1999 Period.

Jumikis, A.R. 1979. Rock Mechanics. Trans. Tech. Publ., Series on rock and soil mechanics, U.S.A.: 216-219.

K

Katz, O. & Reches, Z. 2004. Microfracturing, damage, and failure of brittle granites. J. Geophys. Res.; Vol. 109, No. B1, B01206, 0.1029/2002JB001961.

Kemeny, J.M. 1993. The micromechanics of deformation and failure in rocks. In: Paşamehmetoğu et al. (eds.). Assessment and prevention of failure phenomena in rock engineering. Balkema, Rotterdam: 23-33.

Kemeny, J.M. 2003. The time-dependent reduction of sliding cohesion due to rock bridges along discontinuities: a fracture mechanics approach. Rock Mech. Rock Eng.; 36: 27-38.

Kemeny, J.M. & Cook, N.G.W. 1987. Crack Models for the Failure of Rocks in Compression. In: Proceedings of the 2nd Intern. Conf. on Constitutive Laws for Engineering Materials, Arizona, USA.: 879-887.

Kulatilake, P. H. S. W. & Um, J. 1999. Requirement for accurate quantification of self-affine roughness using the roughness-length method. Int. J. Rock Mech. Min. Sci.; 36: 5-18.

Kuruppu, M.D. 1997. Fracture toughness measurement using chevron notched semi-circular bend specimen. Int. J. Fract.; 86: L33-L38.

L

Labuz, J.F., Shah, S.P. & Dowding, C.H. 1983. Post peak tensile load-displacement response and the fracture process zone in rock. In: Proc. 24th US Symp. Rock Mech. 421-428.

Labuz, J.F. & Biolzi, L. 1998. Characteristic strength of quasi-brittle materials. Int. J. Solids Struct.; 35: 4191-4203.

Labuz, J.F., Shah, S.P. & Dowding, C.H. 1985. Experimental analysis of crack propagation in granite. Int. J. Rock Mech. Min. Sci. & Geomech. Abstr.; 22: 85-98.

Lanaro, F., Jing, L. and Stephansson, O. 1998. 3-D-laser measurements and representation of roughness of rock fractures. In: Rossmainith, H.P. (ed.). Proc. Int. Conf. on Mech. of Jointed and Faulted Rock, MJFR-3. Vienna, Austria. Balkema, Rotterdam: 185-189.

Lawn, B. 1993. Fracture of brittle solids. Cambridge University Press, Cambridge.

Lee, H.-S., Shen, B., Stephansson, O. & Rinne, M. 2003. The modelling of COUPLE hydraulic fracturing experiment with FRACOD. FRACOM Ltd.

Lim, I.L., Johnston, I.W. & Choi, S.K. 1993. Stress intensity factors for semi-circular specimens under three point bending. Eng. Fract. Mech.; 44: 363-382.

Lim, I.L., Johnston, I.W., Choi, S.K. & Boland, J.N. 1994. Fracture Testing of a Soft Rock with Semi-circular Specimens Under Three-point Bending. Part 1 - Mode I. Int. J. Rock Mech. Min. Sci. & Geomech. Abstr.; 31: 185-197.

Liu, D., Wang, S. & Li, L. 2000. Investigation of fracture behaviour during rock mass failure. Int. J. Rock Mech. Min. Sci.; 37: 489-497.

Lockner, D.A. 1995. Rock Failure. In: Rock Physics and Phase Relations, AGU Reference Shelf; 3: 127-146.

Lockner, D.A., Moore, D.E. & Reches, Z. 1992. Microcrack interaction leading to shear fracture. In: Tillerson & Wawersik (eds.). Rock Mechanics. Balkema, Rotterdam: 807-816.

Lundborg, N. 1968. Strength of Rock-Like Materials. Int. J. Rock Mech. Min. Sci. & Geomech. Abstr.; 5: 427-454.

M

Malinverno, A. 1990. A simple method to estimate the fractal dimension of a self-affine series. Geophys. Res. Lett.; 17: 1953-6.

Marder, M. & Fineberg, J. 1996. How Things Break. Physics Today: 24-29.

Means, W. D. 1976. Stress and strain. Basic concepts of continuum mechanics for geologists. Springer-Verlag, New York.

Melin, S. 1986. When does a crack grow under mode II condition? Int. J. Fract.; 30: 103-114.

Melin, S. 1989. Why are crack paths in concrete and mortar different from those in PMMA? Matér. Constr.; 22: 23-27.

Meredith, P.G. 1983. A fracture mechanics study of experimentally deformed crustal rocks. PhD thesis, University of London.

Meredith, P.G. 1989. Comparative fracture toughness testing of rock. In: Mihashi et al. (eds). Fracture toughness and fracture energy. Balkema, Rotterdam.

Moore, D.E. & Lockner, D.A. 1995. The role of microcracking in shear-fracture propagation in granite. J. Struct. Geol.; 17: 5-114.

Müller, W. 1984. Bruchzähigkeitsmessungen an Gesteinen. Diplomarbeit, Institut für Geophysik, Ruhr-University Bochum, Germany.

Müller, W. & Rummel, F. 1984. Bruchzähigkeitsmessungen an Gesteinen. Bericht zu den BMFT-FE-Vorhaben 03E-3068-B, Ruhr-University Bochum, Germany.

N

Napier, J.A.L. 1990. Modelling of fracturing near deep level gold mine excavations using a displacement discontinuity approach. In: Rossmanith, H.P. (ed.). Mechanics of Jointed and Faulted Rock. Balkema, Rotterdam: 709-715.

Napier, J.A.L. & Hildyard, M.W. 1992. Simulation of fracture growth around openings in highly stressed, brittle rock. J. S. Afr. Inst. Min. Metall.; 92: 159-168.

Napier, J.A.L. & Malan, D.F. 1997. A viscoplastic discontinuum model of time-dependent fracture and seismicity effects in brittle rock. Int. J. Rock Mech. Min. Sci.; 34: 1075-1089.

Nara, Y., Yoneda, T. & Kaneko, K. 2002. Anisotropy of subcritical crack growth in granite. In: . Choi, Ryu and Moon (eds.). Rock Engineering Problems and Approaches in Underground Construction: 235-242.

Nordlund, E., Li, C. & Carlsson, B. 1999. Mechanical properties of the diorite in the prototype repository at ÄSPÖ HRL – Laboratory tests. Äspö Hard Rock Laboratory – International Progress Report (IPR-99-25).

Nur, A. & Simmons, G. 1970. The origin of small cracks in igneous rocks. Int. J. Rock Mech. Min. Sci. & Geomech. Abstr.; 7: 307-314.

O

Ouchterlony, F. 1982. Review of fracture toughness testing of rock. SM Archives; 7: 131-211.

Ouchterlony, F. 1988. Suggested methods for determining the fracture toughness of rock. Int. J. Rock Mech. Min. Sci. & Geomech. Abstr.; 25: 71-96.

Ouchterlony, F. 1989. On the background to the formulae and accuracy of rock fracture toughness measurements using ISRM standard core specimens. Int. J. Rock Mech. Min. Sci. & Geomech. Abstr.; 26: 13-23.

Ouchterlony, F & Sun, Z.Q. 1983. New methods of measuring fracture toughness of rock cores. 1st Symp. Rock Fragmentation by Blasting. Luleå, Sweden: 199-223.

P

Palmer, A.C. & Rice, J.R.. 1973. The growth of slip surfaces in the progressive failure of over-consolidated clay. Proc. Roy. Soc. Lond.; 332: 527-548.

Park, N., Park, P., Hong, C. & Jeon, S. 2001. Crack propagation and coalescence under uniaxial loading. In: Särkka P. & Eloranta P. (eds.). Rock Mechanics - a challenge for society. Proceedings of the ISRM Regional Symposium EUROCK 2001, Espoo: 271-276.

Petit, J.-P. & Barquins, M. 1988. Can natural faults propagate under Mode II conditions? Tectonics; 7: 1243-1256.

Pollard, D.D. & Aydin, A. 1988. Progress in understanding jointing over the past century. Geol. Soc. Am. Bull.; 100: 1181-1204.

Pyrak-Nolte, L.J. & Morris, J.P. 2000. Single fractures under normal stress: The relation between fracture specific stiffness and fluid flow. Int. J. Rock Mech. Min. Sci.; 37: 245-262.

R

Rao, Q. 1999. Pure shear fracture of brittle rock. Doctoral thesis, Division of Rock Mechanics, Luleå University, Sweden.

Rao, Q., Sun, Z., Stephansson, O., Li, C. & Stillborg, B. 2003. Shear fracture (Mode II) of brittle rock. Int. J. Rock Mech. Min. Sci.; 40: 355-375.

Reches, Z. & Lockner, D.A. 1994. Nucleation and growth of faults in brittle rocks. J. Geophys. Res.; 99-B9: 18,159-18,173.

Rice, J.R. 1968. A Path Independent Integral and the Approximate Analysis of Strain Concentration by Notches and Cracks. J. Appl. Mech.: 379-386.

Rice, J.R. 1980. The mechanics of earthquake rupture. In: Dziewonski, A.M. & Boschi, E. (eds.). Physics of the Earth's Interior, Italy: 555-649.

Rice, R.W., Freiman, S.W. & Becher, P.F. 1981. Grain size development of fracture energy in ceramics. J. Am. Ceram. Soc.; 64: 345-354.

Rinne, M., Shen, B. & Lee, H.-S. 2003. Äspö Pillar Stability Experiment. Modelling of fracture stability by Fracod – Preliminary results. SKB Internal Progress Report IPR-03-05.

Rocscience. 1999. Phase^2. Users Manual.

Rummel, F. & Winter, R.B. 1982. Application of laboratory fracture mechanics data to hydraulic fracturing field tests. Proc. 1st Japan-USA Symposium on Fracture Mechanics Approach – Hydraulic Fracture and Geothermal Energy, Sendai, Japan: 495-501.

Rummel, F., Mohring-Erdmann, G. & Baumgartner, J. 1986. Stress contrasts and hydro fracturing field stress data for the Continental crust. PAGEOPH, 124, No. 4-5: 875-895.

S

Sammis, C.G. & Ashby, M.F. 1986. The failure of brittle porous solids under compressive stress states. Acta metal.; 34: 511-526.

Sagong, M. & Bobet, A. 2002. Coalescence of multiple flaws in a rock-model material in uniaxial compression. Int. J. Rock Mech. Min. Sci.; 39: 229-241.

Scavia, C. 1995. A method for the study of crack propagation in rock structures. Géotechnique; 45: 447-463.

Schmidt, R.A. 1980. A microcrack model and its significance to hydraulic fracturing and fracture toughness testing. In: Proc. 21st US Symp. Rock Mech.: 581-590.

Scholz, C.H., Dawers, N.H., Yu, J.-Z., Cowie, P.A. & Anders, M.H. 1993. Fault Growth and Fault Scaling Laws: Preliminary Results. J. Geophys. Res. 98; B12: 21,951-21,961.

Shen, B. 1995. The mechanism of fracture coalescence in compression - experimental study and numerical simulation. Eng. Fract. Mech.; 51: 73-85.

Shen, B. 2002. FRACOD Version 1.1, User's manual. Fracom Ltd.

Shen, B. & Stephansson, O. 1993. Modification of the G-criterion of crack propagation in compression. Int. J. Eng. Fract. Mech.; 47: 177-189.

Shen, B., Stephansson, O., Einstein, H.H. & Ghahreman, B. 1995. Coalescence of fracture under shear stress experiments. J. Geophys. Res.; 100: 5975-5990.

Shen, B., Stephansson, O. & Rinne, M. 2002. Simulation of borehole breakouts using Fracod^{2D}. Oil Gas Sci. Tech.; 57: 579-590.

Shiryaev, A. & Kotkis, A.M. 1982. Methods for determining fracture toughness of brittle porous materials. Industrial Laboratory; 48: 917-918.

Simmons, G. & Richter, D. 1976. Microcracks in rocks. In: Stens, R.G.J. (ed.). The physics and chemistry of minerals and rocks. Wiley, New York.: 105-136.

Singh, R.N. & Sun, G.X. 1989. Relationships between fracture toughness, hardness indices and mechanical properties of rock. Mining Department Magazine, University of Nottingham, England: 49-62.

Sneddon, I.N. 1945. The stress distribution in the neighbourhood of a crack in an elastic solid. Proc. Camb. Phil. Soc.; 42: 229-260.

Stanchits, S., Backers, T., Stephansson, O. & Dresen, G. 2003. Comparison of Acoustic Emission Events and Micromechanics of granite under Mode I and Mode II loading. In: Makurat, A. & Curri, P. (eds.). EURO-Conference on Rock Physics and Geomechanics – Micromechanics, Flow and Chemical Reactions. Extended Abstract Volume, 7-11 September 2003, Delft, Netherlands.

Staub, I., Janson, T. & Fredriksson, A. 2003. Äspö Pillar Stability Experiment - Geology and properties of the rock mass around the experiment volume. Äspö Hard Rock Laboratory – International Progress Report (IPR-99-25).

Stephansson, O., Backers, T. & Rybacki, E. 2001. Shear fracture mechanics of rocks and a new testing method for K_{IIC}. In: Särkka P. & Eloranta P. (eds.). Rock Mechanics - a challenge for society. Proceedings of the ISRM Regional Symposium EUROCK 2001, Espoo: 163-168.

Stephansson, O., Shen, B., Rinne, M., Backers, T., Ishida, T., Moro, Y., Amemiya, K. & Nakama, S. 2003. Geomechanical evaluation and analysis of research shafts and galleries in MIU Project, Japan. In: Saito, T. & Murata, S. (eds.). Environmental Rock Engineering. Proceedings to the 1st Kyoto International Symposium on Underground Environment. Pre-Print Proceedings: 39-49.

Sun, Z. & Ouchterlony, F. 1986. Fracture toughness of stripa granite cores. Int. J. Rock Mech. Min. Sci. & Geomech. Abstr.; 23: 399-409.

Swartz, S.E. & Taha, N.M. 1990. Mixed mode crack propagation and fracture in concrete. Eng. Fract. Mech.; 35: 137-144.

Szwedzicki, T. 2003. Rock mass behaviour prior to failure. Int. J. Rock Mech. Min. Sci.; 40: 573-584.

T

Tang, C.A., Lin, P., Wong, R.H.C. & Chau, K.T. 2001. Analysis of crack coalescence in rock-like materials containing three flaws - Part II: numerical approach. Int. J. Rock Mech. Min. Sci.; 38: 925-939.

Thallak, S., Holder, J. & Gray, K.E. 1993. The pressure dependence of apparent hydrofracture toughness. Int. J. Rock Mech. Min. Sci. & Geomech. Abstr.; 30: 831-835.

Thiercelin, M. & Roegiers, J.M. 1986. Fracture toughness with the modified ring test. In: Proc. 27th US Symp. Rock Mech., Alabama: 284-290.

Thouless, M.D., Evans, A.G., Ashby, M.F. & Hutchinson, J.W. 1987. The edge cracking and spalling of brittle plates. Acta mater.; 35: 1333-1341.

U

Underwood, E.E. 1970. Quantitative stereology. Addison-Wesley Publ. Comp., Phillipines.

V

Vermilye, J.M. & Scholz, H.C. 1999. Fault propagation and segmentation: insight from the microstructural examination of a small fault. J. Struct. Geol.; 21: 1623-1636.

W

Wang, Q.Z. 1998. Stress Intensity Factors of the ISRM Suggested CCNBD Specimen Used for Mode-I Fracture Toughness Determination. Int. J. Rock Mech. Min. Sci.; 35: 977-982.

Wang, Q.Z. & Xing, L. 1999. Determination of fracture toughness Kic by using the flattened Brazilian disk specimen for rocks. Eng. Fract. Mech.; 64: 193-201.

Wang, Q.Z., Jia, X.M., Kou, S.Q., Zhang, Z.X. & Lindqvist, P.-A. 2003. More accurate stress intensity factor derived by finite element analysis for the ISRM suggested rock fracture toughness specimen – CCNBD. Int. J. Rock Mech. Min. Sci.; 40: 233-241.

Watkins, J. 1983. Fracture toughness test for soil-cement samples in Mode II. Int. J. Fract.; 23: 135-138.

Watkins, J. & Liu, K.L.W. 1985. A finite element study of the short beam test specimen under mode II loading. Int. J. Cement Composites and Lightweight; 7: 39-47.

Westergaard, H.M. 1939. Bearing Pressures and Cracks. J. Appl. Mech.; 24: 361-364.

Whittaker, B.N., Singh, R.N. & Sun, G. 1992. Rock Fracture Mechanics, Principles, Design and Applications. Developments in Geotechnical Engineering, 71. Elsevier, Amsterdam.

Wikberg, P, Gustafson, G, Rhen, I & Stanfors, R. 1991. Äspö Hard Rock Laboratory. Evaluation and conceptual modelling based on the pre-investigations. SKB TR 91-22.

Winter, R. 1983. Bruchmechanische Gesteinsuntersuchungen mit dem Bezug zu hydraulischen Frac-Versuchen in Tiefbohrungen. Dissertationsschrift der Ruhr-Universität Bochum.

Wong, R.H.C., Chau, K.T. & Wang, P. 1996. Microcracking and Grain Size Effect in Yuen Long Marbles. Int. J. Rock Mech. Min. Sci.; 33: 479-485.

Wong, R.H.C. & Chau, K.T. 1998. Crack coalescence in a rock-like material containing two cracks. Int. J. Rock Mech. Min. Sci.; 35:147-164.

Wong, R.H.C., Chau, K.T., Tang, C.A. & Lin, P. 2001. Analysis of crack coalescence in rock-like materials containing three flaws - Part I: experimental approach. Int. J. Rock Mech. Min. Sci.; 38: 909-924.

Y

Yacoub-Tokatly, Z., Barr, B. & Norris, P. 1989. Mode III fracture – a tentative test geometry. In: Shah, S.P., Swartz, S.E. & Barr, B. (eds.). Fracture of Concrete and Rock – recent developments. Elsevier, University Press, Cambridge, UK: 596-604.

Yoon, J. & Jeon, S. 2003. An experimental study on Mode II fracture toughness determination of rock. Tunnel & Underground; 13: 64-75.

Z

Zang, A. 1997. Akustische Emissionen beim Sprödbruch von Gestein. Habilitationsschrift, University of Potsdam, Scientific Technical Report STR97/19, Germany.

Zang, A., Wagner, F.C., Stanchits, S., Dresen, G., Andresen, R. & Haidekker, M. 1998. Source analysis of acoustic emissions in Aue granite cores under symmetric and asymmetric compressive loads. Geophysical Journal International; 135: 1113-1130.

Zang, A., Wagner, F.C., Stanchits, S., Janssen, C. & Dresen, G. 2000. Fracture process zone in granite. J. Geophys. Res.; 105-B10: 23,654-23,661.

Zhang, Z.X. 2002. An empirical relation between mode I fracture toughness and the tensile strength of rock. Int. J. Rock Mech. Min. Sci.; 39: 401-406.

Zhang, Z.X., Kou, S.Q., Yu, J., Yu, Y., Jiang, L.G. & Lindqvist, P.A. 1999. Effects of loading rate on rock fracture. Int. J. Rock Mech. Min. Sci.; 36: 597-611.

Zietlow, W.K. & Labuz, J.F. 1998. Measurement of the intrinsic process zone in rock using acoustic emission. Int. J. Rock Mech. Min. Sci.; 35: 291-299.

APPENDIX

APPENDIX

APPENDIX A

A PUBLICATIONS

The publications appear in chronological order. The list includes journal papers, conference contributions, and the diploma thesis.

Stephansson O., Backers T. & Rybacki E. 2001. Shear fracture mechanics of rocks and a new testing method for K_{IIC}. In: Särkka P. & Eloranta P. (eds.). *Rock Mechanics - a challenge for society. Proceedings of the ISRM Regional Symposium EUROCK 2001*, Espoo: 163-168. [Proceedings & Presentation]

Backers, T. 2001. Zur Rißausbreitung in Gesteinen - ein Versuch den Spannungsintensitätsfaktor K_{IIC} experimentell zu bestimmen. Proceedings of 13. Nationale Tagung für Ingenieurgeologie. [Extended Abstract & Poster]

Backers T. 2001. Punch-through shear test of drill core – a new method for K_{IIC} testing. Unpublished Diploma thesis, Division of Engineering Geology, Technical University Berlin, Germany. [Diploma Thesis]

Stephansson O., Shen B., Rinne M. & Backers T. 2002. Simulation of fracture propagation and borehole breakouts using FRACOD^{2D} (Simulering av sprickpropagering kring bergborrhål med FRACOD^{2D}). *Swedish Rock Mechanics Day, March 2002, Swedish Rock Engineering Foundation,* Stockholm, Sweden. [Presentation]

Backers T., Stephansson O. & Rybacki E. 2002. Rock Fracture Toughness Testing in Mode II – Punch-Through Shear Test. *Int. J. Rock Mech. Min. Sci,* 39: 755-769. [Journal Paper]

Backers T., Rybacki E., Alber M. & Stephansson O. 2002. Fractography of rock from the new Punch-Through Shear Test. In: Dyskin, A.V., Hu, X. & Sahouryeh, E. (eds.). *Structural Integrity and Fracture – The International Conference on Structural Integrity and Fracture,* Perth, Australia: 303-308. [Proceedings & Presentation]

Backers T., Fardin N., Dresen G. & Stephansson O. 2003. Effect of Loading Rate on Mode I Fracture Toughness, Roughness and Micromechanics of Sandstone. *Int. J. Rock Mech. Min. Sci.,* 40: 425-433. [Journal Paper]

Stephansson O., Shen B., Rinne M., Backers T., Ishida T., Moro Y., Amemiya K. & Nakama S. 2003. Geomechanical evaluation and analysis of research shafts and galleries in MIU Project, Japan. Key-Note lecture. In: Saito, T. & Murata, S. (eds). *Environmental*

Rock Engineering. Proceedings to the 1st Kyoto International Symposium on Underground Environment. Pre-Print Proceedings: 39-49. [Proceedings & Presentation]

Backers T., Stanchits S., Stephansson O. & Dresen G. 2003. The Influence of Loading Rate on Mode I Acoustic Emission and Micromechanics of Sandstone. In: Makurat A. & Curri P. (eds.). *EURO-Conference on Rock Physics and Geomechanics – Micromechanics, Flow and Chemical Reactions.* Extended Abstract Volume, 7-11 September 2003, Delft, Netherlands. [Extended Abstract & Presentation]

Stanchits S., Backers T., Stephansson O. & Dresen G. 2003. Comparison of Acoustic Emission Events and Micromechanics of granite under Mode I and Mode II loading. In: Makurat A. & Curri P. (eds.). *EURO-Conference on Rock Physics and Geomechanics – Micromechanics, Flow and Chemical Reactions.* Extended Abstract Volume, 7-11 September 2003, Delft, Netherlands. [Extended Abstract & Poster]

Backers T., Stanchits S. & Dresen G. submitted. Tensile Fracture Propagation and Acoustic Emission Activity in Sandstone: The Effect of Loading Rate. *Int. J. Rock Mech. Min. Sci.* [Journal Paper]

Backers T., Dresen G., Rybacki E. & Stephansson O. 2004. New Data on Mode II Fracture Toughness of Rock from Punch-Through Shear (PTS) Test. *Int. J. Rock Mech. Min. Sci.*, Proceedings of the ISRM SINOROCK 2004 symposium, International Symposium on Rock Mechanics – Rock Characterization, Modelling and Engineering Design Methods. 41: 351-352. [Proceedings, Abstract Journal Paper & Presentation]

B SPECIMEN REGISTER AND TEST RESULTS

B.1 Chevron Bend testing

Id.: Specimen Identifier; Rock type: ÄD: Äspö diorite, AG: Aue granite, CM: Carrara marble, FB: Flechtingen sandstone, RL: Rüdersdorf limestone, TG: Mizunami granite; D: diameter; L: length; S: support span; a_0: initial notch depth; t: notch width; COD rate: clip gage opening rate; K_{IC}: uncorrected fracture toughness; p: plasticity correction factor; K^C_{IC}: corrected fracture toughness.

No.	Sample Id.	Rock Type	Dimensions D [mm]	L [mm]	S [mm]	a_0 [mm]	t [mm]	COD rate [N/s]	[mm/s]	Results/Analysis Max. load [kN]	K_{IC} [MPam$^{1/2}$]	p [ ]	K^C_{IC} [MPam$^{1/2}$]
1	L1	RL	50.0	260	166.5	7.7	1.2	100	-	1.04	0.94	-	-
2	L2	RL	50.0	252	166.5	7.7	1.2	100	-	1.22	1.22	-	-
3	L4	RL	50.0	245	166.5	7.4	1.2	-	0.007	1.25	1.15	-	-
4	L5	RL	50.0	252	166.5	7.7	1.2	-	0.0005	1.10	1.04	0.12	1.17
5	L6	RL	50.0	230	166.5	7.6	1.2	-	0.0002	1.04	0.97	0.06	1.03
6	L7	RL	50.0	230	166.5	7.8	1.2	-	0.0001	1.04	0.99	0.10	1.09
7	L8	RL	50.0	245	166.5	7.7	1.2	-	0.0001	1.12	1.05	0.12	1.18
8	M2	CM	50.0	240	166.5	7.5	1.2	100	-	1.21	1.14	-	-
9	M3	CM	50.0	252	166.5	7.6	1.2	-	0.0001	1.07	1.00	-	-
10	M5	CM	50.0	242	166.5	7.6	1.2	-	0.0001	1.07	1.00	0.10	1.10
11	M6	CM	50.0	262	166.5	7.6	1.2	-	0.0001	1.05	0.98	0.30	1.34
12	M20	CM	50.0	225	166.5	7.5	1.2	-	0.0005	-	-	-	-
13	Z22	CM	50.0	>200	166.5	7.5	1.2	-	0.0005	1.89	1.77	0.30	2.41
14	Z23	CM	50.0	>200	166.5	7.5	1.2	-	0.0005	1.74	1.62	0.34	2.31
15	Z24	CM	50.0	>200	166.5	7.5	1.2	-	0.0005	1.92	1.79	0.29	2.42
16	Z34	CM	50.0	>200	166.5	7.5	1.2	-	0.0005	2.00	1.87	0.28	2.49
17	Z35	CM	50.0	>200	166.5	7.5	1.2	-	0.0005	1.97	1.83	0.32	2.55
18	G1	AG	50.0	255	166.5	7.5	1.2	-	0.0001	1.21	1.14	0.35	1.64
19	G2	AG	50.0	251	166.5	7.6	1.2	-	0.0001	1.14	1.07	0.31	1.47
20	G3	AG	50.0	263	166.5	7.7	1.2	-	0.0004	1.41	1.32	0.28	1.76
21	G4	AG	50.0	259	166.5	7.6	1.2	-	0.0001	1.21	1.14	0.21	1.41
22	G6	AG	50.0	255	166.5	7.7	1.2	-	0.0004	1.31	1.24	0.32	1.73
23	G7	AG	50.0	255	166.5	7.5	1.2	-	0.0004	1.30	1.23	-	-
24	T1-1	TG	64.0	228	213.0	3.3	1.2	-	0.0005	3.51	1.61	0.34	2.31
25	T3-1	TG	64.0	227	213.0	3.3	1.2	-	0.0005	3.79	1.74	0.28	2.31
26	T4-1	TG	64.0	228	213.0	3.2	1.2	-	0.0005	4.54	2.07	0.21	2.56

No.	Id.	Rock	D	L	S	a_0	t	COD rate		Max. load	K_{IC}	p	K^C_{IC}
27	T8-1	TG	64.0	225	213.0	3.3	1.2	-	0.0005	3.72	1.71	0.32	2.38
28	T8-2	TG	64.0	225	213.0	3.3	1.2	-	0.0005	3.35	1.54	0.33	2.17
29	T8-3	TG	64.0	215	213.0	3.2	1.2	-	0.0005	4.72	1.92	0.28	2.56
30	T14-1	TG	64.0	229	213.0	3.3	1.2	-	0.0005	2.41	1.11	0.36	1.61
31	T15-1	TG	64.0	206	213.0	3.2	1.2	-	0.0005	3.72	1.35	0.34	1.93
32	T16-1	TG	64.0	219.0	213.0	3.3	1.2	-	0.0005	2.59	1.06	0.41	1.64
33	LT-1	TG	50.0	221.0	166.5	7.5	1.2	-	0.0005	2.35	-	-	-
34	FB1	FB	50.0	>200	166.5	7.6	1.2	-	0.0005	0.79	0.71	0.43	1.12
35	FB2	FB	50.0	>200	166.5	7.5	1.2	-	0.00005	0.73	0.67	0.48	1.13
36	FB4	FB	50.0	>200	166.5	7.6	1.2	-	0.005	0.72	0.67	0.44	1.07
37	FB5	FB	50.0	>200	166.5	7.5	1.2	-	0.000005	0.65	0.61	0.58	1.18
38	FB6	FB	50.0	>200	166.5	7.4	1.2	-	0.000005	0.69	0.64	0.59	1.26
39	Z29	FB	50.0	>200	166.5	7.5	1.2	-	0.0005	1.08	1.01	0.46	1.66
40	Z30	FB	50.0	>200	166.5	7.5	1.2	-	0.0005	1.20	1.12	0.47	1.86
41	Z31	FB	50.0	>200	166.5	7.5	1.2	-	0.0005	1.04	0.97	0.49	1.66
42	Z32	FB	50.0	>200	166.5	7.5	1.2	-	0.0005	1.15	1.07	0.49	1.82
43	Z33	FB	50.0	>200	166.5	7.5	1.2	-	0.0005	1.12	1.04	0.48	1.75
44	D1	ÄD	50.0	260	166.5	7.5	1.2	-	0.0005	3.65	3.30	0.18	3.80
45	D2	ÄD	50.0	250	166.5	7.5	1.2	-	0.0005	3.03	2.81	0.32	3.79
46	D3	ÄD	50.0	290	166.5	7.5	1.2	-	0.0005	3.78	3.43	0.12	3.87
47	D4	ÄD	50.0	260	166.5	7.5	1.2	-	0.0005	3.30	2.98	0.25	3.84

B.2 Punch-Through Shear testing

Id.: Specimen Identifier; Rock type: ÄD: Äspö diorite, AG: Aue granite, CM: Carrara marble, FB: Flechtingen sandstone, RL: Rüdersdorf limestone, TG: Mizunami granite; D: diameter; W height; ID: inner notch diameter; t: notch width; a: upper notch depth; b: lower notch depth; IP: intact rock portion, P: confining pressure; rate: displacement rate; σ_{max}: axial peak stress; K_{IIC}: fracture toughness.

Sample			Dimensions							Variables		Results/Analysis			
No	Id.	Rock type	D	W	ID	t	a	b	IP	P	rate	Max. load	σ_{max}	τ_{max}	K_{IIC}
			[mm]	[mm]	[mm]	[mm]	[mm]	[mm]	[mm]	[MPa]	[mm/min]	[kN]	[MPa]	[MPa]	[MPam$^{1/2}$]
1	D1-1	ÄD	50.98	50.03	25.00	1.50	5.66	30.33	14.04	30	0.200	142.2	289.7	121.7	10.8
2	D1-2	ÄD	50.93	50.10	25.00	1.50	5.25	30.61	14.24	70	0.200	170.7	347.7	144.0	12.9
3	D1-3	ÄD	51.01	50.07	25.00	1.50	5.17	30.66	14.24	15	0.200	122.6	249.8	103.4	9.3
4	D2-1	ÄD	50.91	49.94	25.00	1.50	5.32	30.21	14.41	70	0.200	170.0	346.3	141.7	12.9
5	D2-2	ÄD	50.94	50.00	25.00	1.50	5.37	30.66	13.97	70	0.200	-	-	-	-
6	D2-3	ÄD	50.94	50.06	25.00	1.50	5.69	30.66	13.71	30	0.200	159.0	323.9	139.3	12.1
7	D2-4	ÄD	50.94	50.01	25.00	1.50	5.55	30.19	14.27	15	0.200	123.6	251.9	104.1	9.4
8	D3-1	ÄD	50.90	50.14	25.00	1.50	5.07	30.63	14.44	50	0.200	163.0	332.1	135.6	12.4
9	D3-2	ÄD	50.91	50.05	25.00	1.50	5.31	30.18	14.56	5	0.200	91.2	185.9	75.3	7.0
10	D3-3	ÄD	50.97	48.57	25.00	1.50	5.48	30.19	12.90	0	0.200	56.2	114.6	52.4	4.3
11	D4-1	ÄD	50.89	50.12	25.00	1.50	5.52	30.77	13.83	50	0.200	175.0	356.5	152.0	13.3
12	D4-2	ÄD	50.95	50.13	25.00	1.50	5.30	30.69	14.14	5	0.200	86.0	175.2	73.0	6.6
13	D4-3	ÄD	51.11	50.03	25.00	1.50	5.38	30.64	14.01	0	0.200	53.7	109.5	46.1	4.1
14	G1-1	AG	50.00	50.00	22.00	1.50	4.80	27.90	17.30	5	0.200	84.9	223.3	66.5	-
15	G1-2	AG	50.00	50.00	30.00	1.50	8.00	29.76	12.24	5	0.200	62.3	88.1	51.4	-
16	G1-3	AG	50.00	50.00	25.00	1.50	4.70	34.60	10.70	5	0.200	64.4	131.2	72.3	-
17	G2-1	AG	50.00	50.00	25.00	1.50	5.00	30.00	15.00	30	0.200	162.2	330.5	129.9	12.3
18	G3-1	AG	50.00	50.00	25.00	1.50	4.70	27.80	17.50	5	0.200	86.7	176.6	59.5	6.6
19	G3-2	AG	50.00	50.00	25.00	1.50	4.70	41.39	3.91	5	0.200	32.6	66.5	100.2	-

Sample			Dimensions							Variables		Results/Analysis			
No	Id.	Rock type	D	W	ID	t	a	b	IP	P	rate	Max. load	σ_{max}	τ_{max}	K_{IIC}
			[mm]	[mm]	[mm]	[mm]	[mm]	[mm]	[mm]	[MPa]	[mm/min]	[kN]	[MPa]	[MPa]	[MPam$^{1/2}$]
20	G3-3	AG	50.00	50.00	25.00	1.50	4.90	24.80	20.30	5	0.200	89.4	182.1	52.9	-
21	G4-1	AG	50.00	50.00	25.00	1.50	4.60	40.20	5.20	5	0.200	40.3	82.1	93.0	-
22	G4-2	AG	50.00	50.00	25.00	1.50	5.00	35.49	9.51	5	0.200	55.6	113.3	70.2	-
23	G5-1	AG	50.00	50.00	25.00	1.50	4.80	25.42	19.78	5	0.200	94.7	192.9	57.5	-
24	G5-2	AG	50.00	50.00	25.00	1.50	4.60	30.00	15.40	5	0.200	60.8	123.9	47.4	4.6
25	G5-3	AG	50.00	50.00	25.00	1.50	4.50	30.15	15.35	10	0.200	103.8	211.4	81.2	7.9
26	G5-4	AG	50.00	50.00	25.00	1.50	5.00	30.00	15.00	70	0.200	192.7	392.5	154.3	14.6
27	G6-1	AG	50.00	50.00	25.00	1.50	5.00	30.00	15.00	50	0.200	191.5	390.1	153.3	14.6
28	G7-1	AG	50.00	50.00	25.00	1.50	4.90	29.92	15.18	5	0.200	63.8	130.0	50.5	4.9
29	G7-2	AG	50.00	50.00	25.00	1.50	5.10	29.70	15.20	15	0.200	123.4	251.4	97.5	9.4
30	G10-1	AG	50.00	50.00	25.00	1.50	4.90	30.00	15.10	0	0.200	41.0	83.5	32.6	3.1
31	G10-2	AG	50.00	50.00	25.00	1.50	5.00	30.00	15.00	60	0.200	187.3	381.6	150.0	14.2
32	G10-3	AG	50.00	50.00	25.00	1.50	5.00	30.00	15.00	30	0.200	160.3	326.6	128.4	12.2
33	G11-1	AG	49.94	50.18	22.00	1.50	5.60	31.28	13.30	5	0.200	73.9	194.5	75.3	-
34	G11-2	AG	49.97	50.28	22.00	1.50	6.30	32.60	11.38	5	0.200	67.9	178.7	80.9	-
35	G11-3	AG	49.94	50.15	30.00	1.50	5.40	30.61	14.14	5	0.200	64.7	91.5	46.2	-
36	G11-4	AG	50.09	50.16	30.00	1.50	5.30	30.58	14.28	5	0.200	64.5	91.2	45.6	-
37	G12-1	AG	50.13	50.22	25.00	1.50	5.00	30.23	14.99	40	0.200	157.4	320.7	126.1	12.0
38	G12-2	AG	50.04	49.96	25.00	1.50	4.70	30.00	15.26	40	0.200	161.0	328.0	126.7	12.2
39	G15-1	AG	50.00	50.10	25.00	1.50	4.90	30.10	15.10	5	2.000	86.6	176.3	68.8	6.6
40	G15-2	AG	50.00	50.20	25.00	1.50	4.90	29.80	15.50	5	2.000	91.4	186.2	70.8	7.0
41	G15-3	AG	50.00	50.20	25.00	1.50	4.90	30.00	15.30	5	20.000	100.6	205.0	79.0	7.7
42	G15-4	AG	50.00	50.20	25.00	1.50	5.10	30.00	15.10	5	20.000	92.7	188.7	73.7	7.1
43	G15-5	AG	50.00	49.70	25.00	1.50	4.90	29.90	14.90	5	0.020	64.7	131.7	52.1	4.9
44	G15-6	AG	50.00	50.10	25.00	1.50	5.00	30.20	14.90	5	0.020	70.7	144.1	57.0	5.4
45	G15-7	AG	50.00	50.15	25.00	1.50	4.90	30.00	15.25	5	0.200	77.7	158.3	61.2	5.9
46	G16-1	AG	50.00	50.00	25.00	1.50	5.00	30.00	15.00	40	0.200	171.9	350.3	137.7	13.1
47	AB1	AG	113.00	44.00	25.00	2.17	5.30	24.90	13.80	5	0.200	125.0	254.6	106.1	-
48	AB2	AG	113.00	45.00	50.00	2.70	5.20	23.10	16.70	5	0.200	214.0	109.0	77.4	-
49	AB3	AG	113.00	44.50	62.00	4.00	5.20	24.30	15.00	5	0.200	265.0	87.8	85.2	-
50	AB4	AG	113.00	54.00	50.00	2.70	5.10	30.86	18.04	5	0.200	233.0	118.7	78.0	-
51	AB5	AG	113.00	52.50	62.00	4.00	5.10	31.20	16.20	5	0.200	259.0	85.8	77.1	-
52	AB6	AG	113.00	53.30	25.00	3.30	5.10	30.95	17.25	5	0.200	125.0	254.6	81.5	-
53	JM-1	CM	50.09	49.98	25.00	1.50	5.19	30.92	13.87	5	0.200	55.9	113.9	48.4	4.3
54	JM-2	CM	49.60	49.67	25.00	1.50	4.90	30.49	14.28	30	0.200	91.1	185.6	76.6	6.9
55	JM-3	CM	49.63	50.11	25.00	1.50	5.16	30.59	14.36	50	0.200	102.1	208.0	85.4	7.7
56	M1-1	CM	50.00	50.00	25.00	1.50	4.92	37.00	8.08	5	0.200	32.9	67.0	48.9	-
57	M1-2	CM	50.00	50.00	25.00	1.50	4.30	22.60	23.10	5	0.200	60.2	122.7	31.3	-
58	M1-3	CM	50.00	50.00	25.00	1.50	4.65	30.00	15.35	10	0.200	68.4	139.4	53.5	5.2
59	M1-4	CM	50.00	50.00	25.00	1.50	5.25	40.80	3.95	5	0.200	13.2	27.0	40.3	-
60	M2-2	CM	50.00	50.00	22.00	1.50	4.57	28.57	16.86	5	0.200	55.0	144.7	44.2	-
61	M2-4	CM	50.00	50.00	30.00	1.50	5.34	30.00	14.66	5	0.200	51.3	72.6	35.4	-
62	M3-1	CM	50.00	50.00	25.00	1.50	4.85	29.88	15.27	5	0.200	55.2	112.5	43.4	4.2
63	M3-2	CM	50.00	50.00	25.00	1.50	5.20	29.75	15.05	5	0.200	max. 54	-	corr. 98 %	
64	M3-3	CM	50.00	50.00	25.00	1.50	5.00	29.95	15.05	5	0.200	max. 16	-	corr. 30 %	
65	M3-4	CM	50.00	50.00	25.00	1.50	5.00	10.00	35.00	10	0.001	62.8	127.9	21.6	-
66	M4-1	CM	50.00	50.00	25.00	1.50	4.80	38.10	7.10	5	0.200	27.7	56.4	46.9	-
67	M4-2	CM	50.00	50.00	25.00	1.50	4.60	25.00	20.40	5	0.200	54.3	110.6	32.0	-
68	M4-3	CM	50.00	50.00	25.00	1.50	5.23	30.19	14.58	0	0.200	34.2	69.7	28.2	2.6
69	M5-1	CM	50.00	50.00	25.00	1.50	4.50	35.00	10.50	5	0.200	38.6	78.6	44.2	-
70	M5-2	CM	50.00	50.00	25.00	1.50	4.52	29.30	16.18	5	0.200	57.6	117.3	42.7	4.4
71	M5-3	CM	50.00	50.00	25.00	1.50	4.70	30.53	14.77	5	0.200	36.0	73.3	29.3	2.7
72	M5-4	CM	50.00	50.00	25.00	1.50	4.40	30.30	15.30	0	0.200	36.0	73.3	28.3	2.8
73	M6-1	CM	50.00	50.00	25.00	1.50	4.95	30.15	14.90	5	0.200	56.6	115.3	45.6	4.3

Sample			Dimensions							Variables		Results/Analysis			
No	Id.	Rock type	D	W	ID	t	a	b	IP	P	rate	Max. load	σ_{max}	τ_{max}	K_{IIC}
			[mm]	[mm]	[mm]	[mm]	[mm]	[mm]	[mm]	[MPa]	[mm/min]	[kN]	[MPa]	[MPa]	[MPam$^{1/2}$]
74	M6-2	CM	50.00	50.00	25.00	1.50	4.80	34.26	10.94	5	0.200	43.6	88.7	47.8	-
75	M6-3	CM	50.00	50.00	25.00	1.50	4.50	29.70	15.80	5	0.200	55.3	112.6	42.0	4.2
76	M6-4	CM	50.00	50.00	25.00	1.50	4.30	29.60	16.10	15	0.200	79.7	162.3	59.4	6.1
77	M6-5	CM	50.00	50.00	25.00	1.50	5.00	30.00	15.00	15	0.200	-	-	-	-
78	M7-1	CM	50.00	50.00	25.00	1.50	5.00	30.00	15.00	20	0.200	81.7	166.4	65.4	6.2
79	M10-1	CM	50.00	50.00	25.00	1.50	5.00	30.00	15.00	70	0.200	115.6	235.4	92.5	8.7
80	M10-2	CM	50.00	50.00	25.00	1.50	5.00	30.00	15.00	50	0.200	112.6	229.5	90.2	8.5
81	M10-3	CM	50.00	50.00	25.00	1.50	5.00	30.00	15.00	60	0.200	113.0	230.2	90.5	8.5
82	M10-4	CM	50.00	50.00	25.00	1.50	5.00	30.00	15.00	40	0.200	104.6	213.1	83.8	7.9
83	M10-5	CM	50.00	50.00	25.00	1.50	5.00	30.00	15.00	30	0.200	101.9	207.6	81.6	7.8
84	M10-6	CM	49.92	49.93	25.00	1.50	29.86	5.39	14.68	5	0.200	45.3	92.3	37.1	3.5
85	M10-7	CM	49.91	49.95	25.00	1.50	31.09	5.24	13.62	5	0.200	39.7	80.8	35.0	3.0
86	M10-8	CM	50.08	49.59	25.00	1.50	30.31	5.03	14.25	5	0.200	27.0	max. 55	-	-
87	M10-9	CM	50.00	50.20	25.00	1.50	30.18	5.19	14.83	5	0.200	50.8	103.4	41.1	3.9
88	M11-1	CM	50.10	49.60	22.00	1.50	6.47	34.84	8.29	5	0.200	23.0	60.4	37.5	-
89	M11-2	CM	50.01	50.05	22.00	1.50	6.36	34.22	9.47	5	0.200	39.5	103.8	56.5	-
90	M11-3	CM	50.00	50.14	30.00	1.50	5.00	30.32	14.82	5	0.200	50.5	71.4	34.4	-
91	M11-4	CM	50.05	50.08	30.00	1.50	5.09	30.36	14.63	5	0.200	58.3	82.4	40.2	-
92	M12-1	CM	49.94	50.14	25.00	1.50	4.96	30.32	14.86	40	0.200	101.4	206.6	82.0	7.7
93	M12-2	CM	50.03	50.12	25.00	1.50	5.02	30.90	14.20	40	0.200	100.4	204.5	84.9	7.6
94	M15-1	CM	50.00	50.20	25.00	1.50	5.30	30.20	14.70	5	2.000	59.3	120.8	48.5	4.5
95	M15-2	CM	50.00	50.10	25.00	1.50	5.10	30.10	14.90	5	2.000	58.0	118.2	46.8	4.4
96	M15-3	CM	50.00	50.10	25.00	1.50	5.20	30.20	14.70	5	20.000	58.5	119.2	47.8	4.5
97	M15-4	CM	50.00	50.20	25.00	1.50	5.00	30.10	15.10	5	20.000	64.9	132.2	51.6	5.0
98	M15-5	CM	50.00	50.10	25.00	1.50	5.10	30.30	14.70	5	0.200	52.3	106.5	42.7	4.0
99	M15-6	CM	50.00	50.00	25.00	1.50	30.00	5.00	15.00	5	0.200	49.7	101.1	39.8	3.8
100	M15-7	CM	50.00	50.00	25.00	1.50	5.00	30.00	15.00	5	0.020	54.3	110.5	43.5	4.1
101	M15-8	CM	50.00	50.00	25.00	1.50	5.00	30.30	14.70	5	0.020	54.9	111.8	44.9	4.2
102	M15-9	CM	50.00	50.10	25.00	1.50	5.30	30.50	14.30	5	0.002	50.7	103.3	42.6	3.9
103	M15-10	CM	50.00	50.10	25.00	1.50	5.10	30.20	14.80	5	100.000	50.1	102.1	40.7	3.8
104	ZM-1	CM	49.99	50.12	25.00	1.50	5.09	30.23	14.80	5	0.200	35.7	72.6	28.9	2.7
105	MT-1	CM	49.88	25.05	24.60	0.80	4.50	4.50	16.05	5	0.200	47.2	99.4	36.9	-
106	MT-2	CM	49.88	25.05	24.60	0.80	4.50	4.50	16.05	5	0.200	50.8	106.8	39.6	-
107	MT-3	CM	49.88	25.05	24.60	0.80	4.50	4.50	16.05	5	0.200	53.4	112.4	41.7	-
108	MT-5	CM	49.88	24.99	24.60	0.80	4.50	4.50	15.99	5	0.200	53.6	112.8	42.0	-
109	MT-6	CM	49.88	24.99	24.60	0.80	4.50	4.50	15.99	5	0.200	58.2	122.5	45.6	-
110	MT-7	CM	49.88	24.99	24.60	0.80	4.50	4.50	15.99	5	0.200	58.7	123.5	46.0	-
111	ZM-10	CM	49.70	50.15	25.00	1.49	5.30	30.90	13.95	5	0.200	53.8	109.6	46.3	4.1
112	ZM-11	CM	50.04	50.21	25.00	1.48	5.10	30.07	15.04	5	0.200	56.4	115.0	45.1	4.3
113	ZM-12	CM	49.74	50.14	24.70	3.00	5.20	30.49	14.45	5	0.200	45.2	94.2	35.9	-
114	ZM-13	CM	49.60	50.10	25.00	3.00	4.99	30.75	14.36	5	0.200	47.3	96.3	37.4	-
115	ZM-14	CM	49.60	50.12	22.00	3.00	5.30	30.50	14.32	5	0.200	46.2	121.4	41.0	-
116	S15-1	FB	50.00	50.10	25.00	1.50	5.00	30.40	14.70	5	0.200	41.8	85.2	34.2	3.2
117	S15-2	FB	50.00	50.10	25.00	1.50	5.20	30.40	14.50	4	0.200	33.2	67.7	27.5	2.5
118	S15-3	FB	50.00	50.10	25.00	1.50	5.00	30.40	14.70	5	0.200	39.8	81.1	32.5	3.0
119	S15-4	FB	50.00	50.00	25.00	1.50	5.20	30.10	14.70	5	2.000	39.9	81.2	32.6	3.0
120	S15-5	FB	50.00	50.00	25.00	1.50	5.20	30.30	14.50	5	2.000	35.8	72.8	29.6	2.7
121	S15-6	FB	50.00	50.10	25.00	1.50	5.00	30.30	14.80	5	20.000	42.1	85.7	34.2	3.2
122	S15-7	FB	50.00	50.10	25.00	1.50	4.90	30.30	14.90	5	0.020	33.3	67.9	26.9	2.5
123	S15-8	FB	50.00	50.10	25.00	1.50	5.20	30.20	14.70	5	0.020	34.5	70.2	28.2	2.6
124	S15-9	FB	50.00	50.00	25.00	1.50	5.20	30.30	14.50	5	0.020	29.6	60.3	24.5	2.2
125	S15-10	FB	50.00	50.00	25.00	1.50	5.20	29.90	14.90	0	0.200	14.7	29.9	11.8	1.1
126	S16-1	FB	50.00	50.00	25.00	1.50	5.10	30.20	14.70	10	0.200	36.9	75.1	30.1	2.8
127	S16-2	FB	50.00	50.10	25.00	1.50	5.20	30.30	14.60	10	0.200	35.8	72.9	29.4	2.7

Sample			Dimensions							Variables		Results/Analysis			
No	Id.	Rock type	D	W	ID	t	a	b	IP	P	rate	Max. load	σ_{max}	τ_{max}	K_{IIC}
			[mm]	[mm]	[mm]	[mm]	[mm]	[mm]	[mm]	[MPa]	[mm/min]	[kN]	[MPa]	[MPa]	[MPam$^{1/2}$]
128	S16-3	FB	50.00	49.90	25.00	1.50	5.00	30.30	14.60	30	0.200	73.3	149.3	60.3	5.5
129	S16-4	FB	50.00	50.00	25.00	1.50	5.40	30.10	14.50	50	0.200	76.4	155.6	63.3	5.6
130	S16-5	FB	50.11	49.60	25.00	1.50	5.11	31.05	13.44	70	0.200	76.8	156.5	68.7	5.6
131	S16-6	FB	50.08	50.04	25.00	1.50	5.54	31.29	13.21	40	0.200	66.9	136.2	60.8	5.0
132	L1-1	RL	50.00	50.00	22.00	1.50	20.25	10.25	19.50	5	0.200	53.5	140.7	37.2	-
133	L1-2	RL	50.00	50.00	25.00	1.50	20.25	10.00	19.75	5	0.200	65.2	132.8	39.7	-
134	L1-3	RL	50.00	50.00	22.00	1.50	5.25	38.25	6.50	5	0.200	19.3	50.8	40.2	-
135	L1-4	RL	50.00	25.00	25.00	1.50	4.30	4.75	15.95	15	0.200	42.4	86.4	31.9	3.2
136	L2-1	RL	50.00	50.00	25.00	1.50	10.00	20.00	20.00	15	0.200	75.3	153.4	45.2	-
137	L2-2	RL	50.00	50.00	25.00	1.50	5.00	31.00	14.00	5	0.200	42.8	87.2	36.7	3.3
138	L2-4	RL	50.00	50.00	25.00	1.50	5.00	30.00	15.00	0	0.200	29.9	60.9	23.9	2.3
139	L3-1	RL	50.00	50.00	25.00	1.50	20.00	9.75	20.25	5	0.200	60.3	122.9	35.8	-
140	L3-2	RL	50.00	50.00	30.00	1.50	20.00	10.00	20.00	5	0.200	64.0	90.5	32.3	-
141	L3-3	RL	50.00	50.00	25.00	1.50	4.75	30.25	15.00	15	0.200	60.2	122.6	48.2	4.6
142	L3-4	RL	50.00	25.00	25.00	1.50	6.00	16.80	2.20	5	0.200	8.0	16.3	43.7	-
143	L3-5	RL	50.00	25.00	25.00	1.50	4.90	9.75	10.35	10	0.200	39.2	79.9	45.5	3.0
144	L4-1	RL	50.00	50.00	25.00	1.50	5.00	30.25	14.75	10	0.200	57.0	116.1	46.4	4.3
145	L4-2	RL	50.00	25.00	25.00	1.50	5.25	5.00	14.75	1	0.200	23.1	47.1	18.8	1.8
146	L4-3	RL	50.00	25.00	30.00	1.50	6.30	5.80	12.90	5	0.200	32.9	46.5	25.8	-
147	L4-4	RL	50.00	25.00	25.00	1.50	5.00	10.00	10.00	15	0.200	44.0	89.6	52.9	-
148	L5-1	RL	50.00	50.00	25.00	1.50	5.00	40.00	5.00	5	0.200	23.5	48.0	56.6	-
149	L5-2	RL	50.00	50.00	30.00	1.50	20.00	10.00	20.00	5	0.200	60.0	84.9	30.3	-
150	L5-3	RL	50.00	50.00	25.00	1.50	10.00	17.25	22.75	10	0.200	70.6	143.8	37.3	-
151	L5-4	RL	50.00	25.00	25.00	1.50	4.90	9.60	10.50	5	0.200	28.4	57.9	32.5	-
152	L6-1	RL	50.00	50.00	22.00	1.50	10.00	20.50	19.50	5	0.200	50.8	133.6	35.3	-
153	L6-2	RL	50.00	50.00	22.00	1.50	19.75	9.75	20.50	5	0.200	40.2	105.8	26.6	-
154	L7-1	RL	50.00	25.00	25.00	1.50	6.50	6.70	11.80	5	0.200	34.4	70.1	35.0	2.6
155	L7-2	RL	50.00	50.00	30.00	1.50	20.00	10.00	20.00	5	0.200	78.0	110.3	39.4	-
156	L7-3	RL	50.00	25.00	25.00	1.50	5.00	5.00	15.00	10	0.200	40.8	83.1	32.7	3.1
157	L8-1	RL	50.00	25.00	25.00	1.50	4.90	4.90	15.20	20	0.200	64.5	131.4	51.0	4.9
158	L8-2	RL	50.00	50.00	25.00	1.50	5.00	30.30	14.70	1	0.200	30.6	62.3	25.0	2.3
159	L8-3	RL	50.00	50.00	25.00	1.50	10.00	20.00	20.00	5	0.200	64.0	130.4	38.4	-
160	L9-1	RL	50.00	50.00	25.00	1.50	4.90	35.25	9.85	5	0.200	36.6	74.6	44.6	-
161	L9-2	RL	50.00	50.00	25.00	1.50	5.20	20.10	24.70	5	0.200	72.1	146.9	35.1	-
162	L9-3	RL	50.00	50.00	25.00	1.50	5.50	33.00	11.50	5	0.200	42.8	87.2	44.7	3.3
163	L9-4	RL	50.00	25.00	25.00	1.50	7.75	11.90	5.35	5	0.200	max. 22	-	-	-
164	L10-1	RL	50.00	50.00	25.00	1.50	6.40	34.20	9.40	5	0.200	44.3	90.2	56.6	-
165	L10-2	RL	50.00	50.00	25.00	1.50	7.75	34.40	7.85	5	0.200	max. 40	-	corr. 90%	
166	L10-3	RL	50.00	50.00	25.00	1.50	6.75	34.80	8.45	5	0.200	max. 36	-	corr. 80 %	
167	L10-4	RL	50.00	50.00	25.00	1.50	5.80	32.50	11.70	5	0.200	max. 32	-	corr. 70 %	
168	L10-5	RL	50.00	50.00	25.00	1.50	5.10	29.80	15.10	5	0.200	57.4	116.9	45.7	4.4
169	L10-6	RL	50.00	50.00	25.00	1.50	5.00	20.00	25.00	5	0.200	78.4	159.7	37.7	-
170	L11-1	RL	50.00	50.00	25.00	1.50	6.44	32.75	10.81	10	0.200	47.9	97.6	53.2	-
171	L11-2	RL	50.00	50.00	25.00	1.50	6.75	33.85	9.40	15	0.200	49.1	100.0	62.7	-
172	L12-1	RL	50.00	25.00	25.00	1.50	5.30	0.00	19.70	5	0.200	53.8	109.6	32.8	-
173	L14-1	RL	50.00	50.00	25.00	1.50	30.00	5.00	15.00	30	0.200	55.5	113.1	44.4	4.2
174	L14-2	RL	50.00	50.00	25.00	1.50	5.00	30.00	15.00	30	0.200	63.1	128.5	50.5	4.8
175	L14-3	RL	50.00	50.00	25.00	1.50	5.00	30.00	15.00	30	0.200	65.8	134.0	52.7	5.0
176	L14-4	RL	50.00	50.00	25.00	1.50	5.00	30.00	15.00	10	0.200	56.2	114.4	45.0	4.3
177	L14-5	RL	50.00	50.00	25.00	1.50	5.00	30.00	15.00	20	0.200	56.7	115.4	45.4	4.3
178	L14-6	RL	50.00	50.00	25.00	1.50	5.00	30.00	15.00	40	0.200	80.3	163.6	64.3	6.1
179	L14-7	RL	50.00	50.00	25.00	1.50	5.00	30.00	15.00	40	0.200	-	-	-	-
180	L14-9	RL	50.00	50.00	25.00	1.50	5.00	30.00	15.00	40	0.200	87.9	179.1	70.4	6.6
181	L14-10	RL	50.00	50.00	25.00	1.50	5.00	30.00	15.00	30	0.200	85.7	174.6	68.6	6.5

Sample			Dimensions							Variables		Results/Analysis			
No	Id.	Rock type	D	W	ID	t	a	b	IP	P	rate	Max. load	σ_{max}	τ_{max}	K_{IIC}
			[mm]	[mm]	[mm]	[mm]	[mm]	[mm]	[mm]	[MPa]	[mm/min]	[kN]	[MPa]	[MPa]	[MPam$^{1/2}$]
182	L14-11	RL	50.00	50.00	25.00	1.50	5.00	30.00	15.00	20	0.200	78.4	159.7	62.8	5.9
183	L14-12	RL	50.00	50.00	25.00	1.50	5.00	30.00	15.00	70	0.200	96.1	195.8	77.0	7.2
184	L14-13	RL	50.00	50.00	25.00	1.50	5.00	30.00	15.00	35	0.200	84.6	172.3	67.7	6.4
185	L14-14	RL	50.00	50.00	25.00	1.50	5.00	30.00	15.00	50	0.200	92.5	188.4	74.1	7.0
186	L15-0	RL	50.00	50.00	25.00	1.50	5.00	30.00	15.00	150	0.200	max. 572	-	-	-
187	L15-1	RL	50.00	50.10	25.00	1.50	5.20	30.30	14.60	5	2.000	29.4	60.0	24.2	2.2
188	L15-2	RL	50.00	49.60	25.00	1.50	5.30	30.40	13.90	5	2.000	42.1	85.8	36.4	3.2
189	L15-3	RL	50.00	50.10	25.00	1.50	5.10	30.20	14.80	5	2.000	52.0	105.9	42.2	4.0
190	L15-4	RL	50.00	50.10	25.00	1.50	5.20	30.40	14.50	5	20.000	33.1	67.5	27.4	2.5
191	L15-5	RL	50.00	50.10	25.00	1.50	5.10	30.10	14.90	5	20.000	49.8	101.5	40.2	3.8
192	L15-6	RL	50.00	50.10	25.00	1.50	5.00	30.60	14.50	5	0.020	46.0	93.7	38.1	3.5
193	L15-7	RL	50.00	50.10	25.00	1.50	5.10	30.40	14.60	5	0.020	42.5	86.5	34.9	3.2
194	L17-1	RL	49.87	50.15	25.00	1.50	5.00	30.25	14.90	60	0.200	96.1	195.8	77.5	7.2
195	ZL-1	RL	49.63	50.13	22.00	1.50	6.00	31.92	12.21	5	0.200	32.4	85.3	36.0	-
196	ZL-2	RL	49.64	50.09	22.00	1.50	5.90	33.70	10.49	5	0.200	21.6	56.7	27.8	-
197	ZL-3	RL	50.03	50.10	30.00	1.50	5.00	30.56	14.54	5	0.200	44.5	62.9	30.9	-
198	ZL-4	RL	49.92	50.06	30.00	1.50	6.30	31.76	12.00	5	0.200	28.0	39.6	23.5	-
199	T1-1a	TG	50.00	50.00	25.00	1.50	4.90	29.90	15.20	5	0.200	81.0	165.0	64.0	6.5
200	T1-1c	TG	50.00	49.75	25.00	1.50	5.05	30.00	14.70	15	0.200	118.0	240.4	96.4	9.4
201	T1-1d	TG	50.00	50.00	25.00	1.50	5.00	29.90	15.10	30	0.200	197.0	401.3	156.7	15.6
202	T3-1a	TG	50.00	50.10	25.00	1.50	5.00	30.00	15.10	50	0.200	179.0	364.6	142.4	14.1
203	T3-1b	TG	50.00	50.05	25.00	1.50	5.05	30.05	14.95	70	0.200	177.0	360.6	142.2	13.9
204	T3-1c	TG	50.00	47.80	25.00	1.50	2.80	27.80	17.20	40	0.100	194.4	396.0	135.8	15.4
205	T3-1d	TG	50.00	50.10	25.00	1.50	5.05	29.95	15.10	30	0.200	159.3	324.5	126.7	12.6
206	T4-1a	TG	50.00	49.10	25.00	1.50	4.10	28.90	16.10	0	0.200	55.1	112.2	41.1	4.4
207	T4-1d	TG	50.00	50.10	25.00	1.50	4.60	30.00	15.50	40	0.100	-	-	-	-
208	T8-1a	TG	50.00	50.00	25.00	1.50	5.10	30.00	14.90	50	0.200	177.0	360.6	142.7	14.0
209	T8-1b	TG	50.00	50.15	25.00	1.50	5.00	30.10	15.05	70	0.200	183.0	372.8	146.1	14.4
210	T8-1c	TG	50.00	48.00	25.00	1.50	5.00	30.00	13.00	5	0.200	84.0	171.1	77.6	6.7
211	T8-1d	TG	50.00	49.45	25.00	1.50	5.00	30.05	14.40	15	0.200	119.0	242.4	99.3	9.5
212	T8-2a	TG	50.00	49.70	25.00	1.50	5.05	30.20	14.45	20	0.200	140.0	285.2	116.4	11.1
213	T8-2d	TG	50.00	50.00	25.00	1.50	5.00	30.00	15.00	15	0.200	-	-	-	-
214	T14-1a	TG	50.00	50.05	25.00	1.50	5.00	30.05	15.00	30	0.200	137.3	279.7	109.9	10.9
215	T14-1b	TG	50.00	50.05	25.00	1.50	5.00	29.95	15.10	50	0.200	176.0	358.5	140.0	13.9
216	T14-1c	TG	50.00	50.00	25.00	1.50	5.00	30.15	14.85	15	0.200	115.0	234.3	93.0	9.1
217	T15-1a	TG	50.00	50.00	25.00	1.50	5.00	30.00	15.00	5	0.200	80.0	163.0	64.1	6.4
218	T15-1b	TG	50.00	48.80	25.00	1.50	5.10	30.00	13.70	70	0.200	198.0	403.3	173.6	15.6
219	T16-1a	TG	50.00	50.05	25.00	1.50	5.00	29.95	15.10	30	0.200	197.0	401.3	156.7	15.6

B.3 Other testing

Id.: Specimen Identifier; Rock type: ÄD: Äspö diorite, AG: Aue granite, CM: Carrara marble, FB: Flechtingen sandstone, RL: Rüdersdorf limestone, TG: Mizunami granite; D: diameter; L: length, displ. rate: displacement rate; σ_t: Tensile strength; σ_C: uniaxial compressive strength strength.

Sample			Dimensions/Test Variables				Test Results			Comment
No	Id.	Rock type	D	L	loading rate	displ. rate	Max. load	σ_t	σ_C	
			[mm]	[mm]	[N/s]	[mm/min]	[kN]	[MPa]	[MPa]	
1	FB-B1	FB	49.8	35.2	200	-	17.8	6.5	-	⊥ layering
2	FB-B2	FB	49.7	39.9	400	-	9.1	-	-	⊥ layering
3	FB-B3	FB	50.0	33.6	400	-	16.0	6.1	-	‖ layering
4	FB-B4	FB	49.7	34.3	400	-	15.2	5.7	-	⊥ layering
5	FB-B5	FB	49.7	34.7	400	-	15.2	5.6	-	⊥ layering
6	FB-B6	FB	50.0	35.2	400	-	15.2	5.5	-	‖ layering
7	L-B1	RL	49.8	38.6	400	-	15.0	5.0	-	‖ layering
8	L-B2	RL	49.9	41.6	400	-	23.7	7.3	-	⊥ layering
9	L-B3	RL	50.0	46.5	400	-	29.8	8.1	-	⊥ layering
10	CM-B1	CM	50.0	50.2	400	-	25.6	6.5	-	
11	AG-B1	AG	49.9	49.5	400	-	29.9	7.7	-	
12	AG-B2	AG	49.8	48.8	400	-	28.3	7.4	-	
13	TG-B1	TG	50.0	45.0	400	-	35.0	9.9	-	
14	TG-B2	TG	49.9	43.2	400	-	32.2	9.5	-	
15	TG-B3	TG	50.1	47.8	400	-	34.5	9.2	-	
16	TG-B4	TG	49.5	47.4	400	-	37.0	10.0	-	
17	B1	CM	50.0	100.3	-	0.1	187.0	-	95	
18	B2	CM	49.7	100.1	-	0.1	-	-	-	
19	A1	FB	50.0	100.0	-	0.1	200.0	-	102	‖ layering
20	A2	FB	50.0	100.0	-	0.1	117.2	-	-	‖ layering
21	AT2	CM	50.1	99.5	-	0.1	219.3	-	107	

C TECHNICAL DRAWINGS

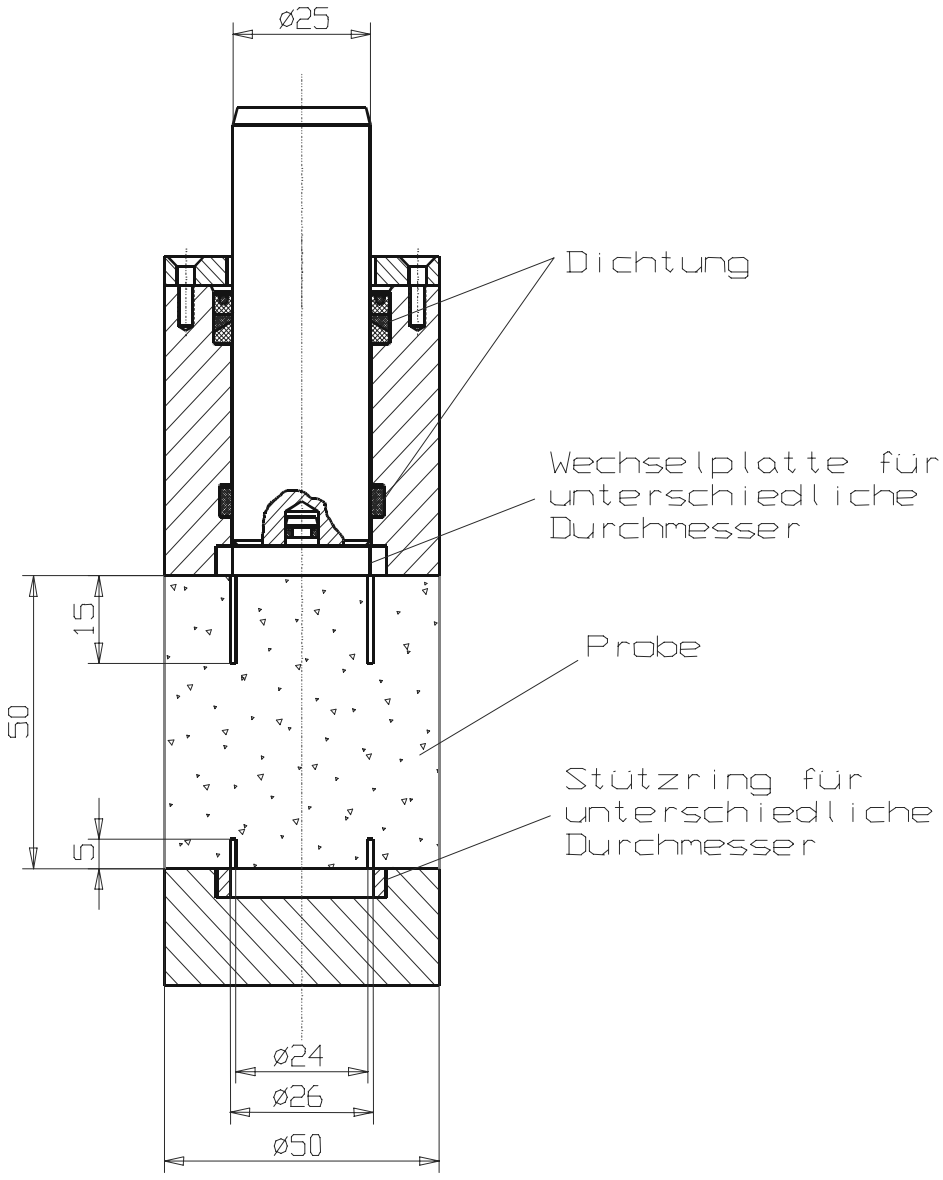

Set-up of PTS-assembly for pressure vessel.

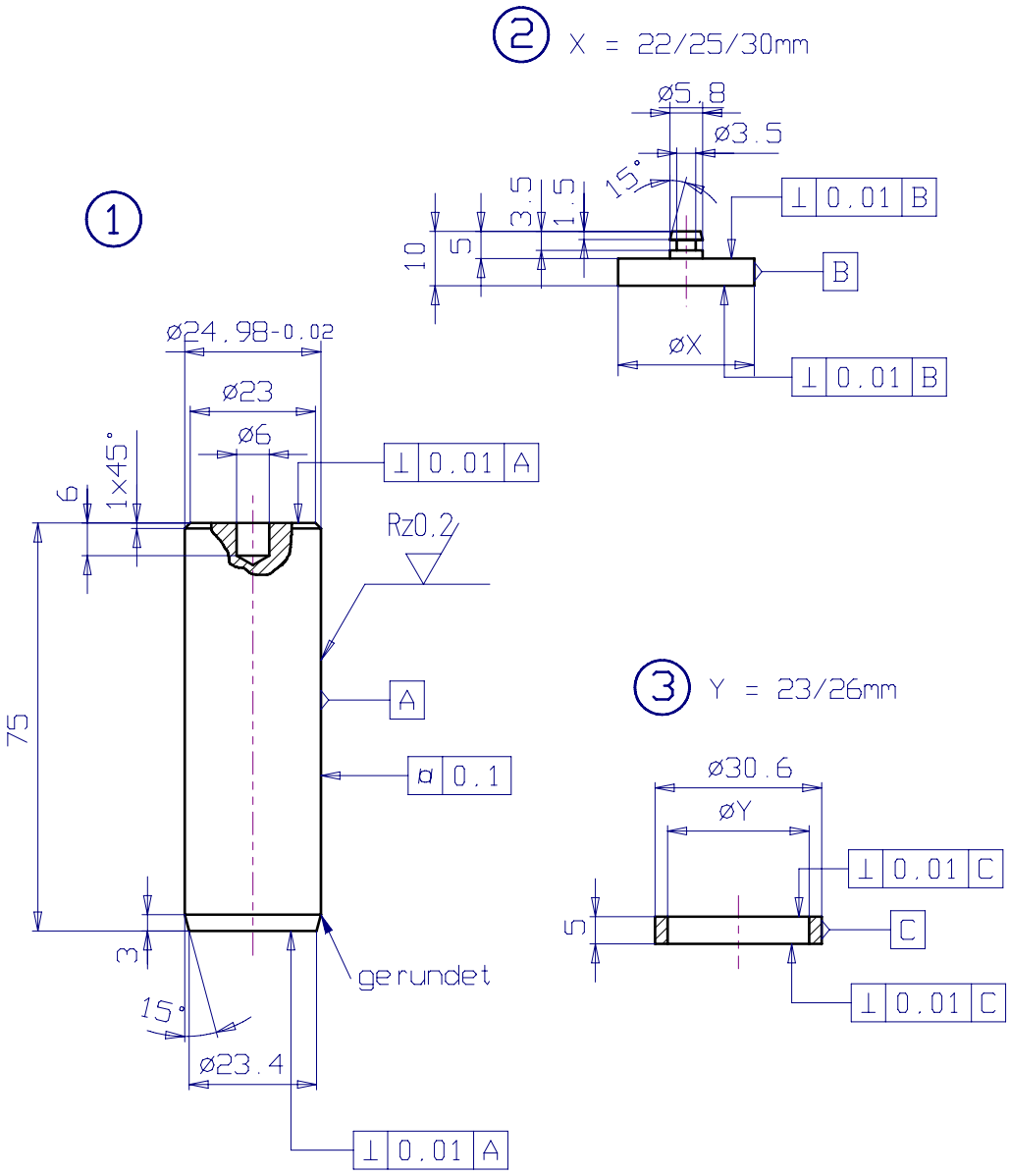

HRC 55+/-2

	M. Naumann				
	Datum		M 1:1	Material 1.2363	
Z.-Nummer MTS-1.1		Z.-Titel MTS - Kammer Stempel / Platte / Ring			
GFZ Potsdam					

PTS- assembly for pressure vessel, stamp.

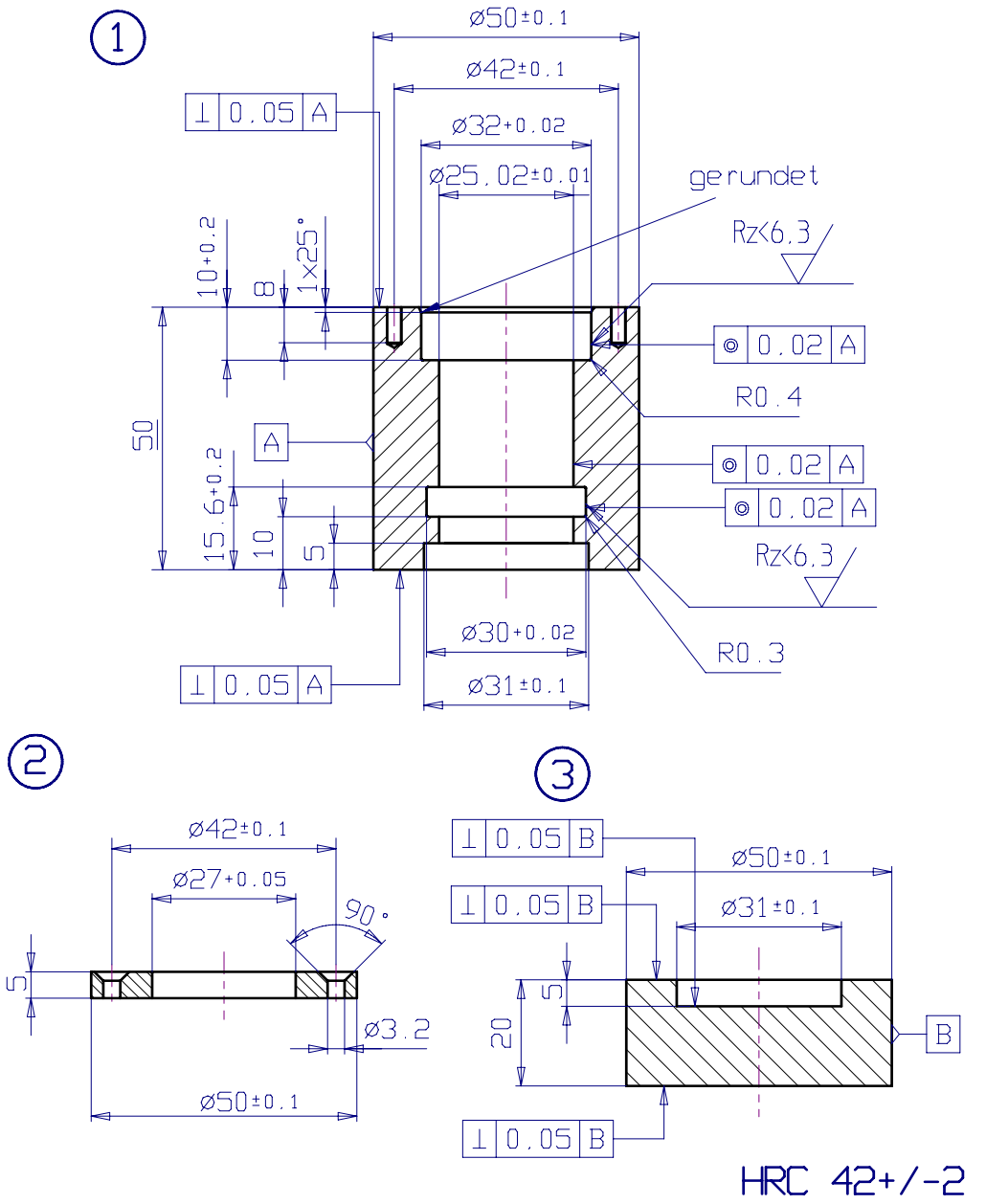

	M. Naumann			
	Datum		M 1:1	Material 1.2343
Z.-Nummer MTS-1.2		Z.-Titel	MTS - Kammer Oberteil / Unterteil	
GFZ Potsdam				

PTS- assembly for pressure vessel, top and bottom support.

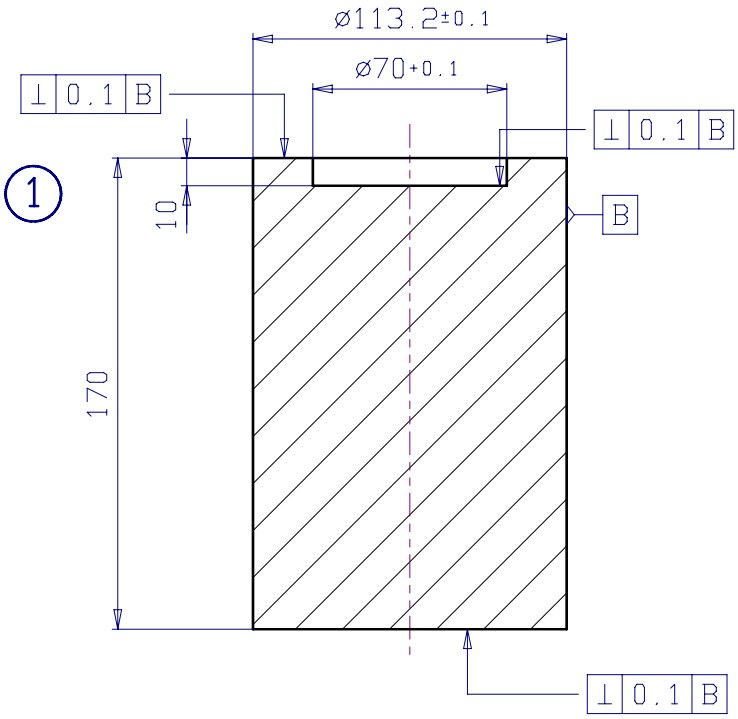

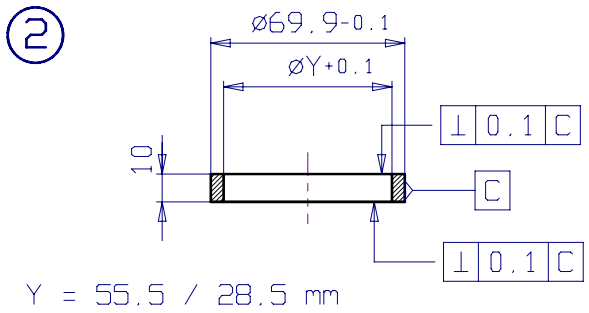

	M. Naumann				
	Datum 30.01.03		M 1:2	Material 1.2363	
Z.-Nummer Hoek-1.0		Z.-Titel	Hoek - Kammer Unterteil		
GFZ Potsdam					

PTS- assembly for large diameter Hoek-Cell, bottom parts

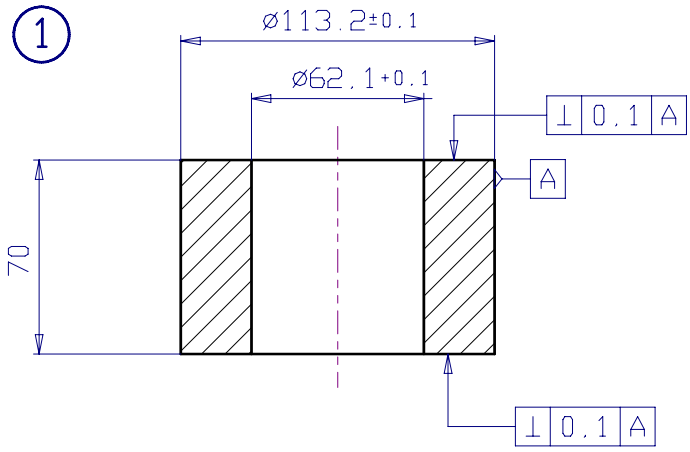

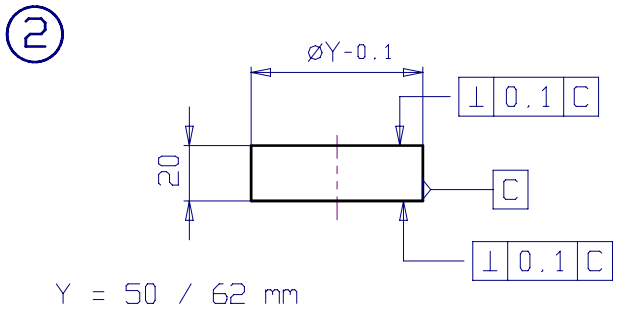

	M. Naumann				
	Datum 30.01.03		M 1:2	Material 1.2363	
Z.-Nummer Hoek-2.0		Z.-Titel	Hoek - Kammer Oberteil		
GFZ Potsdam					

PTS- assembly for large diameter Hoek-Cell, top parts

.

D TEMPLATES

The templates below are for TestWareII by MTS. Note that the corresponding configuration links are not necessarily correct for all systems.

D.1 K_{IC} - template

Procedure Name =
File Specification = D:\
Software Version = 4.0D

Data File Options
File Format = Excel Text File
Log Events = Yes
Include Procedure Description = No

Recovery Options
Autosave disabled.

Sample Information: Step
Step Done Trigger 1 = User Defined Sample Information

General Sample Information: Data Input
Start Trigger = Step Start
End Trigger = <none>
Window = Sample Data Input 1
Utilization = Process Parameterisation

Detailed Sample Information: Data Input
Start Trigger = General Sample Information
End Trigger = <none>
Window = Sample Data Input 2
Utilization = Process Parameterisation

User Defined Sample Information: Data Input
Start Trigger = Detailed Sample Information
End Trigger = <none>
Window = Additional Data Input
Utilization = Process Parameterisation

For each specimen: Begin Loop
Counter Name = nSpecimens
Total Count = 1

Specimen Information: Step
Step Done Trigger 1 = Pre-test Specimen Information

Pre-test Specimen Information: Data Input
Start Trigger = Step Start
End Trigger = <none>
Window = Pre-test Specimen Data Input
Utilization = Process Parameterisation and Execution
Test Type = Fracture Toughness
Test Title = Level-II-Versuch

Test Execution: Step
Step Done Trigger 1 = Operator Terminate Test
Step Done Trigger 2 = END

Query Start of Test: Operator Event
Start Trigger = Step Start
End Trigger = <none>
Button ID = Button 1
Single Shot = Yes
Button Label = Start
Description=Press start test this specimen.
Grab Focus = Yes

Operator Terminate Test: Operator Event
Start Trigger = Query Start of Test
End Trigger = <none>
Button ID = Button 2
Single Shot = Yes
Button Label = Terminate
Description = Press to terminate
Grab Focus = Yes

Data Collection time: Data Acquisition
Start Trigger = Query Start of Test
End Trigger = <none>
Mode = Level Crossing
Buffer Type = Continuous
Master Channel = Time
Slave Channel 1 = Weg
Slave Channel 2 = Kraft 1000kN
Slave Channel 3 = Clip-Gage
Slave Channel 4 = Kraft 25 kN
Data Header = Load Level Crossing Data
Level Increment = 0.25 (Sec)
Buffer Size = 1024

Load Displacement Plot: Run-time Plotting
Start Trigger = Query Start of Test
End Trigger = <none>
Title = Load vs. Clip-Gage
X Axis = Y
Channel = Kraft 25 KN
Scaling = Linear
Minimum = 0.000000 N
Maximum = 1200.000000 N
Y Axis = X
Channel 1 = Clip-gage
Colour = Red
Style = Solid
Minimum = 0.000000 (none)
Maximum = 0.010000 (none)
X Axis Level Cross = Not Enabled
Y Axis Level Cross = Not Enabled
Reduce Rate on Decimation = Not Enabled

time axial displacement: Run-time Plotting
Start Trigger = Query Start of Test
End Trigger = <none>
Title = Plot Title
X Axis = X
Channel = Time
Scaling = Linear
Minimum = 0.000000 Sec
Maximum = 20.000000 Sec
Y Axis = Y
Channel 1 = Weg
Color = Red
Style = Solid
Scaling = Linear
Minimum = 0.000000 mm
Maximum = 0.100000 mm
X Axis Level Cross = Not Enabled
Y Axis Level Cross = Not Enabled
Reduce Rate on Decimation = Not Enabled

Load vs. Time Plot: Run-time Plotting
Start Trigger = Query Start of Test
End Trigger = <none>
Title = Load vs. Time
X Axis = X
Channel = Time
Scaling = Linear
Minimum = 0.000000 Sec
Maximum = 20.000000 Sec
Y Axis = Y
Channel 1 = Kraft 25 kN
Color = Red
Style = Solid
Minimum = 0.000000 N
Maximum = 1000.000000 N
X Axis Level Cross = Not Enabled
Y Axis Level Cross = Not Enabled
Reduce Rate on Decimation = Not Enabled

First Ramp Command: Run-time Rate Control
Start Trigger = Query Start of Test
End Trigger = Initiate First Unload
Segment Shape = Ramp
Visible at Run Time = 0
Record Data = 1
Axial
Control Mode = Clip-Gage SG
Rate Type = 0.000003 m/Sec
Minimum Rate = 0.000000 m/Sec
Maximum Rate = 0.005000 m/Sec
Endlevel = 3 (mm)

Initiate First Unload: Operator Event
Start Trigger = Query Start of Test
End Trigger = <none>
Button ID = Button 1
Single Shot = Yes
Button Label = Unload
Description = Press to initiate first unload.
Grab Focus = Yes

First Unload: Run-time Rate Control
Start Trigger = First Ramp Command
End Trigger = Stop First Unload
Segment Shape = Ramp
Visible at Run Time = 0
Record Data = 1
Axial
Control Mode = Clip-Gage SG
Rate Type = 0.150000 mm/Min
Minimum Rate = 0.000000 mm/Min
Maximum Rate = 300.000011 mm/Min
Endlevel = 0 (mm)

Stop First Unload: Data Limit Detector
Start Trigger = Initiate First Unload
End Trigger = <none>
Data Channel = Kraft 25 kN
Limit Value = 0.15 (kN)
Limit Value is = Absolute
Detector Options = Less than Limit Value
Trigger Option = Trigger Once

Second Ramp Command: Run-time Rate Control
Start Trigger = First Unload
End Trigger = Initiate Second Unload
Segment Shape = Ramp
Visible at Run Time = 0
Record Data = 1
Axial
Control Mode = Clip-Gage SG
Rate Type = 0.150000 mm/Min

Minimum Rate = 0.000000 mm/Min
Maximum Rate = 300.000011 mm/Min
Endlevel = 3 (mm)

Initiate Second Unload: Operator Event
Start Trigger = First Unload
End Trigger = <none>
Button ID = Button 1
Single Shot = Yes
Button Label = Unload
Description= Press to initiate second unload.
Grab Focus = Yes

Second Unload: Run-time Rate Control
Start Trigger = Second Ramp Command
End Trigger = Stop Second Unload
Segment Shape = Ramp
Visible at Run Time = 0
Record Data = 1
Axial
Control Mode = Clip-Gage SG
Rate Type = 0.150000 mm/Min
Minimum Rate = 0.000000 mm/Min
Maximum Rate = 300.000011 mm/Min
Endlevel = 0 (mm)

Stop Second Unload: Data Limit Detector
Start Trigger = Initiate Second Unload
End Trigger = <none>
Data Channel = Kraft 25 kN
Limit Value = 0.15 (kN)
Limit Value is = Absolute
Detector Options = Less than Limit Value
Trigger Option = Trigger Once

Third Ramp Command: Run-time Rate Control
Start Trigger = Second Unload
End Trigger = Initiate Third Unload
Segment Shape = Ramp
Visible at Run Time = 0
Record Data = 1
Axial
Control Mode = Clip-Gage SG
Rate Type = 0.150000 mm/Min
Minimum Rate = 0.000000 mm/Min
Maximum Rate = 300.000011 mm/Min
Endlevel = 3 (mm)

Third Ramp End Time Stamp: Data Acquisition
Start Trigger = Third Ramp Command
End Trigger = <none>
Mode = Timed
Buffer Type = Single
Master Channel = Time
Data Header = RAMP_END
Time Increment = 0.01 (Sec)
Buffer Size = 1

Initiate Third Unload: Operator Event
Start Trigger = Second Unload
End Trigger = <none>
Button ID = Button 1
Single Shot = Yes
Button Label = Unload
Description = Press to initiate third unload.
Grab Focus = Yes

Third Unload: Run-time Rate Control
Start Trigger = Third Ramp Command
End Trigger = Stop Third Unload
Segment Shape = Ramp
Visible at Run Time = 0
Record Data = 1
Axial
Control Mode = Clip-Gage SG
Rate Type = 0.150000 mm/Min
Minimum Rate = 0.000000 mm/Min
Maximum Rate = 300.000011 mm/Min
Endlevel = 0 (mm)

Stop Third Unload: Data Limit Detector
Start Trigger = Initiate Third Unload
End Trigger = <none>
Data Channel = Kraft 25 kN
Limit Value = 0.15 (kN)
Limit Value is = Absolute
Detector Options = Less than Limit Value
Trigger Option = Trigger Once

Fourth Ramp Command: Run-time Rate Control
Start Trigger = Third Unload
End Trigger = Initiate Fourth Unload
Segment Shape = Ramp
Visible at Run Time = 0
Record Data = 1
Axial
Control Mode = Clip-Gage SG
Rate Type = 0.150000 mm/Min
Minimum Rate = 0.000000 mm/Min
Maximum Rate = 300.000011 mm/Min
Endlevel = 3 (mm)

Fourth Ramp End Time Stamp: Data Acquisition
Start Trigger = Fourth Ramp Command
End Trigger = <none>
Mode = Timed
Buffer Type = Single
Master Channel = Time
Data Header = RAMP_END
Time Increment = 0.01 (Sec)
Buffer Size = 1

Initiate Fourth Unload : Operator Event
Start Trigger = Third Unload
End Trigger = <none>
Button ID = Button 1
Single Shot = Yes
Button Label = Unload
Description = Press to initiate fourth unload.
Grab Focus = Yes

Fourth Unload : Run-time Rate Control
Start Trigger = Fourth Ramp Command
End Trigger = Stop Fourth Unload
Segment Shape = Ramp
Visible at Run Time = 0
Record Data = 1
Axial
Control Mode = Clip-Gage SG
Rate Type = 0.150000 mm/Min
Minimum Rate = 0.000000 mm/Min
Maximum Rate = 300.000011 mm/Min
Endlevel = 0 (mm)

Stop Fourth Unload : Data Limit Detector
Start Trigger = Initiate Fourth Unload
End Trigger = <none>
Data Channel = Kraft 25 kN
Limit Value = 0.15 (kN)
Limit Value is = Absolute
Detector Options = Less than Limit Value
Trigger Option = Trigger Once

Fifth Ramp Command : Run-time Rate Control
Start Trigger = Fourth Unload
End Trigger = Initiate Fifth Unload
Segment Shape = Ramp
Visible at Run Time = 0
Record Data = 1
Axial
Control Mode = Clip-Gage SG
Rate Type = 0.150000 mm/Min
Minimum Rate = 0.000000 mm/Min
Maximum Rate = 300.000011 mm/Min
Endlevel = 3 (mm)

Fifth Ramp End Time Stamp : Data Acquisition
Start Trigger = Fifth Ramp Command
End Trigger = <none>
Mode = Timed
Buffer Type = Single
Master Channel = Time
Data Header = RAMP_END
Time Increment = 0.01 (Sec)
Buffer Size = 1

Initiate Fifth Unload : Operator Event
Start Trigger = Fourth Unload
End Trigger = <none>
Button ID = Button 1
Single Shot = Yes
Button Label = Unload
Description = Press to initiate fifth unload.
Grab Focus = Yes

Fifth Unload : Run-time Rate Control
Start Trigger = Fifth Ramp Command
End Trigger = Stop Fifth Unload
Segment Shape = Ramp
Visible at Run Time = 0
Record Data = 1
Axial
Control Mode = Clip-Gage SG
Rate Type = 0.150000 mm/Min
Minimum Rate = 0.000000 mm/Min
Maximum Rate = 300.000011 mm/Min
Endlevel = 0 (mm)

Stop Fifth Unload : Data Limit Detector
Start Trigger = Initiate Fifth Unload
End Trigger = <none>
Data Channel = Kraft 25 kN
Limit Value = 0.15 (kN)
Limit Value is = Absolute
Detector Options = Less than Limit Value
Trigger Option = Trigger Once

Sixth Ramp Command : Run-time Rate Control
Start Trigger = Fifth Unload
End Trigger = Initiate Sixth Unload
Segment Shape = Ramp
Visible at Run Time = 0
Record Data = 1
Axial
Control Mode = Clip-Gage SG
Rate Type = 0.150000 mm/Min
Minimum Rate = 0.000000 mm/Min
Maximum Rate = 300.000011 mm/Min
Endlevel = 3 (mm)

Sixth Ramp End Time Stamp : Data Acquisition
Start Trigger = Sixth Ramp Command
End Trigger = <none>
Mode = Timed
Buffer Type = Single
Master Channel = Time
Data Header = RAMP_END
Time Increment = 0.01 (Sec)
Buffer Size = 1

Initiate Sixth Unload : Operator Event
Start Trigger = Fifth Unload
End Trigger = <none>
Button ID = Button 1
Single Shot = Yes
Button Label = Unload
Description = Press to initiate sixth unload.
Grab Focus = Yes

Sixth Unload : Run-time Rate Control
Start Trigger = Sixth Ramp Command
End Trigger = Stop Sixth Unload
Segment Shape = Ramp
Visible at Run Time = 0
Record Data = 1
Axial
Control Mode = Clip-Gage SG
Rate Type = 0.150000 mm/Min
Minimum Rate = 0.000000 mm/Min
Maximum Rate = 300.000011 mm/Min
Endlevel = 0 (mm)

Stop Sixth Unload : Data Limit Detector
Start Trigger = Initiate Sixth Unload
End Trigger = <none>
Data Channel = Kraft 25 kN
Limit Value = 0.15 (kN)
Limit Value is = Absolute
Detector Options = Less than Limit Value
Trigger Option = Trigger Once

Last Loading : Run-time Rate Control
Start Trigger = Sixth Unload
End Trigger = END
Segment Shape = Ramp
Visible at Run Time = 1
Record Data = 0
Axial
Control Mode = Clip-Gage SG
Rate Type = 0.150000 mm/Min
Minimum Rate = 0.006000 mm/Min
Maximum Rate = 0.600000 mm/Min
Endlevel = 3 (mm)

END : Operator Event
Start Trigger = Stop Sixth Unload
End Trigger = <none>
Button ID = Button 3
Single Shot = Yes
Button Label = END
Description = end of test
Grab Focus = Yes

Release Load From Specimen : Step
Step Done Trigger 1 = Detect Zero Load

Retract Actuator in Stroke Control : Monotonic Command
Start Trigger = Step Start
End Trigger = <none>
Segment Shape = Ramp
Rate = 5e-005 (mm/Sec)
Axial
Control Mode = Clip-Gage SG
End level = 0 (mm)

Detect Zero Load : Data Limit Detector
Start Trigger = Step Start
End Trigger = <none>
Data Channel = Kraft 25 kN
Limit Value = 0 (kN)
Limit Value is = Absolute
Detector Options = Less than Limit Value
Trigger Option = Trigger Once

Specimen Post-test Information : Step
Step Done Trigger 1 = Stop Current Test

Post-test Specimen Information : Data Input
Start Trigger = Step Start
End Trigger = <none>
Window = Post-test Specimen Data Input
Utilization = Process Parameterisation and Execution

Stop Current Test : Program Control
Start Trigger = Post-test Specimen Information
End Trigger = <none>
Action = Program Stop

Message =
Screen = Yes
LUC Display = No
Data File = No

For each specimen : End Loop

D.2 K_{IIC} - templates

D.2.1 Template (Hoek Cell)

Procedure Name =
File Specification = D:\
Software Version = 4.0D

Data File Options
File Format = Plain Text File
Log Events = Yes
Include Procedure Description = No

Recovery Options
Autosave disabled.

Sample Information : Step
Step Done Trigger 1 = User Defined Sample Information

General Sample Information : Data Input
Start Trigger = Step Start
End Trigger = <none>
Window = Sample Data Input 1
Utilization = Process Parameterisation

Detailed Sample Information : Data Input
Start Trigger = General Sample Information
End Trigger = <none>
Window = Sample Data Input 2
Utilization = Process Parameterisation

User Defined Sample Information : Data Input
Start Trigger = Detailed Sample Information
End Trigger = <none>
Window = Additional Data Input
Utilization = Process Parameterisation

For each specimen : Begin Loop
Counter Name = specimen
Total Count = 1
Specimen Pre-test Information : Step
Step Done Trigger 1 = Query Start Test

Specimen Pre-test Information : Data Input
Start Trigger = Step Start
End Trigger = <none>
Window = Pre-test Specimen Data Input
Utilization = Process Parameterisation and Execution

Query Start Test : Operator Event
Start Trigger = Specimen Pre-test Information
End Trigger = <none>
Button ID = Button 1
Single Shot = Yes
Button Label = Start
Description = Press to start the test
Grab Focus = Yes

Test Execution : Step
Step Done Trigger 1 = Button: Operator Terminate the Test
Step Done Trigger 2 = Unloading

Data Collection : Data Acquisition
Start Trigger = Step Start
End Trigger = <none>
Mode = Level Crossing
Buffer Type = Continuous
Master Channel = Time
Slave Channel 1 = Weg
Slave Channel 2 = Kraft 1000kN
Data Header = Begin Level Crossing Data Acq.
Level Increment = 0.5 (Sec)
Buffer Size = 2048

Force vs. Time Plot : Run-time Plotting
Start Trigger = Step Start
End Trigger = <none>
Title = Force vs. Time
X Axis = X
Channel = Time
Scaling = Linear
Minimum = 0.000000 Sec
Maximum = 30.000000 Sec
Y Axis = Y
Channel 1 = Kraft 1000kN
Color = Red
Style = Solid
Scaling = Linear
Minimum = 0.000000 kN
Maximum = 0.500000 kN
X Axis Level Cross = Not Enabled
Y Axis Level Cross = Not Enabled
Reduce Rate on Decimation = Not Enabled

Displacement vs. Time Plot : Run-time Plotting
Start Trigger = Step Start
End Trigger = <none>
Title = Displacement vs. Time
X Axis = X
Channel = Time
Scaling = Linear
Minimum = 0.000000 Sec
Maximum = 30.000000 Sec
Y Axis = Y
Channel 1 = Weg
Color = Red
Style = Solid
Scaling = Linear
Minimum = 0.000000 micron
Maximum = 10.000000 micron
X Axis Level Cross = Not Enabled
Y Axis Level Cross = Not Enabled
Reduce Rate on Decimation = Enabled

Start : Operator Event
Start Trigger = Step Start
End Trigger = <none>
Button ID = Button 1
Single Shot = Yes
Button Label = Start
Description =
Grab Focus = Yes

Load or Strain Control Ramp : Run-time Rate Control
Start Trigger = Start
End Trigger = Button: Unload
Segment Shape = Ramp
Visible at Run Time = 1
Record Data = 1
Axial
Control Mode = Weg SG
Rate Type = 0.200000 mm/Min
Minimum Rate = 0.000100 mm/Min
Maximum Rate = 0.500000 mm/Min
Endlevel = 4.8 (mm)

Button: Unload : Operator Event
Start Trigger = Step Start
End Trigger = <none>
Button ID = Button 2
Single Shot = Yes
Button Label = Unload
Description = press to initiate unloading
Grab Focus = Yes

Button: Operator Terminate the Test : Operator Event
Start Trigger = Step Start
End Trigger = <none>
Button ID = Button 3
Single Shot = Yes
Button Label = Terminate
Description = Press to terminate the test
Grab Focus = Yes

Unloading : Run-time Rate Control
Start Trigger = Load or Strain Control Ramp
End Trigger = <none>
Segment Shape = Ramp
Visible at Run Time = 0
Record Data = 1
Axial
Control Mode = Weg SG
Rate Type = 1.000000 mm/Sec
Minimum Rate = 0.000000 mm/Sec
Maximum Rate = 5.000000 mm/Sec
Endlevel = 0 (mm)

Switch to Stroke Control : Step
Step Done Trigger 1 = Mode Switch

Mode Switch : Hold Command
Start Trigger = Step Start
End Trigger = <none>
Hold Time = 0.1 (Sec)
Axial
Control Mode = Weg SG

Specimen Post-test Information : Step
Step Done Trigger 1 = Stop Current Test

Post-test Specimen Information : Data Input
Start Trigger = Step Start
End Trigger = <none>
Window = Post-test Specimen Data Input
Utilization = Process Parameterization and Execution

Stop Current Test : Program Control
Start Trigger = Post-test Specimen Information
End Trigger = <none>
Action = Program Stop
Message =
Screen = Yes
LUC Display = No
Data File = No

For each specimen : End Loop

D.2.2 Template (pressure vessel)

Procedure Name =
File Specification = D:\
Software Version = 4.0D

Data File Options
File Format = Plain Text File
Log Events = Yes
Include Procedure Description = Yes

Recovery Options
Autosave enabled.
On step done

Sample Information : Step
Step Done Trigger 1 = Sample Information

Sample Information : Data Input
Start Trigger = Step Start
End Trigger = <none>
Window = Additional Data Input
Utilization = Process Parameterization and Execution

Specimen Pre-test Information : Step
Step Done Trigger 1 = Query Start Test

Query Start Test : Operator Event
Start Trigger = Step Start
End Trigger = <none>
Button ID = Button 1
Single Shot = Yes
Button Label = Start
Description = Press to start.
Grab Focus = Yes

Test Execution : Step
Step Done Trigger 1 = Terminate Button
Step Done Trigger 2 = UNLOADING: confinement

Terminate Button : Operator Event
Start Trigger = Step Start
End Trigger = <none>
Button ID = Button 3
Single Shot = Yes
Button Label = Terminate
Description = Press to terminate the test.
Grab Focus = Yes

Data Collection : Data Acquisition
Start Trigger = Step Start
End Trigger = <none>
Mode = Timed
Buffer Type = Continuous
Master Channel = Time
Slave Channel 1 = Weg
Slave Channel 2 = Kraft 1000kN
Data Header = Begin Level Crossing Data Acq.
Time Increment = 0.5 (Sec)
Buffer Size = 2048

PLOT: Force vs. Time : Run-time Plotting
Start Trigger = Step Start
End Trigger = <none>
Title = Force vs. Time
X Axis = X
Channel = Time
Scaling = Linear
Minimum = 0.000000 Sec
Maximum = 30.000000 Sec
Y Axis = Y
Channel 1 = Kraft 1000kN
Color = Red
Style = Solid
Scaling = Linear
Minimum = 0.000000 N
Maximum = 500.000000 N
X Axis Level Cross = Not Enabled
Y Axis Level Cross = Not Enabled
Reduce Rate on Decimation = Not Enabled

PLOT: Displacement vs. Time : Run-time Plotting
Start Trigger = Step Start
End Trigger = <none>
Title = Displacement vs. Time
X Axis = X
Channel = Time
Scaling = Linear
Minimum = 0.000000 Sec
Maximum = 30.000000 Sec

Y Axis = Y
Channel 1 = Weg
Color = Red
Style = Solid
Scaling = Linear
Minimum = 0.000000 mm
Maximum = 0.002000 mm
X Axis Level Cross = Not Enabled
Y Axis Level Cross = Not Enabled
Reduce Rate on Decimation = Enabled

PLOT: Confinement vs. Time : Run-time Plotting
Start Trigger = Step Start
End Trigger = <none>
Title = Confinement vs. Time Plot
X Axis = X
Channel = Time
Scaling = Linear
Minimum = 0.000000 Sec
Maximum = 30.000000 Sec
Y Axis = Y
Channel 1 =
Color = Red
Style = Solid
Scaling = Linear
Minimum = 0.000000 (none)
Maximum = 0.010000 (none)
X Axis Level Cross = Not Enabled
Y Axis Level Cross = Not Enabled
Reduce Rate on Decimation = Not Enabled

LOAD BUTTON: initiate initial loading : Operator Event
Start Trigger = Step Start
End Trigger = <none>
Button ID = Button 1
Single Shot = Yes
Button Label = AXIAL
Description = Press to initiate initial axial loading.
Grab Focus = Yes

LOAD RAMP: Initial loading : Run-time Rate Control
Start Trigger = LOAD BUTTON: initiate initial loading
End Trigger = LOAD DETECTOR: max. Force
Segment Shape = Ramp
Visible at Run Time = 1
Record Data = 1
Axial
Control Mode = Weg SG
Rate Type = 0.200000 mm/Min
Minimum Rate = 0.000010 mm/Min
Maximum Rate = 1.000000 mm/Min
Endlevel = 10 (mm)
LOAD DETECTOR: max. Force : Data Limit Detector
Start Trigger = LOAD BUTTON: initiate initial loading
End Trigger = <none>
Data Channel = Kraft 1000kN
Limit Value = 5 (kN)
Limit Value is = Absolute
Detector Options = Either Transition
Trigger Option = Trigger Once

LOAD STOP: hold axial loading : Hold Command
Start Trigger = LOAD RAMP: Initial loading
End Trigger = <none>
Hold Time = 5 (Sec)
Axial
Control Mode = Weg SG

CONF. BUTTON: Start Applying Confinement : Operator Event
Start Trigger = LOAD STOP: hold axial loading
End Trigger = <none>
Button ID = Button 2
Single Shot = Yes
Button Label = PRESSURE
Description = Press to apply confining pressure.
Grab Focus = Yes

CONF. RAMP: Applying Confining Pressure : Monotonic Command
Start Trigger = CONF. BUTTON: Start Applying Confinement
End Trigger = <none>
Segment Shape = Ramp
Rate = 0.0001666667 MPa/s
Druck
Control Mode = Druck SG
End level = 0.02 MPa

CONF HOLD: hold pressure : Hold Command
Start Trigger = CONF. RAMP: Applying Confining Pressure
End Trigger = <none>
Hold Time = 5 (Sec)
Druck
Control Mode = Druck SG

TEST BUTTON: Start Testing : Operator Event
Start Trigger = CONF HOLD: hold pressure
End Trigger = <none>
Button ID = Button 1
Single Shot = Yes
Button Label = START
Description = Press to start the axial ramp
Grab Focus = Yes

TEST RAMP: Load or Strain Control Ramp : Run-time Rate Control
Start Trigger = TEST BUTTON: Start Testing
End Trigger = TEST STOP BUTTON
Segment Shape = Ramp
Visible at Run Time = 1
Record Data = 1
Axial
Control Mode = Weg SG
Rate Type = 0.200000 mm/Min
Minimum Rate = 0.000100 mm/Min
Maximum Rate = 1.000000 mm/Min
Endlevel = 6 (mm)

TEST STOP BUTTON : Operator Event
Start Trigger = TEST BUTTON: Start Testing
End Trigger = <none>
Button ID = Button 2
Single Shot = Yes
Button Label = UNLOAD
Description = Press to initiate unloading.
Grab Focus = Yes

UNLOADING: confinement : Monotonic Command
Start Trigger = TEST RAMP: Load or Strain Control Ramp
End Trigger = <none>
Segment Shape = Ramp
Rate = 0.0003333333 ((none))
Druck
Control Mode = Druck SG
End level = 0.005 MPa

D.2.3 Cyclic loading

Procedure Name =
File Specification = D:\
Software Version = 4.0D

Data File Options
File Format = Plain Text File
Log Events = Yes
Include Procedure Description = Yes

Recovery Options
Autosave enabled.
On step done

Sample Information : Step
Step Done Trigger 1 = Sample Information

Sample Information : Data Input
Start Trigger = Step Start
End Trigger = <none>
Window = Additional Data Input
Utilization = Process Parameterization and Execution

Specimen Pre-test Information : Step
Step Done Trigger 1 = Query Start Test

Query Start Test : Operator Event
Start Trigger = Step Start
End Trigger = <none>
Button ID = Button 1
Single Shot = Yes
Button Label = Start
Description = Press to start the test
Grab Focus = Yes

Preloading : Step
Step Done Trigger 1 = Terminate Button
Step Done Trigger 2 = CONF HOLD: hold pressure

Terminate Button : Operator Event
Start Trigger = Step Start
End Trigger = <none>
Button ID = Button 3
Single Shot = Yes
Button Label = Terminate
Description = Press to terminate the test.
Grab Focus = Yes

Data Collection : Data Acquisition
Start Trigger = Step Start
End Trigger = <none>
Mode = Timed
Buffer Type = Continuous
Master Channel = Time
Slave Channel 1 = Weg
Slave Channel 2 = Kraft 1000kN
Slave Channel 3 = Druck
Data Header = Begin Level Crossing Data Acq.
Time Increment = 0.5 (Sec)
Buffer Size = 2048

PLOT: Force vs. Time : Run-time Plotting
Start Trigger = Step Start
End Trigger = <none>
Title = Force vs. Time
X Axis = X
Channel = Time
Scaling = Linear
Minimum = 0.000000 Sec
Maximum = 30.000000 Sec
Y Axis = Y
Channel 1 = Kraft 1000kN
Color = Red
Style = Solid
Scaling = Linear
Minimum = 0.000000 N
Maximum = 500.000000 N
X Axis Level Cross = Not Enabled
Y Axis Level Cross = Not Enabled
Reduce Rate on Decimation = Not Enabled

PLOT: Displacement vs. Time : Run-time Plotting
Start Trigger = Step Start
End Trigger = <none>
Title = Displacement vs. Time
X Axis = X
Channel = Time
Scaling = Linear
Minimum = 0.000000 Sec
Maximum = 30.000000 Sec
Y Axis = Y
Channel 1 = Weg
Color = Red
Style = Solid
Scaling = Linear
Minimum = 0.000000 mm
Maximum = 0.002000 mm
X Axis Level Cross = Not Enabled
Y Axis Level Cross = Not Enabled
Reduce Rate on Decimation = Enabled

PLOT: Confinement vs. Time : Run-time Plotting
Start Trigger = Step Start
End Trigger = <none>
Title = Confinement vs. Time Plot
X Axis = X
Channel = Time
Scaling = Linear
Minimum = 0.000000 Sec
Maximum = 30.000000 Sec
Y Axis = Y
Channel 1 = Druck
Color = Red
Style = Solid
Scaling = Linear
Minimum = 0.000000 MPa
Maximum = 0.010000 MPa
X Axis Level Cross = Not Enabled
Y Axis Level Cross = Not Enabled
Reduce Rate on Decimation = Not Enabled

LOAD BUTTON: initiate initial loading : Operator Event
Start Trigger = Step Start
End Trigger = <none>
Button ID = Button 1
Single Shot = Yes
Button Label = AXIAL
Description = Press to initiate initial axial loading.
Grab Focus = Yes

LOAD RAMP: Initial loading : Run-time Rate Control
Start Trigger = LOAD BUTTON: initiate initial loading
End Trigger = LOAD DETECTOR: max. Force
Segment Shape = Ramp
Visible at Run Time = 1
Record Data = 1
Axial
Control Mode = Weg SG
Rate Type = 0.200000 mm/Min
Minimum Rate = 0.000010 mm/Min
Maximum Rate = 1.000000 mm/Min
Endlevel = 10 (mm)

LOAD DETECTOR: max. Force : Data Limit Detector
Start Trigger = LOAD BUTTON: initiate initial loading
End Trigger = <none>
Data Channel = Kraft 1000kN
Limit Value = 5 (kN)
Limit Value is = Absolute
Detector Options = Either Transition
Trigger Option = Trigger Once

LOAD STOP: hold axial loading : Hold Command
Start Trigger = LOAD RAMP: Initial loading
End Trigger = <none>
Hold Time = 5 (Sec)
Axial
Control Mode = Weg SG

CONF. BUTTON: Start Applying Confinement : Operator Event
Start Trigger = LOAD STOP: hold axial loading
End Trigger = <none>
Button ID = Button 2
Single Shot = Yes
Button Label = PRESSURE
Description = Press to apply confining pressure.
Grab Focus = Yes

CONF. RAMP: Applying Confining Pressure : Monotonic Command
Start Trigger = CONF. BUTTON: Start Applying Confinement
End Trigger = <none>
Segment Shape = Ramp
Rate = 0.00025 ((none))
Druck
Control Mode = Druck SG
End level = 0.04 MPa

CONF HOLD: hold pressure : Hold Command
Start Trigger = CONF. RAMP: Applying Confining Pressure
End Trigger = <none>
Hold Time = 5 (Sec)
Druck
Control Mode = Druck SG

Cyclic loading : Begin Loop
Counter Name = loop
Total Count = 50

Test Execution : Step
Step Done Trigger 1 = Terminate Button
Step Done Trigger 2 = Hold

Terminate Button : Operator Event
Start Trigger = Step Start
End Trigger = <none>
Button ID = Button 3
Single Shot = Yes
Button Label = Terminate
Description = Press to terminate the test.
Grab Focus = Yes

Data Collection : Data Acquisition
Start Trigger = Step Start
End Trigger = <none>
Mode = Timed
Buffer Type = Continuous
Master Channel = Time
Slave Channel 1 = Weg
Slave Channel 2 = Kraft 1000kN
Slave Channel 3 = Druck
Data Header = Begin Level Crossing Data Acq.
Time Increment = 0.5 (Sec)
Buffer Size = 2048

PLOT: Force vs. Time : Run-time Plotting
Start Trigger = Step Start
End Trigger = <none>
Title = Force vs. Time
X Axis = X
Channel = Time
Scaling = Linear
Minimum = 0.000000 Sec
Maximum = 30.000000 Sec
Y Axis = Y
Channel 1 = Kraft 1000kN
Color = Red
Style = Solid
Scaling = Linear
Minimum = 0.000000 N
Maximum = 500.000000 N
X Axis Level Cross = Not Enabled
Y Axis Level Cross = Not Enabled
Reduce Rate on Decimation = Not Enabled

PLOT: Displacement vs. Time : Run-time Plotting
Start Trigger = Step Start
End Trigger = <none>
Title = Displacement vs. Time
X Axis = X
Channel = Time
Scaling = Linear
Minimum = 0.000000 Sec
Maximum = 30.000000 Sec
Y Axis = Y
Channel 1 = Weg
Color = Red
Style = Solid
Scaling = Linear
Minimum = 0.000000 mm
Maximum = 0.002000 mm
X Axis Level Cross = Not Enabled
Y Axis Level Cross = Not Enabled
Reduce Rate on Decimation = Enabled

PLOT: Confinement vs. Time : Run-time Plotting
Start Trigger = Step Start
End Trigger = <none>
Title = Confinement vs. Time Plot
X Axis = X
Channel = Time
Scaling = Linear
Minimum = 0.000000 Sec
Maximum = 30.000000 Sec
Y Axis = Y
Channel 1 = Druck
Color = Red
Style = Solid
Scaling = Linear
Minimum = 0.000000 MPa
Maximum = 0.010000 MPa
X Axis Level Cross = Not Enabled
Y Axis Level Cross = Not Enabled
Reduce Rate on Decimation = Not Enabled

TEST BUTTON: Start Testing : Operator Event
Start Trigger = Step Start
End Trigger = <none>
Button ID = Button 1
Single Shot = Yes
Button Label = START
Description = Press to start the axial ramp
Grab Focus = Yes

TEST RAMP: Load or Strain Control Ramp : Run-time Rate Control
Start Trigger = TEST BUTTON: Start Testing
End Trigger = TEST STOP BUTTON
Segment Shape = Ramp
Visible at Run Time = 1
Record Data = 1
Axial
Control Mode = Weg SG
Rate Type = 0.200000 mm/Min
Minimum Rate = 0.000100 mm/Min
Maximum Rate = 1.000000 mm/Min
Endlevel = 10 (mm)

TEST STOP BUTTON : Operator Event
Start Trigger = TEST BUTTON: Start Testing
End Trigger = <none>
Button ID = Button 2
Single Shot = Yes
Button Label = UNLOAD
Description = Press to initiate unloading.
Grab Focus = Yes

UNLOADING : Monotonic Command
Start Trigger = TEST RAMP: Load or Strain Control Ramp
End Trigger = unloading limit
Segment Shape = Ramp
Rate = 0.2 mm/Min
Axial
Control Mode = Weg SG
End level = 0 (mm)

unloading limit : Data Limit Detector
Start Trigger = TEST STOP BUTTON
End Trigger = <none>
Data Channel = Kraft 1000kN
Limit Value = 100 (kN)
Limit Value is = Absolute
Detector Options = Either Transition
Trigger Option = Trigger Once

Hold : Hold Command
Start Trigger = UNLOADING
End Trigger = <none>
Hold Time = 5 (Sec)
Axial
Control Mode = Weg SG

Cyclic loading : End Loop

Unloading : Step
Step Done Trigger 1 = CONF: Unload

Unload : Operator Event
Start Trigger = Step Start
End Trigger = <none>
Button ID = Button 1
Single Shot = Yes
Button Label = Unload
Description =
Grab Focus = Yes

CONF: Unload : Monotonic Command
Start Trigger = Unload
End Trigger = <none>
Segment Shape = Ramp
Rate = 0.00025 ((none))
Druck
Control Mode = Druck SG
End level = 0.005 MPa

E DISPLACEMENT EXTRAPOLATION TECHNIQUE – REFERENCE PLOTS

Refer to Chapter 5.1 and Figure 5-6 for explanation.

E.1 Äspö Diorite

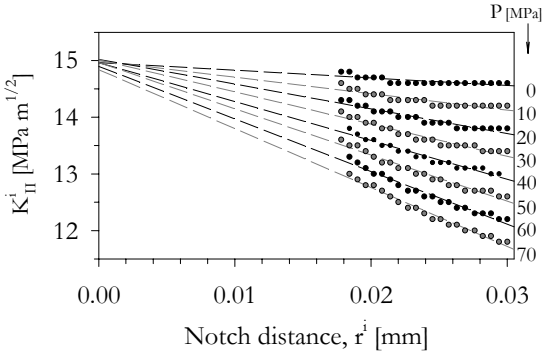

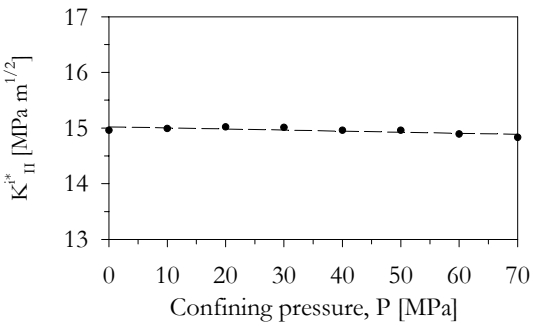

E.2 Aue Granite

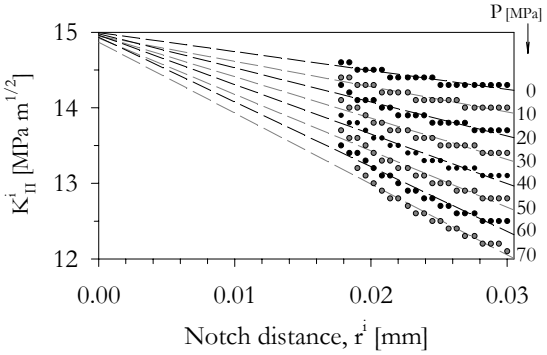

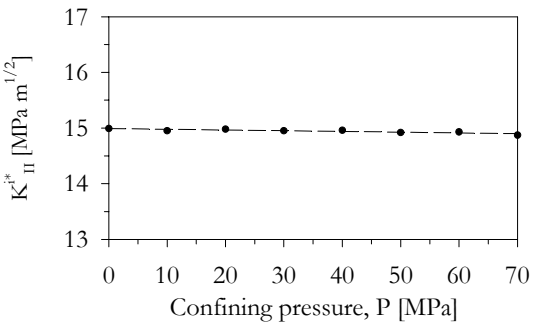

E.3 Carrara Marble

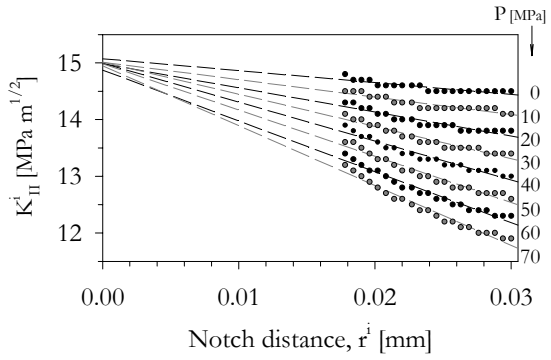

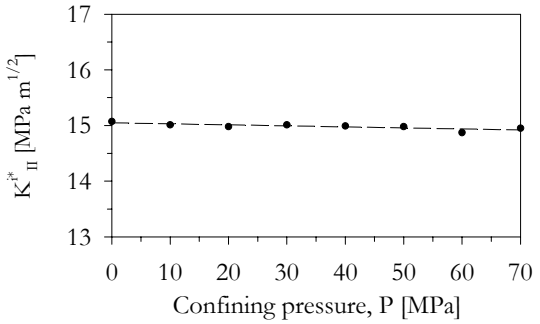

E.4 Flechtingen Sandstone

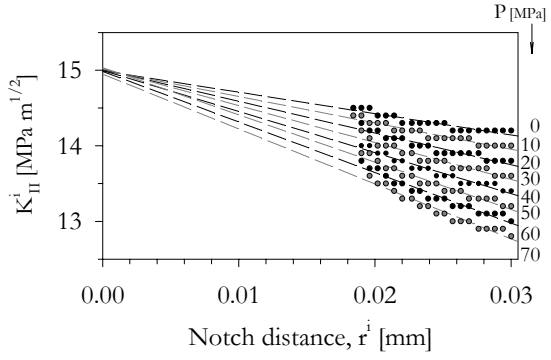

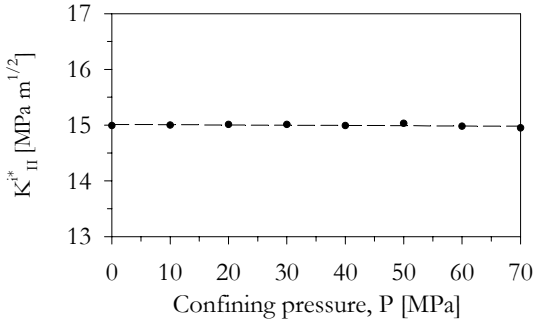

E.5 Rüdersdorf Limestone

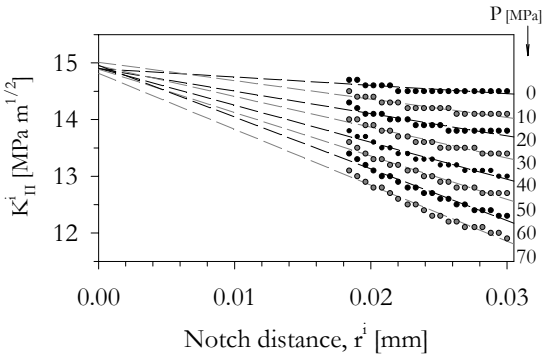

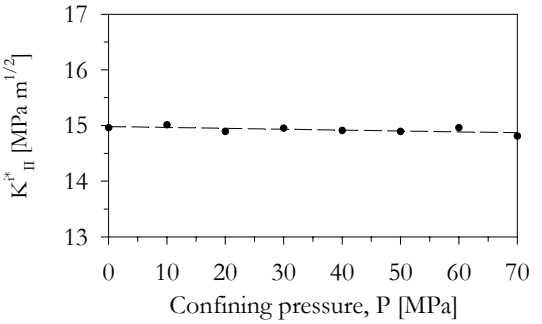

NOTATIONS & ABBREVIATIONS

α	angle
β	regression parameter for K_{II} determination
γ	crack surface energy
γ_{xy}	shear strain
δ_F	maximum load point displacement
δ'_F	load point displacement rate, δ_F/t_C
ΔF	force drop
Δy	distance from the notch tip
$\Delta\tau$	difference in shear stress
Δu	difference in displacement
ζ	ratio K^0_{IIC}/K_{IC}
ν	Poisson's ratio
θ	angle
ϱ	dry density
σ	stress
σ_A	applied stress
σ_{axial}	axial stress
σ_B	stress at crack tip
σ_C	Uniaxial Compressive Strength, UCS
σ_{CT}	stress at crack tip
σ_F	failure stress
σ_{ij}	stress tensor
σ_N	normal stress
σ'_N	effective normal stress
σ_t/σ_T	tensile strength
τ	shear stress
τ_C	shear strength
τ_R	residual shear strength
φ	porosity
χ	ratio of K_{IIC}/K_{IC}
ω	regression parameter for K_{II} determination
a	half crack length (*fracture mechanics*)
a	upper notch depth (*sample)*
a'	fracture velocity
A	amplitude parameter
A	area
a_0	Chevron tip position
a_L	average fracture speed
a_{AE}	average AE propagation velocity
AE	acoustic emission
b	lower notch depth
c	crack length
CB	Chevron Bend
COD	clip gage opening displacement
D	diameter (*sample*)
D	fractal dimension (*fractal*)
d_C	breakdown displacement
E	Young's modulus
E'	Young's modulus for plane strain or plane stress conditions
EOR	enhanced oil recovery
e_{xy}	infinitesimal shear strain
fbz	fracture breakdown zone
F	force
f_{ij}	geometric stress factor
F_{max}	maximum force
FPZ	fracture process zone
gd_{av}	average grain diameter
gd_{max}	maximum grain diameter
g	grain size
G	Energy Release Rate
G	shear modulus
IP	inner notch diameter
J	J-integral
k'	loading rate
K	stress intensity factor
K_C	fracture toughness
K_k	stress intensity factor
K_O	stress intensity factor threshold for subcritical crack growth
K_I	Mode I stress intensity factor
K_{II}	Mode II stress intensity factor
K_{III}	Mode III stress intensity factor
K_{kC}	fracture toughness
K_{IC}	Mode I fracture toughness
K_{ID}	Mode I dynamic fracture toughness
K_{IIC}	Mode II fracture toughness
K^0_{IIC}	Mode II fracture toughness at zero confining pressure
K^8_{IIC}	Mode II fracture toughness at high confining pressure
K_{IIIC}	Mode III fracture toughness
L	Specimen length
L_C	fracture length
lpd	load point displacement
P	confining pressure
p	plasticity correction factor
p_0	pore pressure
P_{TR}	transitional pressure
PTS	Punch Through Shear
r	distance (radius) from crack tip
s	length of fbz
S	support span
SR	Short Rod
S(w)	standard deviation of the reduced asperity height
t	notch width
t_C	corrected time
u	displacement
u_C	critical displacement
U	energy
UCS	Uniaxial Compressive Strength
v	displacement
w	sampling window size
W	sample height